# Modeling disks and jets around forming massive stars, and a look at a remnant neutron star

**Dissertation**

der Mathematisch-Naturwissenschaftlichen Fakultät

der Eberhard Karls Universität Tübingen

zur Erlangung des Grades eines

Doktors der Naturwissenschaften

(Dr. rer. nat)

vorgelegt von

Guillermo Andree Oliva Mercado

aus San Salvador/El Salvador

Tübingen

2022

Gedruckt mit Genehmigung der Mathematisch-Naturwissenschaftliche Fakultät der
Eberhard Karls Universität Tübingen

| | |
|---|---|
| Tag der mündlichen Qualifikation: | 21.10.2022 |
| Dekan: | Prof. Dr. Thilo Stehle |
| 1. Berichterstatter: | Prof. Dr. Rolf Kuiper |
| 2. Berichterstatter: | Prof. Dr. Klaus Werner |

# Zusammenfassung

Massereiche Sterne entstehen und entwickeln sich auf kurzen Zeitskalen verglichen mit ihren masseärmeren Geschwistern, aber ihre Effekte haben Einfluss auf mehreren Größenordungen im Universum. Sie entstehen durch den Gravitationskollaps von kaltem und dichtem Material in Molekülwolken. Ein entstehender massereicher Stern ist von einer Akkretionsscheibe umgeben, die auf Grund von Drehimpulserhaltung während des gravitativen Kollapses entsteht. Die Akkretionsscheibe kann so massereich werden, dass sie selbstgravitierend wird, Spiralarme ausbildet und fragmentiert. Magnetfelder in der Molekülwolke werden vom Gravitationskollaps und der Rotation mitgezogen und starten magnetisch angetriebene Ausströmungen. Diese Ausströmungen sind Ursprung mechanischer Rückwirkung auf die Sternentstehungsumgebung und entfernen Drehimpuls vom Protostern.

In dieser Arbeit erkunde ich, ob Begleitsterne um den entstehenden massereichen Stern durch die Fragmentation der Akkretionsscheibe entstehen können. Ich bearbeite diese Frage indem ich Strahlungshydrodynamik-Simulationen beginnend mit dem Kern einer Molekülwolke analysiere. Ich finde etwa sechs Begleitsterne verteilt in der inneren und äußeren Scheibe, wobei die nahen Begleitsterne auch spektroskopische Binärsterne sein können. Ich untersuche die Prozesse, die beteiligt sind am Starten, Beschleunigen, Ausbreitung und möglichen Stoppen der magnetisch angetriebenen Ausströmungen und untersuche die Effekte von Magnetfeldern auf die Akkretionsscheibe. Basierend auf einem Katalog von 30 Simulationen, die verschiedene Bedingungen für das Eintreten des Gravitationskollaps erkunden, präsentiere ich eine theoretische Erklärung wie die Umgebungsbedingungen in der Entstehung massereicher Sterne die Eigenschaften der Akkretionsscheibe und der Ausströmungen prägen. Außerdem vergleiche ich diese Ergebnisse mit aktuellen Beobachtungen eines Scheiben-Jet Systems um ein junges Sternobjekt in der Sternentstehungsumgebung IRAS 21078+5211.

Am Ende ihrer Entwicklung explodieren massereiche Sterne in einer Supernova. Dieser Prozess liefert schwere Elemente, die die Entstehungsumgebung künftiger Generationen von Sternen und Planeten mit diesen Elementen anreichern. Überreste massereicher Sterne sind kompakte Objekte; entweder Neutronensterne oder schwarze Löcher. Die Struktur von Neutronensternen ist ein ungelöstes Problem der Astrophysik auf Grund des unzureichenden Wissens über die Zustandsgleichung von dichter Kernmaterie. Neutronensterne werden üblicherweise in Form von Pulsaren beobachtet. Dies geschieht dank eines periodischen Signals, das von Hotspots auf der Oberfläche der Neutronensterne erzeugt wird während sie rotieren. Es wird erwartet, dass schnell rotierende Neutronensterne signifikant abgeflacht sind. Diese Abflachung kann approximativ durch das Quadrupolmoment der Masse ausgedrückt werden. Ich untersuche den Effekt des Quadrupolmoments auf die Pulsprofile und das thermische Spektrum mithilfe von Raumzeit Modellen, die darauf abzielen die äußere Raumzeit von schnell rotierenden Neutronensternen zu beschreiben.

# Abstract

Massive stars form and evolve in short times compared to their low-mass siblings, but their effects are felt across several scales in the universe. They form from the gravitational collapse of cold and dense material in molecular clouds. A forming massive star is surrounded by an accretion disk, formed thanks to the conservation of angular momentum during the gravitational collapse. The accretion disk can become massive enough to be self-gravitating and form spiral arms and fragments. Magnetic fields present in the molecular cloud are dragged by the gravitational collapse and rotation and launch magnetically-driven outflows. These outflows are sources of mechanical feedback into the natal environment, and remove angular momentum from the protostar.

In this work, I explore the possibility that the fragmentation of the accretion disk produces companion stars to the central forming massive star. I work in solving this question by analyzing radiation-hydrodynamical simulations of massive star formation from the collapse of a cloud core. I find around six companions distributed in the inner and outer disk, with the close companions having the possibility of becoming spectroscopic companions. I study the processes that intervene in the launching, acceleration, propagation and possible termination of the magnetically driven outflows, and the effects of the magnetic fields on the accretion disk. With a catalog of 30 simulations exploring different conditions for the onset of gravitational collapse, I propose a theoretical picture of how the environmental conditions for massive star formation determine the characteristics of the accretion disk and the outflows. Additionally, I compare those results with recent observations of a disk-jet system around a massive young stellar object in the star-forming region IRAS 21078+5211.

At the end of their evolution, massive stars explode as supernovae, capable of producing and delivering heavy elements that enrich the natal environment of future generations of stars and planets. Stellar remnants of massive stars are compact objects: neutron stars and black holes. The structure of neutron stars is an open problem in Astrophysics due to our insufficient knowledge about the equation of state of dense nuclear matter. Neutron stars are commonly observed as pulsars thanks to periodic signals arising from hotspots on their surfaces while they rotate. Rapidly rotating neutron stars are expected to be significantly flattened; such flattening can be described approximately in terms of a mass quadrupole moment. I use spacetime models that aim to describe the exterior spacetime of a rapidly-rotating neutron star in order to study the effects of the quadrupole moment on the pulse profiles and thermal spectrum.

# Contents

**List of publications** . . . . . 1

**1 Introduction: massive star formation** . . . . . 5
1.1 Massive stars and their importance in astrophysics . . . . . 5
1.2 Natal environment of massive stars . . . . . 6
1.2.1 Molecular clouds . . . . . 6
1.2.2 Massive pre-stellar cloud cores . . . . . 7
1.2.3 Density and angular momentum distribution in cloud cores . . . . . 8
1.2.4 Magnetic fields . . . . . 8
1.3 First and second Larson cores . . . . . 9
1.4 Accretion disks . . . . . 10
1.5 Outflows . . . . . 10
1.6 Arrival into the main sequence . . . . . 11
1.7 The multiplicity problem . . . . . 12

**2 Methods and theoretical background** . . . . . 13
2.1 Modeling matter around a forming massive star . . . . . 13
2.1.1 Magnetohydrodynamics (MHD) . . . . . 13
2.2 Radiation transport . . . . . 14
2.2.1 Stellar irradiation . . . . . 16
2.2.2 Diffusive radiation transport . . . . . 16
2.2.3 Solving for the radiation field . . . . . 17
2.2.4 Gravitational instabilities . . . . . 17
2.2.5 Flux freezing and Alfvén waves . . . . . 18
2.2.6 Magnetic diffusion . . . . . 20
2.2.7 Viscosity as a model for gravitational torques . . . . . 21
2.3 Classical theory of a magneto-centrifugally launched jet . . . . . 21
2.4 Magnetic tower flows . . . . . 22
2.5 Magnetic braking in a collapsing cloud . . . . . 23

**3 Formation of companions via disk fragmentation** . . . . . 25
3.1 Objectives and expected outcome . . . . . 25
3.2 State of the art in simulations . . . . . 25
3.3 Project setup . . . . . 26
3.3.1 Simulations . . . . . 26
3.3.2 Analysis tools . . . . . 26
3.4 Selected results and discussion . . . . . 28
3.4.1 Evolution of the system . . . . . 28
3.4.2 Fragmentation of the accretion disk . . . . . 28
3.4.3 From fragments to companions . . . . . 30

**4 Effects of magnetic fields on the accretion disk** . . . . . 33
4.1 Objectives and expected outcome . . . . . 33
4.2 State of the art in simulations . . . . . 33
4.3 Project setup . . . . . 34
4.3.1 Simulation setup . . . . . 34
4.3.2 Parameter space . . . . . 34
4.4 Selected results and discussion . . . . . 35

4.4.1 Evolution of the system . . . 35
4.4.2 Dynamics of the accretion disk . . . 36
4.4.3 Dependence of the resulting disk properties on initial cloud properties . . . 40

**5 The dynamics of massive protostellar outflows . . . 43**
5.1 Objectives and expected outcome . . . 43
5.2 State of the art in simulations . . . 43
5.3 Selected results and discussion . . . 44
5.3.1 Physical processes in the outflows . . . 44
5.3.2 Effects of resolution . . . 47
5.3.3 Variation of the properties of the outflow with the initial conditions . . . 48

**6 An observational example of a massive protostellar outflow . . . 49**
6.1 Description of the project and participation . . . 49
6.2 Objectives and expected outcome . . . 51
6.3 Results and discussion . . . 51
6.3.1 In search for a simulation match . . . 51
6.3.2 Launching of the jet . . . 52
6.3.3 Re-collimation of the jet . . . 53
6.3.4 Bow shock . . . 53

**7 A look at a stellar remnant: pulses from a neutron star . . . 55**
7.1 Context . . . 55
7.1.1 Endpoints of massive stellar evolution and supernovae . . . 55
7.1.2 Remnants: neutron stars . . . 56
7.1.3 Propagation of light around a neutron star . . . 57
7.1.4 Metrics . . . 58
7.2 Objectives and expected outcome . . . 58
7.3 Method overview . . . 59
7.4 Selected results and discussion . . . 60
7.4.1 Practical use of analytical metrics . . . 60
7.4.2 Thermal spectra . . . 60
7.4.3 Pulse profiles . . . 61

**8 Conclusions . . . 63**

**9 Acknowledgments . . . 65**

**A Accepted publications . . . 75**
A.1 Paper 1 . . . 77
A.2 Paper 2 . . . 99
A.3 Paper 3 . . . 113
A.4 Paper 4 . . . 131
A.5 Paper 5 . . . 151

# List of publications

This doctoral dissertation is presented in the form of a cumulative thesis with the publications and manuscripts detailed in this list. I briefly state my contributions to each article here, but a more complete statement can be found in the summary offered in each chapter dealing with results (ch. 3- 7), where I use the first person singular to refer to my own contributions, the first person plural to refer to collective conclusions, and the initials of an individual author to refer to their specific contribution.

## Accepted publications

### Paper 1

| | |
|---|---|
| Title: | **Modeling disk fragmentation and multiplicity in massive star formation** |
| Authors: | *G.A. Oliva* & R. Kuiper |
| Status: | Published |
| Journal: | Astronomy & Astrophysics |
| Volume: | 644 |
| Page: | A41 |
| Chapter in thesis: | 3 |
| Full text: | Appendix A.1 |

In the article that resulted from this project, we study the formation of companions to a massive star from the fragmentation of the accretion disk. My contributions to the manuscript are: post-processing of simulation data, fragment tracking, analysis of the dynamics of the fragments, estimation of multiplicity, analysis of the effects of resolution, generation of all graphs and illustrations, writing the manuscript.

### Paper 2

| | |
|---|---|
| Title: | **Snapshot of a magnetohydrodynamic disk wind traced by water maser observations** |
| Authors: | L. Moscadelli, A. Sanna, H. Beuther, *G.A. Oliva* & R. Kuiper |
| Status: | Published |
| Journal: | Nature Astronomy |
| Volume: | 6 |
| Page: | 1068 |
| Chapter in thesis: | 6 |
| Full text: | Appendix A.2 |

This article is the fruit of a collaboration between a team of observers (the first three authors) and theoreticians (the last two authors). We present the first direct observations of the launching region of a jet around a forming massive star, and compare the observed kinematics of the flow with the results of a very high resolution simulation that mostly matches the features observed. My contributions to this article are: performing the simulation and its dynamical analysis, exploration of the parameter space for choosing a snapshot close to the observations, comparison the observations and simulations, generation of figures that feature simulation data, writing appendix on the simulations and its comparison to the observed masers.

## Paper 3

| | |
|---|---|
| Title: | **Effects of the treatment of the mass quadrupole moment on ray-tracing applications for rapidly-rotating neutron stars** |
| Authors: | *G.A. Oliva* & F. Frutos-Alfaro |
| Status: | Published |
| Journal: | Monthly Notices of the Royal Astronomical Society |
| Volume: | 505 |
| Page: | 2870 |
| Chapter in thesis: | 7 |
| Full text: | Appendix A.3 |

In this article, I embark on my first independent research project in the field of neutron stars, stellar remnants from massive stars. We produce and utilize a catalog of metrics that aim to model the exterior spacetime around a neutron star and perform ray-tracing to calculate the relativistic corrections to the thermal spectra and the pulse profiles from hotspot emission. My contributions to the article are: conception the central idea: bringing multiple theoretical models of a spacetime (metrics) to possible observational tests (light curves, spectra); implementation of a general relativistic ray-tracing software package, generation of neutron star models, running the simulations in the chosen parameter space, analysis of the results, writing the manuscript.

## Paper 4

| | |
|---|---|
| Title: | **Modeling disks and magnetic outflows around a forming massive star: I. Investigating the two-layer structure of the accretion disk** |
| Authors: | *G.A. Oliva* & R. Kuiper |
| Status: | Accepted for publication |
| Journal: | Astronomy & Astrophysics |
| Chapter in thesis: | 4 |
| Full text: | Appendix A.4 |

For Paper 4 and Paper 5, we performed a series of 30 simulations of a forming massive star to study its associated disk-jet system. This manuscript focuses on the effects of the magnetic field on the disk physics. My contributions are: running the simulations in the parameter space explored, performing the dynamical analysis in the disk (finding and calculating quantities that uncover physical processes), data reduction in the parameter space, writing the manuscript.

## Paper 5

| | |
|---|---|
| Title: | **Modeling disks and magnetic outflows around a forming massive star: II. Dynamics of jets from massive protostars** |
| Authors: | *G.A. Oliva* & R. Kuiper |
| Status: | Accepted for publication |
| Journal: | Astronomy & Astrophysics |
| Chapter in thesis: | 5 |
| Full text: | Appendix A.5 |

This manuscript focuses on the physical processes in the magnetically-driven protostellar outflows. My contributions are: running the simulations in the parameter space explored, performing the dynamical analysis in the jet (finding and calculating quantities that uncover physical processes), data reduction in the parameter space, writing the manuscript.

# Other manuscripts (not included)

During my doctoral studies, I contributed to two additional, not-yet-accepted manuscripts that I decided not to include in this dissertation because of length concerns, and in order to highlight the results that I consider central to my doctoral research project in the document. For completeness, however, I briefly describe the additional collaboration articles as follows.

## Paper 6

| | |
|---|---|
| Title: | **Modelling the formation of massive multiple stellar systems** |
| Authors: | R. Mignon-Risse, *G.A. Oliva*, M. González, R. Kuiper & B. Commerçon |
| Status: | Submitted |
| Journal: | Astronomy & Astrophysics |
| Summary: | In this study, we compare the results of the simulations in Oliva and Kuiper (2020) and Mignon-Risse et al. (2021b) in order to assess the differences produced by the numerical methods as implemented in the codes `Pluto/Belt` and `RAMSES`, respectively. We find some discrepancies in the orbits of the companions produced by disk fragmentation and how disk fragmentation begins in the first place. We explore several possible explanations to those discrepancies, and present the agreements between our results. |
| Contribution: | production of graphs for comparison with the results by Mignon-Risse et al. (2021b), analysis of the results of the comparison, finding possible explanations for the differences. |

## Paper 7

| | |
|---|---|
| Title: | **On gravitational trapping and ram pressure trapping of ultracompact and hypercompact HII regions** |
| Authors: | L. Martini, *G.A. Oliva* & R. Kuiper |
| Status: | Ready for submission |
| Summary: | We perform simulations of the formation and growth of HII regions driven by a forming massive star, in a similar setup to Kuiper and Hosokawa (2018) but omitting the artificial injection of jets on purpose. We find that ram pressure is able to hinder the growth of HII regions in a way consistent to the observed ultracompact and hypercompact phases. |
| Contribution: | In this project, I acted as a co-supervisor of the Master student Lauren Martini (LM). I helped and advised LM in techniques for the analysis of the results and wrote the methods section of the manuscript. |

# 1 Introduction: massive star formation

## 1.1 Massive stars and their importance in astrophysics

A star is described as massive if it contains sufficient mass to produce a compact object (either a neutron star or a black hole) as a stellar remnant at the end of its life. To this end, the stellar mass at the start of the main sequence must exceed around eight times the mass of the Sun. Massive stars develop and evolve in shorter timescales compared to their low-mass counterparts: even though they possess more material to be used for nuclear reactions, those reactions happen at a faster rate than for low mass stars. Similarly, their formation occurs faster because of the stronger gravitational force, and it requires the rapid accumulation of high density material in the star-forming region in the first place. These factors mean that massive stars are relatively rare to observe in the present-day galactic environment, and it is particularly difficult to capture the first stages of their formation (for an introduction to the challenges in understanding massive star formation see, e.g., Zinnecker and Yorke, 2007).

The effects of massive stars on their environment are important for several other astrophysical processes. Massive stars enrich the interstellar medium with heavy elements through the supernova explosions that occur at the endpoint of their evolution. Only a massive enough stellar core is able to provide the energy needed for nucleosynthesis beyond iron at the point of its final gravitational collapse. The increase in ambient metallicity directly impacts the formation of other stars and planets, for example, providing the necessary elements and molecules for the formation of planets that could sustain life. Present-day massive star formation itself is affected by the chemical imprint from previous generations of massive stars: forming massive stars in our galaxy exert stronger radiation pressure onto the material that flows towards them. The heavy elements and dust present in the medium interact more strongly with radiation at high frequencies, and particularly at certain lines in ultraviolet; see §2.2 for more details. In contrast, primordial massive stars seen in distant galaxies are able to reach higher masses than their current counterparts because of the reduced impact of radiation pressure during their formation (for a discussion of the effects of metallicity in massive star formation, see e.g. Vink, 2018).

Figure 1.1 illustrates the different length scales involved in star formation. Stars form from the gravitational collapse of gas and dust in dense cores of molecular clouds, although the transfer of matter from large to small scales is not fully understood in the case of massive stars. The material is delivered to the protostar through an accretion disk that forms around it. Massive protostars thrust material outwards through magnetically-driven outflows originating from the surrounding accretion disks in a process that I explore in detail in the following chapters. The magnetically-driven outflows inject momentum back into the molecular cloud, an example of mechanical *stellar feedback*. Contrary to low-mass stars, massive stars continue their accretion phase even after they start burning hydrogen in their cores. If a star were to form from the radial collapse of material without rotation, the Eddington luminosity limit would be easily reached. Order of magnitude calculations yield that radiation pressure would already halt the collapse when the protostellar mass is about $30\,M_\odot$ assuming an accretion rate of $10^{-3}\,M_\odot\,yr^{-1}$ (see Bodenheimer, 2011, §5.2). Rotation, through the formation of the accretion disk and the subsequent opportunity for outflows to escape along the rotation axis, provides a key way to circumvent of the halting effect of radiation pressure (Kuiper et al., 2010).

When the hydrogen-burning phase starts in the stellar core, ultraviolet radiation is emitted by the young massive star, photoionizing the surrounding hydrogen-rich infalling envelope. This creates an HII region that expands over time. HII regions, in addition to stellar winds, provide an important source of stellar feedback onto the natal environments. They combine

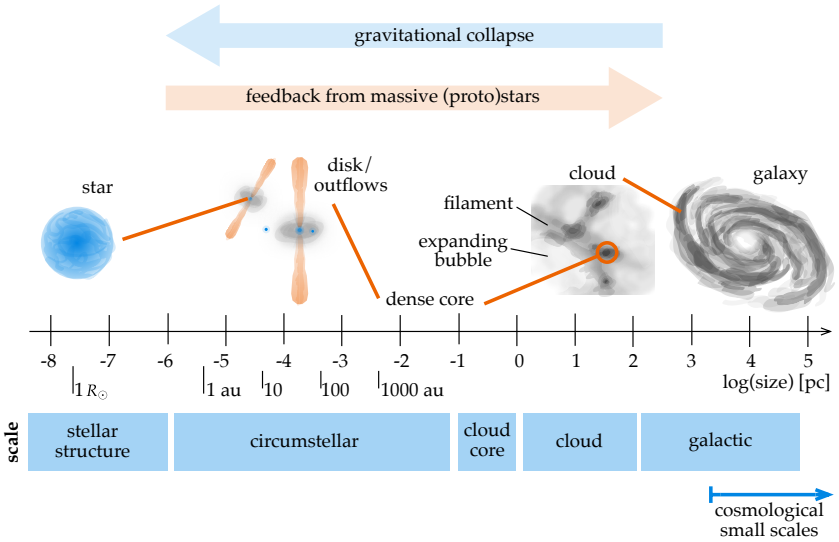



Figure 1.1: Typical scales in massive star formation. The gravitational collapse proceeds from large to small scales, while the feedback processes from the formation of massive stars and from their subsequent supernova explosions influence the medium from small to large scales.

into bubbles and expand through the interstellar medium, reaching large scales in the greater molecular cloud and disrupting and triggering further star formation in the process. For recent observational examples of expanding HII regions and their role in star formation, see Beuther et al. (2022), Luisi et al. (2021) and Duronea et al. (2017). For theoretical models, see e.g., Seifried et al. (2020), Kuiper and Hosokawa (2018), Raskutti et al. (2017) and Raskutti et al. (2016).

Massive stars drive several kinds of stellar winds, specially in solar- to high-metallicity environments. Ultraviolet line-driven winds from young massive stars have been shown to limit accretion from the disk through a process called *disk ablation* (Kee and Kuiper, 2019), thus determining the final mass of the newly-formed star. The influence of the massive star on its environment takes up a renewed role in the late stages of their evolution. Mass loss increases when the giant phases are reached, and it is particularly strong for Wolf-Rayet stars (Smith, 2014). Finally, as discussed above, the supernova explosion injects mechanical feedback and brings newly-formed heavy elements into the interstellar medium. The joint ejected material from clusters of massive stars that undergo supernova explosions also forms expanding bubbles that drive turbulence in molecular clouds. These bubbles collide, resulting in matter distributed in the form of sheets or filaments that eventually form dense cores and induces further star formation. For examples of recent theoretical studies on the effects of supernova feedback in the dynamics of the galaxy and molecular clouds, see Izquierdo et al. (2021), Seifried et al. (2020) and Krause et al. (2013).

## 1.2 Natal environment of massive stars

### 1.2.1 Molecular clouds

Present-day star formation in the local universe occurs in clouds mostly composed of molecular hydrogen ($H_2$) and atomic helium, with the presence of metals (in this context, elements heavier than hydrogen), other molecules (such as CO, which is commonly used as a tracer for density; see Molyarova et al. 2017 as an example) and dust grains. They extend from scales of around 20 pc in the case of giant molecular clouds, to $\sim 0.1$ pc for their dense cloud cores. The number density of molecular hydrogen in the largest scales is of the order of $100\,\mathrm{cm}^{-3}$, increasing all the way to typical number densities of $10^5\,\mathrm{cm}^{-3}$ for the cloud cores. Across scales, temperatures remain of the order of 10 K, which is cold in comparison to the warm neutral and ionized

medium that fills most of the volume of the galactic disk. Even though molecular clouds are gravitationally bound, they are gravitationally collapsing. Considering a cloud core of typical density $\rho$ and temperature $T$, a simple order-of-magnitude calculation of the Jeans mass (see §2.2.4 for a proper definition and derivation) yields

$$M_J \approx 1.1\,\mathrm{M}_\odot \left[\frac{T}{10\,\mathrm{K}}\right]^{3/2} \left[\frac{\rho}{10^{-19}\,\mathrm{g\,cm^{-3}}}\right]^{-1/2} \tag{1.1}$$

and reveals that they are primarily supported by thermal pressure in the case of the formation of low-mass stars (a better approach would be to solve the hydrostatic equations, with which we would find a configuration called a *Bonnor–Ebert sphere*). Larger-scale molecular clouds, however, must be supported by other mechanisms. An analysis with the virial theorem and typical measured values for the velocity dispersion and magnetic field strength reveal that turbulence and magnetic pressure provide the required hydrostatic support. The typical velocity dispersion is of the order of a few kilometers per second, and is subsonic with respect to the warm galactic medium (sound speed: $\sim 10\,\mathrm{km\,s^{-1}}$) but supersonic with respect to the cold molecular medium (sound speed: $\sim 1\,\mathrm{km\,s^{-1}}$). Both turbulence and magnetic fields break the uniformity of the cloud, aiding in the production of elongated structures (sheets and filaments), according to simulations (Hennebelle and Inutsuka, 2019). After the decay of turbulence and the diffusion of magnetic fields, those structures gradually break into dense cloud cores where the gravitational collapse is eventually triggered. A more in-depth introduction to molecular clouds, including the analysis with the virial theorem and the sources for the typical measurements mentioned here, can be found in chapter 2 of Bodenheimer (2011).

### 1.2.2 Massive pre-stellar cloud cores

Dense pre-stellar cores with enough mass for the formation of low-mass stars have been observed and studied. However, no massive pre-stellar cores have been definitively observed so far, meaning that the determination of the initial conditions for massive star formation remains an open problem in astrophysics. From the theoretical point of view, it is not clear whether such objects exist, because they could not be supported by thermal pressure (cf. eq. 1.1), but instead they would need the support from highly supersonic turbulence or magnetic fields, as is the case in the larger scales.

Even though a few candidates for turbulent massive pre-stellar cores have been found (see e.g. Nony et al. 2018), there is mounting theoretical and observational evidence that they might not exist. In this scenario, the additional material is supplied to the already-collapsing cloud core from larger scales. From the theoretical perspective, smoothed particle hydrodynamics models by Smith et al. (2009) show the formation of massive stars but without pre-stellar cores in virial equilibrium. A similar conclusion was reached by the hierarchical collapse scenario studied by Vázquez-Semadeni et al. (2017). From the observational point of view, a study of two intermediate-to-high mass clumps in a molecular cloud conducted with the Atacama Large Millimeter/submillimeter Array (ALMA) by Redaelli et al. (2021) uncovered only the presence of subsonic turbulence, and thus support the scenario that the starless cores within the clumps are already collapsing but still accreting material from their parental environment. A similarly low turbulence level was found in Henshaw et al. (2014), where the authors study the dynamical properties of filaments in the dark cloud G035.39-00.33.

From the perspective of cloud cores with protostars, I cite the study by Beuther et al. (2018), within the context of the CORE large program, a survey carried out using the Northern Extended Millimeter Array (NOEMA). The program aimed to study fragmentation and disk formation within the context of nascent massive stars and included a sample of 20 high-mass star forming regions. A key finding of the program was that the separations between observed fragments was consistent with the Jeans thermal length, and supersonic turbulence was not needed to explain the distribution of fragments. Moreover, their results are consistent with a hierarchical

fragmentation scenario that is discussed in §1.7 and with the assumptions and findings reported in chapter 3.

### 1.2.3 Density and angular momentum distribution in cloud cores

The density distribution inside massive cloud cores has been estimated observationally. Beuther et al. (2002) investigated a large sample of 69 star-forming regions in early stages of massive star formation (most of them before the formation of the HII region) and found that the density of the infalling envelope can be fitted to a power law with an exponent of a mean value of $1.6 \pm 0.5$. A somewhat steeper mean value of $1.8 \pm 0.4$ was found by Mueller et al. (2002) by studying 51 dense cores. In the study of Hatchell and van der Tak (2003), which involved ten cores associated with massive star formation, a uniform distribution of power-law density profiles was found, with exponents ranging between 1.25 and 2.25.

The angular momentum content of the cloud core is decisive for the formation of disks and outflows around the forming massive star, as I show in §4.4.3 and 5.3.3. Analyzing a sample of 40 cores, Goodman et al. (1993) fitted linear gradients to the velocity fields of those cores which had signs of rotation. The cloud cores were found to roughly follow a solid-body rotation profile (i.e., uniform angular velocity), and contain a rotational energy that is of the order of a few per cent of their gravitational energy. The typical value found by the authors for the rotational-to-gravitational energy ratio is 0.02.

### 1.2.4 Magnetic fields

As discussed previously, magnetic fields are a major contributor of the gravitational support at large scales in the molecular cloud. The magnetic field is typically measured in terms of the *mass-to-flux ratio* defined as the ratio of the mass enclosed within a given surface and the magnetic flux that enters or exits such surface. This parameter can be conceptualized in a simple way by considering a spherical cloud of mass $M_C$ and radius $R$, threaded by a uniform magnetic field of magnitude $B$. The virial theorem including magnetic energy but ignoring kinetic and thermal energy is

$$E_B + E_g = 0, \tag{1.2}$$

where in this context $E_B$ and $E_g$ are the total magnetic and gravitational energies contained within the cloud, respectively. Disregarding adimensional factors of order unity, we see that

$$B^2R^3 - \frac{GM^2}{R} \sim 0 \implies B^2R^4 \sim GM^2. \tag{1.3}$$

The left hand side of the last similarity relation is also similar to the square of the magnetic flux through the midplane of the sphere ($\Phi \sim BR^2$). Then, the order-of-magnitude mass-to-flux ratio for a cloud close to equilibrium is

$$\frac{M}{\Phi} \sim \frac{1}{\sqrt{G}}. \tag{1.4}$$

This value is typically referred to as *critical* for the cloud. More detailed calculations by Mouschovias and Spitzer (1976) produce a critical mass-to-flux ratio of $(0.53/[3\pi]) \cdot \sqrt{5/G}$. Throughout this work, I use the parameter $\bar{\mu}$, the mass-to-flux ratio normalized to the critical value found by Mouschovias and Spitzer (1976). From the simple derivation of $\bar{\mu}$, one sees that subcritical values ($\bar{\mu} < 1$) mean that the gravitational collapse is completely prevented by the magnetic field, and supercritical values ($\bar{\mu} > 1$) mean gravitational instability.

The question of how cloud cores become supercritical has currently no clear and definitive answer. At the low densities of large molecular clouds, a process called *ambipolar diffusion*, which is discussed in more detail in §2.2.6, is responsible for the decoupling of magnetic fields and the flow. In a nutshell, the gas in molecular clouds is weakly ionized, which means that

there is a drift between the motion of the neutral species (that possess most of the mass) and the charged species (upon which the magnetic field acts). The drift is partially compensated by the collisions between charged particles and neutrals. This process means that the stabilizing effect of the magnetic field is only partial and the gravitational collapse at cloud core scales can still be triggered by the neutrals and followed by the charged particles. This scenario is described in, for example, Hennebelle and Inutsuka (2019). However, there is observational evidence that indicates that ambipolar diffusion is not the mechanism for the reduction in magnetic fields in low-mass pre-stellar cores (Ching et al., 2022), because the cores were found to be supercritical before being self-gravitating. An alternative to ambipolar diffusion to explain the observational results is turbulent magnetic reconnection.

The magnitudes of the magnetic field in low-mass pre-stellar cores have been found to be of the order of a few to tens of micro Gauss (Ching et al., 2022; Troland and Crutcher, 2008). These values imply mass-to-flux ratios of a few for low-mass star formation. Given the scarcity of information on the conditions for the onset of gravitational collapse in the high-mass case, at least two scenarios are possible (see the discussion in Machida and Hosokawa 2020):

a) that the mass-to-flux ratio scales with mass, which requires that high magnetic field values (of 100 to 1000 $\mu$G) be present in the cloud core prior to the gravitational collapse;

b) that the magnetic field strength in the high-mass case is similar to the low-mass case, which means that the mass-to-flux ratio must be high ($\bar{\mu} \gg 10$).

Both possibilities are explored in the next chapters.

In the small scales, magnetic fields are crucial for several reasons. They are the driving mechanisms of early protostellar outflows: the process of launch, acceleration, propagation and termination of those outflows is studied in detail in chapters 5 and 6. They add magnetic pressure in the accretion disk (chapter 4), which may reduce its fragmentation and thus the formation of multiple systems (§1.7). Conservation of angular momentum implies that the rotation rate of the protostar should continuously increase as the cloud contracts. Magnetic fields reduce angular momentum in the central parts of the cloud in a process known as magnetic braking (§2.5), which is thought to be crucial for a forming protostar not to reach rotation rates that would break it apart. Magnetically-driven protostellar outflows are also capable of removing angular momentum; the long-term contribution of both processes in massive protostars has not been extensively quantified yet.

## 1.3 First and second Larson cores

Once the gravitational collapse begins, material from large scales accumulates in the central parts of the cloud. At first, the gravitational collapse proceeds isothermally because the thermal emission from the dust grains present in the cloud core cools the material efficiently. The central density increases until the material becomes opaque and this cooling mechanism is not efficient anymore. Then, temperature and pressure increase in the dense central region and the collapse is almost halted: a hydrostatically-supported first (Larson) core is thus formed. Detailed calculations of the size and mass of the first core were performed by Bhandare et al. (2018) for a wide variety of cloud core masses. They found that the radius of the first core is of the order of 1 au, with a corresponding enclosed mass of the order of $10^{-2}\,\mathrm{M}_\odot$.

The gravitational collapse is not fully halted, but instead continues as an adiabatic process because the first core is unable to transfer energy outwards efficiently. At first, the adiabat has an index (specific heat ratio) of 5/3 (i.e., it behaves like a monoatomic gas), and then it changes to the diatomic value of 7/5 as the rotational degrees of freedom of the molecules get excited with temperature. The central temperature rises slowly, and eventually reaches $\sim 2000\,\mathrm{K}$. At those temperatures, the kinetic energy of the molecules is enough to break the bond of $H_2$ (*hydrogen dissociation*). Therefore, the energy supplied by the gravitational collapse

is used to dissociate hydrogen instead of increasing thermal energy and pressure. This allows the collapse to proceed (*second collapse*) until most of the $H_2$ has been dissociated and thermal pressure increases again. As a result, a second (Larson) core is formed. Bhandare et al. (2018) found that the second collapse occurs in a significantly shorter timescale (years for a solar mass cloud core) than the first collapse ($\sim 10\,000$ yr under the same conditions). The radii of second cores are found to be of the order of $10^{-2}$ au, that is, a few solar radii, and their temperatures increase to around $10^4$ K. Then, the core grows in size and mass through the main accretion phase until it reaches the conditions for nuclear reactions to start taking place (see §1.6 for a discussion on how the main sequence is reached).

## 1.4 Accretion disks

As a rotating cloud core collapses and its moment of inertia decreases, conservation of the total angular momentum implies that its angular velocity must increase. Locally, angular momentum is transferred from large to small scales until it is enough to move the material in a Keplerian-like orbit around the central forming massive star. Thus, a disk is formed. As it is explored in chapter 3, the disk has enough mass to be self-gravitating, and forms spiral arms and fragments. Those structures exert a gravitational torque on the gas that transports some angular momentum outwards, meaning that accretion happens through the disk onto the forming massive star (Kuiper et al., 2011). In fact, the accretion disk delivers most mass to the protostar, as the polar regions are occupied by outflows. The study of the fragmentation of the accretion disk is of special importance as a possible explanation to the origin of multiple systems (§1.7).

There are several observational examples of accretion disks around massive protostars or very young massive stars. As examples, I cite observations made by Johnston et al. (2015), Ilee et al. (2016), Cesaroni et al. (2017), Ginsburg et al. (2018) and Maud et al. (2019). Observations of the fragmentation occurring in those disks are rarer because of the higher angular resolution needed, the opacity of the infalling medium, and the requirement that the disk should be seen mostly face-on. However, there are some recent examples of such observations: spiral arms and signatures of gravitational instability were observed by Johnston et al. (2020) in a disk of $\sim$ 1000 au in radius around the O-type (proto)star AFGL 4176 mm1. Maud et al. (2019) reported substructures in a Keplerian disk around the O-type star G17.64+0.16. Ilee et al. (2018) observed a fragmented Keplerian disk around the O (proto)star G11.92-061 MM1a, with a fragment (MM1b) located near the outer part of the disk, at $\sim$ 2000 au from the primary. In Beuther et al. (2017), a disk-like structure was detected around the central object in the high-mass hot core G351.77-0.54, with a fragment located at about $\sim$ 1000 au from it.

## 1.5 Outflows

Outflows from the forming massive star propagate for large distances and are far easier to detect observationally than accretion disks. In fact, the presence of outflows in massive star-forming regions was for some time the best available evidence for the existence of accretion disks as a form for delivering mass to the protostar, compared to accretion through streamers formed by supersonic turbulence or other models (such as mergers) that rely less on the existence of an accretion disk.

There are different kinds of outflows. In chapter 5, I present an in-depth study of magnetically-driven outflows that are launched during the early stages of massive star formation. In a nutshell, the interaction between the disk and the magnetic field is capable of removing material from the surface and surroundings of the disk. I explore two mechanisms for which the formation of the magnetically-driven outflow is possible: the magneto-centrifugal launch of the material in a highly-collimated jet, and the slower and broader magnetic tower flow driven by magnetic pressure. In chapter 6, I discuss a recent effort that led to the direct observation of the

launching region of a jet around a massive protostar, and I present a thorough comparison of the observations with the results of one of the simulations performed during my doctoral studies. Apart from magnetically-driven outflows, radiation pressure drives outflows in different forms (HII regions, winds), as previously discussed in §1.1. Then, outflows from massive protostars are expected to be well collimated (jets) in the early stages of star formation; as HII regions and stellar winds appear at late stages, the outflows broaden (Beuther and Shepherd, 2005).

A catalog of 26 candidates of jets around young massive stellar systems was compiled by Purser et al. (2016), who used radio continuum observations. Guzmán et al. (2010) also performed radio observations of jets originating in a massive protostar in the star-forming region IRAS 16562-3959; Sanna et al. (2019) did it for the star-forming region G035.02+0.35. Synchrotron emission has been observed coming from the massive protostellar jets HH 80-81, Cep A HW2 and IRAS 21078+5211, presented respectively in the following studies: Carrasco-González et al. (2010), Carrasco-González et al. (2021) and Moscadelli et al. (2021). This non-thermal emission has been observed in regions at a few hundreds of astronomical units away from the source, and its origin was attributed by Carrasco-González et al. (2021) to the re-collimation of the jet due to magnetic forces. I explore this possibility in chapter 5.

## 1.6 Arrival into the main sequence

As I have highlighted in the preceding sections, the effects of radiation pressure are one of the most important obstacles to overcome for the formation of massive stars. Hosokawa and Omukai (2009) modeled the structure of massive protostars under the high accretion rates necessary for their formation ($\dot{M}_\star > 10^{-4}\,\mathrm{M_\odot\,yr^{-1}}$). The authors calculated evolutionary tracks with properties like the protostellar radius, luminosity and effective temperatures by solving the stellar structure equations without rotation and assuming a constant accretion rate. For the case of a high accretion rate of $10^{-3}\,\mathrm{M_\odot\,yr^{-1}}$, the protostar is found to undergo the following process:

a) *Adiabatic accretion*: as discussed in §1.3, when the central density is high enough, the material becomes opaque to radiation and it becomes unable to efficiently cool (the timescale for cooling is longer than the timescale for accretion). This means that the collapse proceeds adiabatically, or in other words, that its specific entropy remains constant. During this time, both the maximum temperature and the radius of the protostar increase slowly. The luminosity of the protostar is only due to accretion (i.e., it arises from the conversion of gravitational energy into radiant energy). This phase occurs when the mass of the protostar is below $6\,\mathrm{M_\odot}$.

b) *Swelling*: in the interval $6\,\mathrm{M_\odot} \lesssim M_\star \lesssim 10\,\mathrm{M_\odot}$, the outwards heat flow is not negligible anymore, a major redistribution of entropy occurs, and the stellar radius increases dramatically, eventually exceeding $100\,\mathrm{R_\odot}$. During the swelling phase, deuterium begins burning in the inner region of the nascent star.

c) *Kelvin–Helmholtz contraction*: the luminosity wave due to deuterium burning propagates outwards throughout the protostellar interior, and the energy flux eventually reaches the surface. Then, radiation escapes without absorption, with a corresponding decrease in the Kelvin-Helmholtz timescale. The luminosity from the protostar starts to become intrinsic (dominated by nuclear reactions) and surpasses the accretion luminosity. At this point, it becomes a young stellar object. With a more efficient cooling mechanism, the star contracts.

d) *Arrival to the main sequence*: with the preceding phase, the central temperature increases, reaching $10^7\,\mathrm{K}$. Then, the nuclear fusion of hydrogen begins, first with the pp-chain, and then quickly overtaken by the CNO cycle. After this, the star obeys main-sequence relations although accretion is still ongoing.

Contrary to low-mass stars, the steep temperature gradient in the central regions of massive stars makes their cores convective, while their envelopes are radiative. Given that the main ingredient for the standard $\alpha\Omega$ stellar dynamo theory is the presence of strong current loops arising from convection in the envelope, the origin of magnetic fields present in some massive stars remains an unsolved problem. A possibility is that the radiative envelope harbors fossil fields from the formation process, product of flux freezing (§2.2.5). The origin and production of magnetic fields in neutron stars, specially magnetars, is also not entirely clear. If it can be related to the progenitor star, there is a possibility that the environmental conditions for star formation could be able to influence or even determine the magnetic fields of their stellar remnants.

## 1.7 The multiplicity problem

Massive stars are observed in clusters, with a higher multiplicity than low-mass stars (Zinnecker and Yorke, 2007). As an example, the Orion OB1 association contains around 70 OB stars, from which 20% are spectroscopic binaries with periods of less than ten days (Morrell and Levato, 1991). However, an unsolved problem with active current research, is to tackle the question: how are such multiple systems formed?

One possibility is that they are formed by direct fragmentation of the cloud core. This, however, requires inhomogeneities to be present in the gas, either thanks to the original presence of overdensities in the cloud, or by the presence of highly supersonic turbulence that creates substructures like filaments. Even though there are several computational studies that explore the latter (e.g. Krumholz et al. 2007; Rosen et al. 2016 and Rosen and Krumholz 2020), the observational evidence from cloud cores increasingly points towards the first possibility (Beuther et al., 2018).

Assuming negligible turbulence, typical cloud core number densities between $10^5$ and $10^6\,\mathrm{cm}^{-3}$, and a temperature range between 20 and 50 K, the (thermal) Jeans length varies between 5500 and 28 000 au. Therefore, the companions produced by the fragmentation of the cloud are expected to have separations of a few thousands of astronomical units, as explained in Beuther et al. (2018). The formation of very close companions, such as spectroscopic multiples, would require fragmentation mechanisms at scales $< 1000$ au: one mechanism is the fragmentation of the accretion disk, a possibility that I examine in detail in chapter 3. In this scenario, fragmentation is a hierarchical process: first, molecular clouds fragment into cores, then, those cores fragment depending on their internal distribution of density and angular momentum, then, those core fragments form massive stars surrounded by accretion disks that fragment as well and close companions are born, then, the close companions form their own disks that fragment, and the same process continues in smaller and smaller scales.

# 2 Methods and theoretical background

## 2.1 Modeling matter around a forming massive star

### 2.1.1 Magnetohydrodynamics (MHD)

The gas and dust from the collapsing cloud core can be modeled as a single fluid, weakly ionized by cosmic rays. The fluid is described by a density field $\rho$, a velocity field $\boldsymbol{v}$ and a magnetic field $\boldsymbol{B}$. In what follows, I use Gaussian units.

The continuity equation expresses the conservation of mass in every volume element belonging to the fluid

$$\partial_t \rho + \boldsymbol{\nabla} \cdot (\rho \boldsymbol{v}) = 0, \tag{2.1}$$

that is, that the density flux advected through the surface of such element must result in a change of density within the element. The momentum of the fluid is transported in each element according to

$$\partial_t (\rho \boldsymbol{v}) + \boldsymbol{\nabla} \cdot \left[ \rho \boldsymbol{v} \otimes \boldsymbol{v} - \tfrac{1}{4\pi} \boldsymbol{B} \otimes \boldsymbol{B} + P_t \mathsf{I} \right] = \rho \boldsymbol{a}_{\text{ext}}. \tag{2.2}$$

Analogous to eq. 2.1, the time derivative and the first term inside the brackets express the change in time and advection of momentum in a volume element, respectively. The rest of the terms provide force densities, i.e., sources of momentum change: a gradient of the total pressure $P_t = P + P_B$ (the sum of the thermal and magnetic pressures), the magnetic tension force (which tends to straighten magnetic field lines) and the external acceleration (or specific force) source term on the right hand side.

The evolution of the magnetic field in time is dictated by Faraday's law of induction,

$$\partial_t \boldsymbol{B} + \boldsymbol{\nabla} \times (c \boldsymbol{\mathcal{E}}) = 0, \tag{2.3}$$

where $c$ is the speed of light and $\boldsymbol{\mathcal{E}}$ is the electric field, both of which can be substituted by the expression

$$c \boldsymbol{\mathcal{E}} = -\boldsymbol{v} \times \boldsymbol{B} + \eta \boldsymbol{\nabla} \times \boldsymbol{B}, \tag{2.4}$$

which is obtained by combining the Ampère–Maxwell law and Ohm's law ($\eta$ is the Ohmic resistivity). A plasma for which it can be assumed that $\eta = 0$ is called *ideal*.

Finally, the energy transport in a volume element is given by

$$\partial_t (E^K + E^{\text{th}} + E^B) + \boldsymbol{\nabla} \cdot \left[ (E^K + E^{\text{th}} + P) \boldsymbol{v} + c \boldsymbol{\mathcal{E}} \times \boldsymbol{B} \right] = \rho \boldsymbol{v} \cdot \boldsymbol{a}_{\text{ext}}, \tag{2.5}$$

which can be obtained from the first law of thermodynamics. The kinetic energy density $E^K = \frac{1}{2} \rho v^2$ and the thermal (or internal) energy density $E^{\text{th}}$ follow the conservation operators of a continuity equation. The pressure term comes from the mechanical work density advected through the surface of the volume element, while the right-hand side is the work density done to the volume element by external forces in time (dimensions of power density). The magnetic energy density $E^B$ can be dissipated as heat thanks to the resistivity (which can be readily seen by substituting the electric field using eq. 2.4).

In solving the problem of forming a massive star from the gravitational collapse of a cloud core, the external specific force $\boldsymbol{a}_{\text{ext}}$ is given by the sum of the following contributions:

a) the (self-)gravity $\boldsymbol{a}_{\text{sg}} \equiv -\boldsymbol{\nabla} \Phi_{\text{sg}}$ of the material not accreted by the protostar,

b) the gravity of the (already accreted) matter of the protostar $\boldsymbol{a}_{g\star} = -GM_\star / r^2 \, \boldsymbol{e}_r$,

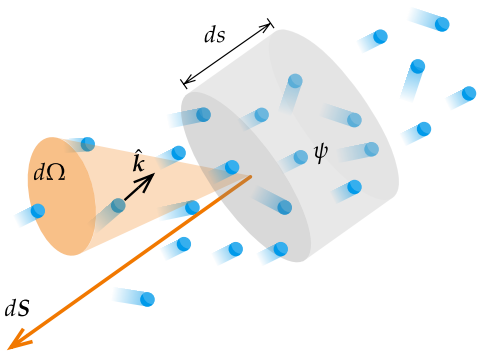



Figure 2.1: Radiation transport: volume element of a space where photons propagate.

c) the (total) radiation specific force $\boldsymbol{a}_{\mathrm{tot,rad}}$.

The self-gravity of the material is obtained by solving for the gravitational potential $\Phi_{\mathrm{sg}}$ with Poisson's equation for gravity,

$$\boldsymbol{\nabla}^2\Phi_{\mathrm{sg}} = 4\pi G\rho. \tag{2.6}$$

The gas is assumed to be calorically perfect, i.e., governed by the calorical equation of state

$$P = (\gamma - 1)E^{\mathrm{th}}, \tag{2.7}$$

with the ratio of specific heats $\gamma$ set to its value for diatomic hydrogen at low temperatures, 5/3.

## 2.2 Radiation transport

The forming massive star radiates energy to its surroundings (*stellar irradiation*), which is then absorbed and re-emitted by the gas and dust. The gas and dust also emit thermal radiation, which permits heat exchange within the material. Motivated by the sources of radiation, we further divide the specific force into a sum of the stellar irradiation component, $\boldsymbol{a}_{\mathrm{irr}}$, and the (re-)emission from the gas and dust, $\boldsymbol{a}_{\mathrm{rad}}$. The goal for a self-consistent description of radiation transport is the calculation of the radiation acceleration that enters eq. 2.5 as an external work density, and eq. 2.2 as an external force density. The first of the two contributions is very important for the accurate description of the thermodynamics of the gas and dust surrounding a forming massive star (disk and outflows), while the latter is of special importance at later stages and the smallest scales of massive protostellar evolution, when radiation pressure exerts a considerable force on the inflow of material onto the forming massive star. In this section, I present a summary of the most relevant elements of radiation transport theory for the solutions of the problems treated during the research. A more detailed view on this subject is available to the reader in Mihalas and Weibel-Mihalas (1999).

Consider a space containing photons of number density $\psi$ and frequency $\nu$, propagating with velocities $c\hat{\boldsymbol{k}}$ ($\hat{\boldsymbol{k}}$ is a unit wave vector). Each photon has energy $h\nu$ and momentum $(h\nu/c)\hat{\boldsymbol{k}}$. An illustration of the situation and geometry is available in fig. 2.1. Now consider a volume element of surface vector $d\boldsymbol{S}$ and thickness $ds$, and the incoming photons from a differential of solid angle $d\Omega$ onto $d\boldsymbol{S}$ at a given time. The monochromatic energy density in the element is found by integrating over the photons incoming from all solid angles into the element:

$$E_{\mathrm{rad}}(\boldsymbol{x}, t; \nu) = h\nu \oint \psi(\boldsymbol{x}, t; \hat{\boldsymbol{k}}, \nu) d\Omega. \tag{2.8}$$

The number of photons crossing the surface element in a time $dt$ is $\psi\,(\hat{\boldsymbol{k}} \cdot d\boldsymbol{S})(d\Omega\, d\nu)(cdt)$. The radiation field can be described by the intensity $I$, which is defined in terms of the energy

transported by the photons crossing the surface element as

$$I(\boldsymbol{x}, t; \hat{\boldsymbol{k}}, \nu) = h\nu\psi(\boldsymbol{x}, t; \hat{\boldsymbol{k}}, \nu) \cdot c. \tag{2.9}$$

In terms of the energy density, this means that

$$E_{\text{rad}}(\boldsymbol{x}, t; \nu) = \frac{1}{c} \oint I(\boldsymbol{x}, t; \hat{\boldsymbol{k}}, \nu) d\Omega. \tag{2.10}$$

The integration in solid angle defines the *zeroth moment* of a given quantity. The energy flux of photons of a given frequency traveling with a direction $\hat{\boldsymbol{k}}$ and incoming to the element from all solid angles is defined in a similar way, with the monochromatic radiation flux as

$$\boldsymbol{F}_{\text{rad}}(\boldsymbol{x}, t; \nu) = \oint I(\boldsymbol{x}, t; \hat{\boldsymbol{k}}, \nu) \hat{\boldsymbol{k}} d\Omega, \tag{2.11}$$

such that $\boldsymbol{F}_{\text{rad}} \cdot d\boldsymbol{S}$ is the net radiant energy flow per unit frequency interval across $d\boldsymbol{S}$. The radiation flux is called the *first moment* of the intensity and it is essentially obtained by multiplying by the direction and integrating over the solid angle space. The second moment is the radiation pressure tensor, defined as

$$\mathsf{P}_{\text{rad}}(\boldsymbol{x}, t; \nu) = \frac{1}{c} \oint I(\boldsymbol{x}, t; \hat{\boldsymbol{k}}, \nu) \hat{\boldsymbol{k}} \otimes \hat{\boldsymbol{k}} d\Omega, \tag{2.12}$$

and that can also be obtained by considering the momentum transfer of the photons per unit time and area.

The transfer of radiation in the volume element is governed by the radiative transfer equation:

$$\left( \frac{1}{c} \frac{\partial}{\partial t} + \hat{\boldsymbol{k}} \cdot \boldsymbol{\nabla} \right) I(\boldsymbol{x}, t; \hat{\boldsymbol{k}}, \nu) = \eta_{\text{em}}(\boldsymbol{x}, t; \hat{\boldsymbol{k}}, \nu) - \chi_{\text{ext}}(\boldsymbol{x}, t; \hat{\boldsymbol{k}}, \nu) I(\boldsymbol{x}, t; \hat{\boldsymbol{k}}, \nu). \tag{2.13}$$

The left-hand side of this equation expresses that the radiation energy field only changes in time or is advected through space if there is emission of radiation (first term on the right-hand side) or extinction of radiation (second term on the right-hand side). The coefficients of emission ($\eta_{\text{em}}$) and extinction ($\chi_{\text{ext}}$, which is a sum of absorption and scattering), depend on the material. Equation 2.13 is often expressed in terms of a source function $\mathcal{S}(\nu) = \eta_{\text{em}}(\nu)/\chi_{\text{ext}}(\nu)$ that under the assumption of *local thermodynamical equilibrium* corresponds to the black body intensity $B^I_{\text{rad}}(\nu, T)$:

$$\left( \frac{1}{c} \frac{\partial}{\partial t} + \hat{\boldsymbol{k}} \cdot \boldsymbol{\nabla} + \chi_{\text{ext}} \right) I(\boldsymbol{x}, t; \hat{\boldsymbol{k}}, \nu) = \chi_{\text{ext}} B^I_{\text{rad}}(\boldsymbol{x}, t; \nu, T). \tag{2.14}$$

In our problem, the extinction coefficient is critically dependent on the dust content of the cloud core. Microscopically, the absorption coefficient can be conceptualized as a sum of the occupation numbers of states capable of absorbing radiation and the cross section of atoms, molecules and dust grains present. The reciprocal of the extinction coefficient is the mean free path of the photons through the material.

Omitting the dependencies with space and time, the zeroth moment of eq. 2.14 is

$$\frac{\partial E_{\text{rad}}(\nu)}{\partial t} + \boldsymbol{\nabla} \cdot \boldsymbol{F}_{\text{rad}}(\nu) = \chi_{\text{ext}} \left[ 4\pi B_{\text{rad}}(\nu, T) - c E_{\text{rad}}(\nu) \right]. \tag{2.15}$$

Now, $B_{\text{rad}}(\nu, T)$ is the black body energy density. The first moment is then obtained by multiplying both sides of eq. 2.16 by $\hat{\boldsymbol{k}}/c$ and integrating over the solid angle:

$$\frac{1}{c^2} \frac{\partial \boldsymbol{F}_{\text{rad}}(\nu)}{\partial t} + \boldsymbol{\nabla} \cdot \mathsf{P}_{\text{rad}}(\nu) = -\frac{\chi_{\text{ext}}}{c} \boldsymbol{F}_{\text{rad}}(\nu). \tag{2.16}$$

This equation can be interpreted as a momentum equation, with the left hand side dealing with the momentum transport, and the right hand side being the radiation force density due to the radiation field. Then, the radiative acceleration is

$$\boldsymbol{a}_{\rm rad} = \chi_{\rm ext}\frac{\boldsymbol{F}_{\rm rad}}{\rho c}. \tag{2.17}$$

It is customary to define

$$\kappa \equiv \frac{\chi_{\rm ext}}{\rho} \tag{2.18}$$

as the *opacity* of the material.

### 2.2.1 Stellar irradiation

The (frequency-dependent) irradiation from the star is easily solved if we assume that the forming massive star is located at the origin of a spherical coordinate system. If the photon travel time can be considered small, then the time derivative in eq. 2.14 can be neglected. Additionally, for treating frequency-dependent stellar irradiation I assume that the radiation emitted by the star is directly absorbed by the surrounding material:

$$\hat{\boldsymbol{k}}\cdot\boldsymbol{\nabla} I(\boldsymbol{x},t;\hat{\boldsymbol{k}},\nu) + \chi_{\rm ext} I(\boldsymbol{x},t;\hat{\boldsymbol{k}},\nu) = 0. \tag{2.19}$$

In spherical coordinates this becomes

$$\partial_r I_\star = -\chi_{\rm ext} I_\star, \tag{2.20}$$

which in terms of the radial flux has a solution

$$F_{{\rm irr}\,\star}(r) = F_{{\rm irr}\,\star}(r_{\rm min}) e^{-\tau}\left(\frac{r_{\rm min}}{r}\right)^2, \tag{2.21}$$

where the optical depth $\tau$ is defined as

$$\tau(r) = \int_{r_{\rm min}}^{r} \chi_{\rm ext} dr, \tag{2.22}$$

and $r_{\rm min}$ corresponds in this case to the radius of the protostar.

For the radiative acceleration, we do not use directly eq. 2.17, but instead the alternative form

$$\boldsymbol{a}_{\rm irr} = -\frac{\boldsymbol{\nabla}\cdot\boldsymbol{F}_{{\rm irr}\,\star}}{c\rho}\hat{\boldsymbol{k}}. \tag{2.23}$$

Conceptually, eq. 2.17 considers the force onto a volume element by the photon flux as it goes through it, being attenuated by the opacity $\kappa$ of the material (which, as explained before, defines a mean free path for radiation). An equivalent way of computing this force is to consider the divergence of the flux through the surface of the volume element, i.e., comparing the fluxes before and after the radiation has gone through it. The latter method has the advantage of being more appropriate for a discretized space (Kuiper et al., 2020).

### 2.2.2 Diffusive radiation transport

As an approximation, the radiative transport due to thermal (re-)emission is assumed to be frequency-independent. For this, we take the zeroth moment of the radiative transfer equation (eq. 2.15) integrated in frequency

$$\frac{\partial E_{\rm rad}}{\partial t} - \boldsymbol{\nabla}\cdot\boldsymbol{F}_{\rm rad} = \rho\kappa_P(4\pi B_{\rm rad}(T) - cE_{\rm rad}), \tag{2.24}$$

where $B_{\rm rad}(T) = aT^4$ (Stefan-Boltzmann law) and $\kappa_P$ is the Planck mean opacity, which is defined as

$$\kappa_P = \frac{\int_0^\infty \kappa(\nu) B_{\rm rad}(\nu, T) d\nu}{\int_0^\infty B_{\rm rad}(\nu, T) d\nu}. \tag{2.25}$$

Equation 2.24 is solved by means of the *flux-limited diffusion* approximation, which consists in setting

$$\boldsymbol{F}_{\rm rad} = -D \boldsymbol{\nabla} E_{\rm rad} \tag{2.26}$$

with

$$D = \frac{\lambda c}{\rho \kappa_R}, \tag{2.27}$$

that is, assuming that radiation transport can be treated as a diffusion problem. The diffusion constant $D$ depends on the parameter $\lambda$, called the *flux limiter*, and the Rosseland mean opacity $\kappa_R$, which is defined as

$$\frac{1}{\kappa_R} = \frac{\int_0^\infty 1/\kappa(\nu, T) \cdot [\partial B_{\rm rad}(\nu, T)/\partial T] \, d\nu}{\int_0^\infty [\partial B_{\rm rad}(\nu, T)/\partial T] \, d\nu}. \tag{2.28}$$

The flux-limited diffusion approximation is valid in the following limiting cases:

a) $\lambda \to 1/3$ for the optically thick regime ($\tau \to \infty$),

b) $\lambda \to \kappa_R \rho E_{\rm rad} / |\boldsymbol{\nabla} E_{\rm rad}|$ for the optically thin regime ($\tau \to 0$).

The material surrounding a forming massive star is in the optically thick regime, and therefore, the flux-limited diffusion approximation can be used to model radiation transport.

### 2.2.3 Solving for the radiation field

Equation 2.24 has two unknowns: $E_{\rm rad}$ and $T$, which means that there is the need for a second equation for the two fields to be determined. The second equation is set by considering the change in thermal energy due to the irradiation of the forming massive star, and the thermal emission and absorption by the material, which is expressed as

$$\frac{\partial E^{\rm th}}{\partial t} = -\boldsymbol{\nabla} \cdot \boldsymbol{F}_{{\rm irr}\star} - \rho \kappa_P (4\pi B_{\rm rad} - c E_{\rm rad}), \tag{2.29}$$

with $E^{\rm th} = c_v \rho T$ ($c_v$ is the specific isochoric heat capacity).

Equations 2.24 and 2.29 form a system from which $E_{\rm rad}$ and $T$ can be determined. With $E_{\rm rad}$, the radiation flux is determined by virtue of eq. 2.26, and in conjunction with eq. 2.17, as well as the radiation acceleration:

$$\boldsymbol{a}_{\rm rad} = -\frac{\lambda}{\rho} \boldsymbol{\nabla} E_{\rm rad}. \tag{2.30}$$

The total radiation acceleration $\boldsymbol{a}_{\rm rad} + \boldsymbol{a}_{\rm irr}$ is then introduced in eqs. 2.2 and 2.5 to solve for the magnetohydrodynamical evolution of the plasma.

### 2.2.4 Gravitational instabilities

Neglecting magnetic fields, the condition for gravitational collapse in a cloud is the fulfillment of the Jeans criterion. The Jeans criterion can be obtained by studying the effect of small perturbations in an astrophysical ideal gas described by equations 2.1, 2.2 and 2.6 (but with $\boldsymbol{B} = \boldsymbol{0}$) which is in principle uniform and in hydrostatic equilibrium ($\boldsymbol{v} = \boldsymbol{0}$). Then, consider a small perturbation in the gas, such that each quantity (density, pressure, velocity and gravitational potential) is altered by adding a small value. By substituting the solution at zero and first orders

into the equations, and writing the equations for the first order variables in terms of the zeroth order solution, one obtains the linearized equations of hydrodynamics

$$\begin{cases} \partial_t \rho_1 + \rho_0 \boldsymbol{\nabla} \cdot \boldsymbol{v}_1 = 0 \\ \rho_0 \partial_t \boldsymbol{v}_1 = -c_s^2 \boldsymbol{\nabla} \rho_1 - \rho_0 \boldsymbol{\nabla} \Phi_{\mathrm{sg}\,1} \\ \boldsymbol{\nabla}^2 \Phi_{\mathrm{sg}\,1} = 4\pi G \rho_1, \end{cases} \tag{2.31}$$

where the subindices indicate the order of the expansion, and $c_s^2 = \gamma P_0/\rho_0$ is the sound speed. In order to study the propagation of the small perturbations, the Fourier transform is next applied:

$$\begin{cases} \omega \rho_1 = \rho_0 \boldsymbol{k} \cdot \boldsymbol{v}_1 \\ \omega \rho_0 \boldsymbol{v}_1 = \boldsymbol{k} c_s^2 \rho_1 + \boldsymbol{k} \cdot \boldsymbol{k} \rho_0 \Phi_{\mathrm{sg}\,1} \\ \boldsymbol{k}^2 \Phi_{\mathrm{sg}\,1} = -4\pi G \rho_1. \end{cases} \tag{2.32}$$

In this context, $\omega$ and $\boldsymbol{k}$ are the frequency and wave vector of the perturbation, respectively. By combining those three equations, we obtain the dispersion relation

$$\omega^2 = c_s^2 \left( k^2 - \frac{4\pi G \rho_0}{c_s^2} \right). \tag{2.33}$$

For the dispersion relation to be real, the second term in the parentheses must be smaller than the first one. This condition defines the Jeans criterion, which can be expressed in terms of a Jeans mass, temperature or length.

Perturbations in a Keplerian-like massive accretion disk can also trigger gravitational collapse. In this case, however, the Jeans criterion is not fully adequate, because it is based on a static zeroth-order solution. Consider a volume element of a Keplerian disk, in orbit at a cylindrical distance $R = R_0$ with an angular velocity $\Omega_0 = \Omega(R_0)$ according to the Keplerian profile. The disk has a surface density $\Sigma$, i.e., the density integrated vertically. If small perturbations to a Keplerian zeroth-order solution are studied with a Fourier analysis, then the dispersion relation

$$\omega^2 = c_s^2 k^2 - 2\pi G \Sigma |k| + \kappa^2 \tag{2.34}$$

is obtained. On the right-hand side, the first term is the stabilizing effect of pressure, the second one is the destabilizing effect of self-gravity, and the last term represents the stabilizing effect of rotation through the *epicyclic frequency* $\kappa$:

$$\kappa \equiv 4\Omega_0^2 + R \frac{d\Omega^2}{dR}. \tag{2.35}$$

Equation 2.34 is a quadratic equation in $k$, so $\omega^2 < 0$ only if the *Toomre parameter*

$$Q \equiv \frac{c_s \kappa}{\pi G \Sigma} \tag{2.36}$$

is less than 1, which indicates instability. See Toomre (1964) for a full derivation of the Toomre parameter.

### 2.2.5 Flux freezing and Alfvén waves

If the Ohmic resistivity $\eta$ is neglected, the induction equation 2.3 becomes

$$\partial_t \boldsymbol{B} = \boldsymbol{\nabla} \times (\boldsymbol{v} \times \boldsymbol{B}). \tag{2.37}$$

Now consider the magnetic flux over a surface $S$, $\Phi = \int_S \boldsymbol{B} \cdot d\boldsymbol{A}$ (where $d\boldsymbol{A}$ is the element of area), as illustrated in fig. 2.2. The Lagrangian derivative of the magnetic flux is

$$\frac{d\Phi}{dt} = \int_S \frac{\partial \boldsymbol{B}}{\partial t} \cdot d\boldsymbol{A} + \int \boldsymbol{B} \cdot \frac{d}{dt} d\boldsymbol{A}. \tag{2.38}$$

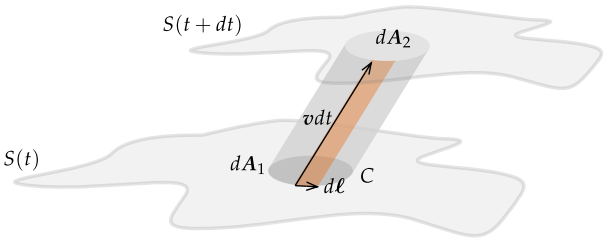



Figure 2.2: Visualization of a small element of area $d\boldsymbol{A}$ which is part of a surface $S$ frozen with the magnetic flux.

The change in time of the element of area can be computed by first dividing the full area in small loops of contour $C$ and line element $d\boldsymbol{\ell}$, and then noticing that the area of each loop sweeps a cylinder because of the motion of the flow. In order to substitute the time derivative of $d\boldsymbol{A}$, we notice that the integral of the vector area of a closed surface is zero:

$$d\boldsymbol{A}_2 - d\boldsymbol{A}_1 - dt \oint \boldsymbol{v} \times d\boldsymbol{\ell} = 0. \tag{2.39}$$

Then,

$$\frac{d\Phi}{dt} = \int_S \frac{\partial \boldsymbol{B}}{\partial t} \cdot d\boldsymbol{A} + \oint_C \boldsymbol{B} \times \boldsymbol{v} \cdot d\boldsymbol{\ell}$$

which implies that

$$\frac{d\Phi}{dt} = \int_S \left[ \frac{\partial \boldsymbol{B}}{\partial t} - \boldsymbol{\nabla} \times (\boldsymbol{v} \times \boldsymbol{B}) \right] \cdot d\boldsymbol{A} = 0 \tag{2.40}$$

by virtue of eq. 2.37. This means that in the ideal MHD regime, the magnetic flux is constant, or that wherever the flow goes, the magnetic field lines accompany it.

The question then arises: under which conditions do the magnetic field lines determine the motion of the plasma, and under which conditions is the motion of the plasma what determines the magnetic field configuration? To solve this question, a study of the propagation of small perturbations in an otherwise static plasma is necessary. As the linearization of the ideal MHD equations is a lengthy process, I only outline the main steps to obtain the result:

a) Every variable $x$ of the MHD equations (density, magnetic field, pressure, external specific force in eqs. 2.1, 2.2, 2.7 and 2.37) is expanded such that $x = x_0 + x_1$, for which $x_1$ is a small perturbation, and with the exception of the velocity, which is zero in the zeroth order.

b) The zeroth order solution to the MHD equations is equilibrium.

c) After simplifications from the zeroth order results, the first order solution to the MHD equations can be integrated such that the first order variables are known as a function of the zeroth order variables. Velocity can replaced as a variable by the Lagrangian displacement, which is a more convenient variable to describe perturbations.

d) The Fourier transform of the first order MHD equations is applied to obtain conditions for the propagation of disturbances as waves.

After the combination of the obtained equations into the Fourier-transformed first order momentum equation, the following result emerges, among others: consider a magnetic field line such that the (unperturbed) magnetic field goes in the direction $\boldsymbol{e}_b$. Now consider a perturbation that displaces the material along $\boldsymbol{\xi}$, in a way that is perpendicular to $\boldsymbol{e}_b$. Then, if the perturbation travels with the wave vector $\boldsymbol{k}$, it follows the dispersion relation

$$\omega^2 = v_A^2 (\boldsymbol{k} \cdot \boldsymbol{e}_b)^2, \tag{2.41}$$

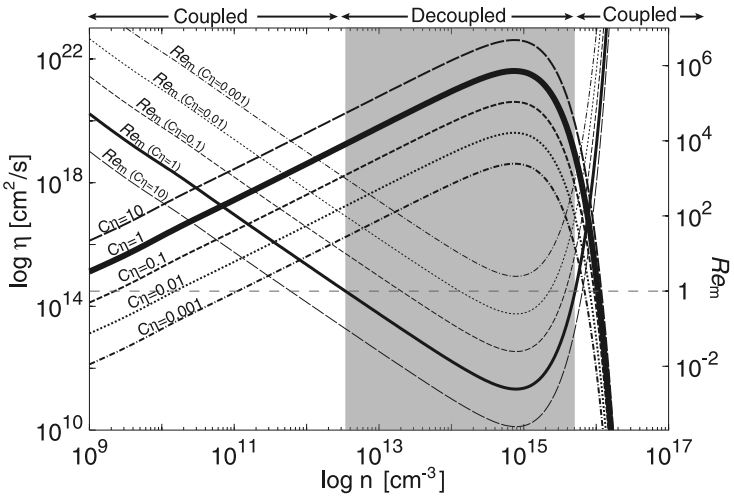



Figure 2.3: Ohmic resistivity $\eta$ as a function of time. From Machida et al. (2007). © 2007 The American Astronomical Society.

where

$$v_A^2 = \frac{B_0^2}{4\pi\rho} \tag{2.42}$$

is the Alfvén speed, i.e., the propagation speed for such waves. A given perturbation that has a velocity $v_1 < v_A$ is then restored by magnetic tension in the form of an Alfvén wave. This defines the *sub-Alfvénic flow*, which means that the flow follows the magnetic field lines. If the perturbation has a velocity $v_1 > v_A$, the magnetic tension is not able to restore the configuration of the magnetic field. This then constitutes the *super-Alfvénic regime*, that is, the condition for which the magnetic field lines follow the flow. A full derivation of Alfvén waves can be found, for example, in Chiuderi and Velli (2015).

### 2.2.6 Magnetic diffusion

In an ideal plasma, the magnetic flux is frozen to the fluid flow. In reality, collisions between the charges (electrons, ions and charged dust grains) against other particles present in the material (mostly against neutral molecules and grains, and —with lesser importance— against other charged particles) cause the magnetic field to diffuse and decouple from the flow. The calculation of the effects of collisions in the material from first principles requires knowledge of the abundances of the different species present in the fluid, and how they change as a function of density, magnetic field and temperature.

As a simplification of the process, and to get a rough idea on how this calculations are done, one can consider a fluid that consists of two species, a plasma and neutrals, each one with their own system of equations of motion (magnetohydrodynamics and hydrodynamics, respectively). The systems of equations are coupled by the addition of terms of the form $\rho_p \rho_n \gamma_{\rho n}(\boldsymbol{v}_p - \boldsymbol{v}_n)$ in their respective momentum equations that represent the exchange of momentum between particles during collisions. The coefficients $\gamma_{\rho n}$ of the momentum transfer terms depend on, e.g., the cross section and the velocity of the particles. The material in a star-forming cloud core is weakly ionized, mostly by cosmic rays, although thermal ionization becomes important once the temperatures increase above 1000 K. Weak ionization allows us to ignore the inertia of the charged particles with respect to the neutrals, and thus the effects of collisions can be treated with drift velocities in a single fluid. For a more detailed view on this subject, I refer the reader to Nakano et al. (2002), Zweibel (2015) and Marchand et al. (2016).

After the treatment of collisions, the induction equation (eq. 2.3) becomes

$$\partial_t \boldsymbol{B} - \boldsymbol{\nabla} \times (\boldsymbol{v} \times \boldsymbol{B}) = -\frac{c^2}{4\pi} \nabla \times \left[ \eta (\boldsymbol{\nabla} \times \boldsymbol{B}) + \eta_H (\boldsymbol{\nabla} \times \boldsymbol{B}) \times \frac{\boldsymbol{B}}{|\boldsymbol{B}|} + \eta_A \frac{\boldsymbol{B}}{|\boldsymbol{B}|} \left( (\boldsymbol{\nabla} \times \boldsymbol{B}) \times \frac{\boldsymbol{B}}{|\boldsymbol{B}|} \right) \right] \tag{2.43}$$

The first term inside of the brackets is Ohmic resistivity, caused by collisions in the same direction as the propagation of the current and therefore resisting the current. The second term is the Hall effect, which is an induction traverse to the current. The third term is the *ambipolar diffusion*, and it is an approximation to the effects of the *ambipolar drift* in a strong coupling approximation. Ambipolar drift is a result of the fact that the electromagnetic forces only affect directly the charged particles and not the neutrals (where most of the mass resides). Collisions between charged particles and the neutrals drag the neutrals, but a small drift remains, decoupling the magnetic field from the flow. In analogy with Ohmic resistivity, one can define a diffusivity for the Hall effect and ambipolar diffusion ($\eta_H$ and $\eta_A$, respectively).

Formally, all three effects should be used when modeling star formation from a collapsing cloud. Ambipolar diffusion has been shown (Marchand et al. 2016; Marchand et al. 2022) to be dominant at low densities, while Ohmic resistivity is dominant at very high densities. Both effects have a similar behavior at the range of number densities that is of our highest interest ($10^7 \lesssim n_H \lesssim 10^{13}\,\mathrm{cm}^{-3}$). While Ohmic resistivity does not depend on the magnetic field strength, the ambipolar diffusivity increases with magnetic field.

For the studies presented in this work, I consider only Ohmic resistivity. The lack of further magnetic diffusivity from the other effects constitutes formally a caveat in my approach, which is amply discussed in the results section. However, a comparison of my results with similar studies that include ambipolar diffusion but neglect Ohmic resistivity, as well as observational results, indicate that we are nevertheless able to capture the most relevant dynamical processes in the disk and outflows. I use the values of the resistivity computed by Nakano et al. (2002), and fitted into an analytical curve by Machida et al. (2007), which is shown in fig. 2.3 and is described by

$$\eta = \frac{740}{X_e} \left( \frac{T}{10\,\mathrm{K}} \right)^{1/2} \left[ 1 - \tanh \left( \frac{n_H}{10^{15}\,\mathrm{cm}^{-3}} \right) \right] \mathrm{cm}^2\,\mathrm{s}^{-1}. \tag{2.44}$$

Resistivity increases with density, as regions with a higher density encourage more frequent collisions that resist the current. At number densities higher than $\sim 10^{15}\,\mathrm{cm}^{-3}$, the temperature reaches values over $\sim 2000\,\mathrm{K}$. The thermal ionization of alkali metals reduces greatly resistivity beyond that point.

### 2.2.7 Viscosity as a model for gravitational torques

In the three-dimensional simulations of a fragmenting accretion disk presented in chapter 3, the angular momentum transport in the self-gravitating accretion disk is provided by the gravitational torque exerted by spiral arms and fragments. However, in the two-dimensional simulations (massive protostellar outflows, chapters 4 and 5), this gravitational torque is missing and must be modeled. The method I use was introduced in Kuiper et al. (2011), and consists in the inclusion of a shear viscosity model that transports angular momentum and mimics the effects of the spiral arms. The shear viscosity adds an acceleration source term

$$\boldsymbol{a}_\nu = \boldsymbol{\nabla} \Pi / \rho, \tag{2.45}$$

where the viscosity tensor $\Pi$ is fixed with the $\alpha$-parametrization of Shakura and Sunyaev (1973) and no bulk viscosity is considered.

## 2.3 Classical theory of a magneto-centrifugally launched jet

Blandford and Payne (1982) built a semi-analytical model to explain the production of jets as winds magneto-centrifugally launched from an accretion disk. In that model, the authors

start from the stationary, axisymmetric, ideal magnetohydrodynamical flow in rotation with a rotation vector $\boldsymbol{\Omega}(R)$ (that can be taken as the Keplerian angular velocity). In cylindrical coordinates, the velocity of such flow is given by

$$\boldsymbol{v} = \frac{k\boldsymbol{B}}{4\pi\rho} + \boldsymbol{\Omega} \times \boldsymbol{R}, \tag{2.46}$$

with a constant $k$ that can be interpreted as the ratio of the constant mass flux to the constant magnetic flux. For this flow, the conditions

$$\boldsymbol{B} \cdot \boldsymbol{\nabla} k = \boldsymbol{B} \cdot \boldsymbol{\nabla} \Omega = 0 \tag{2.47}$$

must be satisfied. There are two constants of motion: the specific energy and the specific angular momentum. The first one is given by

$$e = \frac{1}{2}v^2 + h + \Phi_g - \frac{\Omega R B_\phi}{k}, \tag{2.48}$$

where $h$ is the specific enthalpy, $\Phi_g$ the gravitational potential and the last term of the right hand side, the work done by the magnetic torque. The specific angular momentum is given by

$$l = R v_\phi - \frac{R B_\phi}{k}, \tag{2.49}$$

where the last term corresponds to the magnetic torque. A self-similar solution is considered for the analysis, such that all quantities scale with the spherical radius. The solution aims to describe a Keplerian accretion disk around a black hole, and a given magnetic field distribution.

Using this solution, Blandford and Payne (1982) determine the vertical stability of the trajectory of a particle released from co-rotation with the disk. The co-rotating flow is assumed to be highly supersonic and sub-Alfvénic everywhere on top of the disk. So, a particle released in the unstable region follows a magnetic field line, according to the discussion in §2.2.5. Then, along the flow line, eq. 2.48 holds, and as the particle moves away from the disk, the reduction in the gravitational potential $\Phi_g$ implies an increase in the specific kinetic energy $v^2/2$. It is important to remark that the sub-Alfvénicity of the flow and poloidality of the magnetic field on top of the disk happens in the co-rotating frame of reference. From a viewer in an inertial frame of reference, the magnetic field is poloidal but co-rotates with the disk, which means that the flow spirals out of the disk following a rotating magnetic field line. Far away from the disk, where the flow becomes super-Alfvénic, the rotation of the flow winds the magnetic field lines, increasing the toroidal magnetic field $B_\phi$. This collimates the outflow, i.e., the inwardly-directed Lorentz force dominates over the outwardly-directed centrifugal force in the co-rotating frame. The material on top of the disk, which is launched as a jet, is typically referred to as the disk's *corona*.

The basic theory from Blandford and Payne (1982) is used for a wide variety of jets in Astrophysics, such as those found in active galactic nuclei or around stellar black holes (see, for example, Ouyed and Pudritz 1997; Huarte-Espinosa et al. 2012). However, in magnetically-driven massive protostellar outflows, there is an ingredient missing: the system is deeply embedded in an infalling envelope that provides the mass inflow towards the disk and the forming massive star. The flow on top of the accretion disk can only become sub-Alfvénic if the Alfvén velocity (eq. 2.42) is sufficiently high, which means that the magnetic field has to be sufficiently strong, or that the density has to be sufficiently low. Therefore, we expect differences between jets launched with by the classic Blandford and Payne (1982) mechanism and protostellar jets embedded within an infalling envelope due to the added density.

## 2.4 Magnetic tower flows

An additional mechanism for producing magnetically-driven outflows called *magnetic tower flows* was proposed by Lynden-Bell (1996) and further developed in Lynden-Bell (2003). In this

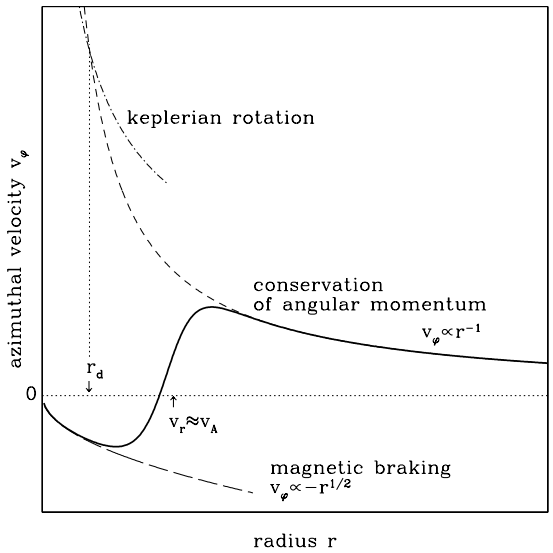



Figure 2.4: Reproduction of Fig. 1 in Galli et al. (2012): schematic behavior of the azimuthal velocity in the equatorial plane of a collapsing cloud as a function of the distance $r$ from the central protostar. © 2012 The American Astronomical Society.

mechanism, the magnetic field lines that thread the disk are wound continuously because of rotation. Then, the vertical gradient of the magnetic pressure increases because of the winding until gravity is overcome and the material above the disk is expelled. Magnetic tower flows are also known as *Poynting flux outflows* because the electromagnetic field predominantly carries the angular momentum and energy from the disk, while the Blandford–Payne magneto-centrifugal mechanism is also known as the *hydromagnetic regime*, where energy and angular momentum are carried by the kinetic flux of the outflow, in addition to being carried by the electromagnetic field (Lovelace and Romanova, 2003).

In Lynden-Bell (2003), the conditions for the launching of tower flows were determined by the principle of virtual work. With a model for the wound magnetic field lines, the work done by the magnetic field is calculated. With the principle of virtual work, the condition for equilibrium against the gravitational field can be determined. Even though they typically produce slower speeds than a magneto-centrifugal jet (see, e.g., Kölligan and Kuiper 2018; Mignon-Risse et al. 2021a), magnetic tower flows propagate for large distances from the disk.

## 2.5 Magnetic braking in a collapsing cloud

The continuous winding of magnetic field lines by rotation exerts a torque that brakes the flow in an ideal plasma. This can be readily seen from the second term of the right-hand side in eq. 2.49. An analytical model for magnetic braking was proposed by Galli et al. (2006, 2012) by first substituting a self-similar solution in the ideal MHD equations that eliminates the time dependencies, and matching both inner and outer solutions for the regimes close to the protostar and in the collapsing envelope. By analyzing the behavior of the specific angular momentum in flow lines, the profile for the azimuthal velocity shown in fig. 2.4 was obtained.

Magnetic braking is seen in the innermost parts of the accretion disk, where the angular velocity abruptly decreases at close distances from the protostar. In the region where the radial velocity is similar to the Alfvén velocity, the material has been depleted of its angular momentum. However, magnetic tension continues to transport angular momentum outwards, which forces the material to counter-rotate. Outside of the magnetic braking radius, however, Keplerian rotation occurs as expected from a non-magnetic disk. Magnetic braking is strongly affected by magnetic diffusion: by transforming magnetic energy into other kinds of energy,

the magnitude of the azimuthal component of thee magnetic field decreases, limiting the effects of magnetic braking.

# 3 Formation of companions via disk fragmentation

The following chapter is a summary of selected results obtained in the first project of my doctoral studies, entitled "Modeling disk fragmentation and multiplicity in massive star formation", and which was published in the peer-reviewed journal *Astronomy & Astrophysics*, volume 644, page A41 with Rolf Kuiper (RK) as a coauthor and supervisor. A full copy of the article can be found in Appendix A.1. The content of this chapter is meant to be a supplement to the article, detailing aspects like the organization of the project, my personal contribution and a highlight of the results that I anticipate are more interesting to the wider community. If desired, the reader can directly skip to the full article and only consult this supplementary information if necessary.

## 3.1 Objectives and expected outcome

As discussed in §1.7, the study of the fragmentation of the accretion disk is a possible route for finding an answer to the problem of massive stellar multiplicity, specially for the production of spectroscopic companions. In this study, we aimed at

a) simulating the formation of a massive star, with focus on the physics of disk fragmentation;

b) studying the physical processes present in the formation, evolution and possible destruction of the fragments; and

c) determining the effects of resolution on the final number of companions predicted by disk fragmentation.

## 3.2 State of the art in simulations

Several authors have used three-dimensional (3D) hydrodynamical simulations of a forming massive star, starting from the collapse of a cloud core, including the important physical effects of self-gravity and radiation transport. Krumholz et al. (2009), Kratter et al. (2010), Rosen et al. (2016), Klassen et al. (2016), Girichidis et al. (2012), and others used adaptive mesh refinement (AMR) grids and sub-grid sink particle models to replace regions of the computational domain where the Jeans length cannot be resolved anymore. Some of those studies start from a cloud core with highly supersonic turbulence and either find no disk but filamentary accretion (Girichidis et al., 2012) or an accretion disk formed thanks to the angular momentum content of the turbulent motions (e.g. Rosen et al. 2016).

The increased uncertainty and parameters introduced by the use of sink particle algorithms leads to great discrepancies between the predicted number of companions in each study. Girichidis et al. (2012) reported as many as $\sim$ 400 sink particles in some of their runs, Rosen et al. (2016) obtained up to about 30; in contrast, Klassen et al. (2016) reported none. Those discrepancies provoke questions on the role of resolution and the criteria for sink particle creation on the predicted multiplicity of massive stellar systems.

Meyer et al. (2017) and Meyer et al. (2018) took an alternative approach and used the code `Pluto` (Mignone et al., 2007) to model the collapse of a cloud core with a grid in spherical coordinates under several possible initial distributions of the density and angular momentum. They found that shallower density profiles with a steep angular momentum distribution yield more fragmentation, as those conditions allow for the formation of a more massive disk that develops earlier in time.

## 3.3 Project setup

### 3.3.1 Simulations

RK ran a series of five 3D hydrodynamical simulations including self gravity and both the gray FLD approximation for radiation transport of the gas and dust and stellar irradiation (§2.2.2 and 2.2.1). The simulations were run in time-independent grids using spherical coordinates $(r, \theta, \phi)$, with the radial coordinate increasing logarithmically with the distance from the center of the cloud core, a uniform distribution of grid cells in the azimuthal direction, and a distribution of cells in the polar direction varying with the cosine of the polar angle, such that the maximum resolution is achieved in the equatorial plane. The grid extends from $r = 30\,\mathrm{au}$ to $r = 0.1\,\mathrm{pc}$. We refer to the region $r < 30\,\mathrm{au}$ as the sink cell, and inside of it, a protostar is modeled to be formed by accretion with the evolutionary tracks of Hosokawa and Omukai (2009) (§1.6).

The simulation set considers the use of five different grids with increasing resolution. The lowest resolution grid is called x1, with a resolution of 34×11×32 cells in each direction, and each subsequent resolution doubles the number of cells in each direction until the grid x16, which has 536×161×512 cells, approximately 26 million of which are used for modeling the accretion disk. The resolution achieved in run x16 is unprecedented, and allowed us to resolve the internal structure of the fragments in most parts of the disk without the need to use a sink particle sub-grid module like previous studies. The simulation ran for approximately one and a half years in about four thousand computing cores, and its results and derived analysis have set the state of the art in the topic.

The cloud core contains initially a mass of $200\,\mathrm{M}_\odot$ distributed with a density profile $\rho \propto r^{-1.5}$, and an angular velocity distribution according to $\Omega(R) \propto R^{-0.75}$, where $R$ is the cylindrical radius. The ratio of rotational to gravitational energy is set to 5%. The initial temperature of the cloud core is uniform with a value of 10 K.

### 3.3.2 Analysis tools

Because sink particles were not used, I needed to develop a method to identify and track the fragments formed in the 3D data, with the aim of following their evolution into possible companions. The method works in the following way: even though the density structure of the disk fragments varies greatly, any fragment that collapses into a first Larson core must have a sufficient central temperature so that its thermal pressure supports it against gravitational collapse. Meanwhile, spiral arms and other features of the disk have a more modest peak in temperature, which is not highly localized. As a result, a good marker for identifying fragments is precisely highly localized maxima in the temperature field. The algorithm I developed then first applies a Gaussian filter to the temperature data in order to diffuse the spiral arms, and then searches for maxima in every snapshot of the data. Then, fragments are tracked in the following way: based on its current location and the velocity field, the algorithm defines a region where the fragment should be located in the next available simulation snapshot. In the next iteration, the region is examined and if a fragment is detected there, it is considered as causally connected with the previous observation. The central temperature of the fragment is then determined and stored, and its mass is computed by integrating the density field over a sphere of a fixed size. With this tool, I was able to track the orbits, temperatures and masses of the fragments in the disk, and after some refinement of the results, I was able to use this information to compile statistics on the formation of fragments, their interactions (for example, mergers), destruction and further evolution.

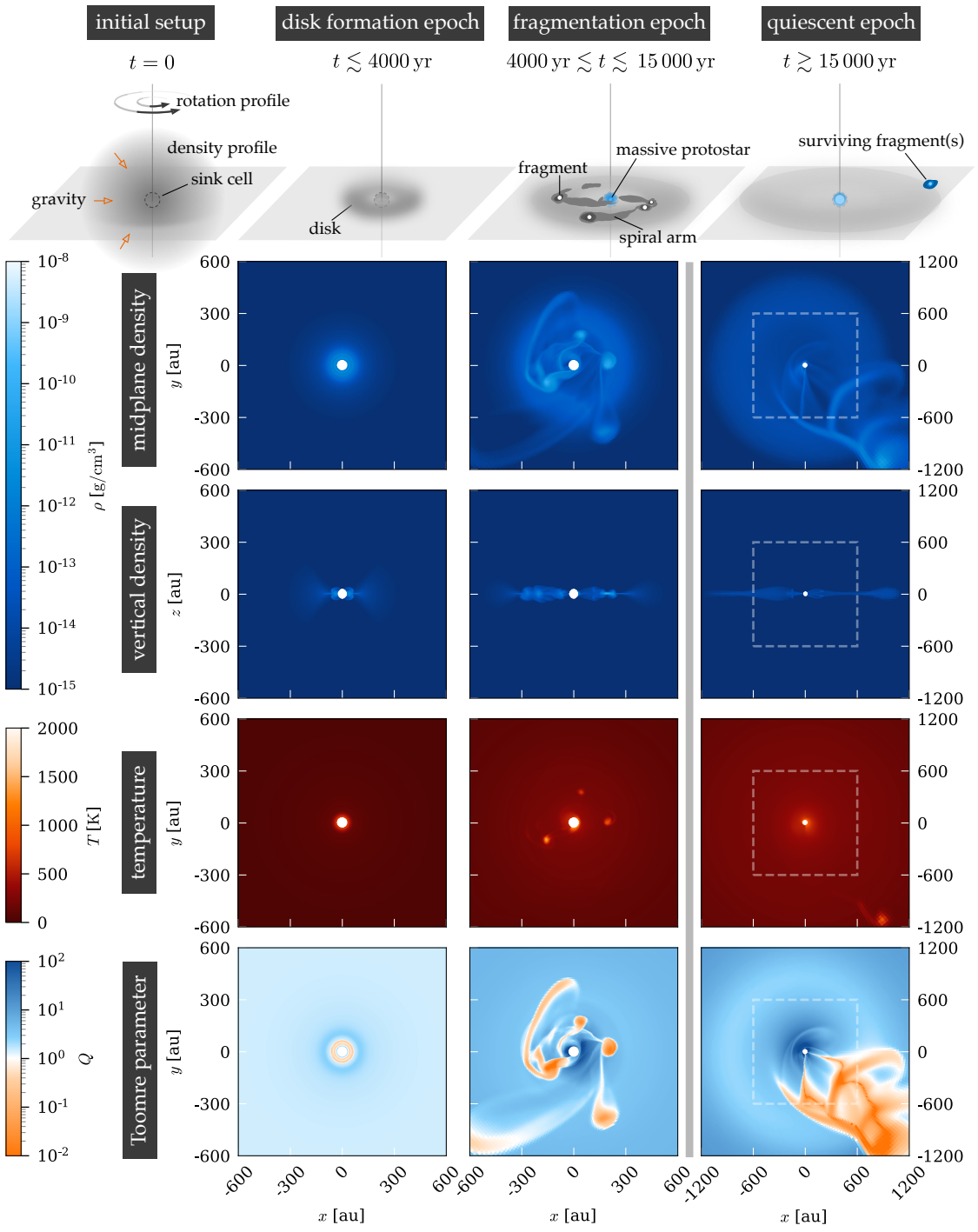



Figure 3.1: Time evolution of the system (run x8). In the elaboration of the plots, snapshots of the simulation were taken specifically at 3.0, 8.0, and 17.5 kyr for each respective column. The rightmost column shows double the size of the other two (the dotted square corresponds to the area shown in the snapshots located to the left). From Oliva and Kuiper (2020), © ESO 2020.

## 3.4 Selected results and discussion

### 3.4.1 Evolution of the system

Figure 3.1 shows an overview of the temporal evolution of the system, using run x8. The first, third and fourth rows present a midplane cut of the density field, temperature field, and the Toomre parameter (§2.2.4), respectively. The second row displays a vertical cut through the density structure. The columns indicate different stages in the evolution of the system, which I describe as follows.

**Collapse and disk formation epoch.** The cloud begins to collapse as soon as the simulation starts. Matter free-falls into the center of the cloud, where the sink cell is located, and eventually forms a massive star there. Simultaneously, because of conservation of angular momentum, an accretion disk is formed, which grows in size over time and it is initially axially symmetric.

**Fragmentation epoch.** At around 4 kyr of evolution, when the disk is about 200 au in size, the axial symmetry in the disk is broken. First, spiral arms appear, and then the disk fragments. The fragments have densities higher than $\sim 10^{-11}\,\mathrm{g\,cm^{-3}}$ and temperatures higher than $\sim 600\,\mathrm{K}$. Spiral arms and other structures in the disk have densities higher than $\sim 10^{-13}\,\mathrm{g\,cm^{-3}}$. I call rest of the material in the disk the *background disk*, and very roughly it has densities higher than $10^{-15}\ \mathrm{g\,cm^{-3}}$. The vertical structure of the disk reveals that it is geometrically very thin. The spiral arms continuously change shape and collide, triggering overdensities that become fragments. We observe fragments to be typically connected to the central massive protostar via spiral arms and filamentary structures. Fragments typically interact through mergers and develop secondary accretion disks around them.

**Quiescent epoch.** At around 15 kyr of evolution, the inner disk stabilizes due to the increase in mass of the central massive protostar and the effects of stellar irradiation, mostly stopping fragmentation in the primary disk until the end of the simulated time. Some fragments survive the fragmentation epoch, but the majority of fragments migrate towards the central massive protostar or get accreted by it.

### 3.4.2 Fragmentation of the accretion disk

#### *3.4.2.1 Formation of the fragments*

Fragments form out of one or more spiral arms, in two mechanisms I identified. The first one is a local collapse within small overdensities that grow in a spiral arm. After the local collapse, the spiral arm starts to deform. The other mechanism involves two spiral arms colliding, with the resulting perturbations creating overdensities that trigger the Toomre instability.

#### *3.4.2.2 Fragment interactions*

The orbits of the fragments are eccentric and highly chaotic because of all the interactions with other fragments and with the spiral arms. They also mostly stay in the midplane, with some small exceptions found in the highest resolution run, where the equatorial symmetry is broken and the orbits acquire a small inclination of $\lesssim 2^\circ$. The average period of the fragments during the main fragmentation epoch is around 1 kyr, and the average eccentricity is $\sim 0.5$. By using the fragment-tracking algorithm I described above, I identified several of the interactions that determine the orbits and fates of the fragments, which are illustrated by figs. 3.2 and 3.3 and that I summarize as follows.

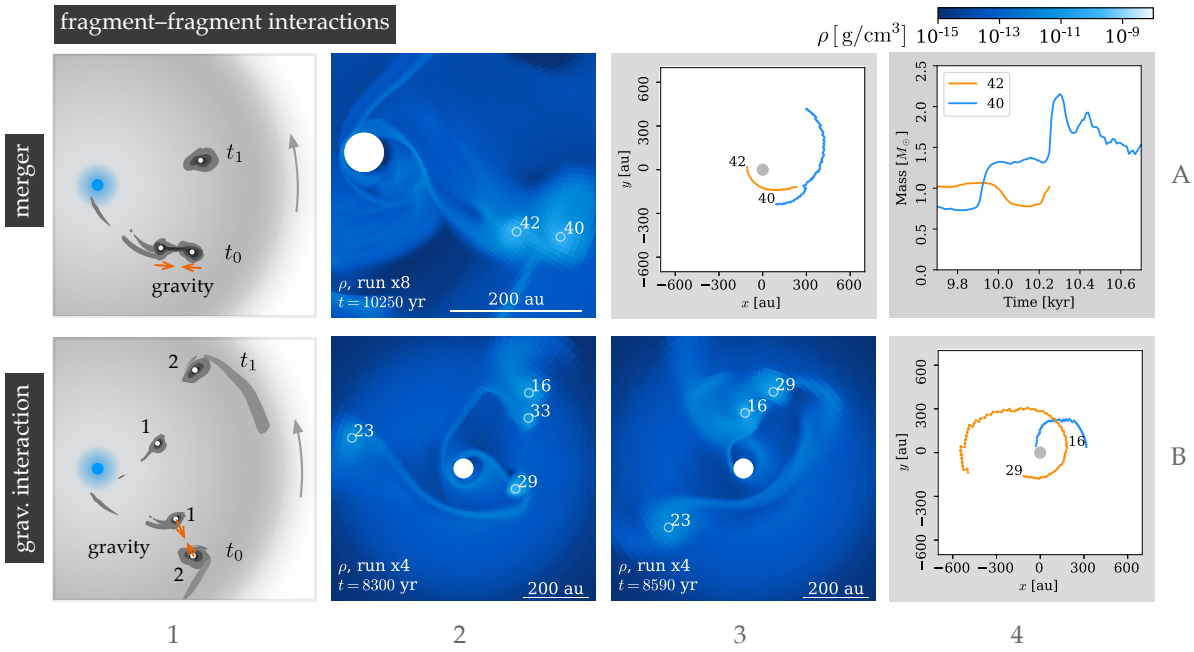



Figure 3.2: Fragment–fragment interactions. In panels A3 and B4, the fragment ID is shown at the starting point of the orbit. In the case of panel A3, the time window shown in the orbits is 1.3 kyr; in the case of panel B4 this is 1.2 kyr. From Oliva and Kuiper (2020), © ESO 2020.

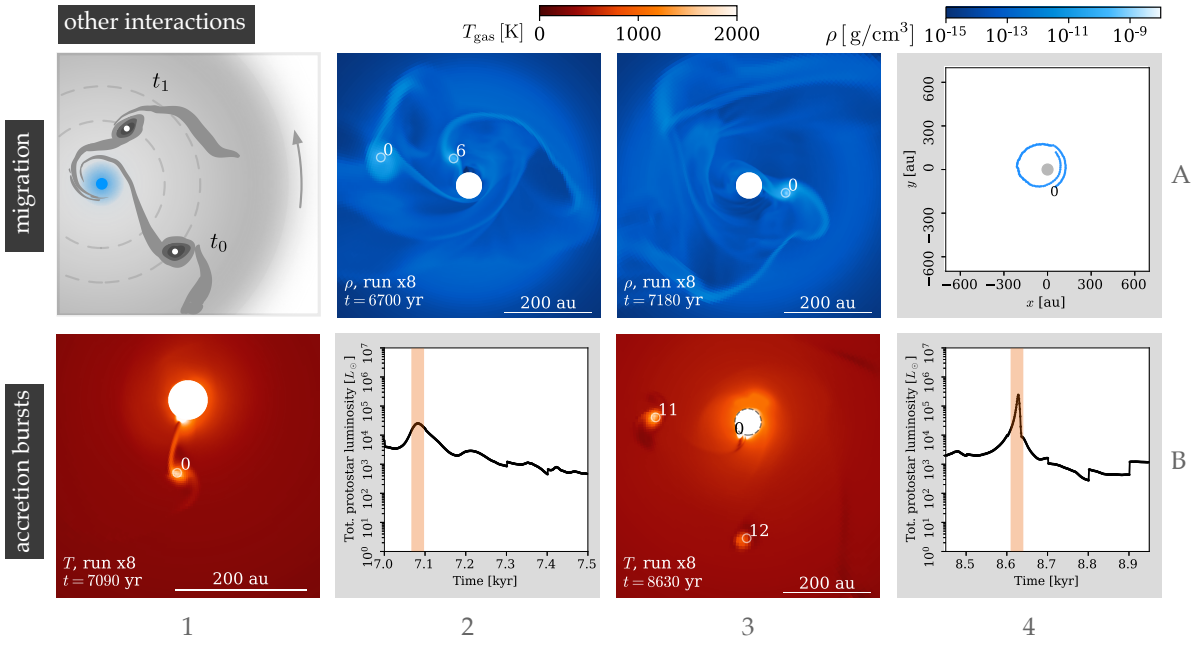



Figure 3.3: Interactions of the fragments with the spiral arms, and with the forming protostar modeled as a central sink cell. The orbit in panel A4 is plotted for a window of 2 kyr, with the fragment ID marking the starting point. From Oliva and Kuiper (2020), © ESO 2020.

**Mergers.** They occur when two fragments have a close encounter, and it is exemplified in row A of fig. 3.2. When fragments labeled 42 and 40 enter in a collision orbit, they merge and the mass of the resulting fragment is the combination of both. Collisions typically do not occur head on, but instead happen with a certain impact parameter, which increases the spin angular momentum of the merged fragment.

**Changes in the orbit due to gravitational interaction.** Fragments that are unconnected by the exchange of matter through a spiral arm still interact gravitationally. For example, in row B of fig. 3.2, fragments 16 and 29 interact in this way: before the interaction event, fragment 29 had an orbit close to the central massive protostar. However, when it interacts with fragment 16 by a mutual gravitational pull, fragment 29 accelerates into a wider orbit, and fragment 16 in turn moves into a closer orbit and is eventually accreted by the central massive protostar.

**Migration.** The gravitational torque exerted by the spiral arms provokes inward migration on the orbit of the fragment (see row A of fig. 3.3).

**Accretion bursts.** When a fragment is accreted by the central massive protostar, the released accretion luminosity occurs in the form of a burst. Accretion from spiral arms also increases the total luminosity, but more gradually and with a different signature compared to the accretion of a fragment (fig. 3.3, row B). The irradiation from accretion bursts sends a heat wave that I named *temperature flash*, which can interfere with the fragments by forcing thermal expansion, and can even destroy fragments with low enough mass.

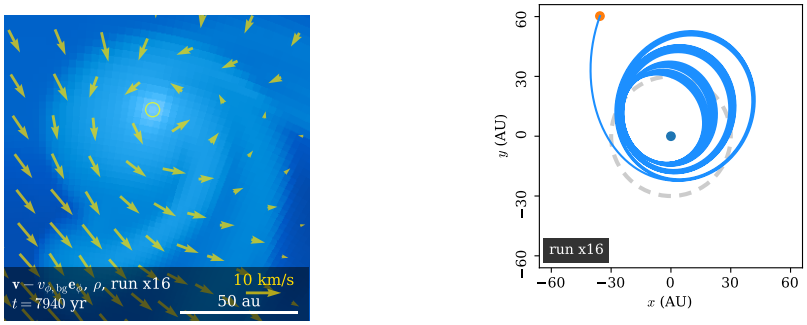
**Shearing.** Fragments that have a highly eccentric orbit can be sheared and destroyed by tidal forces when they get close to the forming massive star. In some cases, I observed the sheared material to be accreted in the form of a temporary ring-like structure that forms around the central massive protostar, instead of producing a sudden accretion event.

### 3.4.3 From fragments to companions

#### *3.4.3.1 First Larson cores*

Shortly after a fragment appears, it collapses gravitationally and forms a first Larson core. In the highest resolution simulations x8 and x16, fragments are observed to develop secondary accretion disks around them (fig. 3.4). Those secondary disks contain substructures themselves: they have spiral arms which are observed to fragment, in a similar process as what I explain above for the primary accretion disk. These results then coincide with the hierarchical fragmentation scenario, in which the companions formed through disk fragmentation of the primary also develop fragmenting accretion disks that can give rise to other companions or possibly planets.

For most grid sizes explored in the simulation set, the diameter of the hydrostatic cores predicted by Bhandare et al. (2018) is not resolved. The fragment is nonetheless supported by thermal pressure in all the simulations with high enough resolution to produce fragmentation. However, the highest resolution simulation, x16, has cell sizes $\lesssim 1$ au for radial positions of $r \lesssim 100$ au, which means that we are able to at least partially resolve hydrostatic cores around those distances. Figures 3.4*a* and 3.5 show an overdensity in the center of the fragment, specifically covering a distance of a few astronomical units. Figure 3.5 shows a vertical cut of the collapse process in fragment 12 of run x16. After the collapse, the secondary disk shown in fig. 3.4 is formed. To check whether the result of the collapse is consistent with the results of Bhandare et al. (2018), I calculated the enclosed mass of the inner $\approx 3$ au in fragment 12. The value of the enclosed mass increases during the collapse, until it reaches a value of a few $10^{-2}\,\mathrm{M}_{\odot}$, as predicted by Bhandare et al. (2018). The first core then accumulates mass (i.e., grows in size), but does not significantly increase its central density.




(a) (b)

Figure 3.4: *a)* Secondary disk with its spiral arms around fragment 12 of run x16. The background map represents density in the midplane (using the same color scale as the rest of the figures), and the arrows show the comoving velocity field. The yellow circle in has a radius of 3 au. *b)* Integrated orbit of fragment 2 of run x16 after it enters the numerical sink cell. The orange dot indicates the initial position of the fragment, and the total time integrated was 3 kyr. The sink cell (dashed circle) has a radius of 30 au. From Oliva and Kuiper (2020), © ESO 2020.




(a) Density, $t = 5.88$ kyr (b) Density, $t = 7.12$ kyr

Figure 3.5: Vertical structure of fragment 12 and its close surroundings (run x16). The yellow circle has a radius of 40 au. The density uses the same color scale as the rest of the figures.

#### 3.4.3.2 *Second Larson cores*

Our simulations do not include the effects of hydrogen dissociation in the gas, which means that the evolution of the fragments into companions cannot be fully studied after the formation of the first core. However, by tracking the central temperature of the fragments, I was able to determine which fragments would dissociate hydrogen and form second cores. After the second collapse, I expect the second core objects to be in more stable orbits than a first core because the drastic reduction in size experienced during this process means that the pressure from the gas in the disk does not exert a considerable force on the second core object, although it still is subject to the gravity of the gas. Therefore, I consider fragments that should undergo second collapse (i.e., when their central temperatures surpass consistently 2000 K) as having a good probability for becoming companions. From the simulations, however, it is not possible to fully conclude that they will become companions: they might still be subject to mergers or even accretion by the primary, but I expect the probabilities for those interactions to be lower than what it is observed for first cores.

Figure 3.6 shows the central temperature of the fragments for run x16, and fig. 3.7, the masses of those fragments. It can be seen from those two figures that the fragments formed earlier in time are overall less massive than those formed later. The masses of the fragments are of the order of one solar mass, although this does not mean that that is their final mass, as they would probably continue to accrete material through their secondary disks. The central temperatures of early-formed fragments are therefore lower as well. After a careful analysis of the temperature curve, I find 10 second core objects formed in run x16.

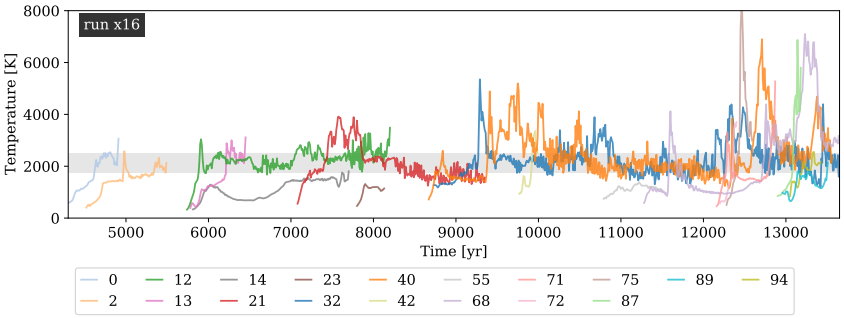



Figure 3.6: Temperature of the fragments with lifespan longer than 200 yr, for run x16. The gray box indicates the hydrogen dissociation limit. From Oliva and Kuiper (2020), © ESO 2020.

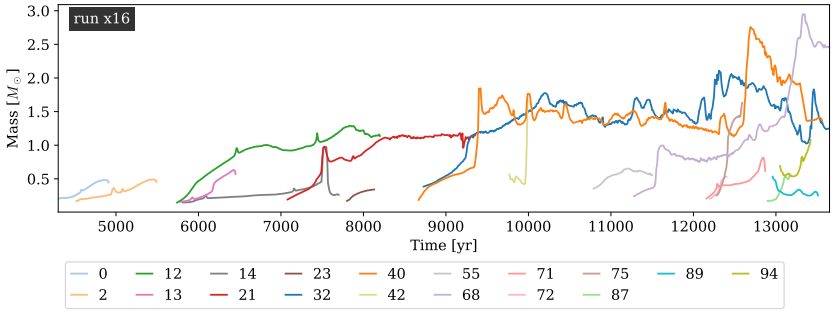



Figure 3.7: Masses of the fragments with life span longer than 200 yr, for run x16. A fixed radius of 40 au is assumed for the calculations of this plot. From Oliva and Kuiper (2020), © ESO 2020.

#### *3.4.3.3 Multiplicity*

A disadvantage of using a sink cell is the impossibility of fully distinguishing an accretion burst (the accretion of a fragment by the primary) from the formation of a close companion. Using the reasoning proposed in §3.4.3.2, one can assume that a first core that moves inside of the sink cell region would end up being accreted by the primary and produce an accretion burst, but a more stable second core would have a good probability of becoming a close companion.

After a close look at all the interactions between the fragments and their environment, and taking into account the formation of second cores, I find that run x16 produces 10 second core objects, of which 3 would become close companions, and 3 would remain in the middle or outer disk. The rest could be subject to mergers, so it is not possible to know their fate with confidence without the consideration of hydrogen dissociation in the simulation. Statistics of the same order of magnitude were found in run x8.

In fig. 3.4*b*, I present the integration of a trajectory that a second core object could follow if the sink cell were not there. For the integration, I took into account the gravity of the central massive protostar and the average gravity of the accretion disk. I find that the orbit of the fragment reduces its semi-major axis over time, principally due to the increasing gravitational force from the primary caused by its gain in mass over time. This constitutes a mechanism for the formation of spectroscopic companions because this process continues over time until accretion is stopped.

At the end of simulation x8, a fragment is observed in the outer disk region in a wide orbit of semi-major axis $\sim$ 1000 au. This coincides reasonably well with what is observed in Ilee et al. (2018) for the slightly more evolved system of fragments MM1a and MM1b in G11.92-0.61.

# 4 Effects of magnetic fields on the accretion disk

The following chapter is a summary of the manuscript entitled "Modeling disks and magnetic outflows around a forming massive star: I. Investigating the two-layer structure of the accretion disk", which has been accepted for publication on the peer-reviewed journal *Astronomy & Astrophysics*, with Rolf Kuiper (RK) as a co-author and supervisor. This manuscript is a part of the second project of my doctoral research, concerning the numerical study of magnetically-driven outflows from a massive protostar. The full text of this manuscript can be found in Appendix A.4. The content of this chapter is meant to be a supplement, detailing aspects like the organization of the project, my personal contribution and a highlight of the results that I anticipate are more interesting to the wider community. If desired, the reader can directly skip to the full manuscript and only consult this supplementary information if necessary.

## 4.1 Objectives and expected outcome

Magnetic fields are of fundamental importance in the formation process of a massive star. They are most likely responsible for the removal of angular momentum through magnetically-driven outflows and magnetic braking as the cloud core collapses, avoiding the centrifugal breakup of the protostar. The added magnetic pressure in the disk could also reduce disk fragmentation by providing additional support against gravity. Magnetically-driven outflows are launched from the material surrounding the forming massive star, especially from the accretion disk. In this study, I take a close look at the interaction between the accretion disk and the magnetic fields, with the aim of

a) performing very high resolution simulations that self-consistently launch magnetically-driven outflows from the accretion disk, starting from the collapse of a cloud core;

b) studying the effects of the magnetic field on the dynamics of the disk; and

c) determining how different environmental conditions for the onset of gravitational collapse affect the outcome of the disk and protostar.

## 4.2 State of the art in simulations

There are several studies available in the literature that aim to solve a similar problem definition as us in the context of massive star formation. By the physical effects considered, I classify them into three categories:

a) studies that treat the weakly ionized gas as a plasma with the ideal MHD approximation;

b) studies that include Ohmic resistivity as a source of magnetic diffusion; and

c) studies that include ambipolar diffusion as a source of magnetic diffusion.

No study available in the literature for massive star formation so far has included both Ohmic resistivity and ambipolar diffusion. To the first category belong the studies by Banerjee and Pudritz (2007), Seifried et al. (2011), Myers et al. (2013) and Rosen and Krumholz (2020). Even though the initial conditions, codes and thermodynamics are different between them, they coincide in obtaining a strongly sub-Keplerian accretion disk, because ideal MHD provides strong magnetic braking, only diminished slightly by numerical magnetic diffusion. Articles in the second category include Matsushita et al. (2017) and Machida and Hosokawa (2020), who

use the same Ohmic resistivity model that we consider here, but a barotropic equation of state instead of solving for the full thermodynamics of the gas and dust. They obtain disks of a few hundreds of astronomical units in radius. The third category includes studies by Mignon-Risse et al. (2021b) and Commerçon et al. (2022), who studied the collapse of cloud cores of $100\,M_\odot$ and a radius of 0.2 pc and mass-to-flux ratios of $\bar{\mu} = 5$ and 2. A key finding in both studies is that the accretion disks are smaller in the case with magnetic fields, with magnetic braking in the outer disk being the reason given by the authors for obtaining smaller disks in their runs that include ambipolar diffusion. All the studies mentioned so far have used AMR Cartesian grids in their respective codes.

Finally, I mention the study by Kölligan and Kuiper (2018), on which I base my project. Kölligan and Kuiper (2018) used an axisymmetric grid in spherical coordinates, which allowed them to self-consistently resolve the dynamics of the launching of the protostellar jet. However, an isothermal equation of state was used, and a grid that corresponds to the coarse grids of my simulation set. Therefore, the improvements that both RK and me brought to the setup are:

a) more realistic thermodynamics by solving for the radiation transport of the gas and dust;

b) the use of a grid of unprecedented resolution, specially in the inner disk;

c) a more complete study of the numerical effects on the results; and

d) the expansion of the parameter space considered to model more environmental conditions for the protostellar collapse.

## 4.3 Project setup

### 4.3.1 Simulation setup

We modeled the dynamics of the gas and dust with the formalism of magnetohydrodynamics using the code `Pluto` (Mignone et al., 2007), with the Ohmic resistivity model by Machida et al. (2007), and we solved for the radiation transport of the gas and dust with the gray FLD approximation using the module `Makemake` (Kuiper et al., 2020).

We considered an axisymmetric grid in spherical coordinates $(r, \theta, \phi)$, assuming midplane symmetry as well. The grid has an inner boundary of 3 au and an outer boundary of 0.1 pc in the fiducial or reference simulation. The radial coordinate $r$ increases logarithmically with distance to the center of the cloud and the polar coordinate $\theta$ is uniformly spaced.

As seen in ch. 3, the formed accretion disk is massive and is expected to undergo fragmentation, which provides the angular momentum transport required for accretion. A limitation of the axisymmetrical setup is the inability to capture the fragmentation physics. For this reason, we use an $\alpha$ shear viscosity model to approximate the gravitational torque of the non-axisymmetric features of the disk. See Kuiper et al. (2011) for an extensive study on this approach and a comparison to three-dimensional simulations.

The formation of an outflow cavity (low density region where the flow is located) close to the forming massive star, where the magnetic fields are particularly strong, means that the Alfvén velocity (§2.2.5) increases greatly, limiting the size of the time step to comply with the Courant–Friedrichs–Lewy (CFL) condition. The CFL condition ensures causality in a simulation. Very small time steps mean that the simulation freezes. To avoid this, Kölligan and Kuiper (2018) used an *Alfvén limiter*, or density floor tied to a maximum value of the Alfvén velocity allowed. We use an Alfvén limiter as well.

### 4.3.2 Parameter space

A large variety of initial conditions, numerical parameters and grid sizes was considered for this project, and they are visualized in a schematic way in the right column of fig. 4.1. In total,

I present 30 simulations, however, the development of the project demanded running several more experimental runs in low resolution whose results I consider redundant, so I did not include them in this work.

I ran the fiducial setup in five different grids with increasing resolution, named x1, x2, x4, x8 and x16. Run x16 is the highest resolution run, with a grid of 896×160 grid cells in the radial and polar directions, respectively. The number of cells in each direction for the other runs can be obtained by dividing successively by a factor of two. The parameters that I studied, which have a direct relation to the environmental conditions of the onset of gravitational collapse, are:

a) the initial mass of the cloud core, $M_C$;

b) the resistivity model considered;

c) the mass-to-flux ratio $\bar{\mu}$ (i.e., the initial magnetic field strength);

d) the initial density profile $\rho \propto r^{\beta_\rho}$ in the cloud core, through its exponent $\beta_\rho$;

e) the initial rotation profile $\Omega \propto R^{\beta_\Omega}$ of the cloud core, through its exponent $\beta_\Omega$ ($R$ is here the cylindrical radius); and

f) the initial rotational energy content of the cloud core, measured as a ratio $\zeta$ to its total gravitational energy.

I ran several values of those parameters in grid x4 (see fig. 4.1 for the full list) and a subset of those values was also run in grid x8. Additionally, I studied the numerical effects that might be produced by the following parameters:

a) the size of the inner boundary or sink cell,

b) the value of the $\alpha$ shear viscosity model, and

c) the value of the Alfvén limiter $v^A_{\max}$.

The variations of those parameters were studied with simulations that use grid x2. To refer to a particular simulation, and for simplicity, I use the following convention: first, the value(s) of the parameter(s) that are different than the fiducial case are written, followed by the grid on which such simulation was run. For example, $\bar{\mu} = 5$ [x8] means the simulation with a mass-to-flux ratio of 5, with the rest of the parameters as in the fiducial case run on grid x8 (for reference, the fiducial value of the mass-to-flux ratio is 20).

## 4.4 Selected results and discussion

### 4.4.1 Evolution of the system

An overview of the evolution of the system is shown in fig. 4.1, based on the results for the fiducial case. A massive protostar is formed in the center of the cloud core, reaching a mass of $\sim 20\,\mathrm{M}_\odot$ after 30 kyr. The luminosity of the protostar is dominated by the accretion luminosity during the period $t \lesssim 20$ kyr. I do not include the effects of stellar irradiation in this work, but it is a task that should be done in the future for studying the outflows during late stages of massive star formation. Not including irradiation forces and other kinds of stellar feedback also means that the final mass of the protostar cannot be determined self-consistently.

The general features of the evolution of the gas and dust can be distinguished as different epochs:

**Gravitational infall epoch.** As soon as the simulation begins, the cloud starts collapsing under its own gravity. The flow quickly becomes super-Alfvénic and the magnetic field lines are dragged by the infall accordingly. The result of the gravitational collapse is that the magnetic field lines adopt an "hourglass" shape, described in Galli et al. (2006) and observed in Beltrán et al. (2019).

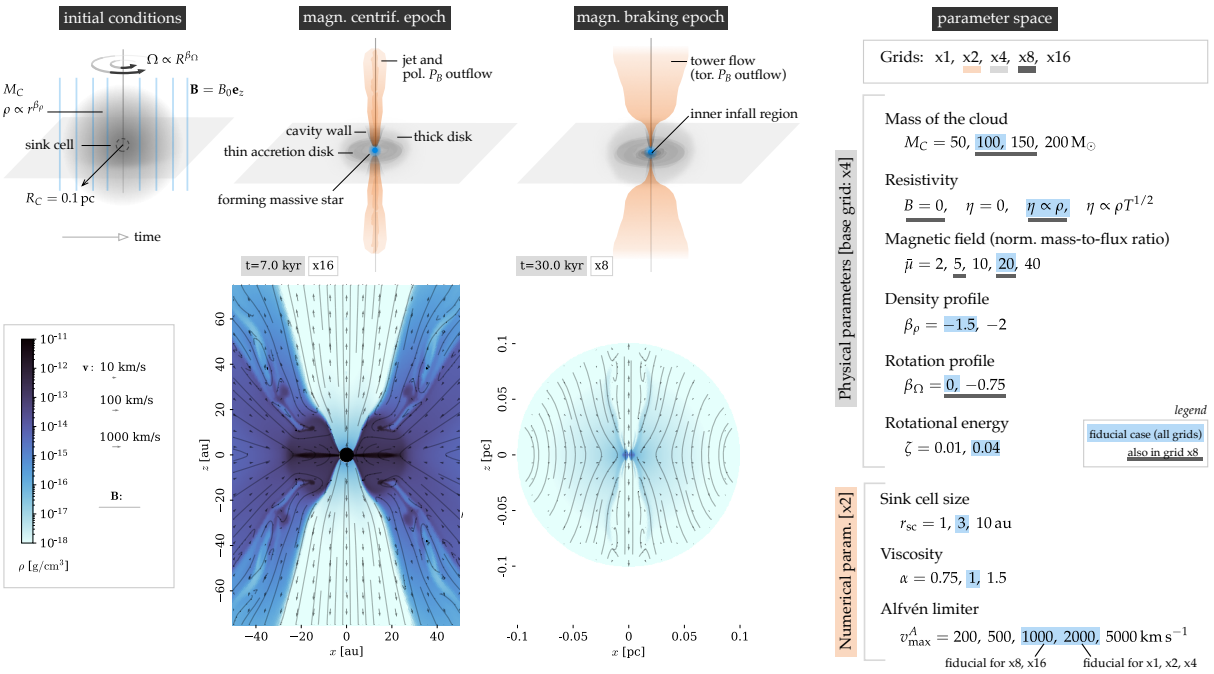



Figure 4.1: Overview of the evolution of the system and parameter space considered in this study. There are 30 simulations considered in total, with their configurations summarized as a diagram in the right panel.

**Magneto-centrifugal epoch.** Due to the conservation of angular momentum, an accretion disk is formed at around $t \sim 5\,\mathrm{kyr}$. I observe the disk to be composed by two layers: a thin disk in the midplane, surrounded by a thick disk of lower density. The thin disk increases towards the center of the cloud from $10^{-16}$ to $10^{-11}\,\mathrm{g\,cm^{-3}}$. The thick disk has a more uniform density of $10^{-14}\,\mathrm{g\,cm^{-3}}$. Roughly at the same time, magnetically-driven outflows are launched, which we classify as a *jet* and a *tower flow*. The jet has typical speeds of $\gtrsim 100\,\mathrm{km\,s^{-1}}$, while the tower flow is broader and slower, with speeds of the order of $10\,\mathrm{km\,s^{-1}}$. I call the interface between inflow from gravity and outflow the *cavity wall*.

**Magnetic braking epoch.** As magnetic field lines are dragged by rotation, the resulting magnetic tension exerts a torque that brakes the gas, resulting in the local loss of angular momentum in the inner disk. The inclusion of Ohmic dissipation makes magnetic braking negligible at early times of the simulation, but at around $t \sim 15\,\mathrm{kyr}$, magnetic braking starts to affect the innermost part of the disk ($r \lesssim 30\,\mathrm{au}$) and the cavity wall. As a result, I observe a region of inner infall. This inner infall modifies the dynamics of the jet. The tower flow broadens over time due to the increase in magnetic pressure caused by the continued dragging of magnetic field lines by rotation, and could offer an explanation for the earliest outflow broadening observed and discussed in Beuther and Shepherd (2005).

## 4.4.2 Dynamics of the accretion disk

### *4.4.2.1 Keplerianity*

The first property of the disk that I studied is the deviation of the azimuthal velocity from its Keplerian value. Ignoring the contributions of the magnetic field and thermal pressure, the radial equilibrium of the material in the disk (in the co-rotating frame) can be determined by

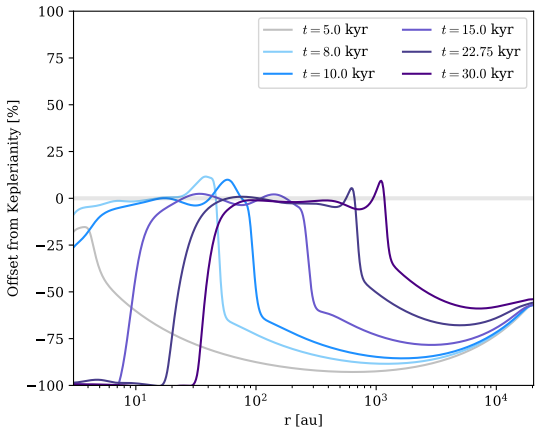



Figure 4.2: Deviation of the azimuthal velocity in the midplane from its Keplerian value, computed with the fiducial simulation on grid x8.

calculating the ratio of the centrifugal to the gravitational force

$$\frac{a_R^c}{\rho g_R} = \frac{\rho v_\phi^2}{r \sin\theta} \cdot \frac{r^2}{\rho G M(r) \sin\theta} = \frac{v_\phi^2}{v_K^2 \sin^3\theta}, \tag{4.1}$$

where $v_K \equiv \sqrt{GM(r)/R}$ is the Keplerian velocity ($M(r)$ is the enclosed mass including the protostar). This equation motivates the definition of the *offset from Keplerianity* as

$$\text{offset from Keplerianity} = \left| \frac{v_\phi}{v_K \sin^{3/2}\theta} \right| - 1. \tag{4.2}$$

The results for the calculation of the offset from Keplerianity in the fiducial case of grid x8, presented as a function of time, are given in fig. 4.2. From the curves for different instants in time, I find the following features:

a) For large distances, one distinguishes the infalling envelope as the region where the material is always sub-Keplerian.

b) I define the disk as the region where the azimuthal velocity has an offset of Keplerianity within $\pm 25\%$.

c) At late times, there is sub-Keplerian material in the innermost $\sim 30\,\text{au}$ of the accretion disk.

#### 4.4.2.2 Specific energies

As a tool for the analysis of the different terms of the MHD equations, I compute the following contributions to the specific energy:

a) the gravitational specific energy

$$e^{\text{grav}} = \frac{GM(r)}{r}, \tag{4.3}$$

b) the thermal specific energy

$$e^{\text{th}} = \frac{P}{\rho(\Gamma - 1)}, \tag{4.4}$$

c) the contribution to the specific kinetic energy by the azimuthal component of velocity

$$e_\phi^K = \frac{v_\phi^2}{2}, \tag{4.5}$$

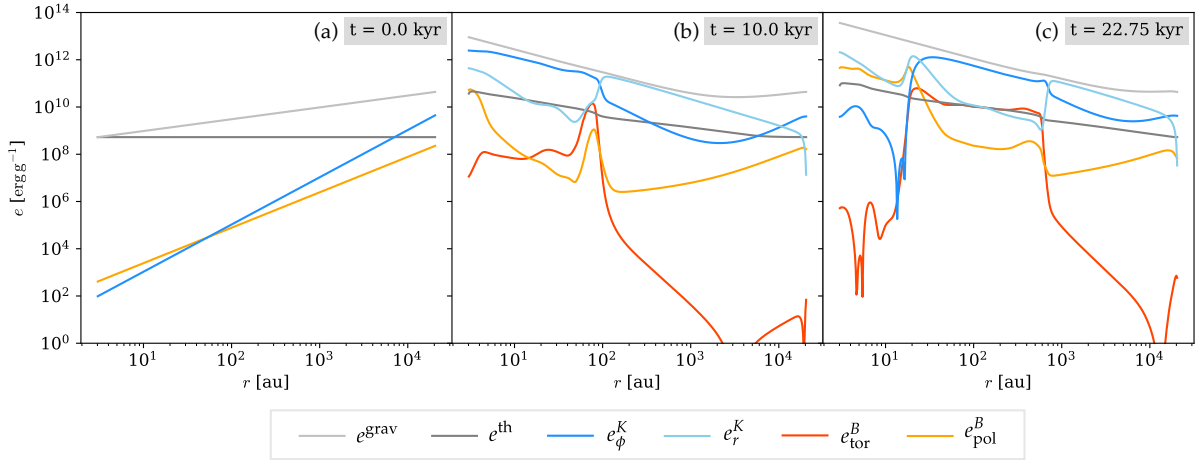



Figure 4.3: Contributions to the specific energy in the midplane, calculated with the fiducial simulation on grid x8. The thin disk can be identified as the region where $e^K_\phi \sim e^{\text{grav}}$.

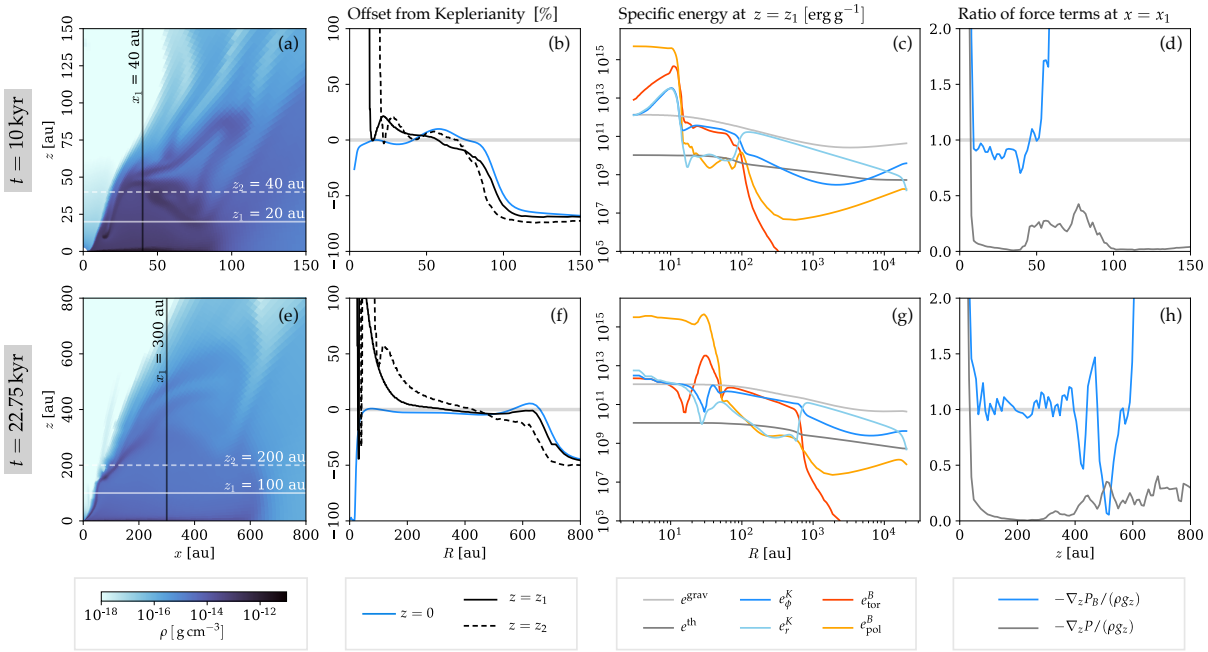



Figure 4.4: Dynamics of the thick disk. The panels of the figure are grouped in columns such that they show: the density structure of the thick disk (*a* and *e*), the offset from Keplerianity at three different heights in the thick disk (*b* and *f*), the contributions to the specific energy (*c* and *g*), and the vertical balance of forces (*d* and *h*). Data from the fiducial simulation on grid x8 was used for this figure.

d) the contribution to the specific kinetic energy by the spherical-radial component of velocity

$$e_r^K = \frac{v_r^2}{2}, \tag{4.6}$$

e) the contribution to the specific magnetic energy by the toroidal component of the magnetic field

$$e_{\rm tor}^B = \frac{B_\phi^2}{8\pi\rho}, \tag{4.7}$$

f) the contribution to the specific magnetic energy by the poloidal component of the magnetic field

$$e_{\rm pol}^B = \frac{B_r^2 + B_\theta^2}{8\pi\rho}. \tag{4.8}$$

The results for each contribution in the midplane, for the fiducial case on grid x8, for three different instants in time, are presented in fig. 4.3. Initially (panel *a*), the gravitational energy is dominated by the contribution of the enclosed mass (increasing with radius), but as the collapse progresses (panel *b*), it decreases with distance because the gravity of the protostar becomes more important than the gravity of the envelope. A comparison of the gravitational specific energy and the radial and azimuthal contributions to the specific kinetic energy reveals the same structures I explained using the analysis of Keplerianity. The same analysis of specific energies can be found in fig. 4.4 for the thick layer of the disk.

#### *4.4.2.3 Thermal and magnetic pressure*

A comparison of the curves for both specific magnetic energy contributions and the thermal specific energy reveals (fig. 4.3*b*) that the thin layer of the accretion disk is dominated by thermal pressure over magnetic pressure. Thermal pressure decreases monotonically with distance, and therefore its gradient exerts a force that always supports against gravity. Magnetic pressure, on the other hand, has regions of increase and decrease within the disk, and so, material can become both slightly super-Keplerian or sub-Keplerian due to the magnetic pressure gradient.

In the thick disk (fig. 4.4, panels *c* and *g*), both contributions to the specific magnetic energy are higher in magnitude than the thermal energy. This implies that the vertical support of the thick layer of the disk is of magnetic origin. This is confirmed by panels *d* and *h* of fig. 4.4, where I compare directly the magnetic and thermal pressure gradient against gravity for the thick disk.

#### *4.4.2.4 Magnetic braking and magnetic diffusion*

As stated above, the magnetic field lines are dragged by rotation as time progresses. This creates increasing magnetic tension, which exerts a torque that tends to brake the gas, specially in the innermost parts of the disk where the flow velocities are highest. The accretion disk, however, is able to exist thanks to magnetic diffusion in the form of Ohmic dissipation, and it can be seen in fig. 4.3 as a reduction of the toroidal contribution to the specific magnetic energy inside the disk.

Magnetic diffusion is not 100% effective because the resistivity is not infinite. The magnetic field lines are decoupled from the azimuthal flow, but over time, the toroidal magnetic field still increases slowly. When enough angular momentum can be taken away from the gas, magnetic braking starts to happen in the innermost parts of the accretion disk, which gives rise to the inner infall region introduced in §4.4.1. Magnetic braking affects also the cavity wall and the thick disk, which provokes the constant replenishment of gas in the inner infall region, which implies that the density is always high in its interior.

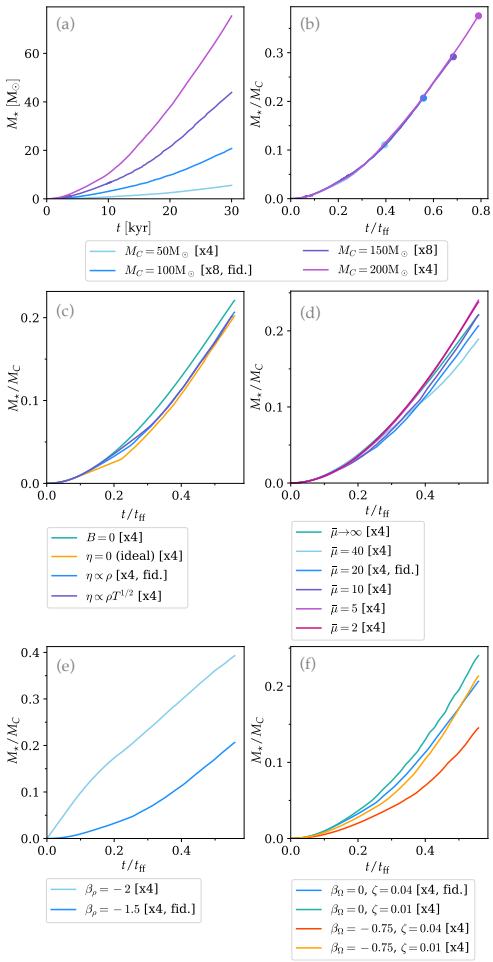



Figure 4.5: Mass of the protostar, corresponding to the mass in the sink cell, for several values of the (*a*–*b*) mass of the cloud, (*c*) resistivity model, (*d*) mass-to-flux ratio, (*e*) density profile, and (*f*) rotation profile and rotational energy. Panel *b* shows the same results as panel *a*, but normalized in such a way that scalability can be readily seen. For panels (c)–(f), $M_C = 100\,\mathrm{M}_\odot$ and $t_{\rm ff} = 53.73\,\mathrm{kyr}$.

Our simulations did not implement the effects of ambipolar diffusion, which is a formal caveat of our results. I expect that with additional magnetic diffusion, the thickness of the disk might be reduced and the appearance of the inner infall region would be delayed.

### 4.4.3 Dependence of the resulting disk properties on initial cloud properties

The next goal of the project is to study how the results obtained in the preceding section change with the initial conditions of the simulation, i.e., the conditions for the onset of gravitational collapse. In order to compare simulations, I reduce the simulation data to three key quantities: the mass of the protostar as a function of time, the (outer) radius of the disk, and the radius of the inner infall region (inner radius of the disk). Those quantities are available in figs. 4.5 and 4.6. In the following sections, I summarize the most important results from the comparison and refer to the respective curves of each quantity in the aforementioned figures.

#### *4.4.3.1 Mass of the cloud core*

I consider cloud cores of several masses ($M_C$): 50, 100, 150 and 200 $\mathrm{M}_\odot$. In principle, the physical effects that we consider in this study are scale-dependent because self-gravity and the micro-physics involved in the treatment of the thermodynamics of the system are scale-dependent.

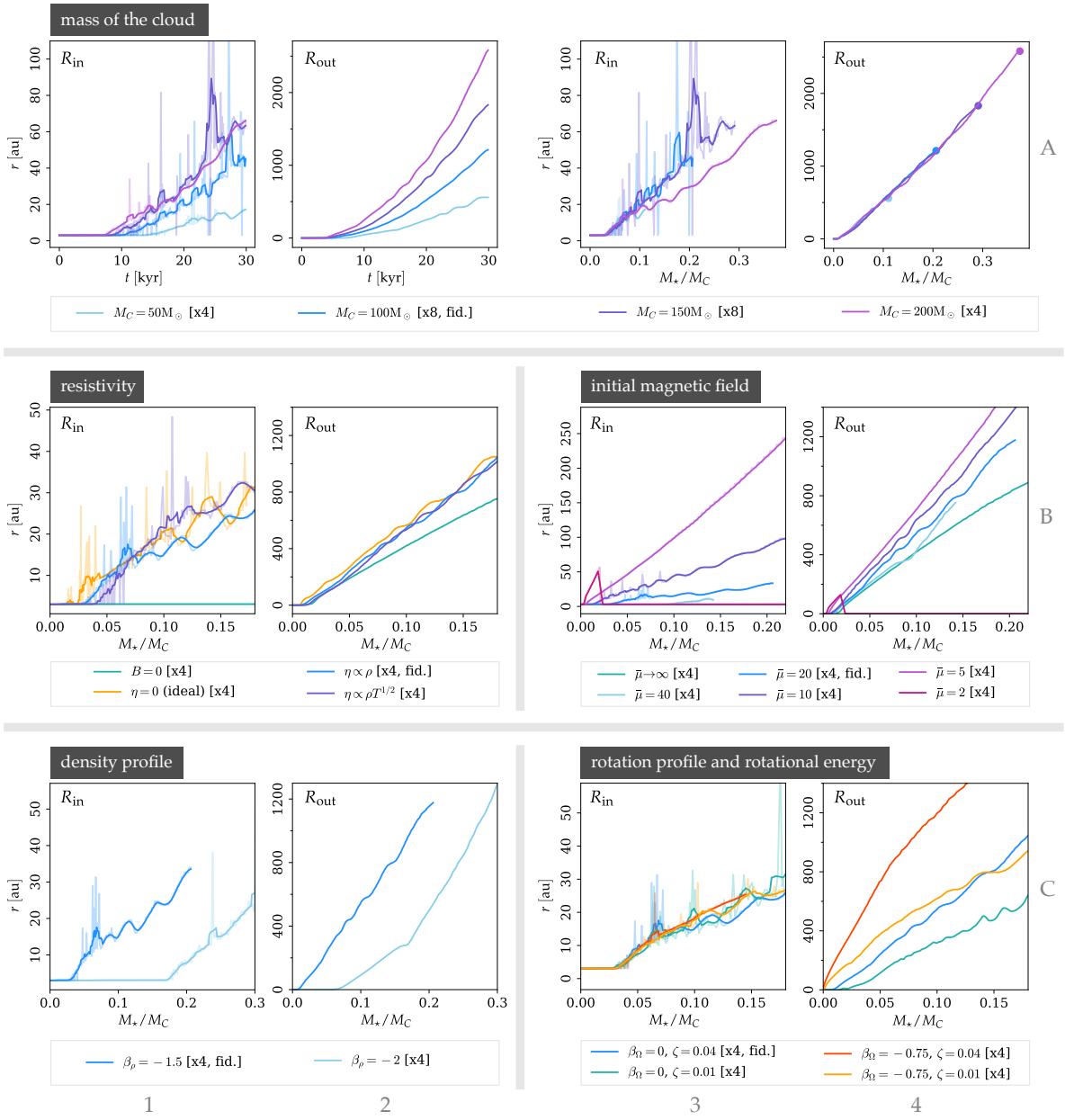



Figure 4.6: Inner and outer radius of the disk for different initial values of the mass of the cloud, magnetic field, density profile, rotational profile, rotational energy and resistivity models. The transparent lines in the panels that show $R_{\rm in}$ indicate the full data, while the solid lines show the moving average. The colored dots in panel A4 indicate $t = 30\,$kyr in each simulation. For all the panels in rows B and C, $M_C = 100\,\mathrm{M}_\odot$ was used.

However, I observed that for the simulations of range of $M_C$ considered, the mass of the protostar as a function of time scales when expressed as a fraction of the mass of their respective cloud core, and when the time is normalized with their respective free-fall timescale. After doing the same normalization for the inner and outer radius of the disk, I find that those quantities also scale. As a consequence, we are able to use the results of our parameter scan in a wide range of cloud masses.

#### 4.4.3.2 Ohmic resistivity

I studied the effect that magnetic fields and the Ohmic resistivity model have on the material of the disk by considering four cases:

a) no magnetic fields,

b) ideal MHD (no resistivity),

c) isothermal resistivity model,

d) temperature-dependent resistivity model.

The isothermal resistivity model differs from the temperature-dependent model by a factor that oscillates between 10 and 100 in the densest regions, and I use both cases to assess the impact of magnetic diffusivity in general and to obtain an indication of the expected trends if more magnetic diffusion (ambipolar diffusion, the Hall effect) were taken into account. I find that the disk is slightly larger with ideal MHD than with resistivity (a result also seen recently by Commerçon et al. 2022) because of the additional magnetic pressure support available in the disk. The start of the magnetic braking epoch is also delayed when more resistivity is used.

#### 4.4.3.3 Initial magnetic field strength

I find that stronger magnetic fields lead to somewhat larger disks because of the increase in magnetic pressure. This trend is opposite to what is reported in the literature, and I attribute it to two factors: different criteria for defining the disk, and previously-done comparisons that did not take into account the initial conditions of the cloud cores. In fact, when carefully comparing simulations from different authors that match most of the initial conditions, I find that the differences with our results are not too large (they are within the same order of magnitude). As expected, I also find that the effects of magnetic braking are stronger with a stronger initial magnetic field.

#### 4.4.3.4 Initial density and rotation profiles

A major conclusion of this project is that the initial density profile and the angular momentum content and distribution are the biggest determinants of the size of the accretion disk, as opposed to the magnetic field or the diffusivity of the material. The curves for the radius of the disk that I calculated are based on the ranges of values of those quantities that are estimated from observations (see §1.2), and so, I expect a wide range of sizes of accretion disks in nature, without confining the radius of such disks to the $\sim 50$ au typically mentioned in the literature.

# 5 The dynamics of massive protostellar outflows

The following chapter is a summary of the manuscript entitled "Modeling disks and magnetic outflows around a forming massive star: II. Dynamics of jets from massive protostars", which has been accepted for publication in the peer-reviewed journal *Astronomy & Astrophysics*, with Rolf Kuiper (RK) as a co-author and supervisor. This part of the project is a continuation of what is presented in ch. 5. I use the same set of simulations already discussed to study the magnetically-driven outflows that form self-consistently within the simulation domain. The full text of this manuscript can be found in Appendix A.5. The content of this chapter is meant to be a supplement, detailing aspects like the organization of the project, my personal contribution and a highlight of the results that I anticipate are more interesting to the wider community. If desired, the reader can directly skip to the full manuscript and consult this supplementary information if necessary.

## 5.1 Objectives and expected outcome

In §2.3 and §2.4, I presented the main aspects of the classical models for jets, particularly suited to describe the dynamics of jets launched by, for example, black holes or active galactic nuclei. Neither of the two studies considers the system to be embedded in an infalling envelope, which is the case for massive protostellar outflows. With this in mind, the aims of this part of the project are:

a) simulating magnetically-driven outflows in a way such that they are self-consistently launched from the circumstellar disk,

b) understanding the processes involved in the launching, acceleration, collimation, propagation and termination of massive protostellar jets, offering a unified theoretical picture of the occurrence of those processes,

c) determining the impact of the conditions of the onset of gravitational collapse on the resulting outflows, and

d) determining the effects of resolution on the simulation of massive protostellar jets.

## 5.2 State of the art in simulations

The same literature review already mentioned in §4.2 also applies here. So far, none of the studies of massive protostellar jets that use AMR Cartesian grids (e.g. Seifried et al. 2011; Machida and Hosokawa 2020 and Commerçon et al. 2022) have been able to self-consistently launch jets whose velocities exceed $\sim 50\,\mathrm{km\,s^{-1}}$. The primary reason for this is insufficient resolution in the launching region of the jet. Moreover, some studies (Banerjee and Pudritz, 2007; Seifried et al., 2012) do not find evidence of magneto-centrifugal launching of the outflows and only find evidence for a tower flow. The studies that do find some evidence of the magneto-centrifugal mechanism are vague in the description of how the jet is launched and accelerated. The first study that reports jet velocities over $\sim 100\,\mathrm{km\,s^{-1}}$ is Kölligan and Kuiper (2018), on which we base this work. By using a polar grid and a radial coordinate that increases logarithmically with distance, both Kölligan and Kuiper (2018) and our study are able to resolve the inner $\sim 50\,\mathrm{au}$ close to the protostar, a length scale of critical importance for the magneto-centrifugal launch of a fast jet.

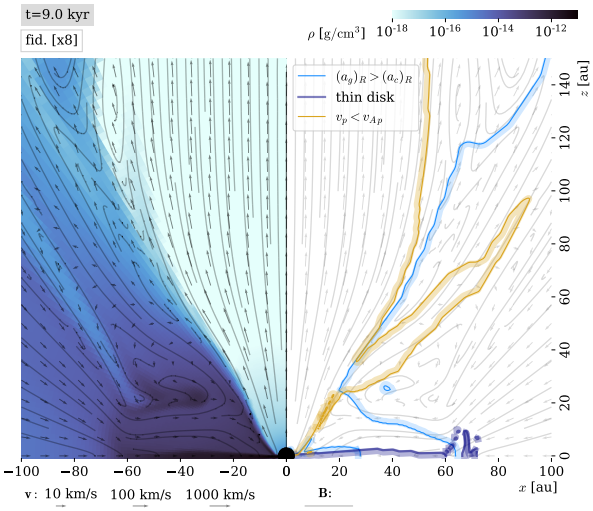



Figure 5.1: Magneto-centrifugal launching of the jet. The left panel shows a morphological view (density, velocity and magnetic field), while the right panel presents directed contours of quantities that provide information on forces acting on the plasma.

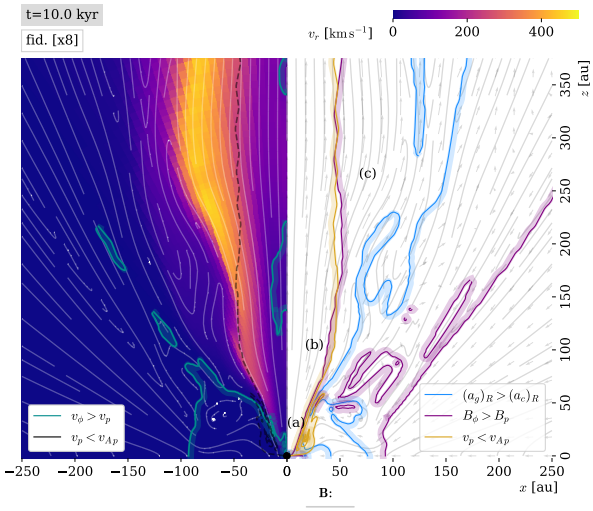



Figure 5.2: Acceleration of the flow in the jet cavity. The scale of radial velocities is saturated at 500 km s$^{-1}$ and only shows positive values. The region labeled *a* corresponds to the same as displayed in fig. 5.1.

From the observational point of view, the existence of jets with high speeds is expected and inferred from information obtained from larger scales (Moscadelli et al., 2021). Moreover, radio observations of protostellar jets both in their early formation (Moscadelli et al., 2021) or later stages (Carrasco-González et al., 2021) reveal sources of synchrotron emission within the jet re-collimation region. This means that particles in the flow are expected to reach relativistic speeds along their propagation, and simulations of massive protostellar jets should at least offer clear indications of the physical processes involved in reaching those magnitudes in speed.

## 5.3 Selected results and discussion

### 5.3.1 Physical processes in the outflows

#### *5.3.1.1 Magneto-centrifugal mechanism*

In order to visualize the effects of the different forces that intervene in the dynamics of the material in a simultaneous way, I constructed a set of contour lines that are followed by an adjacent shadow of the same color, which I call *directed contours*. A directed contour separates space into two regions according to an inequality (listed in the legend of the plot): the shadowed part corresponds to the region where the inequality holds true.

According to the jet theory of Blandford and Payne (1982) (see also §2.3), the material from the "disk's corona" is in the sub-Alfvénic regime, which means that it is forced to follow the poloidal magnetic field lines (in the co-rotating frame), resulting in the centrifugal ejection of the material. I therefore looked in the simulation for the region that simultaneously satisfies: a) the presence of a sub-Alfvénic flow, and b) the dominance of the centrifugal force over gravity, projected in the cylindrical radial direction.

The right panel of fig. 5.1 aids in the investigation of the conditions for the magneto-centrifugal launch of the jet, by visualizing the region where both conditions intersect. Contrary to classical jet theory, I find that the launching region is on the part of the cavity wall that is in contact with the disk, instead of being located on top of the entire disk. Both the material infalling from large scales and the presence of the disk exert ram pressure and an increment

of density that prevent the conditions for a sub-Alfvénic flow to be satisfied. This means that, instead of a "full disk wind", I obtain a narrower (more collimated) outflow from its launching point.

To be more concrete, consider a parcel of gas that falls in from large scales into the accretion disk. Then, it is transported through the disk until it reaches the cavity wall. If the parcel enters the cavity, it experiences a larger centrifugal force than gravitational force in the cylindrical-radial direction. In absence of magnetic fields, the parcel would tend to move cylindrical-radially outwards. However, the parcel enters simultaneously the sub-Alfvénic regime, which means that the flow must follow the mostly-poloidal magnetic field lines, resulting in the parcel being thrust outwards in the spherical-radial direction.

#### 5.3.1.2 Acceleration and re-collimation

Continuing the description of the same parcel of plasma, I performed a dynamical analysis of its acceleration process which is shown in fig. 5.2. The launching region is marked with the label *a*. Once the parcel of plasma is in the cavity, its acceleration can be studied with the energy equation

$$\boldsymbol{\nabla} \cdot \left[ (E^g + E^K + E^{\text{th}} + P)\boldsymbol{v} + c\boldsymbol{\mathcal{E}} \times \boldsymbol{B} \right] = 0, \tag{5.1}$$

ignoring radiation transport and considering a stationary state where gravity does not change much in time. Given that in the cavity we can ignore Ohmic dissipation, from the induction equation one finds that $c\boldsymbol{\mathcal{E}} = -\boldsymbol{v} \times \boldsymbol{B}$. As discussed, the sub-Alfvénicity of the flow close to the launching area causes $\boldsymbol{B} \parallel \boldsymbol{v}$, which implies $c\boldsymbol{\mathcal{E}} \times \boldsymbol{B} = -(\boldsymbol{v} \times \boldsymbol{B}) \times \boldsymbol{B} = \boldsymbol{0}$ and allows us to conclude from eq. 5.1 that

$$E^g + E^K + E^{\text{th}} + P = \text{constant} \tag{5.2}$$

along the flow in the cavity. This expression is equivalent to the Bernoulli equation for a given streamline. A consequence of the energy analysis made in ch. 4 (panels *c* and *d* of fig. 4.4) is that, in the cavity, the thermal pressure (and energy) is significantly lower than the magnetic, gravitational and kinetic energies. So, in the end, eq. 5.2 expresses the simple conservation of mechanical energy. Consider a poloidal magnetic field line that roughly follows a spherical radial shape, marked in fig. 5.2 as *b*. When the parcel of plasma moves from *a* to *b*, its gravitational energy decreases. This means that its kinetic energy must increase. I observe then on the left panel of fig. 5.2 that the flow gains radial velocity from $\sim 0$ to $\sim 400\,\text{km}\,\text{s}^{-1}$ and moves along the magnetic field lines. Then, it goes outside of the Alfvén surface and into the region where the magnetic field lines are more toroidal than poloidal (label *c*). There, the material feels the force of the magnetic pressure gradient and it accelerates upwards further.

The material is collimated since its launch because of the geometry of the launching region. However, it accelerates spherical-radially outwards. The wound magnetic field lines exert a Lorentz force (*magnetic hoop stress*) that re-collimates the material, aided by the ram pressure from the infalling envelope (cf. fig. 5.3). The material is re-collimated at distances of $\sim 10\,000$ au from the protostar, and in the highest resolution simulation it can reach speeds of up to $\sim 5000\,\text{km}\,\text{s}^{-1}$. While those speeds are not yet relativistic ($\approx 0.02c$), the theoretical maximum speed cannot be determined from our simulations because it is artificially restricted by the Alfvén limiter (§4.3). However, the re-collimation of the jet that we observe in the simulations provides a theoretical support for the mechanism proposed in Carrasco-González et al. (2021) for the production of synchrotron emission at similar distances from the source.

#### 5.3.1.3 Cavity wall ejections

I observe that the ejection of material in the jet is not smooth but rather episodical. Material from the cavity wall sometimes contributes to the inflow and sometimes to the outflow. When it contributes to the outflow, it forms "protuberances" (fig. 5.4) that develop a narrow neck until the magnetic field lines reconnect. Then, the discrete piece of material is ejected through the

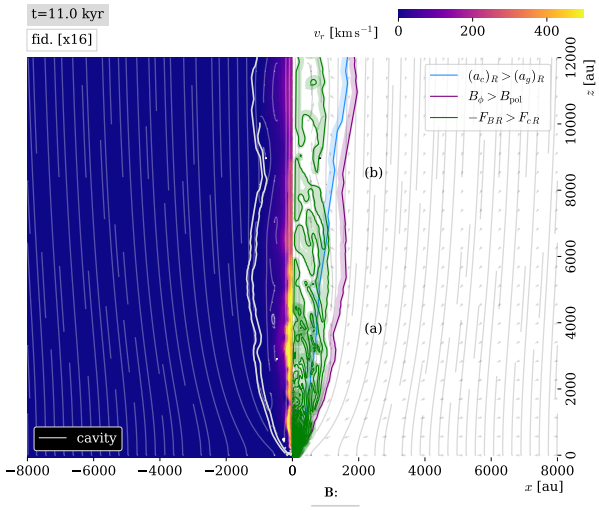



Figure 5.3: Re-collimation of the jet. The color scale of the radial speeds has been saturated to 500 km s$^{-1}$ and only shows positive values.

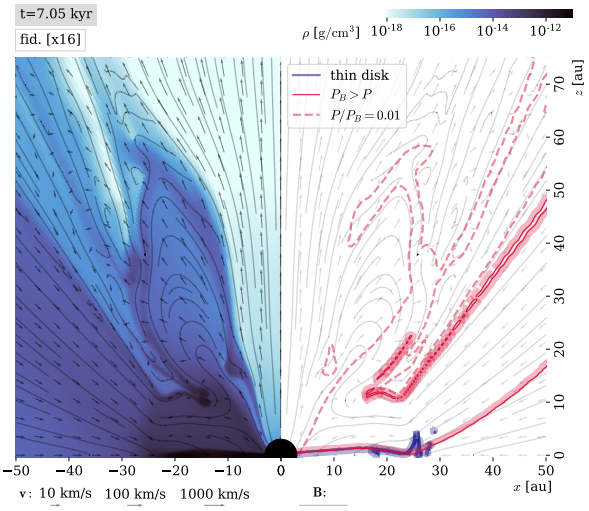



Figure 5.4: Cavity wall ejection. The dashed contour shows how thermal energy increases temporarily due to magnetic dissipation.

cavity. This process could be affected if other forms of magnetic diffusivity were included, so further work is needed to confirm its correspondence to a realistic situation.

#### 5.3.1.4 *Magnetic tower flow*

Apart from the (magneto-centrifugally launched) jet, we also observe a tower flow. The right-hand panel of fig. 5.5 presents two directed contours: the red directed contour indicates the region where the spherical-radial component of the magnetic pressure gradient is larger than gravity. That contour indicates that the outflow observed at large scales is thus driven by magnetic pressure. The purple directed contour indicates the region where the magnetic field lines are wound by rotation, and it also coincides with the tower flow. This means that the origin of the magnetic pressure gradient is indeed the winding of magnetic field lines by the disk.

#### 5.3.1.5 *Bow shock*

My explanation of the magneto-centrifugal mechanism in §5.3.1.1 relies on the low-density cavity already being present for the sub-Alfvén flow to be possible. Then, the question arises: how is the cavity formed in the first place? To this end, I present a dynamical analysis of the first stages of the launching of the jet in fig. 5.6. At that instant, the disk is only a few astronomical units in size, and the cavity is too narrow to support effective magneto-centrifugal launching of material from the disk. However, from the red and purple contours I see that the conditions for a magnetic tower flow are achieved, and so I conclude that the cavity is formed by magnetic pressure. Once the material expands, the densities inside reach sufficiently low values for sub-Alfvénicity, and the magneto-centrifugal mechanism can begin the launch of the fast jet.

During the formation of the cavity, material from the envelope is pushed out as the cavity expands and a bow shock appears. This bow shock propagates outwards over time. Even though the formation of the cavity is not the only mechanism that could produce a bow shock, its propagation over space could be theoretically used to estimate the age of a massive protostar.

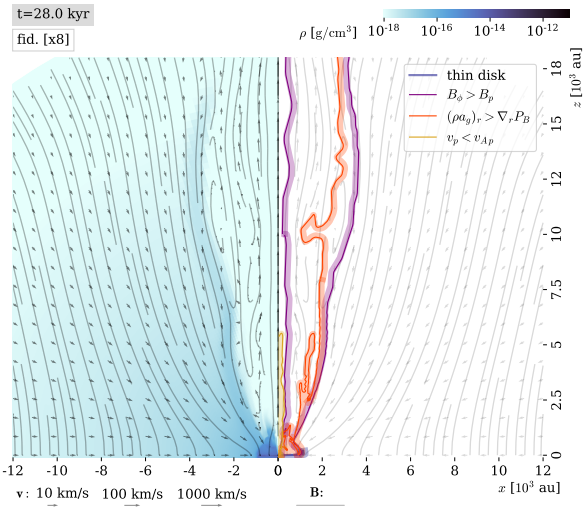



Figure 5.5: Magnetic tower flow.

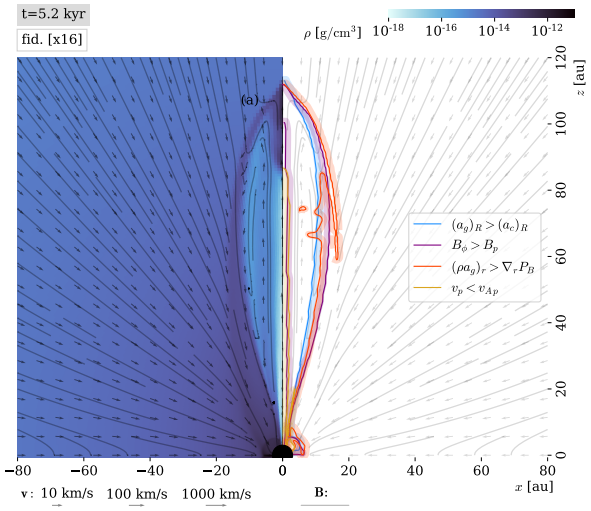



Figure 5.6: Production of the bow shock that gives rise to the jet cavity.

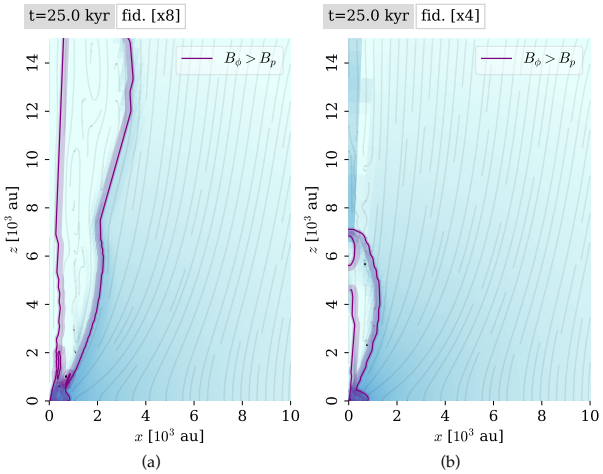



Figure 5.7: Effects of resolution on the propagation of the tower flow.

#### 5.3.1.6 *Magnetic braking*

Because the cavity wall is affected by magnetic braking starting at $t \sim 15$ kyr, the magneto-centrifugal mechanism is also affected. The innermost parts of the cavity narrow considerably, but the material is still magneto-centrifugally launched at higher (and outer) points from the disk. The tower flow is unaffected by this process, and the continuous increase in magnetic pressure by the rotational dragging of magnetic field lines broadens the tower flow over time.

### 5.3.2 Effects of resolution

I studied the effects of resolution by solving the fiducial case in five different grid configurations. Additionally, I tested the effects of several numerical parameters in the stability of the results I present. A highlight of the resolution study is illustrated in fig. 5.7, which corresponds to a snapshot of the fiducial case at $t = 25$ kyr, run in grids x8 (left panel) and x4 (right panel). In run x8, the tower flow expands freely through the cloud. In run x4, the tower flow is contained to a region of $\sim 7\,000$ au in size. At that point, even though the material located at larger scales still flows out, the physics of the re-collimation of the flow cannot be adequately resolved anymore. Because of the key finding mentioned in the previous section, I restrict the parameter study for

jet simulations to only the two highest-resolution grids.

### 5.3.3 Variation of the properties of the outflow with the initial conditions

All simulations displayed a similar behavior in terms of the kinds of outflows launched, and the processes that drive them. However, there are a few morphological and dynamical differences between them that I summarize next.

**Mass of the cloud core.** For a more massive cloud core ($M_C = 150\,\mathrm{M}_\odot$), the cavity becomes slightly broader. However, I find that the linear momentum expelled by the jet divided by the total cloud mass as a function of the fraction of the free-fall time elapsed is the same for both the $150\,\mathrm{M}_\odot$ case and the fiducial ($100\,\mathrm{M}_\odot$) case. This means that in principle, the results are qualitatively scalable with the initial mass of the cloud core, in a similar way as we found in ch. 4.

**Magnetic field strength.** The jet is launched earlier in the case of strong magnetic fields ($\bar{\mu} = 5$) compared to the fiducial case ($\bar{\mu} = 20$). However, magnetic braking completely disrupts the outflow at late times. This result must be checked by the inclusion of ambipolar diffusion, whose diffusivities are more notorious in the case of strong magnetic fields.

**Angular momentum content.** Using a steep initial angular momentum profile ($\Omega \propto R^{-0.75}$) produces a flatter disk, and the cavity becomes more cylindrical in shape.

# 6 An observational example of a massive protostellar outflow

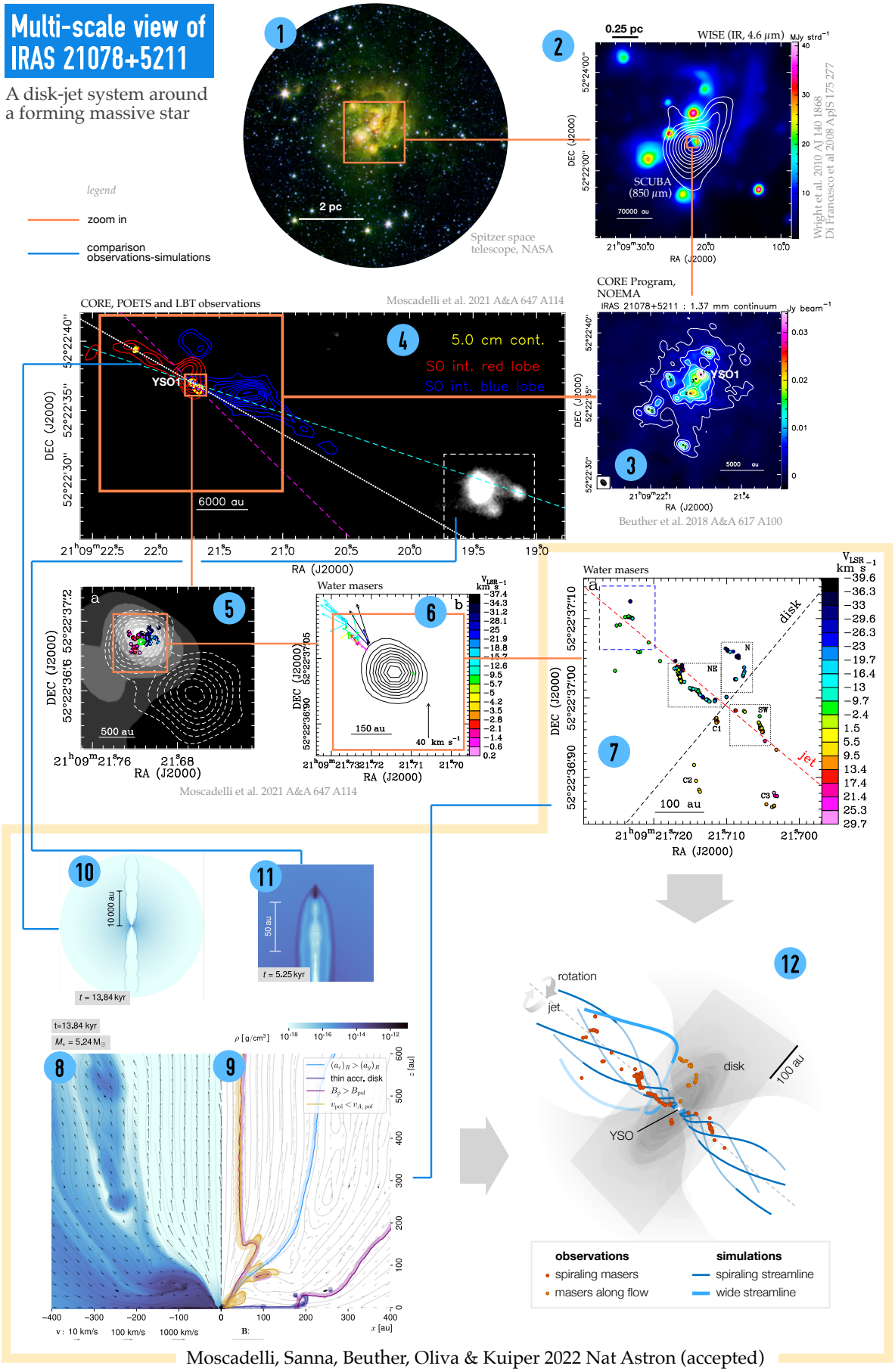
In this chapter, I describe and discuss my contributions to the article entitled "Snapshot of a magnetohydrodynamic disk wind", which has been published in the peer-reviewed journal *Nature Astronomy*, volume 6, page 1068. The full list of authors is: Luca Moscadelli (LM), Alberto Sanna (AS), Henrik Beuther (HB), André Oliva (AO) and Rolf Kuiper (RK). The full accepted version of this article is attached in Appendix A.2. Given that the article contains a strong observational component in which I did not take direct part, this chapter is meant to provide a more in-depth view of my contributions to the project, as well as context on previous observations to which the article frequently refers.

## 6.1 Description of the project and participation

This work is the result of a collaboration between a group dedicated to performing observations (LM, AS, HB) and a group focused on theoretical modeling with simulations (AO, RK). A schematic view of the context and results of this project is offered in fig. 6.1, where I enclose the new observations and simulation with a yellow border. In the rest of the chapter, I simply refer to each panel of that figure with a number inside parentheses.

For the first time, individual streamlines coming from a massive protostellar jet have been observed thanks to the detection of 22 GHz water masers in the innermost $\sim 100$ au close to the forming massive star. IRAS 21078+5211 is a star-forming region located at a distance of 1.6 kpc (1,2), which contains forming massive stars. Beuther et al. (2018) performed observations using the Northern Extended Millimeter Array (NOEMA) as part of the CORE program (3) and found a young stellar object (YSO1) with a mass of $5.6 \pm 2\,M_\odot$ surrounded by other (probably cloud) fragments at a few thousands of astronomical units. Moscadelli et al. (2021) conducted large multi-scale study of the system, using a wide variety of observations from different programs and instruments, and which I summarize next. Radio observations at 5 cm performed with the Jansky Very Large Array (JVLA) revealed the existence of a collimated jet (4) originating from YSO1. Further observations were made in order to uncover the accretion disk and the launching region of the jet. The size of the accretion disk (5) is around $\sim 400$ au (i.e., a radius of $\sim 200$ au). Using the Very Long Baseline Array (VLBA), observations of maser emission of the water molecule (22 GHz) were made (6), revealing proper motions of the material from around $\approx 100$ au from YSO1. The observed velocities were found to be consistent with a fast jet with speeds of at least $\approx 200\,\mathrm{km\,s^{-1}}$, magneto-centrifugally launched from the disk.

For this project, LM, AS and HB used all the telescopes available in the VLBI network to perform water maser observations in the region within 100 au of YSO1 (7). The VLBI network included 16 antennae of the European VLBI network (EVN) and 10 antennae of the VLBA. The spatial resolution of the observation was $\approx 0.05$ au. From the point of view of theory, only the simulations performed by RK and I (ch. 4 and 5) are currently able to reach those levels of resolution at the launching point. Specifically, grids x8 and x16 have minimum cell sizes of 0.06 and 0.03 au at $r = 3$ au, respectively. As discussed in §5.3.2, grid x4 and coarser are not able to resolve the large-scale propagation of the jet, although the launching region is reasonably resolved. This means that previous simulations from Kölligan and Kuiper (2018) could also be used for a comparison at small scales, but not at intermediate or large scales in the cloud core. As examples of the feasibility of comparisons of the observational results of this project with simulations based on an AMR Cartesian grid, I cite the recent works by Commerçon et al. 2022 and Mignon-Risse et al. 2021b), which use minimum cell sizes of 5 au. Moreover, their sink




Moscadelli, Sanna, Beuther, Oliva & Kuiper 2022 Nat Astron (accepted)

Figure 6.1: Schematic view of the results of the project.

particle models are set up in a way that there is an accretion radius of 20 au, meaning that their results are influenced by numerical effects inside that radius and cannot be used to compare against observations.

I performed a comparison of the kinematic footprint unveiled by the masers and the simulations, which allowed us to confirm that the launching of the flow is consistent with a magneto-centrifugally launched jet. Because the manuscripts associated to chapters 4 and 5 have not been accepted yet at the time of writing of this thesis, this article also constitutes an advance peer-reviewed publication of the results of one of the simulations from the previously mentioned simulation set.

## 6.2 Objectives and expected outcome

For my part in the project, I expected to

a) find a snapshot from my simulation catalog that resembles the most the observed features of the jet,

b) test the consistency of the magnetic field line and streamline configuration obtained in the simulations with the observed maser points, and

c) offer an explanation for the features of the large-scale propagation of the jet.

## 6.3 Results and discussion

### 6.3.1 In search for a simulation match

A major conclusion of the results presented in ch. 4 and 5 is that there are several combinations of initial conditions that produce a disk of a given size and a jet, for a protostar of a given mass. This means that, in principle, the problem is underdetermined and only an example initial configuration from the simulations can be formally given. However, I used as much information as possible from the observations to constrain the parameter space of the simulation catalog.

First of all, none of the effects associated with magnetic braking is visible in the observations. This can be due to several causes: the system is too young for magnetic braking to be of importance, or the simulations are missing magnetic diffusivity (which delays the braking), or the initial magnetization is very low. Then, I did not include any simulation that displays signs of magnetic braking for $M_\star \approx 5.6\,\mathrm{M}_\odot$. An additional evidence for the system to be young is that its luminosity is not too large yet ($\approx 10^4\,\mathrm{L}_\odot$, cf. Davies et al. 2011). The radius of the accretion disk is estimated in around 200 au, which further restricts the parameter space in terms of the initial angular momentum and density distributions. According to fig. 4.6, a steep angular momentum profile yields a large accretion disk; interestingly, for the observed mass of the protostar, the fiducial case yields a disk size in the observed range. The steepness of the initial density distribution also affects the size of the disk dramatically. However, shallower density profiles produce more fragmentation and so, for the high level of fragmentation observed in the cloud core (panel 3) and possibly even in the disk, I expect the density profile not to be steep. Finally, a comparison of the propagation of the bow shock (see §6.3.4) further constrained the parameter space to the fiducial case. Because of this, I was able to use the highest resolution simulation in the catalog, x16, which was run until $t = 13.84$ kyr due to its high computational cost. At that instant in time, the protostar in the simulation had fortunately reached a value of the mass within the observed interval: $M_\star = 5.24\,\mathrm{M}_\odot$.

### 6.3.2 Launching of the jet

The masers are distributed very close to the jet axis, at distances of $\sim 30$ au from it. Water masers trace internal shocks in the flow, but they are also observed in external shocks, for example, collisions against the cavity wall or a bow shock. LM and AS argue that for these observations, the attribution to external shocks is less plausible. The water maser observations (7) show two kinds of kinematic signature:

a) The NE and SW regions are consistent with helical motion.

b) The masers in the N region show an acceleration along the curve.

Panels (8) and (9) show the same dynamical analysis of the magneto-centrifugal mechanism that is explained in ch. 5, for the selected snapshot. Our simulations show that the Alfvén surface of a massive protostellar jet is narrowed by the infalling envelope. The magnetic field lines are mostly poloidal inside of the Alfvén surface, but mostly toroidal on top of most of the disk. From (9), I observe that the change from sub- to super-Alfvenicity roughly follows the observed narrow distribution of masers captured in (6) and (7). RK and I then propose that a possible explanation for the origin of the internal shock that gives rise to the observed water masers is this transition of the flow.

In order to visualize the situation and test the hypothesis, I traced streamlines from a three-dimensional projection of the velocity data from the simulation (12). I assumed a small inclination angle such that the upper part of the jet points slightly towards the observer, in accordance to what is suggested by the Doppler shift at small scales in the observations. The streamlines were integrated such that they touch $R = 50$ au at a height of $z = 500$ au, i.e., they correspond approximately with the limit between a sub- and super-Alfvénic flow. The flow is highly helical the closer it is to the protostar, and the positions of the masers in the NE and SW regions coincide well with the regions in the simulation where the motion is most helical. The helical motion is due to the flow being in almost co-rotation with the disk, as the flow is sub-Alfvénic in the co-rotating frame. The mostly poloidal magnetic field lines guide the flow outwards as it rotates.

For the wide flow seen in the N region, the coincidence is not perfect, but I obtained a reasonably good approximation to the kinematic signature of the flow by choosing a streamline such that it passes through $R = 140$ au (i.e., it corresponds to the outer disk) at a height of $z = 500$ au. The parcel of material rotates in the outer disk and it reaches the region above the disk where the centrifugal force dominates against gravity (9). In that region, the flow is not sub-Alfvénic, however, the vertical magnetic pressure gradient is stronger than gravity (the magnetic field lines are wound by rotation) and it pushes the material outwards. The result is a streamline that follows a sharp turn as seen from the assumed perspective (12). The lack of coincidence of the position of the streamlines can be due to several factors, such as an incorrect assumed perspective or a thinner disk in reality. However, we are able to replicate the kinematics of the N masers to a reasonable degree.

#### *Production of panel 12*

For completeness, I describe next the specific method of production of (12). I programmed a script in Python that does the following tasks: a) it extends the two-dimensional simulation data into the azimuthal and polar directions using the boundary conditions; b) it interpolates the data into a three-dimensional fine Cartesian grid; and c) it plots the velocity streamlines with the parameters mentioned above using the open-source software package `Mayavi`. Then, I used the graphical interface of Mayavi to set the 3D view such that there is a small inclination angle between the midplane and the observer, following what is expected from the observations. Using a high-precision vector graphics design program, I manually traced the snapshot of the 3D view of the streamlines, such that the data points always lie within the width of the line (i.e.,

the resulting streamline plot is accurate up to the width of each line). Using an identical 3D view plotted in Mayavi, but with an $Rz$ plane that partially blocks the view of the streamlines, I added emphasis to the parts of the streamlines located closer to the observer, and transparency to the parts away from the observer. This guides the reader to interpret the 3D nature of each streamline.

Both the Mayavi-generated plot and the maser observations contained size bars and guides, which I used to place the maser points over the streamlines. I took the color-coded velocity information out of the maser points, replacing it with the following color code: red points show the position of the masers with the helical kinematics, and orange points do so for the masers that show acceleration along the flow. The simulated streamlines are represented by two shades of blue: the dark blue lines show a spiraling streamline, close to the Alfvén surface, and the light blue lines show wide streamlines from the outer disk. To provide context for the reader, I used an identical 3D view plotted in Mayavi but with a $Rz$ cut through the density field (fully available to the reader in panel 8) in order to sketch the main density features of the simulation (the disk, cavity and the infalling envelope). Those sketches, including the YSO, are clearly shown in grayscale to distinguish them from the data.

### 6.3.3 Re-collimation of the jet

In §5.3.1.1, I presented a description and analysis of the re-collimation zone in the jet (fig. 5.3), and put forward possible scenario that connects my results to the non-thermal radio lobes observed around protostellar jets. For IRAS 21078+5211, the radio lobes are located at around $\sim 6000$ au from YSO1. I see re-colimation zones in the large-scale propagation of the jet in the simulations (10). In fig. 5.3, which was also computed with simulation x16 but at an earlier time than the selected snapshot for the comparison, I see that the highest speeds of the re-collimation zone are obtained in the region $3000 \lesssim z \lesssim 6000$ au, which coincides quite well with the positions of the radio lobes observed in (4).

### 6.3.4 Bow shock

The bow shock produced during the formation of the cavity (11) would provide a possible explanation for the bow shock observed in (4) (white grayscale image in the bottom right corner). From (4), I see that the bow shock is located at $\approx 36\,000$ au away from YSO1. That distance is outside of the computational domain for the simulation snapshot I selected, so I estimate the mean propagation speed of the bow shock as $\sim 3.3 \cdot 10^3$ au kyr$^{-1}$. Given that the bow shock is launched at $\sim 5$ kyr, I estimate that at $t = 13.84$ kyr, the bow shock would be located at $\sim 30\,000$ au, in good agreement with the observation at (4).

# 7 A look at a stellar remnant: pulses from a neutron star

This chapter contains a summary of the article entitled "Effects of the treatment of the mass quadrupole moment on ray-tracing applications for rapidly rotating neutron stars", which is the result of an independent research project done during my doctoral studies in collaboration with Francisco Frutos-Alfaro (FF) from the University of Costa Rica, and which was enriched by discussions with members of the Theoretical Astrophysics group in the University of Tübingen. This research project consists in the utilization of metrics that aim to describe the exterior spacetime around a rapidly rotating (thus flattened) neutron star for calculations of the relativistic corrections to their thermal spectra and the light curves from hotspots on their surfaces (*pulse profiles*). I aimed to compute the uncertainty in those observational applications that the use of different approximations to the metric introduces. The results of this project were published in 2021 as a research article in the peer-reviewed journal *Monthly Notices of the Royal Astronomical Society*, as an article in volume 505, page 2870.

Even though the topic of this project is beyond the general area of massive star formation, I decided to extend the scope of this thesis and include it as an example of the study of a stellar remnant formed from a massive star. The link between compact objects and their progenitor massive stars is a topic of active research. Theoretically some connections could be drawn between properties of an isolated progenitor and its stellar remnant, which could be traced back to the star-formation process. For example, the total angular momentum available from the progenitor may determine the final angular momentum of the neutron star, which in turn determines its rotational deformation (the main focus of interest in this project). The final angular momentum of a massive star after its formation is strongly constrained by the processes discussed in chapters 4 and 5, i.e., the removal of angular momentum by outflows and magnetic braking. In this project, though, the ultimate unsolved problem of interest is how the mass quadrupole moment of a rapidly rotating neutron star can theoretically be used to constrain its equation of state.

The full text of this article can be found in Appendix A.3. If desired, the reader can skip directly to the full text, however, this chapter offers a wider introduction to the topic than what it is offered in the article. Details about the project, personal contribution and selected results can also be found in this chapter.

## 7.1 Context

### 7.1.1 Endpoints of massive stellar evolution and supernovae

At the end of the main sequence, the stellar core is mostly depleted of hydrogen; the reduced radiation pressure from the nuclear reactions triggers gravitational collapse. The central temperatures increase so that the remaining hydrogen in a shell around the core is ignited, followed by the burning of helium, and in the case of massive stars, by heavier elements in several steps until the burning of silicon to iron. During this phase, the increased temperature in the core expands the stellar envelope and the star enters its giant phase. However, the steady production of elements heavier than iron[1] becomes endothermic, and the star loses its ability to halt the gravitational collapse.

The timescale for core collapse is about one second. The outer core collapses supersonically, but the inner core does it subsonically. The central density increases until eventually electrons

[1] To be more precise, nuclei like $^{56}$Fe and $^{56}$Ni have the highest binding energy.

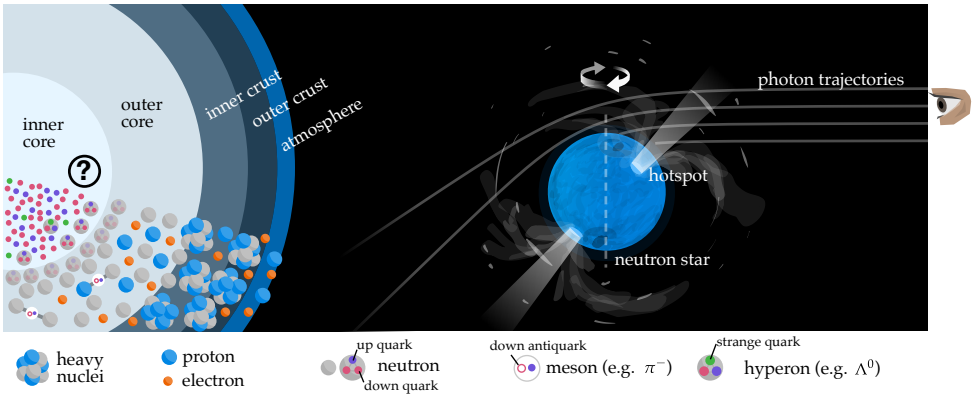



Figure 7.1: Left: a possible structure and composition of a neutron star. Right: classical picture of a pulsar.

become degenerate, but the resulting degeneracy pressure is not enough to halt the gravitational collapse. Nuclear densities ($\sim 10^{14}\,\mathrm{g\,cm^{-3}}$) are reached in the inner core, which triggers the otherwise energetically unfavorable process of inverse beta decay, and neutrons begin to form alongside heavy nuclei. In this state, nucleons (protons and neutrons) feel the repulsive effects of residual strong interaction (force between nucleons), and in the most massive cases, matter starts to feel the degeneracy pressure arising from the degeneracy of neutrons. If those factors are able to halt the gravitational collapse in the inner core, a neutron star is formed, and in the contrary scenario, a black hole is formed. When the collapse stops, the falling outer core is forced to rebound and sends out a pressure shock wave. The process of rebound and the subsequent acceleration of material as a supernova explosion is not fully understood, but it could be powered by the interaction of neutrinos with the most dense material. Neutronization in the inner core releases copious amounts of energy-carrying neutrinos, which become trapped in the inner core due to the density of the material and the velocity of the core collapse. Neutrinos diffuse outwards until they encounter the low-density threshold beyond which they interact only weakly with matter, pushing material in the process, which is then thrust outwards into the interstellar medium. The scenario painted in this paragraph corresponds to a very simplified toy model of a type-II supernova explosion. For an up-to-date introduction to supernova explosions, see ch. 2 of Bandyopadhyay and Kar (2022). For a comprehensive overview of the different types of supernova explosions, depending on the mass of the progenitor massive star and its metallicity, see Heger et al. (2003).

### 7.1.2 Remnants: neutron stars

Neutron stars are formed by neutronization during the core collapse process. They have a restricted interval of masses between $\approx 1.1\,\mathrm{M}_\odot$ and $2\,\mathrm{M}_\odot$ (although the maximum possible mass of a neutron star is still unknown) and radii of the order of $15 \pm 6\,\mathrm{km}$ (Özel and Freire, 2016).

The internal structure and composition of a neutron star is not well known and it constitutes a major unsolved problem in Astrophysics (see fig. 7.1). Current theoretical models divide the basic structure of a neutron star into the following main regions (from Haensel et al., 2007):

a) A thin atmosphere (order of millimeters to centimeters) composed by plasma where the thermal radiation spectrum of the neutron star is formed. This thermal radiation carries important information and can be used for measurements of the mass and radius.

b) An outer crust a few hundred meters thick where the densities increase to $\rho \sim 10^{11}\,\mathrm{g\,cm^{-3}}$, and composed mostly of (heavy) ions and electrons. In this layer, electron degeneracy

becomes important and starts to provide pressure. In the deep layers of the outer crust, the ions usually solidify and beta captures enrich the nuclei with neutrons.

c) An inner crust of about a kilometer in thickness, where neutron dripping starts to happen: nuclei decay and neutrons start to be freed. Here, the equation of state softens because of the free neutrons.

d) An outer core where the density reaches nuclear saturation, and which consists of mostly neutrons with varying percentages of protons, electrons and possibly muons. Here, models of nucleon interaction become important.

e) An inner core where the density reaches more than twice the nuclear saturation density. Its composition is very model dependent. Among several possibilities, neutrons may be deconfined into quarks, or strange quarks might appear forming hyperons.

There are several models to approximate the interactions of nuclear matter. As an example, I cite the *relativistic mean field approximation*: the interactions between baryons are modeled as an exchange of scalar, vector and isovector mesons. The Lagrangian density field to produce the Dirac equation for baryons is simplified by using the expectation values of the meson fields as an approximation. For modeling quark matter that might be present in the inner core, one can use a perturbative approach to quantum chromodynamics for weakly interacting free quarks. See, for example, §3.5 of Bandyopadhyay and Kar (2022) for more details.

Different models of nuclear matter produce different equations of state, i.e., the calculation of the bulk properties of the material. Particularly, they produce different compressiblities. Therefore, a way to constrain models of equations of state is through measurements of quantities that depend on compressibility, such as simultaneous measures of the mass and radius, deformation by rapid rotation or tidal deformability.

### 7.1.3 Propagation of light around a neutron star

The masses of neutron stars can be well constrained in the case they are part of a binary system. One way of measuring the radius of a neutron star is by using its spectrum assuming black body emission, and applying relativistic corrections due to the gravitational bending of light in its way to the observer.

Due to the conservation of angular momentum during the core collapse process, a neutron star spins considerably faster than its progenitor. The most extreme case known so far is the pulsar PSR J1748-2446ad, which has a rotation frequency of 716 Hz. Hot emitting regions (*hotspots*, see fig. 7.1) on the surface of neutron stars form a periodic signal in the form of highly regular pulses (*pulsars*). Pulse-profile modeling is a technique that uses the general relativistic effect on the X-ray emission from hotspots in order to measure neutron star parameters (see e.g. Watts et al., 2016; Bogdanov et al., 2019).

The Neutron Star Interior Composition (NICER) mission has made possible in recent years to directly observe pulse profiles with unprecedented precision. Using pulse-profile modeling, it is now possible to obtain not only high-precision measurements of the radius of the neutron star, but also predictions of the shape and locations of the hotspots (Miller et al., 2019; Riley et al., 2019). However, because of the high computational cost of the fitting process, an approximation based on integrated geodesics using the Schwarzschild metric with the manual addition of other effects has been used. For this reason, the NICER mission has only studied isolated pulsars of rotation frequencies of $\sim 200$ Hz, where the approximation is valid. The Schwarschild metric is an exact exterior solution of the Einstein field equations for a non-rotating and spherically symmetric object. The equations that produce an interior solution under those circumstances are called the *Tolman-Oppenheimer-Volkoff* equations, and are often used to study the structure of slowly rotating (freq. $\lesssim 100$ Hz) neutron stars given an equation of state and a central density.

### 7.1.4 Metrics

Finding exact solutions for the Einstein field equations for a rapidly rotating neutron star is an open problem, in part for the uncertainties of the equation of state, but also for the treatment of the rotational deformation. This flattening is usually modeled in terms of an expansion in mass multipoles. Solutions for the interior and exterior spacetime of a rapidly rotating neutron star can be obtained numerically, for example with the software package RNS (Stergioulas and Friedman, 1995), which progressively adds rotation to the solution of the Tolman-Oppenheimer-Volkoff equations. For analytical solutions, several exact and approximate metrics exist for the exterior spacetime of the neutron star. We considered in this study the following:

- Quevedo–Mashhoon (QM) metric (Quevedo, 1990): it is an exact solution of the Einstein field equations that contains mass, rotation and (mass) quadrupole moment. It reduces to the Kerr metric when the quadrupole moment is zero, and to the Erez–Rosen metric when rotation is zero (the Erez–Rosen metric is an exact solution for a flattened and non rotating body).
- Manko–Novikov (MN) metric (Manko and Novikov, 1992): it is also an exact solution of the Einstein field equations, for arbitrary mass multipoles and rotation. It reduces to the Kerr metric but not to the Erez–Rosen metric. The version we use was corrected by FF.
- Hartle–Thorne (HT) metric (Hartle and Thorne, 1968): it is an approximate metric for slow rotation and mass quadrupole moment. FF expanded the original expression to its correct orders of validity.
- Glampedakis–Babak (GB) metric (Glampedakis and Babak, 2006): it is an approximate metric that contains the Kerr metric with an additive correction for the quadrupole moment.
- Frutos–Alfaro 2016 metric (Fru16) (Frutos-Alfaro, 2016): it is an approximate metric that contains the Kerr metric with a multiplicative correction for the quadrupole moment.

## 7.2 Objectives and expected outcome

With the metrics in §7.1.4, I wanted to know:

a) What are the differences between them? Are photon trajectories different around them? Could we use photon trajectories in principle to discriminate them by accuracy?

b) The expressions on the QM and MN metrics are very complex. Are they practical for use in general relativistic ray-tracing applications?

c) Are there ways to use the shape of pulse profiles to estimate the mass quadrupole moment?

To answer those questions, I used the metrics prepared and provided by FF to:

a) Compute analytically the Christoffel symbols and solve the null geodesic equations numerically. For this task, I rewrote an integrator that I used previously for my Master's degree thesis (Oliva-Mercado et al., 2015).

b) Compare directly the components of the metric to the numerical metric produced by the RNS code.

c) Use the obtained null geodesics to calculate:

   a) the shape of the neutron star as seen by a distant observer,
   b) the gravitational and Doppler shift,
   c) the corrections to the thermal spectrum of the neutron star,
   d) the shape of the pulse profiles.

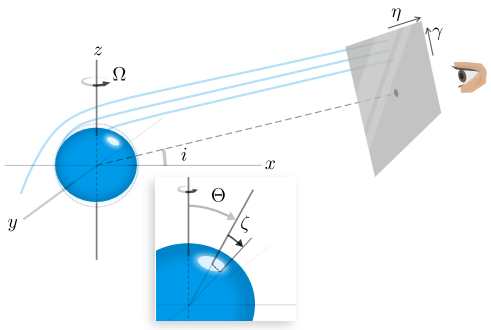



Figure 7.2: Set up for general relativistic ray tracing around a neutron star. The observer is assumed to be located at infinity, in such a way that the rays become parallel. From Oliva and Frutos-Alfaro (2021).

## 7.3 Method overview

For this project, I created an open-source package called *Ujti* [2] that performs the following tasks:

a) It calculates symbolically the geodesic equations given an axisymmetric metric. For this task, the derivatives of the metric are computed with a script for the software package *Maxima*, which outputs Fortran code.

b) It solves the geodesic equations with the adaptive Runge–Kutta–Fehlberg method. The photon trajectories are integrated backwards, i.e., they originate at the observer. It assumes that the observer is far away so that the trajectories are originally parallel.

c) It forms a grid of photon trajectories such that photons that originate everywhere on the surface of the neutron star reach the observer (see fig. 7.2)

d) It computes the ratio of frequencies between the observer and the source of the photon (Doppler shift).

e) It isolates the photons that originate from the surface of the neutron star, and from an arbitrary region defined on its surface.

f) It computes the frequency-dependent flux measured by the observer by using the black body intensity and the Doppler shift. For this task, I followed Bauböck et al. (2015).

g) It computes the pulse light curve by assuming emission coming from a monochromatic hotspot, and correcting for the time of arrival of each photon to the observer.

In order to use a given metric, the values for the mass, specific angular momentum and quadrupole moment must be known. For the solution of the geodesic equations, the surface of the neutron star must be known. To this end, I created a program that explores the central density space to compute neutron star models with RNS for four different configurations[3]:

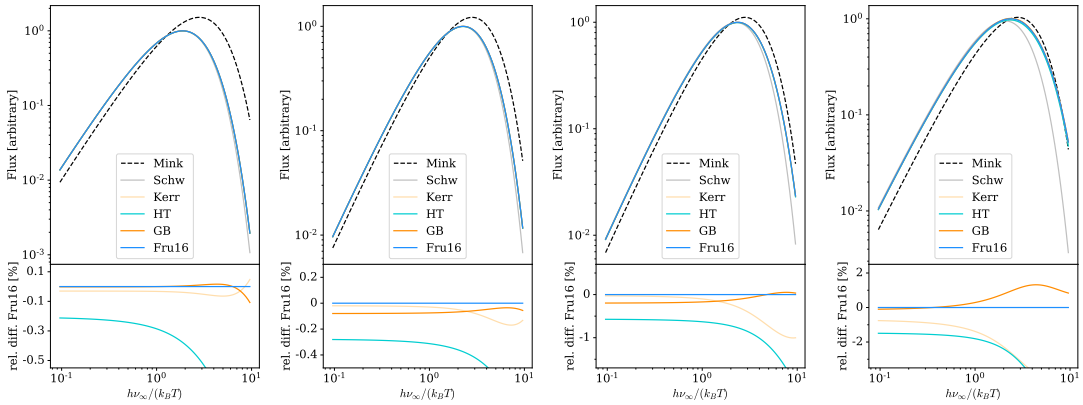
a) BWFX: a relatively fast rotating pulsar (Black Widow Pulsar, 622 Hz) assuming a moderately stiff equation of state (FPS),

b) SHFT: the fastest known pulsar (PSR J1748-2446ad, 716 Hz) assuming the equation of state FPS,

c) KAFT: a hypothetical kilohertz pulsar assuming the equation of state FPS, and

d) KALN: a hypothetical kilohertz pulsar assuming the unrealistically stiff equation of state L as an extreme case.

[2] "Path" in Nawat language. The source code is available from `http://cinespa.ucr.ac.cr`.
[3] The names of the equations of state correspond to the catalog in Cook et al. (1994).




(a) BWFX (b) SHFT (c) KAFT (d) KALN

Figure 7.3: Thermal (black body) spectrum for different neutron star configurations. From Oliva and Frutos-Alfaro (2021).

## 7.4 Selected results and discussion

### 7.4.1 Practical use of analytical metrics

I computed the null geodesics for selected photon array configurations in order to study how light scatters close to the surface of the neutron star, as predicted by all the metrics in the catalog. This helped me assess the computational time needed for using a given analytical model in ray-tracing applications. As a general guide, I call $\tau$ the computing time for tracing a geodesic with the HT metric. Then, the GB metric takes $1.15\tau$; the Fru16 metric, $2.7\tau$; the MN metric, $350\tau$, and the QM metric, $600\tau$. Meanwhile, the Kerr metric, which lacks quadrupole moment, takes $0.8\tau$ and the Schwarzschild metric, $0.3\tau$. Even though the MN and QM metrics satisfy the Einstein field equations exactly, they are still approximations to the exterior spacetime of a neutron star because of the multipole expansion and their lack of matching to an interior solution. After the analysis, I conclude that the metrics based on approximations (HT, GB and Fru16) offer reasonable accuracy for the computing time needed.

### 7.4.2 Thermal spectra

Figure 7.3 displays the results of my calculations for the thermal spectrum of the neutron star on the configurations I considered. Below each panel, I present the relative difference of each curve with respect to the Fru16 metric. Each set of curves is also accompanied by the non-relativistic spectrum, displayed with dashed lines. I find that only in the most extreme configurations, the differences between the metrics become more than a few per cent.

For BWFX, the spectrum is simultaneously broadened towards lower frequencies and red-shifted due to the increase in apparent area due to gravitational lensing and the gravitational redshift, in comparison to the non-relativistic curve, which corresponds to the emitted spectrum at the surface of the neutron star. A relativistic correction on the observed black body temperature (obtained from the peak temperature) can be derived from the curves. When increasing the spin in the rest of the configurations, however, the peak of the observed spectrum becomes closer to the value at the surface. This is a surprising result and I propose the following explanation: the relativistic correction in BWFX comes primarily from the purely gravitational redshift. However, with an increase in spin, the Doppler shift from rotation becomes dominant over the purely gravitational redshift. In the most extreme configurations KAFT and KALN, we even observe blueshift in some parts of the surface of the neutron star.

I also find that the Kerr metric is a reasonable approximation for the cases BWFX and SHFT, although, similar to the HT metric, it becomes increasingly divergent at high frequencies. At

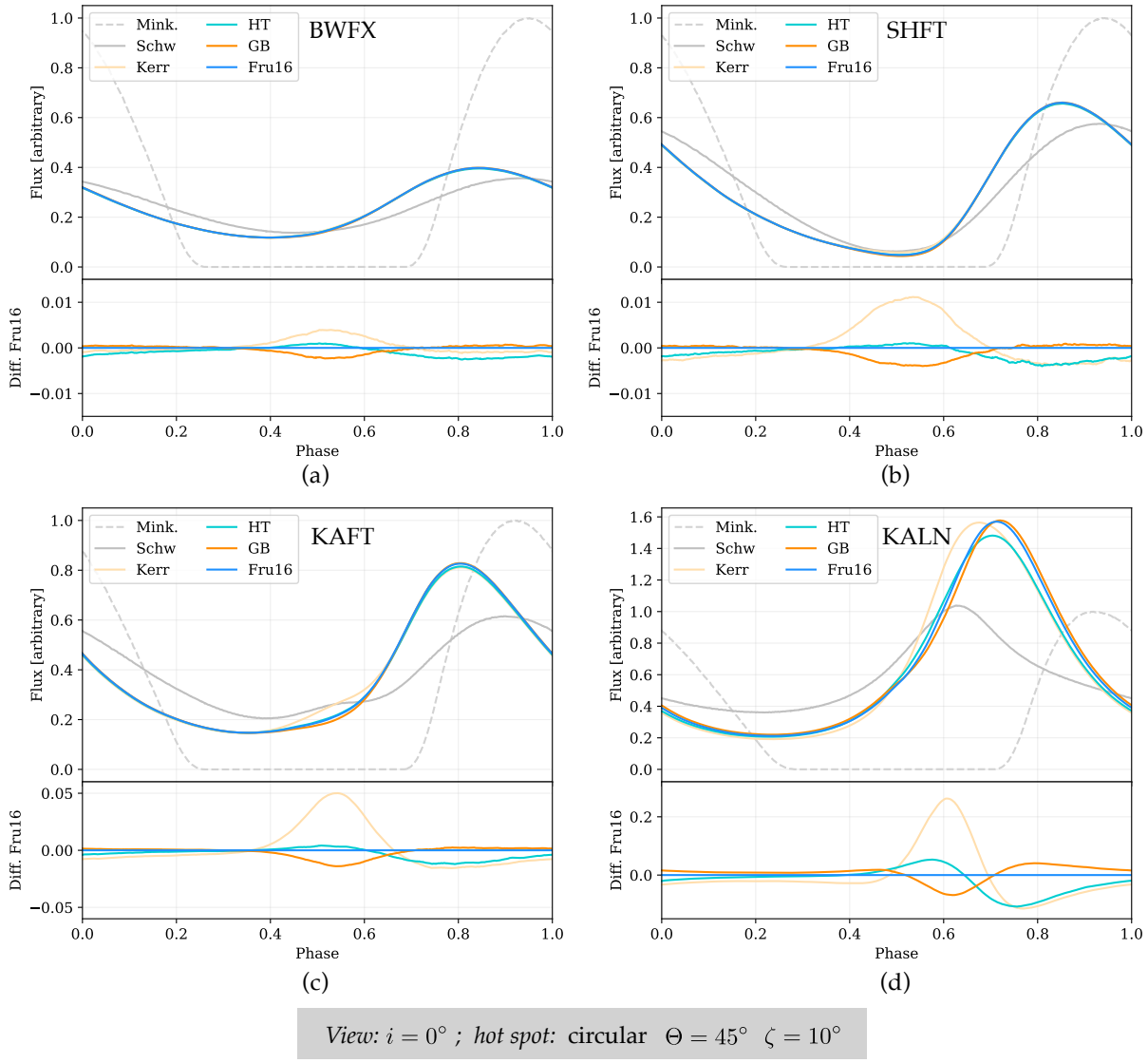



Figure 7.4: Light curves from hotspots: comparison of the neutron star configurations and metrics. From Oliva and Frutos-Alfaro (2021).

high frequencies, any small differences in the redshift are amplified when performing the flux calculation.

### 7.4.3 Pulse profiles

In fig. 7.4, I present some of the results for the light curves using the four neutron star configurations considered in the study. Under each case, the reader can find the absolute difference with each of the metrics and the Fru16 metric. For this particular figure, I used a circular hotspot viewed such that the rotation axis is parallel to the plane of the observer. I find no strong differences between the different models for BWFX. The differences between metrics become more obvious with the more extreme configurations, to the point that the light curves for KALN could be used to distinguish between different metric models, or alternatively, the differences between KAFT and KALN could be used to distinguish between equations of state.

For the pulses using the configurations SHFT, KAFT and KALN, the lower part of the curve reveals a discrepancy between the results for the Kerr metric, where the object is spherically symmetric but rotating, and the metrics that consider quadrupole moment. For context, the

dashed line provides the non-relativistic perspective, where the hotspot disappears from the view of the observer when it is located on the far side of the neutron star. In the relativistic cases, the curves are always visible because the trajectories of photons emitted on the far side of the neutron star are curved by the spacetime and are able to reach the observer. The minimum of the curve corresponds approximately to a hotspot located at the far side of the neutron star (the time of arrival must be considered to be more precise). Upon close examination of the situation, I concluded that the difference in shape between the curves for the Kerr metric and the metrics with quadrupole moment is mainly caused by the difference in shape of the neutron star as the hotspot reaches the far side of its surface. Additionally, photons that originate on the far side of the neutron star are more affected by the peculiarities of each spacetime model because they spend more time close to the surface before reaching the observer. Then, theoretically this difference in the pulse profile could be used to calculate the quadrupole moment from an observation and constrain the equation of state or the model of spacetime.

# 8 Conclusions

Throughout the different projects that constitute this doctoral dissertation, I had the opportunity to contribute to the efforts within the community towards answering burning questions about the birth and aftermath of massive stars. In this section, I highlight the major conclusions obtained for the central scientific question targeted in each project.

### How do companions to massive stars form from disk fragmentation?

By performing and analyzing the highest-resolution simulations to date of a fragmenting accretion disk around a massive protostar, starting from the gravitational collapse of a cloud core, we were able to resolve the first stages of companion formation (first Larson core). We observed how fragmentation happens hierarchically, first with the formation of spiral arms, then fragments, then those fragments develop fragmenting disks of their own. Using a fragment tracking tool I developed, we were able to push the limits of the simulation results and obtain the subset of the first Larson cores that evolve further into second cores, and have good probabilities of becoming companions. We concluded that the amount of companions produced by disk fragmentation (Toomre instability) is of the order of six. Some of the orbits of the objects predicted to become second cores reduce their separation from the primary as a function of time. From this observation we concluded that disk fragmentation is a viable way to produce close (potentially spectroscopic) companions.

### How are accretion disks around a massive protostar affected by magnetic fields?

We constructed a wide catalog of simulations that allowed us to build a unified theory of the properties and dynamical processes in the accretion disk and outflows driven by magnetic fields. Under the assumption of an initially uniform magnetic field, using Ohmic dissipation as a non-ideal MHD effect and considering radiation transport of the thermal emission from the dust and gas, I observed two main effects: a) a two-layer structure in the accretion disk, b) an inner infall region driven by magnetic braking at late stages of star formation, within the innermost $\sim 50$ au of the cloud core. The two layers of the accretion disk, a thin and a thick layer, are distinguished by the support of thermal and magnetic pressure, respectively. I conclude that Ohmic dissipation does not prevent completely magnetic braking in the disk, because magnetic diffusivity is not infinite and the decoupling of the magnetic field and the flow is not complete. Moreover, I saw how increasing Ohmic dissipation delays magnetic braking in the disk. Even though these results have to be confirmed by the addition of other diffusive effects like ambipolar diffusion and the Hall effect in the future, I put forward a clear mechanism and test to assess the role of magnetic diffusivity in the accretion disk around a forming massive star. With the full catalog data, we concluded that the size of the accretion disk is more strongly determined by the range of initial angular momentum and density distributions expected from observational constraints than by the range of initial magnetic field strengths expected. We saw that stronger initial magnetic fields produce larger disks because of the additional magnetic pressure.

### How are magnetic outflows from massive protostars produced?

With the same catalog of simulations, I also built a unified theoretical framework for studying the launch, acceleration, propagation and termination of magnetically-driven outflows launched by the massive protostar. By a precise calculation of the conditions necessary for magneto-centrifugal launching, I identified the launching region of the jet and concluded that

this is the origin of the fast component of the outflow. I showed how the flow accelerates along the magnetic field lines in the cavity. I concluded that the Alfvén surface is narrowed by the infalling material from the envelope, which modifies the geometry of jet launching in comparison to the classical jet theory. A comparison to maser observations of unprecedented resolution, which trace individual stream lines of the protostellar jet in IRAS 21078+5211, revealed a close correspondence between the kinematics predicted by our simulations and the observations.

After an analysis of forces in the plasma, I observed a re-collimation region due to magnetic forces. I argued that, under more realistic conditions for the simulation, this mechanism could produce the synchrotron radiation observed in protostellar jets around massive protostars, an idea previously put forward by Carrasco-González et al. (2021). I concluded that the position of the re-collimation region approximately corresponds to the radio lobes observed in IRAS 21078+5211 by Moscadelli et al. (2021). During the formation of the cavity, I observed the launch and propagation of a bow shock, offering a possible explanation to the bow shock observed in IRAS 21078+5211, and a possible indicator of the age of the system. During the project, I also studied how magnetic pressure arising from the dragging of magnetic field lines by rotation drives a slower component of the magnetically-driven outflow that propagates for large distances.

### How could we measure the mass quadrupole moment of rapidly-rotating neutron stars using photons?

By building four neutron star models and performing general-relativistic ray tracing using several analytical models to their exterior spacetime, I was able to study the effects that the mass quadrupole moment has on pulse profiles from a pulsar and its thermal spectrum as measured from infinity. This brings us one step closer to the possibility of constraining the mass quadrupole moment —and with it, the equation of state— of a rapidly rotating neutron star by using the radiation coming from it. I concluded that the relativistic corrections to the thermal spectrum are smaller in the case of very rapidly rotating neutron stars in comparison to slowly rotating cases, because the Doppler shift coming from the rotation of the neutron star dominates in comparison to the purely gravitational redshift and mostly cancels the corrections out. I also put forward a configuration of hotspots that produces a distinct pulse shape in the case of rotational deformation compared to the assumption of a rotating sphere. This configuration could theoretically be used to distinguish between spacetime models or equations of state in the most rapidly rotating cases.

# 9 Acknowledgments

My doctoral studies would not have been possible without the financial support from the Deutscher Akademischer Austauschdienst (DAAD), under their program "Research Grants – Doctoral Projects in Germany". I also acknowledge complementary financial support from the University of Costa Rica, as part of their scholarship program for postgraduate studies in foreign institutions. Several of the jet simulations were run on the `BinAC` High Performance Computing cluster.

I am extremely grateful to everybody who contributed to the realization of my academic dream of pursuing a doctorate in Germany. During this journey, I learned more than what I could ever imagine, and I had incredible experiences, both academically and personally.

I want to thank my whole family, especially my parents Max and Roxana, and my sister Violeta, for their loving support during these years I have been away. Thank you for always being there for me, encouraging me from the bottom of your heart, as if no ocean were between Costa Rica and Germany. The same goes to my dear friend Esteban, who has never let me fall down and who is always there for sharing the joy of achieving even a small milestone.

This project would not have been possible at all without the amazing support and mentoring of my supervisor Rolf. I sincerely thank him for taking me in as a PhD student and teaching me how to be a computational astrophysicist: I always took his great advice at heart and tried my best to follow his lead. Thanks for guiding me when I had no clue what was wrong with my results and analysis, and for helping me improve my scientific communication skills. I am grateful for the additional mentoring of my late second supervisor Willy Kley. Being almost next to his office brought me a lot of cherished moments where I discovered what kind of academic and person I aspire to be.

This adventure brought me new friends and colleagues whose contributions I wish to acknowledge. Thank you Thomas Rometsch, for all the fruitful discussions that helped me to keep my spirits up during the whole project, and for introducing me to the amazing world of wine making. Thank you Tobi Moldenhauer, for being my trainer in the gym. Thank you Alex Ziampras, for the spontaneous Friday beer and for your fast and accurate language check of this document. Thank you Oliver Schön, for helping me fix my bike so many times so I could go to work on time. Thanks, Christoph Burger, Lucas Jordan and everybody else from the group on Massive Star Formation and the CPT group: I would need a couple of pages more to state all the things you guys did that I am grateful for. The same goes to the TAT group, including Kostas Kokkotas, Daniela Doneva, Sourabh Nampalliwar, Arthur Suvorov, Christian Krüger, Sebastian Völkel, and all others, particularly during the making of Paper 3 and the projects derived from it.

I am extremely grateful to my collaborator Luca Moscadelli for letting me be a part of the team that produced Paper 2, and to all other collaborators and colleagues who enriched my academic experience. I wish to thank the members of the Space Research Center (Cinespa) at the University of Costa Rica, especially to Francisco Frutos and Heidy Gutiérrez, for their trust and incredible support in offering me a path to continue serving people with passion by staying in academia.

# Bibliography


Bandyopadhyay, D. and Kar, K. (2022). *Supernovae, Neutron Star Physics and Nucleosynthesis*. Springer Nature Switzerland.

Banerjee, R. and Pudritz, R. E. (2007). Massive Star Formation via High Accretion Rates and Early Disk-driven Outflows. *Astrophys. J.*, 660(1):479–488.

Bauböck, M., Özel, F., Psaltis, D., and Morsink, S. M. (2015). Rotational Corrections to Neutron-star Radius Measurements from Thermal Spectra. *Astrophys. J.*, 799(1):22.

Beltrán, M. T., Padovani, M., Girart, J. M., Galli, D., Cesaroni, R., Paladino, R., Anglada, G., Estalella, R., Osorio, M., Rao, R., Sánchez-Monge, Á., and Zhang, Q. (2019). ALMA resolves the hourglass magnetic field in G31.41+0.31. *Astron. Astrophys.*, 630:A54.

Beuther, H., Mottram, J. C., Ahmadi, A., Bosco, F., Linz, H., Henning, T., Klaassen, P., Winters, J. M., Maud, L. T., Kuiper, R., Semenov, D., Gieser, C., Peters, T., Urquhart, J. S., Pudritz, R., Ragan, S. E., Feng, S., Keto, E., Leurini, S., Cesaroni, R., Beltran, M., Palau, A., Sánchez-Monge, Á., Galvan-Madrid, R., Zhang, Q., Schilke, P., Wyrowski, F., Johnston, K. G., Longmore, S. N., Lumsden, S., Hoare, M., Menten, K. M., and Csengeri, T. (2018). Fragmentation and disk formation during high-mass star formation. IRAM NOEMA (Northern Extended Millimeter Array) large program CORE. *Astron. Astrophys.*, 617:A100.

Beuther, H., Schilke, P., Menten, K. M., Motte, F., Sridharan, T. K., and Wyrowski, F. (2002). High-Mass Protostellar Candidates. II. Density Structure from Dust Continuum and CS Emission. *Astrophys. J.*, 566(2):945–965.

Beuther, H., Schneider, N., Simon, R., Suri, S., Ossenkopf-Okada, V., Kabanovic, S., Röllig, M., Guevara, C., Tielens, A. G. G. M., Sandell, G., Buchbender, C., Ricken, O., and Güsten, R. (2022). FEEDBACK from the NGC 7538 H II region. *Astron. Astrophys.*, 659:A77.

Beuther, H. and Shepherd, D. (2005). Precursors of UCHII Regions and the Evolution of Massive Outflows. In Kumar, M. S. N., Tafalla, M., and Caselli, P., editors, *Astrophysics and Space Science Library*, volume 324 of *Astrophysics and Space Science Library*, page 105.

Beuther, H., Walsh, A. J., Johnston, K. G., Henning, T., Kuiper, R., Longmore, S. N., and Walmsley, C. M. (2017). Fragmentation and disk formation in high-mass star formation: The ALMA view of G351.77-0.54 at 0.06" resolution. *Astron. Astrophys.*, 603:A10.

Bhandare, A., Kuiper, R., Henning, T., Fendt, C., Marleau, G.-D., and Kölligan, A. (2018). First core properties: from low- to high-mass star formation. *Astron. Astrophys.*, 618:A95.

Blandford, R. D. and Payne, D. G. (1982). Hydromagnetic flows from accretion disks and the production of radio jets. *Mon. Not. R. Astron. Soc.*, 199:883–903.

Bodenheimer, P. H. (2011). *Principles of Star Formation*. Springer Berlin Heidelberg.

Bogdanov, S., Lamb, F. K., Mahmoodifar, S., Miller, M. C., Morsink, S. M., Riley, T. E., Strohmayer, T. E., Tung, A. K., Watts, A. L., Dittmann, A. J., Chakrabarty, D., Guillot, S., Arzoumanian, Z., and Gendreau, K. C. (2019). Constraining the Neutron Star Mass-Radius Relation and Dense Matter Equation of State with NICER. II. Emission from Hot Spots on a Rapidly Rotating Neutron Star. *Astrophys. J. Lett.*, 887(1):L26.

Carrasco-González, C., Rodríguez, L. F., Anglada, G., Martí, J., Torrelles, J. M., and Osorio, M. (2010). A Magnetized Jet from a Massive Protostar. *Science*, 330(6008):1209.

Carrasco-González, C., Sanna, A., Rodríguez-Kamenetzky, A., Moscadelli, L., Hoare, M., Torrelles, J. M., Galván-Madrid, R., and Izquierdo, A. F. (2021). Zooming into the Collimation Zone in a Massive Protostellar Jet. *Astrophys. J. Lett.*, 914(1):L1.

Cesaroni, R., Sánchez-Monge, Á., Beltrán, M. T., Johnston, K. G., Maud, L. T., Moscadelli, L., Mottram, J. C., Ahmadi, A., Allen, V., Beuther, H., Csengeri, T., Etoka, S., Fuller, G. A., Galli, D., Galván-Madrid, R., Goddi, C., Henning, T., Hoare, M. G., Klaassen, P. D., Kuiper, R., Kumar, M. S. N., Lumsden, S., Peters, T., Rivilla, V. M., Schilke, P., Testi, L., van der Tak, F., Vig, S., Walmsley, C. M., and Zinnecker, H. (2017). Chasing discs around O-type (proto)stars: Evidence from ALMA observations. *Astron. Astrophys.*, 602:A59.

Ching, T. C., Li, D., Heiles, C., Li, Z. Y., Qian, L., Yue, Y. L., Tang, J., and Jiao, S. H. (2022). An early transition to magnetic supercriticality in star formation. *Nature*, 601(7891):49–52.

Chiuderi, C. and Velli, M. (2015). *Basics of Plasma Astrophysics*. Springer Italia.

Commerçon, B., González, M., Mignon-Risse, R., Hennebelle, P., and Vaytet, N. (2022). Discs and outflows in the early phases of massive star formation: Influence of magnetic fields and ambipolar diffusion. *Astron. Astrophys.*, 658:A52.

Cook, G. B., Shapiro, S. L., and Teukolsky, S. A. (1994). Rapidly Rotating Neutron Stars in General Relativity: Realistic Equations of State. *Astrophys. J.*, 424:823.

Davies, B., Hoare, M. G., Lumsden, S. L., Hosokawa, T., Oudmaijer, R. D., Urquhart, J. S., Mottram, J. C., and Stead, J. (2011). The Red MSX Source survey: critical tests of accretion models for the formation of massive stars. *Mon. Not. R. Astron. Soc.*, 416(2):972–990.

Duronea, N. U., Cappa, C. E., Bronfman, L., Borissova, J., Gromadzki, M., and Kuhn, M. A. (2017). Triggered massive star formation associated with the bubble Hii region Sh2-39 (N5). *Astron. Astrophys.*, 606:A8.

Frutos-Alfaro, F. (2016). Approximate Kerr-Like Metric with Quadrupole. *Int. J. Astron. Astrophys.*, 6(3):334–345.

Galli, D., Lizano, S., Shu, F. H., and Allen, A. (2006). Gravitational Collapse of Magnetized Clouds. I. Ideal Magnetohydrodynamic Accretion Flow. *Astrophys. J.*, 647(1):374–381.

Galli, D., Lizano, S., Shu, F. H., and Allen, A. (2012). ERRATUM: "Gravitational Collapse of Magnetized Clouds. I. Ideal Magnetohydrodynamic Accretion Flow". *Astrophys. J.*, 754(1):78.

Ginsburg, A., Bally, J., Goddi, C., Plambeck, R., and Wright, M. (2018). A Keplerian Disk around Orion SrCI, a$\sim$ 15 M $_\odot$ YSO. *Astrophys. J.*, 860(2):119.

Girichidis, P., Federrath, C., Banerjee, R., and Klessen, R. S. (2012). Importance of the initial conditions for star formation - II. Fragmentation-induced starvation and accretion shielding. *Mon. Not. R. Astron. Soc.*, 420(1):613–626.

Glampedakis, K. and Babak, S. (2006). Mapping spacetimes with LISA: inspiral of a test body in a 'quasi-Kerr' field. *Class. Quantum Grav.*, 23(12):4167–4188.

Goodman, A. A., Benson, P. J., Fuller, G. A., and Myers, P. C. (1993). Dense Cores in Dark Clouds. VIII. Velocity Gradients. *Astrophys. J.*, 406:528.

Guzmán, A. E., Garay, G., and Brooks, K. J. (2010). A String of Radio Emission Associated with IRAS 16562-3959: A Collimated Jet Emanating from a Luminous Massive Young Stellar Object. *Astrophys. J.*, 725(1):734–741.

Haensel, P., Potekhin, A. Y., and Yakovlev, D. G. (2007). *Neutron Stars 1: Equation of State and Structure*. Springer New York.

Hartle, J. B. and Thorne, K. S. (1968). Slowly Rotating Relativistic Stars. II. Models for Neutron Stars and Supermassive Stars. *Astrophys. J.*, 153:807.

Hatchell, J. and van der Tak, F. F. S. (2003). The physical structure of high-mass star-forming cores. *Astron. Astrophys.*, 409:589–598.

Heger, A., Fryer, C. L., Woosley, S. E., Langer, N., and Hartmann, D. H. (2003). How Massive Single Stars End Their Life. *Astrophys. J.*, 591(1):288–300.

Hennebelle, P. and Inutsuka, S.-i. (2019). The role of magnetic field in molecular cloud formation and evolution. *Frontiers in Astronomy and Space Sciences*, 6:5.

Henshaw, J. D., Caselli, P., Fontani, F., Jiménez-Serra, I., and Tan, J. C. (2014). The dynamical properties of dense filaments in the infrared dark cloud G035.39-00.33. *Mon. Not. R. Astron. Soc.*, 440(3):2860–2881.

Hosokawa, T. and Omukai, K. (2009). Evolution of Massive Protostars with High Accretion Rates. *Astrophys. J.*, 691(1):823–846.

Huarte-Espinosa, M., Frank, A., Blackman, E. G., Ciardi, A., Hartigan, P., Lebedev, S. V., and Chittenden, J. P. (2012). On the structure and stability of magnetic tower jets. *The Astrophysical Journal*, 757(1):66.

Ilee, J. D., Cyganowski, C. J., Brogan, C. L., Hunter, T. R., Forgan, D. H., Haworth, T. J., Clarke, C. J., and Harries, T. J. (2018). G11.92-0.61 MM 1: A Fragmented Keplerian Disk Surrounding a Proto-O Star. *Astrophys. J. Lett.*, 869(2):L24.

Ilee, J. D., Cyganowski, C. J., Nazari, P., Hunter, T. R., Brogan, C. L., Forgan, D. H., and Zhang, Q. (2016). G11.92-0.61 MM1: a Keplerian disc around a massive young proto-O star. *Mon. Not. R. Astron. Soc.*, 462(4):4386–4401.

Izquierdo, A. F., Smith, R. J., Glover, S. C. O., Klessen, R. S., Treß, R. G., Sormani, M. C., Clark, P. C., Duarte-Cabral, A., and Zucker, C. (2021). The Cloud Factory II: gravoturbulent kinematics of resolved molecular clouds in a galactic potential. *Mon. Not. R. Astron. Soc.*, 500(4):5268–5296.

Johnston, K. G., Hoare, M. G., Beuther, H., Kuiper, R., Kee, N. D., Linz, H., Boley, P., Maud, L. T., Ahmadi, A., and Robitaille, T. P. (2020). Spiral arms and instability within the AFGL 4176 mm1 disc. *Astron. Astrophys.*, 634:L11.

Johnston, K. G., Robitaille, T. P., Beuther, H., Linz, H., Boley, P., Kuiper, R., Keto, E., Hoare, M. G., and van Boekel, R. (2015). A Keplerian-like Disk around the Forming O-type Star AFGL 4176. *Astrophys. J. Lett.*, 813(1):L19.

Kee, N. D. and Kuiper, R. (2019). Line-driven ablation of circumstellar discs: IV. The role of disc ablation in massive star formation and its contribution to the stellar upper mass limit. *Mon. Not. R. Astron. Soc.*, 483(4):4893–4900.

Klassen, M., Pudritz, R. E., Kuiper, R., Peters, T., and Banerjee, R. (2016). Simulating the Formation of Massive Protostars. I. Radiative Feedback and Accretion Disks. *Astrophys. J.*, 823(1):28.

Kölligan, A. and Kuiper, R. (2018). Jets and outflows of massive protostars. From cloud collapse to jet launching and cloud dispersal. *Astron. Astrophys.*, 620:A182.

Kratter, K. M., Matzner, C. D., Krumholz, M. R., and Klein, R. I. (2010). On the Role of Disks in the Formation of Stellar Systems: A Numerical Parameter Study of Rapid Accretion. *ApJ*, 708(2):1585–1597.

Krause, M., Fierlinger, K., Diehl, R., Burkert, A., Voss, R., and Ziegler, U. (2013). Feedback by massive stars and the emergence of superbubbles. I. Energy efficiency and Vishniac instabilities. *Astron. Astrophys.*, 550:A49.

Krumholz, M. R., Klein, R. I., and McKee, C. F. (2007). Radiation-Hydrodynamic Simulations of Collapse and Fragmentation in Massive Protostellar Cores. *Astrophys. J.*, 656(2):959–979.

Krumholz, M. R., Klein, R. I., McKee, C. F., Offner, S. S. R., and Cunningham, A. J. (2009). The Formation of Massive Star Systems by Accretion. *Science*, 323(5915):754.

Kuiper, R. and Hosokawa, T. (2018). First hydrodynamics simulations of radiation forces and photoionization feedback in massive star formation. *Astron. Astrophys.*, 616:A101.

Kuiper, R., Klahr, H., Beuther, H., and Henning, T. (2010). Circumventing the Radiation Pressure Barrier in the Formation of Massive Stars via Disk Accretion. *Astrophys. J.*, 722(2):1556–1576.

Kuiper, R., Klahr, H., Beuther, H., and Henning, T. (2011). Three-dimensional Simulation of Massive Star Formation in the Disk Accretion Scenario. *Astrophys. J.*, 732(1):20.

Kuiper, R., Yorke, H. W., and Mignone, A. (2020). Makemake + Sedna: A Continuum Radiation Transport and Photoionization Framework for Astrophysical Newtonian Fluid Dynamics. *Astrophys. J. Suppl. Ser.*, 250(1):13.

Lovelace, R. V. E. and Romanova, M. M. (2003). Relativistic Poynting Jets from Accretion Disks. *Astrophys. J. Lett.*, 596(2):L159–L162.

Luisi, M., Anderson, L. D., Schneider, N., Simon, R., Kabanovic, S., Güsten, R., Zavagno, A., Broos, P. S., Buchbender, C., Guevara, C., Jacobs, K., Justen, M., Klein, B., Linville, D., Röllig, M., Russeil, D., Stutzki, J., Tiwari, M., Townsley, L. K., and Tielens, A. G. G. M. (2021). Stellar feedback and triggered star formation in the prototypical bubble RCW 120. *Science Advances*, 7(15):eabe9511.

Lynden-Bell, D. (1996). Magnetic collimation by accretion discs of quasars and stars. *Mon. Not. R. Astron. Soc.*, 279(2):389–401.

Lynden-Bell, D. (2003). On why discs generate magnetic towers and collimate jets. *Mon. Not. R. Astron. Soc.*, 341(4):1360–1372.

Machida, M. N. and Hosokawa, T. (2020). Failed and delayed protostellar outflows with high-mass accretion rates. *Mon. Not. R. Astron. Soc.*, 499(3):4490–4514.

Machida, M. N., Inutsuka, S.-i., and Matsumoto, T. (2007). Magnetic Fields and Rotations of Protostars. *Astrophys. J.*, 670(2):1198–1213.

Manko, V. S. and Novikov, I. D. (1992). Generalizations of the kerr and kerr-newman metrics possessing an arbitrary set of mass-multipole moments. *Class. Quantum Grav.*, 9(11):2477–2487.

Marchand, P., Guillet, V., Lebreuilly, U., and Mac Low, M.-M. (2022). Fast methods to track grain coagulation and ionization. II. Extension to thermal ionization. *arXiv e-prints*, page arXiv:2202.11625.

Marchand, P., Masson, J., Chabrier, G., Hennebelle, P., Commerçon, B., and Vaytet, N. (2016). Chemical solver to compute molecule and grain abundances and non-ideal MHD resistivities in prestellar core-collapse calculations. *Astron. Astrophys.*, 592:A18.

Matsushita, Y., Machida, M. N., Sakurai, Y., and Hosokawa, T. (2017). Massive outflows driven by magnetic effects in star-forming clouds with high mass accretion rates. *Mon. Not. R. Astron. Soc.*, 470(1):1026–1049.

Maud, L. T., Cesaroni, R., Kumar, M. S. N., Rivilla, V. M., Ginsburg, A., Klaassen, P. D., Harsono, D., Sánchez-Monge, Á., Ahmadi, A., Allen, V., Beltrán, M. T., Beuther, H., Galván-Madrid, R., Goddi, C., Hoare, M. G., Hogerheijde, M. R., Johnston, K. G., Kuiper, R., Moscadelli, L., Peters, T., Testi, L., van der Tak, F. F. S., and de Wit, W. J. (2019). Substructures in the Keplerian disc around the O-type (proto-)star G17.64+0.16. *Astron. Astrophys.*, 627:L6.

Meyer, D. M. A., Kuiper, R., Kley, W., Johnston, K. G., and Vorobyov, E. (2018). Forming spectroscopic massive protobinaries by disc fragmentation. *Mon. Not. R. Astron. Soc.*, 473(3):3615–3637.

Meyer, D. M. A., Vorobyov, E. I., Kuiper, R., and Kley, W. (2017). On the existence of accretion-driven bursts in massive star formation. *Mon. Not. R. Astron. Soc.*, 464(1):L90–L94.

Mignon-Risse, R., González, M., and Commerçon, B. (2021a). Collapse of turbulent massive cores with ambipolar diffusion and hybrid radiative transfer. II. Outflows. *Astron. Astrophys.*, 656:A85.

Mignon-Risse, R., González, M., Commerçon, B., and Rosdahl, J. (2021b). Collapse of turbulent massive cores with ambipolar diffusion and hybrid radiative transfer. I. Accretion and multiplicity. *Astron. Astrophys.*, 652:A69.

Mignone, A., Bodo, G., Massaglia, S., Matsakos, T., Tesileanu, O., Zanni, C., and Ferrari, A. (2007). PLUTO: A Numerical Code for Computational Astrophysics. *Astrophys. J. Suppl. Ser.*, 170(1):228–242.

Mihalas, D. and Weibel-Mihalas, B. (1999). *Foundations of radiation hydrodynamics*. Dover Publications, New York.

Miller, M. C., Lamb, F. K., Dittmann, A. J., Bogdanov, S., Arzoumanian, Z., Gendreau, K. C., Guillot, S., Harding, A. K., Ho, W. C. G., Lattimer, J. M., Ludlam, R. M., Mahmoodifar, S., Morsink, S. M., Ray, P. S., Strohmayer, T. E., Wood, K. S., Enoto, T., Foster, R., Okajima, T., Prigozhin, G., and Soong, Y. (2019). PSR J0030+0451 Mass and Radius from NICER Data and Implications for the Properties of Neutron Star Matter. *Astrophys. J. Lett.*, 887(1):L24.

Molyarova, T., Akimkin, V., Semenov, D., Henning, T., Vasyunin, A., and Wiebe, D. (2017). Gas Mass Tracers in Protoplanetary Disks: CO is Still the Best. *Astrophys. J.*, 849(2):130.

Morrell, N. and Levato, H. (1991). Spectroscopic Binaries in the Orion OB1 Association. *Astrophys. J. Suppl. Ser.*, 75:965.

Moscadelli, L., Beuther, H., Ahmadi, A., Gieser, C., Massi, F., Cesaroni, R., Sánchez-Monge, Á., Bacciotti, F., Beltrán, M. T., Csengeri, T., Galván-Madrid, R., Henning, T., Klaassen, P. D., Kuiper, R., Leurini, S., Longmore, S. N., Maud, L. T., Möller, T., Palau, A., Peters, T., Pudritz, R. E., Sanna, A., Semenov, D., Urquhart, J. S., Winters, J. M., and Zinnecker, H. (2021). Multi-scale view of star formation in IRAS 21078+5211: from clump fragmentation to disk wind. *Astron. Astrophys.*, 647:A114.

Mouschovias, T. C. and Spitzer, L., J. (1976). Note on the collapse of magnetic interstellar clouds. *Astrophys. J.*, 210:326.

Mueller, K. E., Shirley, Y. L., Evans, Neal J., I., and Jacobson, H. R. (2002). The Physical Conditions for Massive Star Formation: Dust Continuum Maps and Modeling. *Astrophys. J. Suppl. Ser.*, 143(2):469–497.

Myers, A. T., McKee, C. F., Cunningham, A. J., Klein, R. I., and Krumholz, M. R. (2013). The Fragmentation of Magnetized, Massive Star-forming Cores with Radiative Feedback. *Astrophys. J.*, 766(2):97.

Nakano, T., Nishi, R., and Umebayashi, T. (2002). Mechanism of Magnetic Flux Loss in Molecular Clouds. *Astrophys. J.*, 573(1):199–214.

Nony, T., Louvet, F., Motte, F., Molet, J., Marsh, K., Chapillon, E., Gusdorf, A., Brouillet, N., Bontemps, S., Csengeri, T., Despois, D., Nguyen Luong, Q., Duarte-Cabral, A., and Maury, A. (2018). Detection of a high-mass prestellar core candidate in W43-MM1. *Astron. Astrophys.*, 618:L5.

Oliva, G. A. and Frutos-Alfaro, F. (2021). Effects of the treatment of the mass quadrupole moment on ray-tracing applications for rapidly rotating neutron stars. *Mon. Not. R. Astron. Soc.*, 505(2):2870–2885.

Oliva, G. A. and Kuiper, R. (2020). Modeling disk fragmentation and multiplicity in massive star formation. *Astron. Astrophys.*, 644:A41.

Oliva-Mercado, G. A., Bonatti-González, J., Cordero-García, I., and Frutos-Alfaro, F. (2015). Visualización de geodésicas nulas para el dipolo masivo de bonnor. *Rev. Mat. Teor. Apl.*, 22(2):255.

Ouyed, R. and Pudritz, R. E. (1997). Numerical Simulations of Astrophysical Jets from Keplerian Disks. I. Stationary Models. *Astrophys. J.*, 482(2):712–732.

Özel, F. and Freire, P. (2016). Masses, Radii, and the Equation of State of Neutron Stars. *Annu. Rev. Astron. Astrophys.*, 54:401–440.

Purser, S. J. D., Lumsden, S. L., Hoare, M. G., Urquhart, J. S., Cunningham, N., Purcell, C. R., Brooks, K. J., Garay, G., Gúzman, A. E., and Voronkov, M. A. (2016). A search for ionized jets towards massive young stellar objects. *Mon. Not. R. Astron. Soc.*, 460(1):1039–1053.

Quevedo, H. (1990). Multipole moments in general relativity —static and stationary vacuum solutions—. *Fortschritte der Phys.*, 38(10):733–840.

Raskutti, S., Ostriker, E. C., and Skinner, M. A. (2016). Numerical Simulations of Turbulent Molecular Clouds Regulated by Radiation Feedback Forces: I. Star Formation Rate and Efficiency. *The Astrophysical Journal*, 829(2):130.

Raskutti, S., Ostriker, E. C., and Skinner, M. A. (2017). Numerical simulations of turbulent molecular clouds regulated by radiation feedback forces. II. radiation–gas interactions and outflows. *The Astrophysical Journal*, 850(2):112.

Redaelli, E., Bovino, S., Giannetti, A., Sabatini, G., Caselli, P., Wyrowski, F., Schleicher, D. R. G., and Colombo, D. (2021). Identification of pre-stellar cores in high-mass star forming clumps via $H_2D^+$ observations with ALMA. *Astron. Astrophys.*, 650:A202.

Riley, T. E., Watts, A. L., Bogdanov, S., Ray, P. S., Ludlam, R. M., Guillot, S., Arzoumanian, Z., Baker, C. L., Bilous, A. V., Chakrabarty, D., Gendreau, K. C., Harding, A. K., Ho, W. C. G., Lattimer, J. M., Morsink, S. M., and Strohmayer, T. E. (2019). A NICER View of PSR J0030+0451: Millisecond Pulsar Parameter Estimation. *Astrophys. J. Lett.*, 887(1):L21.

Rosen, A. L. and Krumholz, M. R. (2020). The Role of Outflows, Radiation Pressure, and Magnetic Fields in Massive Star Formation. *Astron. J.*, 160(2):78.

Rosen, A. L., Krumholz, M. R., McKee, C. F., and Klein, R. I. (2016). An unstable truth: how massive stars get their mass. *Mon. Not. R. Astron. Soc.*, 463(3):2553–2573.

Sanna, A., Moscadelli, L., Goddi, C., Beltrán, M., Brogan, C. L., Caratti o Garatti, A., Carrasco-González, C., Hunter, T. R., Massi, F., and Padovani, M. (2019). Protostellar Outflows at the EarliesT Stages (POETS). II. A possible radio synchrotron jet associated with the EGO G035.02+0.35. *Astron. Astrophys.*, 623:L3.

Seifried, D., Banerjee, R., Klessen, R. S., Duffin, D., and Pudritz, R. E. (2011). Magnetic fields during the early stages of massive star formation - I. Accretion and disc evolution. *Mon. Not. R. Astron. Soc.*, 417(2):1054–1073.

Seifried, D., Haid, S., Walch, S., Borchert, E. M. A., and Bisbas, T. G. (2020). SILCC-Zoom: $H_2$ and CO-dark gas in molecular clouds - the impact of feedback and magnetic fields. *Mon. Not. R. Astron. Soc.*, 492(1):1465–1483.

Seifried, D., Pudritz, R. E., Banerjee, R., Duffin, D., and Klessen, R. S. (2012). Magnetic fields during the early stages of massive star formation - II. A generalized outflow criterion. *Mon. Not. R. Astron. Soc.*, 422(1):347–366.

Shakura, N. I. and Sunyaev, R. A. (1973). Black holes in binary systems. Observational appearance. *Astron. Astrophys.*, 24:337–355.

Smith, N. (2014). Mass loss: Its effect on the evolution and fate of high-mass stars. *Annual Review of Astronomy and Astrophysics*, 52(1):487–528.

Smith, R. J., Longmore, S., and Bonnell, I. (2009). The simultaneous formation of massive stars and stellar clusters. *Mon. Not. R. Astron. Soc.*, 400(4):1775–1784.

Stergioulas, N. and Friedman, J. L. (1995). Comparing Models of Rapidly Rotating Relativistic Stars Constructed by Two Numerical Methods. *Astrophys. J.*, 444:306.

Toomre, A. (1964). On the gravitational stability of a disk of stars. *Astrophys. J.*, 139:1217–1238.

Troland, T. H. and Crutcher, R. M. (2008). Magnetic Fields in Dark Cloud Cores: Arecibo OH Zeeman Observations. *Astrophys. J.*, 680(1):457–465.

Vázquez-Semadeni, E., González-Samaniego, A., and Colín, P. (2017). Hierarchical star cluster assembly in globally collapsing molecular clouds. *Mon. Not. R. Astron. Soc.*, 467(2):1313–1328.

Vink, J. S. (2018). Very massive stars: a metallicity-dependent upper-mass limit, slow winds, and the self-enrichment of globular clusters. *Astron. Astrophys.*, 615:A119.

Watts, A. L., Andersson, N., Chakrabarty, D., Feroci, M., Hebeler, K., Israel, G., Lamb, F. K., Miller, M. C., Morsink, S., Özel, F., Patruno, A., Poutanen, J., Psaltis, D., Schwenk, A., Steiner, A. W., Stella, L., Tolos, L., and van der Klis, M. (2016). Colloquium: Measuring the neutron star equation of state using x-ray timing. *Rev. Mod. Phys.*, 88(2):021001.

Zinnecker, H. and Yorke, H. W. (2007). Toward Understanding Massive Star Formation. *Annu. Rev. Astron. Astrophys.*, 45(1):481–563.

Zweibel, E. G. (2015). Ambipolar diffusion. In Lazarian, A., de Gouveia Dal Pino, E. M., and Melioli, C., editors, *Magnetic Fields in Diffuse Media*, chapter 11, page 285. Springer Berlin Heidelberg.

# A Accepted publications

A&A 644, A41 (2020)
https://doi.org/10.1051/0004-6361/202038103
© ESO 2020

Astronomy & Astrophysics

# Modeling disk fragmentation and multiplicity in massive star formation

G. André Oliva and R. Kuiper

Institute for Astronomy and Astrophysics, University of Tübingen, Auf der Morgenstelle 10, 72076 Tübingen, Germany
e-mail: guillermo.oliva-mercado@student.uni-tuebingen.de; rolf.kuiper@uni-tuebingen.de

Received 6 April 2020 / Accepted 30 August 2020

**ABSTRACT**

*Context.* There is growing evidence that massive stars grow by disk accretion in a similar way to their low-mass counterparts. Early in evolution, these disks can achieve masses that are comparable to the current stellar mass, and therefore the forming disks are highly susceptible to gravitational fragmentation.
*Aims.* We investigate the formation and early evolution of an accretion disk around a forming massive protostar, focussing on its fragmentation physics. To this end, we follow the collapse of a molecular cloud of gas and dust, the formation of a massive protostar, the formation of its circumstellar disk, and the formation and evolution of the disk fragments.
*Methods.* We used a grid-based, self-gravity radiation hydrodynamics code including a sub-grid module for stellar evolution and dust evolution. We purposely do not use a sub-grid module for fragmentation such as sink particles to allow for all paths of fragment formation and destruction, but instead we keep the spatial grid resolution high enough to properly resolve the physical length scales of the problem, namely the pressure scale height and Jeans length of the disk. Simulations are performed on a grid in spherical coordinates with a logarithmic spacing of the grid cells in the radial direction and a cosine distribution of the grid cells in the polar direction, focusing the spatial resolution on the disk midplane. As a consequence, roughly 25% of the total number of grid cells, corresponding to ∼26 million grid cells, are used to model the disk physics. These constitute the highest resolution simulations performed up to now on disk fragmentation around a forming massive star with the physics considered here. For a better understanding of the effects of spatial resolution and to compare our high-resolution results with previous lower resolution studies in the literature, we perform the same simulation at five different resolutions, each run differing in resolution from its predecessor by a factor of two.
*Results.* The cloud collapses and a massive (proto)star is formed in its center surrounded by a fragmenting Keplerian-like accretion disk with spiral arms. The fragments have masses of $\sim 1\,M_{\odot}$, and their continuous interactions with the disk, spiral arms, and other fragments result in eccentric orbits. Fragments form hydrostatic cores surrounded by secondary disks with spiral arms that also produce new fragments. We identified several mechanisms of fragment formation, interaction, and destruction. Central temperatures of the fragments can reach the hydrogen dissociation limit, form second Larson cores, and evolve into companion stars. Based on this, we study the multiplicity predicted by the simulations and find approximately six companions at different distances from the primary: from possible spectroscopic multiples, to companions at distances between 1000 and 2000 au.

**Key words.** stars: formation – stars: massive – accretion, accretion disks – stars: protostars – methods: numerical

## 1. Introduction

During the formation of massive stars ($\gtrsim 8\,M_{\odot}$), radiation pressure becomes important against the gravity of the collapsing molecular cloud. The formation of an accretion disk with polar outflows provides a mechanism for circumventing the radiation pressure barrier (see, e.g., Kuiper et al. 2010a) and allows the forming star to become massive. This disk is expected to fragment and produce companion stars. There is growing observational evidence that supports this scenario. Observations of disks around massive (proto-)stars are reported by, for example Johnston et al. (2015), Ilee et al. (2016), Cesaroni et al. (2017), Ginsburg et al. (2018), and Maud et al. (2019). Some of these disks have also been shown to be Keplerian-like.

Moreover, there is evidence that, early in evolution, these disks gain enough mass to become self-gravitating, form spiral arms, and fragment. Ilee et al. (2018) observed a fragmented Keplerian disk around the proto-O star G11.92-0.61 MM1a, with a fragment MM1b in the outskirts of the disk, at ∼2000 au from the primary. Beuther et al. (2017) reported a smaller disk-like structure around the central object in the G351.77-0.54 high-mass hot core, and a fragment at about ∼1000 au. Johnston et al. (2020) also observed spiral arms and instability in a disk of radius ∼1000 au around the O-type star AFGL 4176 mm1. Maud et al. (2019) reported substructures in a Keplerian disk around the O-type (proto-)star G17.64+0.16.

Several studies have used three-dimensional hydrodynamical simulations of a collapsing cloud, including radiation transport and self gravity, in order to study the formation of a massive star. Some of them lead to a massive star surrounded by a fragmenting accretion disk, and some form stars via filament accretion (we offer a literature review, including methods, initial conditions, and results in Sect. 9). Krumholz et al. (2009), Kratter et al. (2010), Rosen et al. (2016), Klassen et al. (2016), Girichidis et al. (2012), and others used adaptive mesh refinement (AMR) grids and sub-grid sink particle models. In the case of Girichidis et al. (2012), as many as approximately 400 sink particles were reported in some of their runs, or in the case of Rosen et al. (2016), up to about 30; in contrast, Klassen et al. (2016) report none. These large disparities in the number of possible formed companions under similar conditions provokes questions on the role played by spatial resolution and the sink particle algorithms

A&A 644, A41 (2020)

used in these studies in the final outcome of the system. In Sects. 8 and 9, we explore this matter in detail, and find that higher resolution is needed to resolve the Jeans length than used in previous studies.

Accretion in fragmented disks is expected not to be a smooth process, but to be characterized by episodic accretion of some fragments. The release of gravitational potential energy creates an increase in luminosity, i.e., an accretion burst. Accretion bursts offer an explanation for the luminosity burst events in regions of massive star formation which have been reported by Hunter et al. (2017), Caratti o Garatti et al. (2017), and Sugiyama et al. (2019) for example. Recently, Chen et al. (2020) reported the observation of disk substructures associated with an accretion burst event, thus providing a link between the two phenomena. The simulations in Meyer et al. (2017, 2018, 2019) show accretion bursts; these latter authors performed an extensive analysis of the accretion process and the intensity and frequency of the bursts.

Massive stars do not typically form in isolation. Studies on multiplicity in more evolved systems of massive stars show that a large portion of them are spectroscopic binaries (see, e.g., Sana et al. 2012; Kobulnicky et al. 2014; Dunstall et al. 2015). The observations of fragmenting accretion disks suggest the possibility that close binaries may form by disk fragmentation and later inward migration of the companions (Meyer et al. 2018).

In this study, we present the highest-resolution self-gravity-radiation-hydrodynamical simulations of disk fragmentation around a forming massive (proto)star to date. We continue the approach taken by Meyer et al. (2018), in which no sink particles are set purposely, so that fragmentation is described self-consistently as the interplay of self-gravity of the gas, cooling of the gas, shear of the disk, and other gravito-radiation-hydrodynamical processes. Instead, we used a time-independent grid whose spatial resolution scales logarithmically with radius, allowing very high resolution in the areas of most interest. We set up a series of simulations with increasing resolutions, and explore the physical processes that occur in fragmentation (how fragments evolve and interact), the properties of the fragments (orbits, mass, and temperatures), their fate (whether they evolve further and eventually become companion stars), and the effects that resolution has on fragment statistics.

The outcome of our simulation was already used in Ahmadi et al. (2019) to produce synthetic observations with ALMA and NOEMA. In that paper, many observationally relevant quantities were computed, including 1.37 mm continuum images, integrated intensity and intensity-weighted peak velocity maps of $CH_3CN(12_4-11_4)$, position–velocity plots, and Toomre $Q$ maps, taking into account several inclinations. We refer the reader to that article for an ample discussion on the observability of the results presented here.

This paper is organized as follows. Sections 2 and 4 present the methodology of both the simulations, and the post-processing of the generated data. Sections 3 and 5–7 present our results and a discussion of disk fragmentation, the fragments themselves, and companion formation. Section 8 contains a convergence study of our results, and Sect. 9 a literature review and comparison of our results with previous studies.

## 2. Setup of the simulations

### 2.1. Physics

In order to model the problem, we consider the three-dimensional collapse of an initially axially symmetric molecular cloud of total mass 200 $M_\odot$ and radius 0.1 pc. The initial density and rotational profiles are given in Sect. 2.3.

The cloud dynamics are modeled as an ideal gas with the hydrodynamics equations:

$$\frac{\partial \rho}{\partial t} + \boldsymbol{\nabla} \cdot (\rho \boldsymbol{v}) = 0, \tag{1}$$

$$\frac{\partial}{\partial t}(\rho \boldsymbol{v}) + \boldsymbol{\nabla} \cdot (\rho \boldsymbol{v} \otimes \boldsymbol{v} + P\mathsf{I}) = \rho \boldsymbol{a}_{\rm ext}, \tag{2}$$

$$\frac{\partial E}{\partial t} + \boldsymbol{\nabla} \cdot ((E + P)\boldsymbol{v}) = \rho \boldsymbol{v} \cdot \boldsymbol{a}_{\rm ext}, \tag{3}$$

where $\rho$, $P$, and $E$ are the density, pressure, and energy density, respectively; $\boldsymbol{v}$ is the velocity, and $\boldsymbol{a}_{\rm ext}$ is the acceleration source term. These equations are solved with the hydrodynamics module of the numerical grid code Pluto (Mignone et al. 2007), with additional modules for handling radiation transport and self-gravity.

The gravity of the forming massive star, the self-gravity of the fluid, and the radiation forces are incorporated into the code via the acceleration source term, such that $\boldsymbol{a}_{\rm ext} = \boldsymbol{a}_\star + \boldsymbol{a}_{\rm sg} + \boldsymbol{a}_{\rm rad}$, and

$$\boldsymbol{a}_\star = -\frac{GM_\star}{r^2}\boldsymbol{e}_r, \tag{4}$$

$$\boldsymbol{a}_{\rm sg} = -\boldsymbol{\nabla}\Phi_{\rm sg}, \text{ where } \quad \boldsymbol{\nabla}^2\Phi_{\rm sg} = 4\pi G\rho, \tag{5}$$

$$\boldsymbol{a}_{\rm rad} = -\frac{\boldsymbol{\nabla}\cdot\boldsymbol{F}_\star}{\rho c}\boldsymbol{e}_r - \kappa_R\frac{D\boldsymbol{\nabla}E_R}{c}. \tag{6}$$

The variables involved in $\boldsymbol{a}_{\rm rad}$ are detailed below. The Poisson equation of self gravity is solved by means of a diffusion ansatz. More details on the implementation of the Poisson solver for the self-gravity module are given in Kuiper et al. (2010a).

The gas is assumed to be calorically perfect, that is, governed by the calorical equation of state $P = (\gamma - 1)E_{\rm int}$ (where $\gamma = 5/3$, the value for $H_2$ at low temperatures, and $E_{\rm int}$ is the internal energy density).

Radiation transport is incorporated by the method described in Kuiper et al. (2010b), but advanced to a two-temperature approach, which we summarize in the remainder of this section. We treat the star as an emitter of radiation, which the dust and gas present in the cloud absorb and re-emit in addition to the thermal radiation due purely to hydrodynamic compression. This treatment allows us to divide the total radiation flux $\boldsymbol{F}_{\rm tot}$ into two contributions: the flux from the star, $\boldsymbol{F}_\star$, and the flux from thermal (re-)emission from dust and gas, $\boldsymbol{F}$.

Stellar irradiation is solved by means of the time-independent radiation transport equation (with the valid assumption that the photon travel time is small compared to the time-step of the simulation, and only considering absorption), which yields

$$\boldsymbol{F}_\star(\nu, r) = \boldsymbol{F}_\star(\nu, R_\star)\left(\frac{R_\star}{r}\right)^2 e^{-\tau(\nu,r)}, \text{where } \tau(r,\nu) = \int_{R_\star}^{r}\kappa(\nu, r)\rho {\rm d}r \tag{7}$$

is the optical depth, $\kappa(\nu, r)$ the frequency-dependent opacity, and $R_\star$ the stellar radius. This equation is integrated for each ray direction and frequency bin in each time-step of the hydrodynamical simulation.

The frequency-dependent opacity $\kappa(\nu)$ is the sum of the dust and gas opacities. For the dust opacities, we use the tabulated values by Laor & Draine (1993), including 79 frequency bins, and we calculate the local evaporation temperature of the dust

**Table 1.** Designation code of each simulation (Col. 1), number of cells for each coordinate (Cols. 2–4); approximate number of cells in the region $r < 1500$ au, i.e., the approximate number of cells that resolve the physics of the disk (Col. 5); cell size at $r = 30$ au (Col. 6), cell size at $r = 1500$ au (Col. 7).

| run | $n_r$ | $n_\theta$ | $n_\phi$ | $n_{\rm disk}$ | $\Delta x_{30}$ | $\Delta x_{1500}$ |
|---|---|---|---|---|---|---|
| x1 | 34 | 11 | 32 | $7.0 \times 10^3$ | 6.36 | 359 |
| x2 | 67 | 21 | 64 | $5.3 \times 10^4$ | 3.07 | 167 |
| x4 | 134 | 41 | 128 | $4.2 \times 10^5$ | 1.50 | 77.8 |
| x8 | 268 | 81 | 256 | $3.3 \times 10^6$ | 0.74 | 37.5 |
| x16 | 536 | 161 | 512 | $2.6 \times 10^7$ | 0.368 | 18.4 |

**Notes.** $\Delta x_{30}$ is also the minimum cell size of the computational domain in the midplane of the disk, and $\Delta x_{1500}$ represents roughly the cell size in the outer region of the disk.

grains using the formula of Isella & Natta (2005). The gas opacity is set to a constant value of 0.01 cm$^2$ g$^{-1}$. We also require the flux of the forming star at the stellar radius $R_\star$, for which we use tabulated evolutionary tracks for accreting high-mass stars calculated by Hosokawa & Omukai (2009).

For the remaining thermal (re-)emission contribution, $\boldsymbol{F}$ is assumed to be frequency-independent. First, we take the zeroth moment of the radiation transport equation

$$\frac{\partial E_{\rm rad}}{\partial t} - \boldsymbol{\nabla} \cdot \boldsymbol{F} = \rho \kappa_P (4\pi B_{\rm rad} - c E_{\rm rad}), \tag{8}$$

where $B_{\rm rad} = aT^4$ is the black-body energy density, $c$ is the speed of light in vacuum, and $\kappa_{\rm P}$ is the Planck mean opacity. This equation is solved by means of the flux-limited diffusion (FLD) approximation, which consists in setting $\boldsymbol{F} = -D\boldsymbol{\nabla} E_{\rm rad}$, that is, assuming that radiation transport can be treated as a diffusion problem. The diffusion constant is $D = \lambda c/\rho\kappa_{\rm R}$, where $\lambda$ is the flux limiter, and $\kappa_{\rm R}$ is the Rosseland mean opacity. The change of internal energy of the system is

$$\frac{\partial E_{\rm int}}{\partial t} = -\rho\kappa_{\rm P}(4\pi B_{\rm rad} - cE_{\rm rad}) - \boldsymbol{\nabla} \cdot \boldsymbol{F}_\star, \tag{9}$$

where, for the ideal gas, $E_{\rm int} = c_v \rho T$. We solve Eqs. (8) and (9) for the unknowns $E_{\rm rad}$ and $T$ using the so-called two-temperature linearization approach, described in Commerçon et al. (2011a).

### 2.2. Geometry

The equations described in the previous section are solved in a three-dimensional, spherical, time-independent grid at five different resolutions, which are detailed in Table 1. The computational domain extends from $r = 30$ au to $r = 20\,626.5$ au (=0.1 pc). The coordinate grid is built as follows: the radial coordinate increases logarithmically from the inner boundary; the polar angle varies with the cosine function so that maximum resolution is achieved in the midplane ($z = 0$); and the azimuth is uniformly discretized. In the midplane the cells are approximately cubical, with two example cell sizes given as $\Delta x$ in Table 1.

This choice of coordinates is explained and justified in more detail in Kuiper et al. (2011); briefly, a spherical grid guarantees strict angular momentum conservation around the central massive protostar, and the logarithmic grid in $r$ allows for a focus on the phenomena closer to the forming massive star, while saving computational power. An explanation of how well this choice of grids resolves the phenomena studied here is presented in Sect. 9.2 together with a comparison to the grid choices of previous studies.

### 2.3. Initial and boundary conditions

The initial density profile is spherically symmetric, and has the general form

$$\rho(r, t = 0) = \rho_0 \left(\frac{r}{r_0}\right)^{\beta_\rho}. \tag{10}$$

We choose $\beta_\rho = -3/2$, and from the total mass and radius of the cloud, $\rho_0$ is determined to be $\approx 4.79 \times 10^{-12}$ g cm$^{-3}$ at $r_0 = 1$ au. The value of $\beta_\rho$ was chosen based on the results of previous simulations and observations of massive dense cores (see the discussion in Sect. 9.3).

The initial angular velocity is given by the profile

$$\Omega(R, t = 0) = \Omega_0 \left(\frac{R}{R_0}\right)^{\beta_\Omega}, \tag{11}$$

where $R$ is the cylindrical radius, and we choose $\beta_\Omega = -3/4$. The ratio of kinetic energy to gravitational potential energy is set to 5%, which fixes the normalization parameter $\Omega_0$ to $\approx 9.84 \times 10^{-11}$ s$^{-1}$ at $R_0 = 10$ au. The normalization process is described in more detail in Meyer et al. (2018), together with a parameter scan for other choices of $\beta_\Omega$. The selection of $\beta_\Omega = \beta_\rho/2$ keeps the ratio of kinetic energy to gravitational energy independent of the radius of the cloud; the value for this ratio in turn was chosen in accordance with the typical values found in Goodman et al. (1993) and Palau et al. (2014), for example. The initial radial and polar velocities are set to zero.

In summary, we give a low initial angular momentum to the cloud so that it forms a disk while collapsing. In a more realistic situation, inhomogeneities in the density profile may be present, as well as some initial subsonic turbulence and magnetic fields. However, the aim of this work is to study fragmentation of the disk due to the development of Toomre instabilities in the accretion disk that forms in the process, hence our choice of initial conditions. A more detailed discussion on the effects of the initial conditions and the inclusion of additional physical effects on the outcome of the simulations can be found in Sect. 9.3.

Both the inner and outer boundaries of the computational domain are semi-permeable, that is, matter is allowed to leave the computational domain but it cannot re-enter it. For the purposes of the calculations involving the forming massive star, all the mass in the sink cell is considered as accreted by the central massive protostar that forms within it. The initial temperature is 10 K throughout the computational domain, and the initial dust-to-gas mass ratio (used in the calculation of $\kappa(\nu)$) is chosen to be 1% (Draine et al. 2007).

## 3. Overview of the temporal evolution of the system

In the following sections, we use the data from runs x8 and x16 as a reference for the description and analysis of our results. A discussion of the results for the other runs can be found in Sect. 8.

Figure 1 shows an overview of the time evolution of the system (for run x8) with maps of the density in the midplane ($z = 0$), the density in the $xz$-plane – to give an idea of the vertical structure of the system – the temperature, and the Toomre parameter (which is introduced in Sect. 4.1).

A&A 644, A41 (2020)

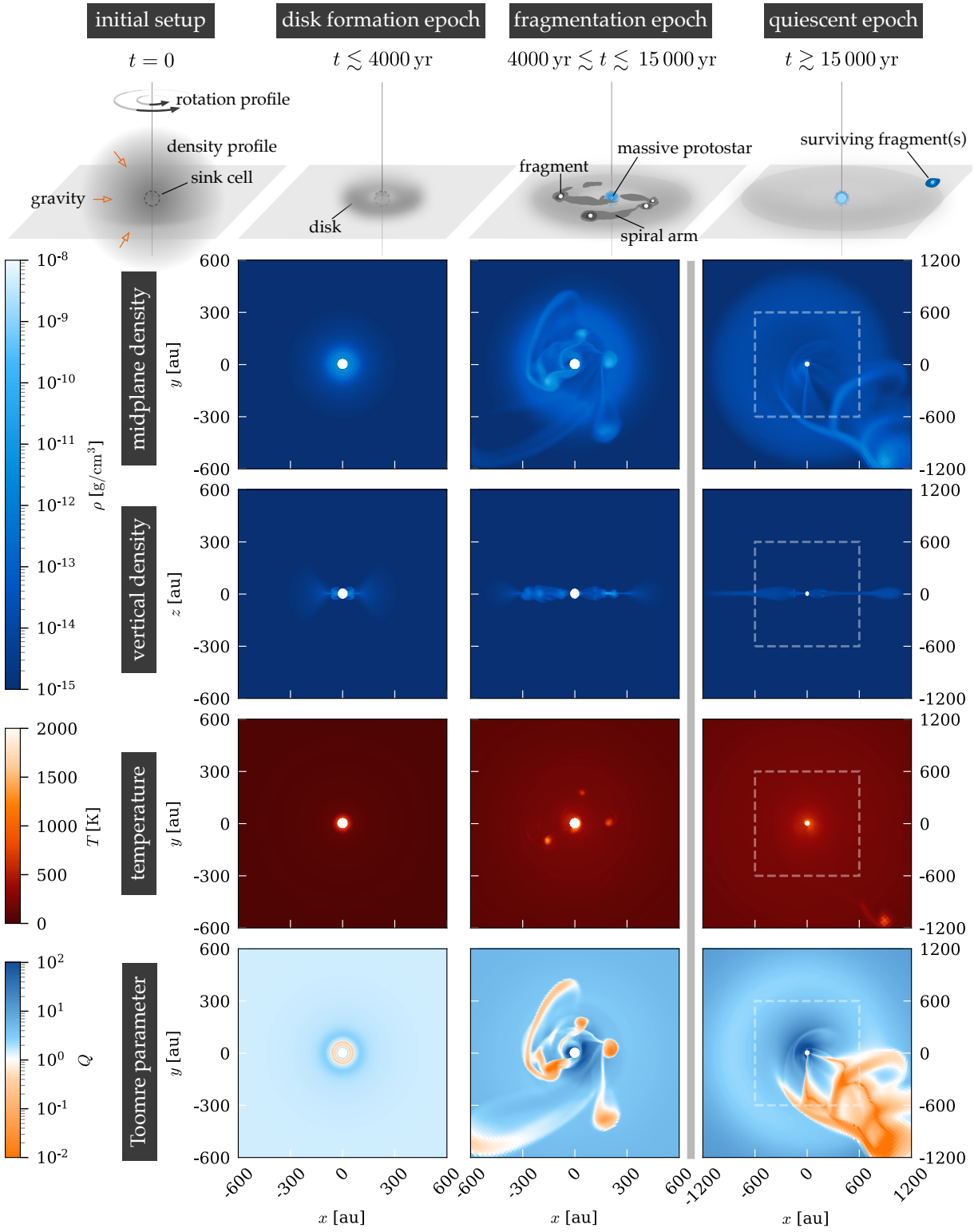



**Fig. 1.** Time evolution of the system (run x8). In the elaboration of the plots, snapshots of the simulation were taken specifically at 3.0, 8.0, and 17.5 kyr for each respective column. The *rightmost column* shows double the size of the other two (the dotted square corresponds to the area shown in the snapshots located to the left). For the rightmost column, notice the existence of a surviving fragment at $\boldsymbol{r} \sim (900, -1200)$ au for the midplane views.

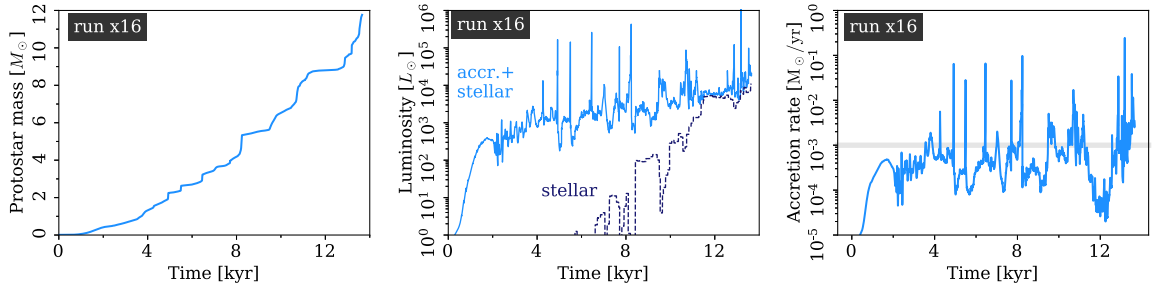



**Fig. 2.** (*a*) Mass, (*b*) luminosity, and (*c*) accretion rate of the central massive protostar, as formed in run x16. The dotted line in *panel b* corresponding to the stellar luminosity is calculated using the evolutionary tracks of Hosokawa & Omukai (2009). The gray line in *panel c* shows a reference accretion rate of $10^{-3}\,M_\odot\,\mathrm{yr}^{-1}$.

The cloud begins to collapse as soon as the simulation starts. Matter free-falls into the center of the cloud, where the sink cell is located, and eventually forms a massive star there. Simultaneously, angular momentum conservation yields an initially axially symmetric accretion disk that grows in size over time.

At around 4 kyr, when the disk is about 200 au in size, the axial symmetry is broken: spiral arms appear and then the disk fragments. The fragments form, interact with the disk, spiral arms, and other fragments, and can be destroyed. Very roughly, fragments have densities of more than $\sim 10^{-11}\,\mathrm{g\,cm^{-3}}$ and temperatures higher than ~600 K, while spiral arms and other filamentary structures have densities higher than $\sim 10^{-13}\,\mathrm{g\,cm^{-3}}$. The background accretion disk has densities higher than $10^{-15}\,\mathrm{g\,cm^{-3}}$. As shown in the density maps of Fig. 1, the whole disk (including spiral arms) is relatively thin; the pressure scale height is shown below in Fig. 23. The spiral arms and filaments are dynamic: they continuously change shape, form, and merge in the course of an orbit, and they extend throughout the disk. Fragments are typically connected to each other and to the central massive protostar via spiral arms and filaments. Some fragments have the potential to form companion stars, as we describe in Sect. 7. Fragments can also be surrounded by secondary disks with their own spiral arms that can lead to the formation of more fragments. These mechanisms are described in Sect. 6.1.

The disk stabilizes at around 15 kyr due to the increase in mass of the central massive protostar and the effects of stellar irradiation in the innermost part of the disk, stopping fragmentation of the primary disk until the end of the simulated time. We refer to this period as the quiescent epoch. Some fragments survive the fragmentation epoch, but the majority of fragments migrate toward the central massive protostar or get accreted by it. Run x8 ends at $t = 0.52 t_{\mathrm{ff}}$, where $t_{\mathrm{ff}} \sim \sqrt{R^3/(GM)}$ is the free fall time of the cloud; run x16 ends at $t = 0.40 t_{\mathrm{ff}}$.

Interestingly, the final state of run x8 is reminiscent of the young protostellar object G11.92–0.61 MM 1 reported in Ilee et al. (2018). This similarity was not intended a priori in the simulation setup. We compare the outcome of run x8 and the properties of the fragment produced to this potential observational counterpart in Sect. 6.8.

The central massive protostar formed by accretion from the disk is about $12\,M_\odot$ after ~14 kyr of evolution, as shown in Fig. 2a. The total luminosity of the protostar is calculated by summing the luminosity predicted by the evolutionary tracks of Hosokawa & Omukai (2009), and the accretion luminosity, that is, the gravitational energy released by accretion, and computed with $L_{\mathrm{acc}} = GM_\star \dot{M}/(2R_\star)$, where $\dot{M}$ is the accretion rate onto the (proto)star (Fig. 2c). The total luminosity is shown in Fig. 2b together with the stellar luminosity component. At around 12 kyr, the massive protostar starts burning hydrogen, and the stellar luminosity becomes comparable and later dominates over the accretion luminosity. Prior to that, the luminosity of the central massive protostar is dominated by accretion, which causes accretion-driven bursts; these can be seen in Fig. 2b and are discussed in Sects. 6.6.2 and 7.3.1.

## 4. Post-processing methods

Since fragmentation was studied without the use of sink particles, sophisticated post-processing algorithms had to be developed in order to track their properties in time, which we present in this section together with strategies for isolating the properties of the background disk.

### 4.1. Properties of the disk

During the fragmentation epoch, the density maps of Fig. 1 show three distinct components (background disk, spiral arms, and fragments), which we mentioned in the preceding section. In order to study the properties of the background disk, the spiral arms and fragments have to be filtered out from the data. We do this with a combination of the two following methods. First, in order to get the radial profile of a quantity $q$ measured for the background disk in the midplane, we take the median of all values along the azimuthal direction, that is, for each discretized radial distance $r_i$,

$$q_{\mathrm{bg,midpl}}(r_i) = \underset{k}{\mathrm{median}}\, q(r_i, \theta = \pi/2, \phi_k). \tag{12}$$

Taking the median filters out most of the variability caused by the presence of fragments and spiral arms. For some radial profiles, an average of the radial profile in some interval of time is also used in order to eliminate strong but short-term variations. As fragments and spiral arms are highly dynamic, a time average filters out sudden changes and yields the long-term behavior of the background disk. With this method, one can isolate, for example, the density and temperature profiles of the primary disk, which we present and discuss in Sect. 5.1. The specific time intervals used for the average are specified in the caption of the relevant plots.

In order to determine whether or not the formed disk is Keplerian, the deviation from gravito-centrifugal equilibrium, or Keplerianity, of the background disk is calculated as the relative difference between the angular velocity $\Omega$ (taken for the

A&A 644, A41 (2020)

background disk in the midplane) and its Keplerian value, $\Omega_K$:

$$\text{Keplerianity} = \frac{\Omega - \Omega_K}{\Omega_K}, \text{ where } \Omega_K(r) = \sqrt{\frac{GM_{\text{encl}}(r)}{r^3}} \quad (13)$$

is the Keplerian angular velocity, and $M_{\text{encl}}(r)$ is the total mass enclosed in a sphere of radius $r$; that is, the sum of the mass of the central massive protostar and the portion of the disk enclosed. The Keplerianity was used to define the disk radius, as is mentioned in Sect. 5.1.

The accretion rate onto the central massive protostar, as well as its mass, are calculated by integrating the incoming mass from all directions at the surface of the sink cell. One general limitation of the sink cell approach is the inability to distinguish between accretion of fragments onto the stellar surface and formation of close companions. This problem is discussed in Sect. 7, together with the implications for the values obtained with the method described here.

We remind the reader that no artificial viscosity is introduced in these simulations to compensate for unresolved physics; self-gravity instead is the process that provides angular momentum transport. This motivates us to calculate how the mass is transported by the background primary disk, that is, $\dot{M}(r)$. We take the background disk density $\rho_{\text{bg}}(r_i, \theta_j)$ and radial velocity $v_{\text{r,bg}}(r_i, \theta_j)$ and then we integrate in a spherical shell according to

$$\dot{M}(r_i) = -\sum_j \rho_{\text{bg}}(r_i, \theta_j) v_{\text{r,bg}}(r_i, \theta_j) r_i^2 \sin(\theta_j) \cdot 2\pi \cdot \Delta\theta_j. \quad (14)$$

Outside of the disk, this quantity simply expresses the mass flux transported by the infalling large-scale envelope.

In order to quantify gravitational instabilities, we use the Toomre parameter $Q$ (Toomre 1964). This parameter measures gravitational stability against small perturbations in a rotating, self-gravitating disk, and is defined as

$$Q = \frac{c_s \Omega}{\pi G \Sigma}, \quad (15)$$

where $\Sigma = \int \rho \, dz$ is the surface density and $c_s$ is the speed of sound; $Q < 1$ indicates instability.

### 4.2. Fragment detection

In order to study the different properties of the fragments, one must first clearly define what a fragment is. One possibility is to use the fact that fragments appear as hot points in comparison with the background disk and spiral arms (see, e.g., the temperature plot during the fragmentation epoch in Fig. 1). In comparison, the density data for the same time show spiral arms, filaments, and other structures that make the definition of a fragment more difficult. In other words, spiral arms generally have temperatures that are similar to the background disk, in sharp contrast to the fragments, allowing us to fix a criterion for fragment detection. Detecting a fragment then reduces to correctly detecting maxima in the temperature data for the midplane. Fragments are expected to gravitationally collapse, and therefore increase their temperature, if they have a possibility to form stars (below, we show that not all fragments can evolve further into stars).

In order to filter out the spiral arms and the disk, a Gaussian filter is first applied to the temperature data (this blurs out the spiral arms), and then the radial disk temperature profile is subtracted from the temperature data. After that, a temperature threshold is set so that the fragments are detected (~400 K). The parameters for such filters were manually tuned by selecting the values that produce fewer false positives and do not leave fragments undetected. This process produces "fragment candidates". However, it should be noted that the data reveal cold high-density regions that are not considered as fragments unless they overcome the temperature-detection threshold. The fragment candidates are also checked by eye to filter out any remaining false positives that, when compared against the density data, turn out to be hot areas of spiral arms and not clump-like structures.

### 4.3. Fragment tracking

We are interested in calculating the properties of the fragments, and their evolution in time; therefore, we require a way to track them using the data snapshots that are output every 10 yr of evolution, which is a much smaller timescale than the duration of one orbit ($\gtrsim$500 yr at ~100 au). This is done as follows: for every fragment, the next predicted position on its orbit is estimated for a time $t_{\text{current}} + \Delta t$ with $\Delta\phi \sim v_\phi \Delta t$. Time is then advanced by $\Delta t$, and maxima in the temperature are searched for in a region surrounding the predicted position. When a matching fragment is found in the predicted region, a connection is made and it is registered as a fragment with a unique identification number. As a warning to the reader, even though the identification number for new fragments increases with time, it cannot be used as an indication of the total number of fragments present because manual corrections to the output of our algorithm cause missing identification numbers.

### 4.4. Properties of the fragments

Once the trajectory of the fragments is known, we can easily track other properties, such as the central temperature or the mass of the fragments. The central temperature is the maximum value of the temperature field of a three-dimensional region that contains the fragment. The mass of the fragment $M_{\text{fragm}}$ is obtained by integrating the density in a spherical region of a fixed radius (all fragments are assumed to have the same radius). A first guesstimate from the x8 density maps is $R_{\text{fragm}} \sim 50$ au.

In order to obtain an idea of the upper limit of the radius of a fragment, we can estimate the order of magnitude of this radius assuming hydrostatic equilibrium (pressure of self-gravity $P \sim GM_{\text{fragm}}^2/R_{\text{fragm}}^4$ is equal to the pressure of the ideal gas $P \sim \langle n \rangle k_B T$), using a mean number density $\langle n \rangle \sim 1.5 \times 10^{17}$ cm$^{-1}$ extracted from the density data, and a temperature of 2000 K. This yields $R_{\text{fragm}} \sim 30$ au for a fragment of 1 $M_\odot$, and $R \sim 50$ au for a fragment of 2 $M_\odot$.

To justify our choice, we performed mass calculations with several assumed radii (the results are shown in Fig. 3). Small assumed radii give a steep gradient in the mass value, suggesting that most of the mass of the fragment has not yet been enclosed in the region of integration. At around 50 au for run x8, the curve shows a more stable value. Bigger radii would not only enclose the fragment but also parts of the disk and surrounding spiral arms. A similar analysis done for run x16 yields a radius of 40 au. These considerations mean that the mass of the fragments reported here have an uncertainty of around 20%.

## 5. The fragmenting accretion disk

The following sections present the results of the highest resolution simulations, and an in-depth analysis of the internal processes that govern fragmentation in the disk.

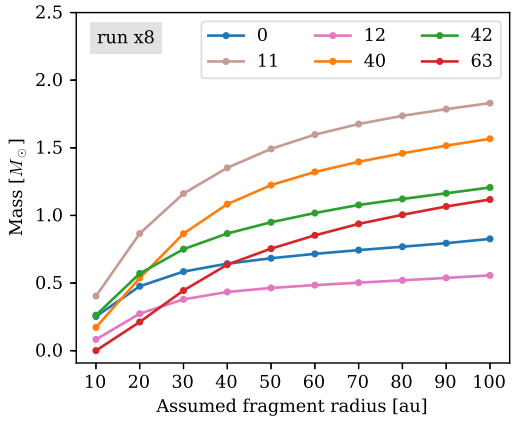



**Fig. 3.** Variation of the time-averaged mass of a sample of fragments as a function of the assumed radius taken for integration.

### 5.1. Properties of the disk

Radial profiles of several quantities related to the background disk are presented in Fig. 4, obtained using the data from run x8. The density, Keplerianity, and radial mass flow are averaged in time, as discussed in Sect. 4.

After the disk-formation epoch (from 4 kyr until the end of the simulation), the disk is approximately Keplerian, as shown by the Keplerianity profile, with a variability of ∼10%. We used this fact to define the disk radius as the point at which the Keplerianity of the background disk drops below −15%. For larger scales, the low values of Keplerianity indicate infall from the large-scale envelope, which replenishes the disk. The initial rotation profile chosen, with $\beta_\Omega = -3/4$, means that the gas is uniformly non-Keplerian, and during the disk formation epoch (0 to 4 kyr), the disk builds up until it reaches gravito-centrifugal equilibrium. In some of the panels, the disk radius is indicated as a reference with filled diamonds. The density profiles show that the background disk stays mainly between $10^{-15}$ and $10^{-13}$ g cm$^{-3}$. A higher density region is observed near the edge of the disk, and corresponds to a centrifugal barrier.

As expected, the temperature profile of the collapsing cloud, including the accretion disk, increases over time, although we observe that the profile increases more slowly during the fragmentation epoch. The temperature profile is approximately proportional to $r^{-0.5}$. At the late stages of the simulation (cf. the line for 16 kyr in Fig. 4c), there is an increase in temperature in the inner parts of the disk ($\lesssim$40 au) that is probably due to stellar irradiation because the central massive protostar has just begun burning hydrogen at that time.

The radial mass flow transported by the background disk is different from the radial flow in the infalling large-scale envelope. This shows that mass from the infalling envelope is not only being transported onto the central massive protostar but is also deposited into the fragments and spiral arms, and that during the fragmentation epoch most of the mass is delivered to the massive protostar by means of the spiral arms and fragment accretion and not through the background disk.

Data from run x8 reveal a region with a seemingly unusual overdensity (more associated with the densities of spiral arms) at about 12 kyr in the region $r \lesssim 100$ au, which is particularly evident on the surface density and radial mass flow profiles. As a result of an accretion event in run x8, the inner disk temporarily acquires a higher density "ring like" accretion structure. As a consequence, computing the background disk density as the median value in an annulus yields a higher density. Such accretion structures are also occasionally observed in the other runs, although with shorter durations. Disregarding this short-term feature, the general trends shown in Fig. 4 are also observed in the other runs.

The accretion rate onto the central massive protostar as a function of time shows great variability, because fragmentation creates small accretion events on top of having a very smooth, constant process, as described in Sects. 6.6.2 and 7.3.1. Nevertheless, the mean accretion rate in the fragmentation epoch is fairly constant, at about $10^{-3}\,M_\odot\,\mathrm{yr}^{-1}$, although a slight increment with time in the accretion rate is observed in both panels e and f, which is due to simple acceleration of the gas in free fall.

### 5.2. Local versus global Toomre parameter

The Toomre maps in Fig. 1 show that the Toomre parameter is highly dependent on position and time. In Fig. 5, we present the Toomre parameter as a function of radius, averaged in time for the fragmentation epoch. The curve for $Q_{\rm disk}$ is calculated by taking the azimuthal median of all the variables and then computing $Q$, and corresponds to the values for the background disk. On the contrary, the curves for $Q_{\rm mean}$ and $Q_{\rm min}$ are obtained by first calculating $Q(r,\phi)$ and then taking the mean and the minimum, respectively. $Q_{\rm min}$ represents the regions of the disk that undergo most fragmentation, that is, spiral arms and fragments, while $Q_{\rm mean}$ may be interpreted as a value of $Q(r)$ obtained observationally for spatially unresolved sources (i.e., substructures such as spiral arms and fragments are not detected).

The background disk is Toomre-stable, and no fragmentation is expected to occur in these regions; however, spiral arms and fragments are subject to fragmentation. The mean value, on the other hand, shows stability. The whole disk is therefore globally stable while being locally unstable. This means that the substructures of the disk have to be resolved accurately in order to capture fragmentation; an insufficiently resolved disk may appear to be Toomre-stable while undergoing fragmentation at unresolved scales.

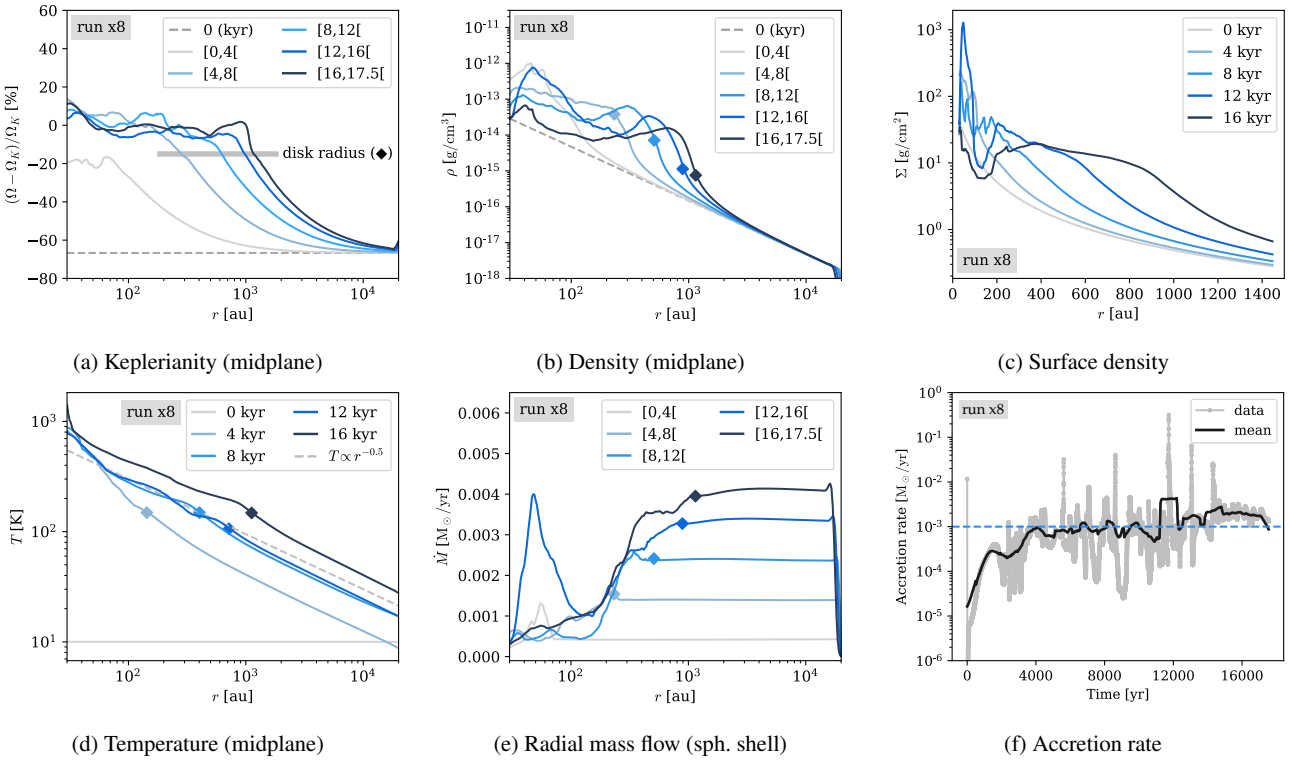
### 5.3. Spiral arm formation

In all runs, at the end of the disk formation epoch ($t \sim 400$ yr, see Fig. 1), a ring-shaped region in the disk becomes Toomre-unstable and develops small inhomogeneities that become two primordial spiral arms at opposite sides of the disk, that is, they arise from the $m = 2$ mode described in Laughlin & Rozyczka (1996) (see also, e.g., Kratter et al. 2008; Kuiper et al. 2011). The first fragments form at the outermost parts of the spiral arms.

New spiral arms are created by convergent flows, as shown in Fig. 13a; the flows left of and below the fragment are convergent and mass accumulates as spiral arms. These type of flows are frequently created by turbulent motions arising after fragment interactions.

## 6. Fragments

In the following sections, we examine the different physical processes that occur during the lifetime of a fragment: its formation, the formation of a secondary disk around it, the interactions with other fragments and their environment. Additionally, we present some properties of the fragments: the number of fragments present in the primary disk, their masses and their orbits, all of which were calculated with with the methods presented in Sect. 4.




(a) Keplerianity (midplane) (b) Density (midplane) (c) Surface density

(d) Temperature (midplane) (e) Radial mass flow (sph. shell) (f) Accretion rate

**Fig. 4.** (*a*)–(*e*) Radial profiles of several quantities for the background disk. The intervals in profiles (*a*), (*d*), and (*e*) mean that the quantity has been time-averaged in that interval, excluding the endpoint. The filled diamond indicates the value at the disk radius. (*f*) Accretion rate into the central massive protostar as a function of time.

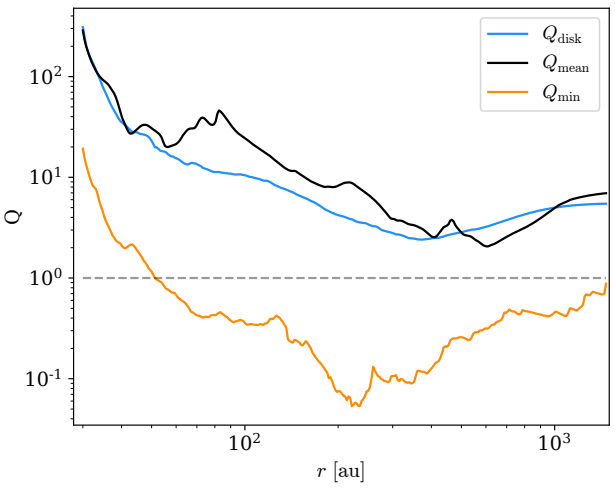



**Fig. 5.** Comparison of the Toomre parameter values computed for the background disk ($Q_{\rm disk}$), the mean value ($Q_{\rm mean}$), and the minimum values corresponding to the effects of the fragments and spiral arms (corresponding to $Q_{\rm min}$). These curves were calculated with run x16, and they are time-averaged for the fragmentation epoch.

### 6.1. Fragment formation

Fragments form out of one or more spiral arms. This two-step fragmentation process (first the disk forms spiral arms, and then they fragment) is in agreement with what Takahashi et al. (2016) reported in the context of simulations of self-gravitating protoplanetary disks. We have identified two distinct mechanisms of fragment formation in our simulations: a local collapse within a spiral arm and a formation triggered by a collision of two spiral arms. These mechanisms are present at two different scales: the primary disk, and the secondary disks that form around the fragments (we discuss the latter in more detail in Sect. 6.7).

The first process, local collapse within spiral arms, is illustrated in panels A1 and A2 of Fig. 6. When small inhomogeneities are developed within a spiral arm or when a spiral arm develops a crease, it becomes Toomre-unstable and some regions inside it begin to collapse, forming small fragments that deform the spiral arm. This process is exemplified by the creation of fragments 16, 13, and 14 of panel A3 (run x16), where the spiral arm develops inhomogeneities that grow into fragments. The other example is given in panel A4, where fragments 54 and 59 are formed by a previous crease; in the case of fragment 59, the crease was formed in a spiral arm of the secondary disk around fragment 40.

The second process, spiral arm collision, is illustrated in panels B1 and B2. When two spiral arms or regions of high density collide, they create perturbations that make the region Toomre-unstable and therefore, a collapse is triggered. The example in panel B3 is from run x8, and shows the formation of fragment 32, which is generated by this mechanism. Panel B4 provides an additional example from run x16, where two spiral arms, connecting fragments 32 and 68 to the inner disk, have collided and have given rise to fragment 71.

Early during the fragmentation epoch, both processes occur predominantly in the primary disk. However, towards the end of the fragmentation epoch, and as fragments gain more mass, the

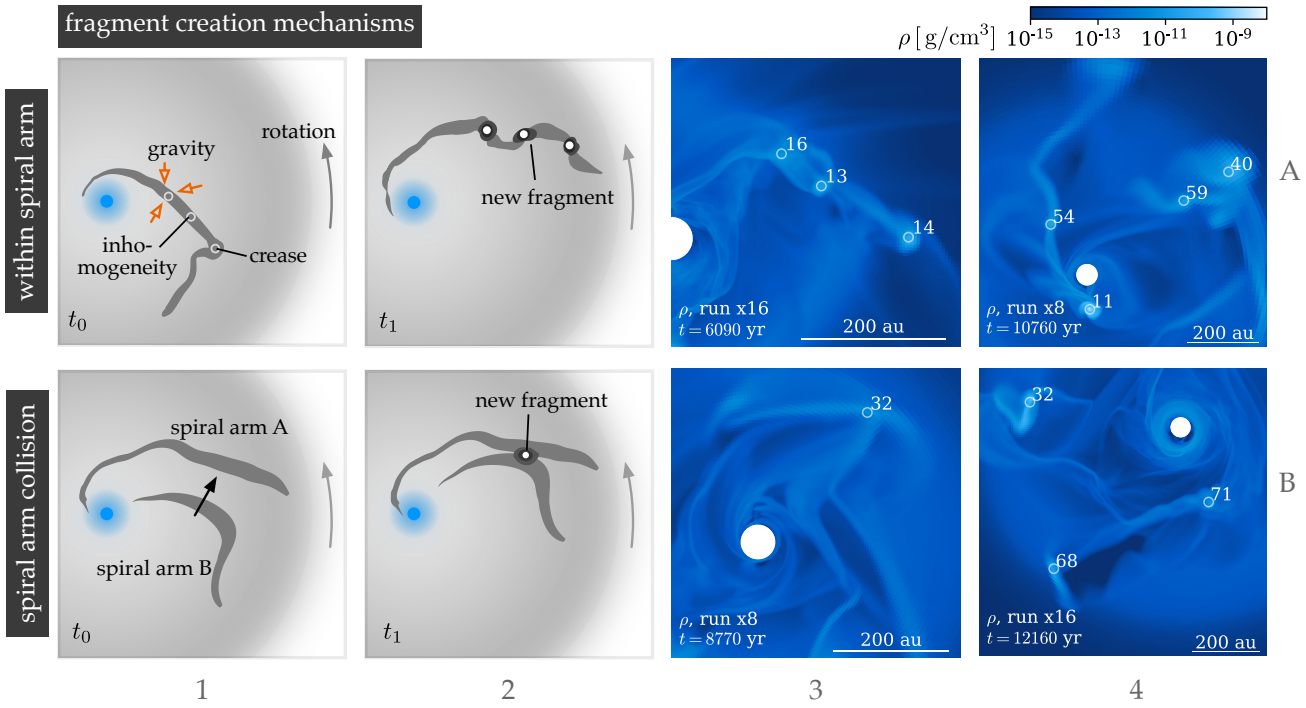



**Fig. 6.** Fragment creation mechanisms. The color scale for the midplane density maps is the same as the one shown in Fig. 1.

fragmentation inside substructures becomes dominant: the spiral arm breakdown and spiral arm collisions become more frequent in the secondary disks and yield fragmentation. This behavior was observed especially in runs x4 and x16. This hierarchical fragmentation is in principle analogous with the observations and conclusions offered in Beuther et al. (2015, 2019).

### 6.2. Number of fragments

The number of fragments present in run x8 as a function of time is plotted in Fig. 7. We remind the reader that the numbers next to the fragments in the plots throughout this paper are mere identification numbers. In total, 60 fragments are detected during the fragmentation epoch (4–15 kyr). From these, 22 live longer than 200 yr; these fragments will be the focus of the analysis that follows. At a given time, there are fewer than 9 fragments present in the disk. A discussion about the number of surviving fragments is offered in Sect. 7.2. A peak in fragmentation is seen at around 9 kyr, although we do not consider it to be of great interest, because it is not observed in the other runs (see Fig. 20).

Lifetimes of the fragments (color code) and the radial location when they are formed (vertical axis) are shown in Fig. 7b as a function of time (horizontal axis). We see that the longest lived fragments are formed in the outer disk, and that the inner disk forms fewer fragments over time. This trend is tied to the fact that fragmentation is occurring in the spiral arms of the primary disk. The figure was generated with the data from run x8. In run x16, as the spiral arms of the secondary disks fragment, new long-lived fragments start to form again in the inner disk.

### 6.3. Mass

Figures 8 and 9 (corresponding to runs x8 and x16, respectively) show the masses of the fragments obtained using the method described in Sect. 4. The masses of the fragments are of a few solar masses, and increase over time. Peaks and sudden increases are observed, and correspond to fragment mergers, which are described in Sect. 6.6. Some decreases and oscillatory behavior are caused by the action of spiral arms associated to the secondary disk, as described in Sect. 6.7. The first fragments formed tend to have lower masses than the fragments formed later in time. This is not surprising, because the fragments form at larger radii, where larger portions of the disk become unstable, but also because the radial mass flow of the background disk increases both with the radial position as well as with time. More massive fragments tend to have longer lifetimes as well because they are more strongly gravitationally bound and are more immune to the fragment-destruction mechanisms described in the following sections.

Two special cases occurring in Fig. 8 merit a more detailed discussion. Fragments 11 and 94 show unusually high masses; fragment 94 in particular shows high variability. Fragment 11 undergoes several mergers and gains mass just before it goes into the sink cell. The erratic behavior of fragment 94, on the other hand, is mostly numeric: it moves outwards in the simulation domain, where there is less resolution; and by effect of numerical diffusion, increases in radius, making our assumed radius of 50 au insufficient in the calculation. The mass of fragment 94, assuming a larger radius of ~100 au, is ~6.5 $M_\odot$ at $t$ = 13 kyr.

### 6.4. Hydrostatic cores

As we discuss in Sect. 7, fragments collapse and form hydrostatic cores. We remind the reader that the masses presented in this section are calculated by assuming a fixed fragment radius of 50 au for run x8, and 40 au for run x16, which means that the enclosed region includes the hydrostatic core as well as the secondary disk. This is important when comparing to models of core collapse, such as the ones described in Bhandare et al. (2018): for an initial core mass of a few solar masses, they find

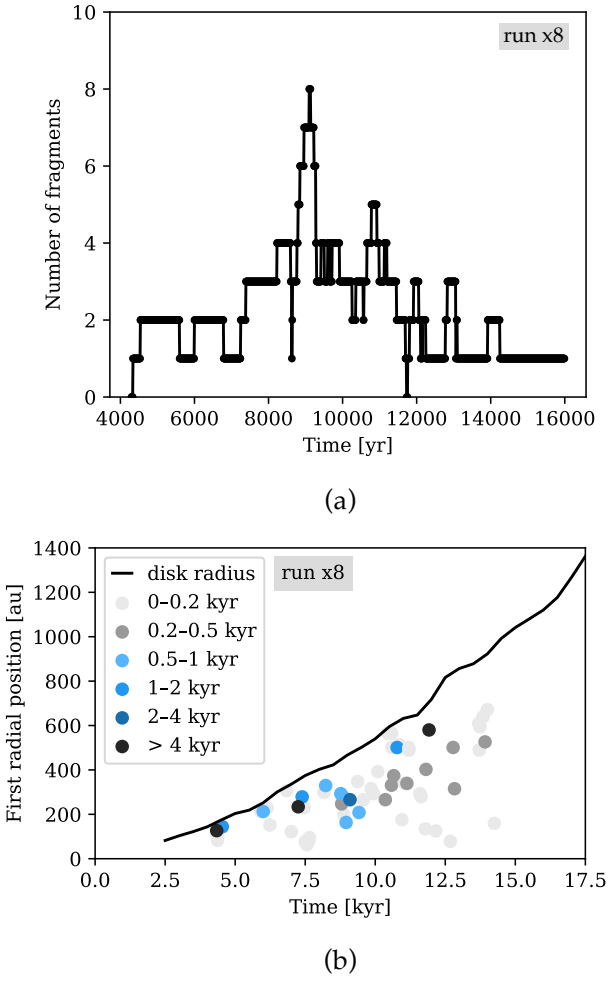



**Fig. 7.** (*a*) Number of fragments with a minimum lifetime of 200 yr present in the simulation as a function of time. (*b*) Radial position at formation time for each fragment, color-coded with the fragment lifetime.

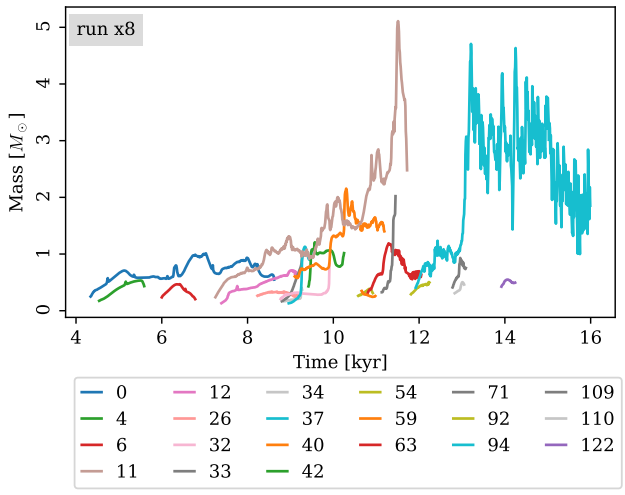



**Fig. 8.** Mass of the fragments with life span longer than 200 yr. A fixed radius of 50 au is assumed for the calculations of this plot.

hydrostatic first Larson cores of ∼3 au in radius, with masses of the order of a few $10^{-2}\,M_\odot$.

In run x16, cell sizes of $\lesssim$1 au are reached at radial positions of $r \lesssim 100$ au, barely allowing us to resolve the hydrostatic core region of fragments located there with a few grid cells, enough for an order of magnitude check with a core collapse model. We calculated the enclosed mass in the inner ≈3 au of fragment 12 (run x16) over its evolution. During the gravitational collapse of the fragment (Fig. 14a), the mass of the inner ≈3 au increased, until a value of a few $10^{-2}\,M_\odot$ was reached, consistent with the results of Bhandare et al. (2018). This high-density inner region is also shown in Figs. 13b and 14b, surrounded by the secondary disk (the figures correspond to the midplane and vertical cuts in the density field, respectively). As a reference for the reader, the yellow circle in Fig. 13b indicates the inner 3 au (roughly the size of the first core), and the yellow circle in both panels of Fig. 14 indicates the assumed size of a fragment, which was used for the calculation of its (total) mass.

### 6.5. Fragment dynamics: orbits

The remainder of Sect. 6 is devoted to the study of how fragments move in space, their interactions with their environment, and their substructures. First, an overview of the orbits is presented. In Fig. 10, the orbits of long-lived fragments (>1 kyr) have been plotted. During the simulated time period, only about eight fragments complete more than one orbit (both runs). The orbits of the fragments are highly influenced by their interactions with spiral arms and other fragments (fast migration, mergers, etc.; more details are given below). They also stay in the midplane, except for some orbits of run x16 that show a small inclination ($\lesssim 2°$) with respect to the midplane during certain times. The average period is ∼1 kyr. The orbits of the fragments are highly eccentric, with an average eccentricity of ∼0.5, which was calculated by taking the minimum and maximum radial positions of the fragments. Fragments undergo different types of interactions that cause changes in the eccentricity of their orbits, including fast inward migration due to spiral arm action and gravitational interaction with other fragments.

The orbits of long-lived fragments 40 and 32 of run x16 (Fig. 10b) develop in the middle disk, and correspond to fragments that survive at the end of the simulated time. These fragments are also more massive than short-lived ones (according to Fig. 9, their masses are $\sim 1.5\,M_\odot$), and therefore their self-gravity provides more stability against interactions with the environment.

However, the orbits presented here do not take into account the effects of the formation of second Larson cores and the fate of fragments that enter the numerical sink cell. A more detailed discussion is presented in Sect. 7.2.

### 6.6. Interactions

#### 6.6.1. Fragment–fragment interactions

Fragments interact with each other in two distinct ways: they can merge, or change orbits due to gravitational interaction and angular momentum transfer. Mergers (panel A1 of Fig. 11) occur when the fragments have a close encounter, usually in a collision orbit. As shown in the example provided in panels A2, A3, and A4 of Fig. 11, fragments 42 and 40 are in a collision orbit and merge. The masses of the fragments combine, as shown by the spike in the mass of 40 in panel A4. However, we highlight

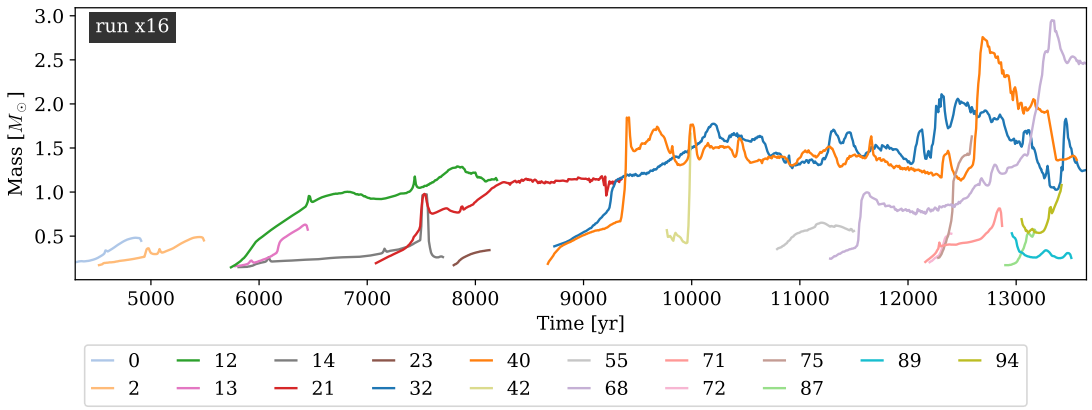
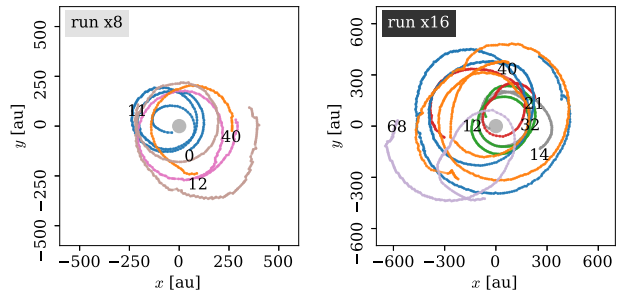



**Fig. 9.** Masses of the fragments with life span longer than 200 yr, for run x16. A fixed radius of 40 au is assumed for the calculations of this plot.




(a) (b)

**Fig. 10.** (*a*) Orbits of fragments with a life longer than 1 kyr during the time interval [6, 10] kyr, for run x8. (*b*) Orbits of all the fragments with a life longer than 1 kyr during all of the simulated time for run x16. The fragment identification number is located at the starting point of the orbit, and the color code is the same as that used in Figs. 8 and 9.

several features of a typical merger: first, the mass of fragment 42 increases slightly near the collision time. This can easily be explained by the fact that the mass integration domains start to overlap because they are spheres of a fixed radius. A second feature is the decrease in mass, with small oscillations being observed after the collision. Collisions typically do not occur head on, but with a certain impact parameter, which increases the spin angular momentum of the merged fragment. In the frame of reference of the fragment, the increased centrifugal force favors the development of secondary spiral arms, which can transport mass outwards, as explained in Sect. 6.7. During the fragmentation epoch in run x8, we recorded about 13 mergers in total. This kind of interaction can only be captured by simulating and resolving the full hydrodynamics of a fragment, and not by a sub-grid particle model.

Changes in the orbit due to gravitational interaction of fragments that are unconnected by a spiral arm are somewhat more complex, less frequent, and more difficult to determine. However, a general picture is provided by panel B1 of Fig. 11: two fragments approach and their gravitational interaction slows down fragment 1, therefore moving it to a lower orbit, and accelerates fragment 2, moving it to a higher orbit. Panel B4 provides an example of this kind of interaction: just after the orbits of fragments 16 and 29 cross each other, fragment 16 slows down and enters into a collision orbit with the central massive protostar, while fragment 29 gets accelerated into a higher orbit. However, the moments leading to the orbit crossing are another example of the effects of a gravitational interaction: in panels B2 and B3, we see how fragment 29, originally in a low orbit, migrates towards fragment 16 and vice versa, until they cross each other and the scenario illustrated as $t_0$ in panel B1 is reached. The example provided here comes from the data of run x4, but we also observed a similar behavior in run x8, but without the orbit crossing. Some of these interactions have also been observed previously in 2D simulations in the context of planet formation (see, e.g., Zhu et al. 2012). The outcome of these interactions (a change in the orbit or a merger) depends on the approach velocities and the mass ratio of the interacting fragments. In the example given in panels B2–4, the masses were comparable.

### 6.6.2. Fragment interactions with spiral arms and the massive protostar

The gravitational torques exerted by the spiral arms can cause migration, as shown by panels A1–4 of Fig. 12. In this case, the eccentric orbit of fragment 0 reduces its periastron due to the action of the connecting spiral arm.

Accretion onto the central massive protostar is not a smooth process, as depicted in the accretion rate shown in Fig. 4f. There are many discrete accretion events caused by infall of matter through a spiral arm or the complete accretion of a fragment. The transformation of gravitational energy into radiation is made in the form of accretion-driven bursts, that is, sudden increases in the luminosity of the forming massive star (see Fig. 2b). This phenomenon was reported in theoretical studies in the context of massive star formation by Meyer et al. (2017, 2019), where a system of magnitudes was also developed to describe them.

Panels B1–4 of Fig. 12 show two examples of accretion bursts: both the infall of matter through a spiral arm, as shown in panels B1–2, and the complete accretion of a fragment (panels B3–4) produce accretion bursts. However, the accretion of a fragment produces a much sharper and brighter peak in luminosity compared to accretion through a spiral arm. Accretion bursts are also accompanied by overall increases in the temperature of the disk, which we term temperature flashes, which typically last ~30 yr and heat up the fragments and spiral arms, as we discussed in the previous section.

Nevertheless, we must discuss the effects of the inner boundary conditions (size of the central sink cell) on these accretion bursts. As matter is only allowed to cross the sink cell inwards, we are not taking into account how outflows affect the accreted

A&A 644, A41 (2020)

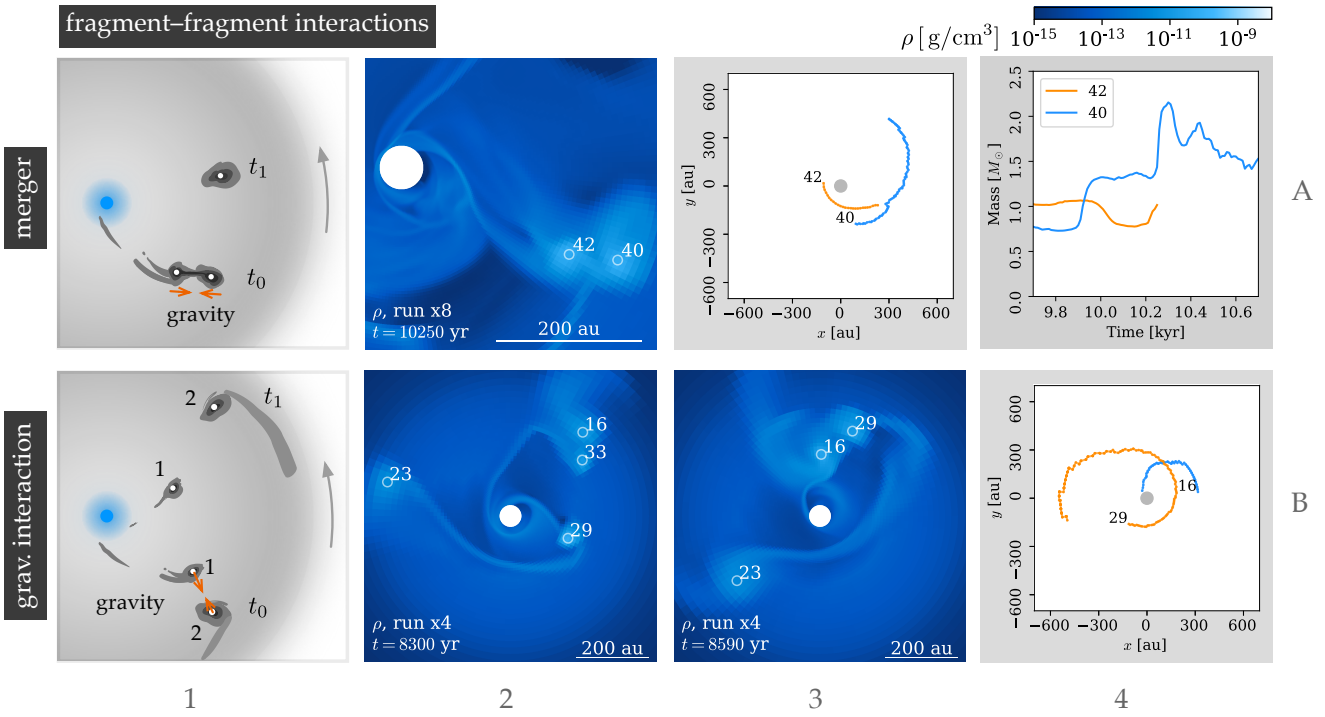



**Fig. 11.** Fragment–fragment interactions. *Panels A3 and B4*: the fragment ID is shown at the starting point of the orbit. *Panel A3*: the time window shown in the orbits is 1.3 kyr; *panel B4*: this is 1.2 kyr.

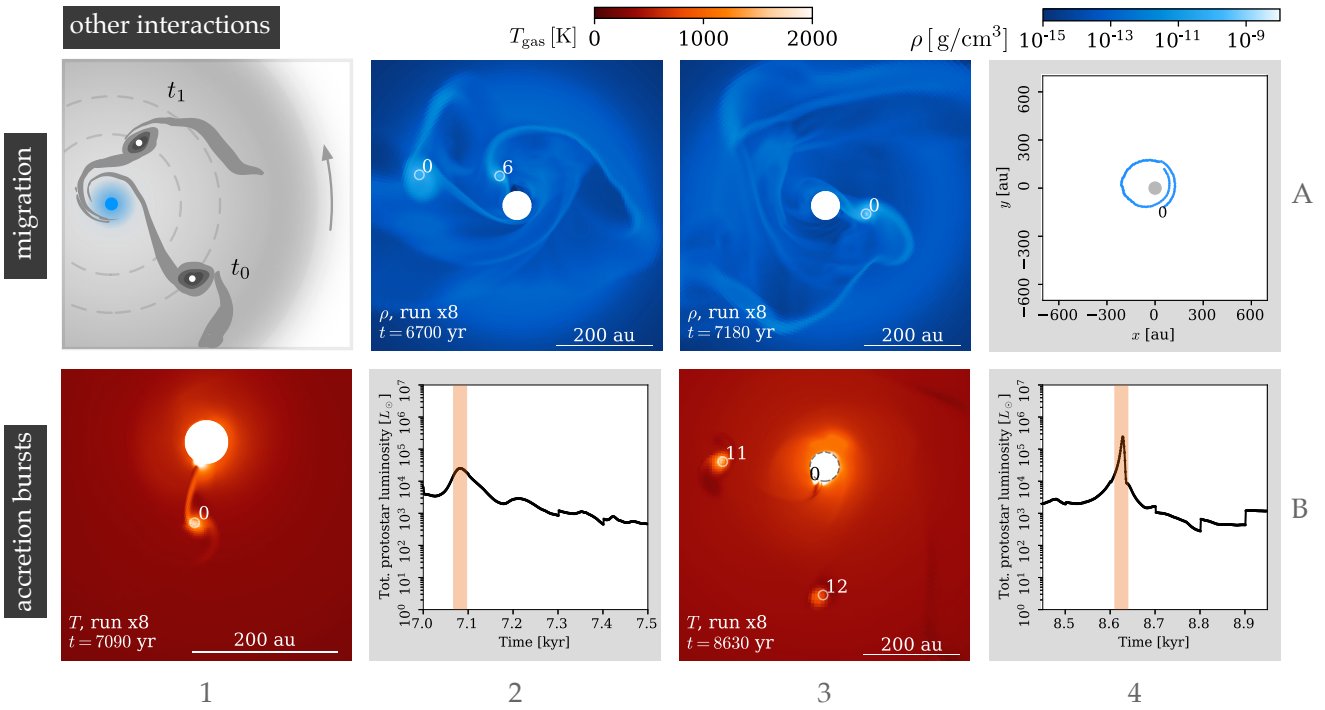
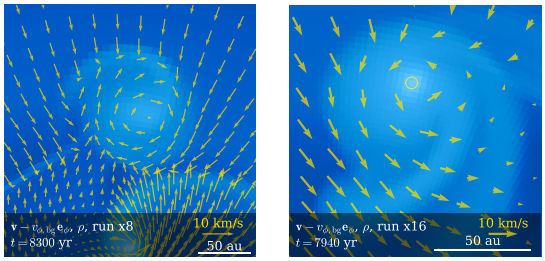
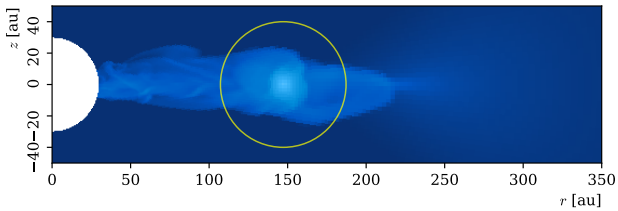



**Fig. 12.** Interactions of the fragments with the spiral arms, and with the forming protostar modeled as a central sink cell. The orbit in *panel A4* is plotted for a window of 2 kyr, with the fragment ID marking the starting point.

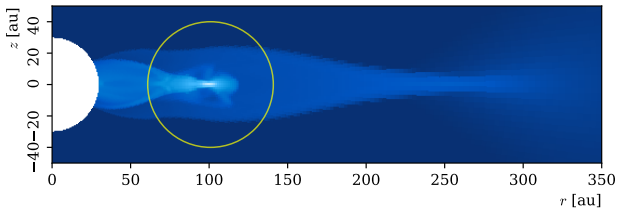



(a) (b)

**Fig. 13.** Secondary disk with its spiral arms around (*a*) fragment 11 of run x8, and (*b*) fragment 12 of run x16. The background map represents density in the midplane (using the same color scale as the rest of the figures), and the arrows show the comoving velocity field. The central massive protostar is located beyond the bottom of the plotted areas in both cases. The yellow circle in (*b*) has a radius of 3 au.




(a) Density, $t$ = 5.88 kyr




(b) Density, $t$ = 7.12 kyr

**Fig. 14.** Vertical structure of fragment 12 and its close surroundings (run x16). The yellow circle has a radius of 40 au. The density uses the same color scale as the rest of the figures.

mass. Some fragments that the simulation shows as accreted into the sink cell could also only be in an elliptical orbit, as discussed in Sect. 7, especially if they have already undergone second collapse, meaning that they are less susceptible to shearing and subsequent accretion. These considerations could make strong luminosity accretion bursts less frequent and intense than presented here.

### *6.7. Secondary disks*

Fragments frequently develop a secondary disk with spiral arms, which is embedded in the primary disk, as shown in Fig. 13. The figures show the comoving velocity field, $\boldsymbol{v} - v_{\phi,\mathrm{bg}}\boldsymbol{e}_\phi$, where $v_{\phi,\mathrm{bg}}$ is the angular velocity profile of the primary disk. In Fig. 13a, we observe a typical secondary disk, with the densest and hottest region (fragment) in its center. We also observe how converging flows form spiral arms. Converging flows form frequently when shearing and turbulent motion (due to activity of fragments and other spiral arms) produce a region with a net outward flow that encounters the inward radial flow from global mass transport.

Spiral arms in secondary disks can also be drifted off the fragment, a phenomenon exemplified in Fig. 13b: the spiral arm encounters a decelerating inward flow that makes it drift apart. As a result, the calculated mass plot (Fig. 9) shows a decrease because the mass of the spiral arm is lost from the fixed integration domain used. If the spiral arms are bounded to the fragment, the plotted mass of the fragment only shows an oscillation, but frequently the spiral arm gets absorbed by other spiral arms, provoking a real mass loss in the fragment with a consequent temperature variation over time. This mechanism provides a way to transfer some matter from fragments back to the disk or the central massive protostar. This process can also trigger fragmentation, as was the case of the spiral arm that gives rise to fragment 59 shown in Fig. 6A4.

Figure 14 shows the vertical structure of a fragment using the highest resolution dataset. When the fragment is forming (Fig. 14a), it has an approximately spherical shape. However, Fig. 14b shows the vertical structure of the secondary disk shown in Fig. 13b: the fragment indeed gets flattened down, with the highest density in the center.

### *6.8. Comparison to observations*

#### 6.8.1. G11.92–0.61 MM 1

Observations of the massive young stellar object G11.92–0.61 MM 1 reported in Ilee et al. (2018) show a fragmented Keplerian disk around a proto-O star. The main object, MM1a, is reported to be ∼40 $M_\odot$ (with between 2.2 and 5.8 $M_\odot$ attributed to the disk, and the rest to the protostar), and the fragment MM1b is reported to be ∼0.6 $M_\odot$, located at around ∼2000 au from MM1a.

This seems to be especially compatible with the general results in run x8, but later in time (the disk reported in the observations is bigger, and the central star is more massive). However, there are several warnings that should be taken into account. From the results in Ilee et al. (2018), the mass ratio of the disk and the primary is between 0.055 and 0.145. In our simulations, the mass of the central massive protostar at ∼16 kyr is ∼20 $M_\odot$ (cf. Fig. 19). We calculated the mass of the disk including the fragments and spiral arms (integration of density in a cylinder of 1500 au in radius and 20 au in height), and the mass of the background disk. The mass of the disk including substructures is comparable to the mass of the primary, as expected from a fragmenting disk; however, if substructures are excluded, the mass of the disk increases more slowly. After ∼16 kyr, the mass of the background disk is ∼5 $M_\odot$, which means a mass ratio of ∼0.25. In addition, the surviving fragment (94) in run x8 is located at ∼1500 au from the primary, although at the end of the simulation it is moving outwards. The mass of fragment 94 is of the order of a few solar masses, although this value includes the mass of the secondary disk.

Given that the masses of most of the fragments produced in our simulations are of the order of 1 $M_\odot$, and given the position and size of the disk both reported here and in the observations, we think that the scenario described in Ilee et al. (2018) could plausibly be obtained with a setup similar to ours.

#### 6.8.2. Accretion burst event in G358.93-0.03

Disk substructures associated to an accretion burst were observed and reported in Chen et al. (2020) for the high-mass young stellar object G358.93-0.03. The flaring event was reported in Sugiyama et al. (2019). Chen et al. (2020) performed a kinematic model that describes the accretion flow as occurring along two spiral arms, although they also acknowledge the compatibility of their observations with the accretion of a fragment.

A&A 644, A41 (2020)

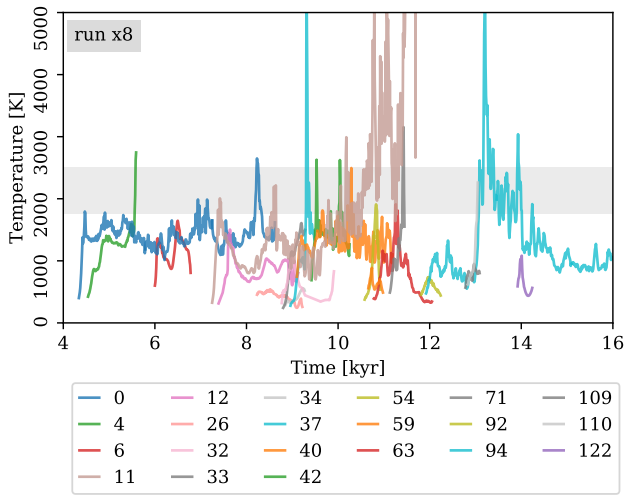



**Fig. 15.** Temperature of the fragments with lifespan longer than 200 yr, for run x8. The gray box indicates the hydrogen dissociation limit.

The results of our simulations support the second scenario, as do the results in Meyer et al. (2017, 2018). The processes described in Sects. 6.5, 6.6.1, and 6.6.2, namely the gravitational interactions between fragments (as exemplified in panel B4 of Fig. 11), and the gravitational torques exerted by the spiral arms can cause the fragment to lose angular momentum, leading to accretion by the primary, and thus an accretion burst.

## 7. Companion formation

As fragments contract by their self-gravity, their temperatures increase, which in turn causes an increase in their internal pressure, halting the collapse (classical Kelvin-Helmholtz contraction). However, fragments whose central temperature goes beyond ≈2000 K start to experience hydrogen dissociation, which means that gravitational energy is not converted into thermal kinetic energy, but rather is used to dissociate hydrogen molecules, therefore allowing for further (second) collapse, until a second Larson core is formed.

The exact temperature for hydrogen dissociation is density-dependent; we verified that for the central densities of the fragments, the temperature is between 1700 K (10% dissociation) and 2300 K (90% dissociation) (D'Angelo & Bodenheimer 2013). According to Bhandare et al. (2018), second Larson cores formed from reservoirs of a few solar masses have radii of the order of a few solar radii. Based on the free-fall timescale of a fragment of a few solar masses, we use the conservative estimate of 80 yr for the duration of the second collapse. After the second core is formed, contraction continues to drive the temperature up, continuing the evolution of the protostar.

The simulations presented here do not include hydrogen dissociation. However, by tracking the central temperature of a fragment, one can determine if it should undergo second collapse and form a second core. This allows us to hypothesize the ultimate fate of the fragments if more realistic physics were considered.

### 7.1. Central temperature of the fragments

Figures 15 and 16 show the tracked central temperature of the fragments as a function of time, for runs x8 and x16, respectively. The shadowed box shows the threshold for hydrogen dissociation, which, as mentioned above, is not included in our simulations. This is why we see high temperatures and fragments crossing the threshold both ways over time. In both figures, we see some high and short-lived spikes in the central temperature, which are the result of rapid mass increase, for example due to mergers or accretion onto the fragment. The small periodic variations of the temperature are caused by the interactions between the fragments and their environment, including the development of secondary spiral arms. The mechanism of secondary spiral arm drift explained in Sect. 6.7, which produces a lowering in the mass of the fragment, also produces a lowering in its temperature (due to decompression). The variation of the observed central temperature of the fragments with resolution is discussed in Sect. 8.2.

Longer lived fragments tend, in general, to have higher temperatures of at least ∼1000 K. Fragments formed later in time tend to also reach higher central temperatures, because they have more mass (cf. Sect. 6.3).

Fragments that cross the hydrogen dissociation temperature threshold undergo second collapse and become second cores. As a reference, we count the number of fragments that have a temperature higher than ∼2000 K for a time longer than ∼80 yr, which is our estimate of the time needed to form a second core. In run x8, four second core objects are formed, and in run x16, ten second core objects are formed.

### 7.2. Fate of the fragments

Only after the second collapse has taken place would a fragment reduce its radius from the order of a few astronomical units to a few stellar radii. However, merely from the data provided by the simulations presented here, it is impossible to know whether or not the temperature continues to rise after the second collapse and whether or not the second cores become actual companion stars. Nevertheless, one point to take into account is that many fragments develop secondary disks, which means that after the second collapse, more mass can be delivered to the second core and potentially allow a temperature increase and continuation of the evolutionary process.

Fragments of sizes of a few solar radii would be unresolvable with our current simulation setup. However, since their compactness would also provide stability, it would be safe to add a sub-grid particle model in order to study their behavior. However, before the second collapse happens, fragments are mere hydrostatic cores with strong interactions with the disk, spiral arms, and other fragments, and some of these interactions are strong enough to destroy them. The following sections describe these mechanisms, and consider the effects that our simulation setup with a central sink cell have on the number of companions that are formed according to the simulations.

#### 7.2.1. Fragment destruction mechanisms

Fragments that move in an eccentric orbit near the central primary protostar with high speeds experience shearing, which typically causes their destruction, as illustrated in panel A1 of Fig. 17, and exemplified by panel A2. A similar process can be found in simulations of fragmentation in protoplanetary disks, as described in Lichtenberg & Schleicher (2015). It is also common in this scenario that some matter of the fragment gets accreted by the central protostar, sometimes forming a "ring-like" accretion structure like the one discussed in Sect. 5. However, in the particular example of panel A2, matter is not accreted. The sheared

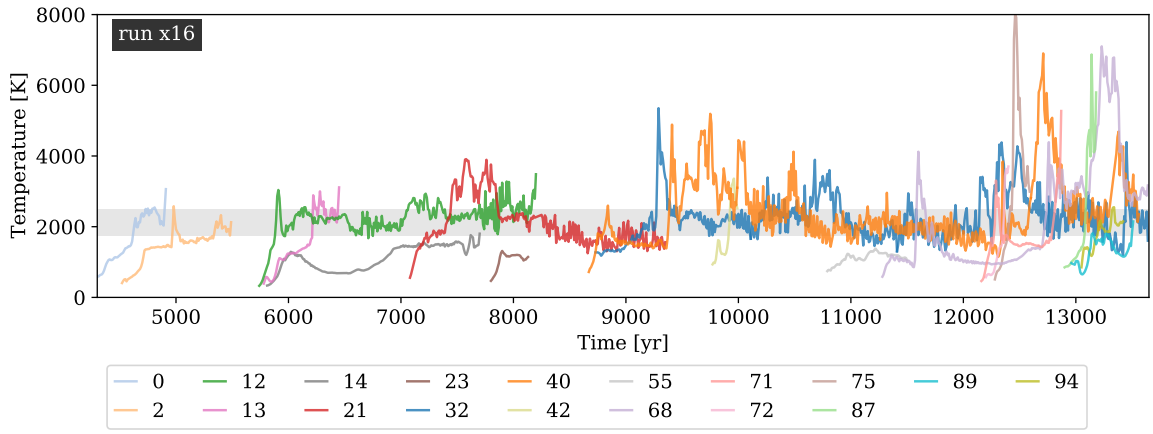



**Fig. 16.** Temperature of the fragments with lifespan longer than 200 yr, for run x16. The gray box indicates the hydrogen dissociation limit.

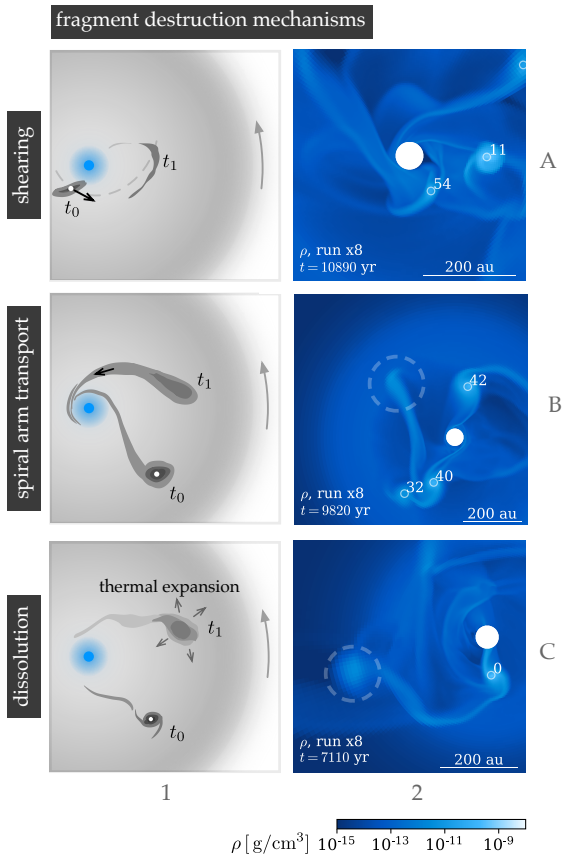



**Fig. 17.** Fragment-destruction mechanisms.

material expands and becomes absorbed by spiral arms, providing converging flows needed for further fragmentation according to the mechanisms discussed above.

Spiral arms can also cause mass loss from the fragment by transporting matter along them (Fig. 17B1), eventually destroying the fragment. As an example, fragment 43 of run x8, shown in panel B2, is drained by a spiral arm that is being stretched, and delivers the material to fragments 32 and 40.

Another fragment-destruction mechanism occurs as a consequence of temperature flashes associated with accretion bursts (described in Sect. 6.6.2). Fragments and spiral arms are heated up by the temperature flash. This triggers thermal expansion, which in turn lowers the density and central temperature of the fragment, compared with the values before the flash. If the fragment already has a low temperature and density, this thermal expansion and cooling can take the fragment below the detection threshold. After manually following the remaining matter, we see that it gets partially dissolved into the disk, absorbed into a spiral arm, absorbed by other fragments, or is sheared apart. An example of this behavior is provided by panels C1 and C2 of Fig. 17.

These destruction mechanisms severely affect the lifetime of fragments if they are in their hydrostatic core phase, and show that sub-grid sink particle models may overestimate the number of formed companions. Only by resolving the substructure of the fragments do these interactions become apparent.

### 7.2.2. Fragment dynamics after the second collapse

Once a second core is formed, the question arises as to how such an object will interact with the environment, and therefore, how the fragment destruction and merger mechanisms discussed above will impact the fate of a fragment. Although second cores would experience the same gravitational interactions as a hydrostatic core, they would not experience the same pressure gradient from the rest of the gas due to their compactness. A second core would have less probability of colliding and merging with another second core because of the reduction in the collisional cross section. A merger between a first core and a second core is a possible scenario: the first core would likely be sheared apart, and would form a denser secondary accretion disk around the second core, ultimately being accreted by the latter.

### 7.2.3. Formation of spectroscopic multiples

As mentioned in Sect. 4, one disadvantage of using a central sink cell is the inability to distinguish between accretion and the formation of close companions. This is especially true for fragments that have undergone second collapse, and therefore do not suffer the destruction mechanisms mentioned above. Once a fragment enters the numerical sink cell ($r$ = 30 au), its mass is counted as being accreted by the central massive protostar, when in reality, if the fragment is a second core, it might be in an orbit instead of a merger with the primary.

A&A 644, A41 (2020)

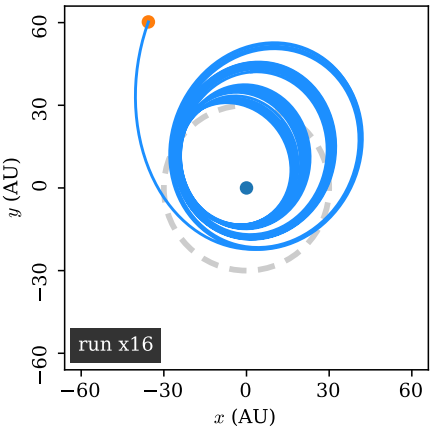



**Fig. 18.** Integrated orbit of fragment 2 of run x16 after it enters the numerical sink cell. The orange dot indicates the initial position of the fragment, and the total time integrated was 3 kyr. The sink cell (dashed circle) has a radius of 30 au.

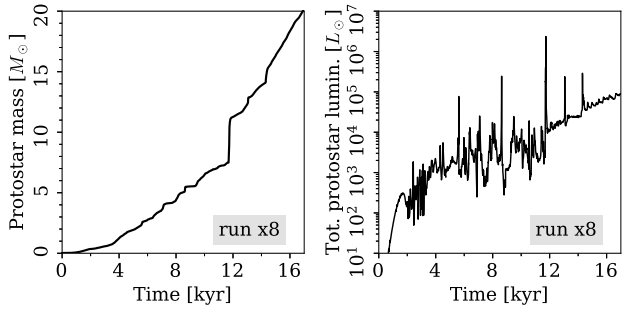



**Fig. 19.** (*a*) Mass and (*b*) luminosity of the central massive protostar, as formed in run x8.

Migration and gravitational interactions with other fragments are some of the responsible mechanisms for getting a fragment into an orbit closer to 30 au (the radius of the sink cell). In order to study the possible fate of a second core, we integrated the orbit of fragment 2 of run x16 (Fig. 18), which undergoes second collapse shortly before it enters the sink cell. In the integration, we considered the gravitational force of the central massive protostar and the gravitational force of the background disk, but no other interactions. Fragment 2 was originally dragged into the sink cell by gravitational torques arising from spiral arm interaction. The predicted integrated orbit is elliptical, and it gets smaller in time because of the increase in mass of the central massive protostar. Some "jumps" can also be seen in the orbit, which are caused every time the central massive protostar accretes (non-second core) fragments, that is, when its mass suddenly increases by a discrete amount. After 3 kyr of integration, the orbit of the fragment has a periastron of ∼15 au. At the time, the simulation is at $t = 7.9$ kyr, and the mass of the central protostar is $\sim 4\,M_\odot$. As time progresses and the central protostar becomes more massive, the orbit of the fragment should become smaller and smaller, thus providing a mechanism for the formation of spectroscopic multiples.

### *7.3. Implications*

#### 7.3.1. Accretion bursts

In run x8, fragment 11 reaches the hydrogen dissociation temperature at 10.22 kyr and would undergo second collapse if the simulation had implemented it. At the time, the mass of the fragment is $1.8\,M_\odot$. At 11.47 kyr, fragment 11 then merges with fragment 71, which greatly increases the temperature (cf. Fig. 15), and its mass briefly reaches $5\,M_\odot$. This would be an example of a second core merging with a hydrostatic core, and we would expect, in a more realistic setup, that fragment 11 would at least partially accrete the material from fragment 71 through the secondary accretion disk. However, the interaction between fragments 11 and 71 alters the orbit of fragment 11 and it ultimately reaches the sink cell. On the other hand, a second core entering the sink cell might produce a companion instead of an accretion event. For the plots of run x8 presented in this paper, this means that, at $t \sim 11.5$ kyr, (i) the high peak in the accretion rate (Fig. 4f), the $\gtrsim 10^6\,L_\odot$ accretion burst shown in Fig. 19b, and the bump in the mass of the central massive protostar (Fig. 19a) might not take place; and (ii) the subsequent inner disk overdensity that arises in the radial profiles for run x8 (Figs. 4a, b and e) during the interval [12, 16[ kyr as a result of the shearing and accretion of fragment 11 might not be there.

According to the preceding discussion, very high luminosity bursts are less likely to occur than what is shown in Fig. 2b, because they require the accretion of a significantly large mass in a short time. Fragments that have the required mass have most likely undergone a second collapse, and, according to the integrated orbits we presented above, they will likely form close companions instead of being accreted. The possibility that a second core be accreted is not excluded, but it should be rare based on collisional cross section considerations.

#### 7.3.2. Number of companions

Taking into account the preceding elements, we summarize here the results of our simulations regarding companion formation. There are four second core objects produced in run x8. From them, one (fragment 94) survives in the outer disk ($r \sim 1400$ au at the end of the simulation). Fragments 0 and 11 form close companions, and fragment 37 merges with another fragment (so its fate is unclear from our simulations).

In run x16, ten second core objects are produced. Fragments 0, 12, and 13 form close companions, and fragments 40, 32, and 68 survive the simulation in the middle region of the disk (see discussion in Sect. 6.5). The rest merge with other fragments, and therefore, again, their fate is uncertain from our simulation.

By analyzing which of the fragments that get close to the central massive protostar produce accretion bursts indeed, and which ones satisfy the conditions for further stellar evolution, we find that the number of possible close companions produced in our simulations is low. This result is consistent with observations of more evolved systems, such as Sana et al. (2012), Kobulnicky et al. (2014), and Dunstall et al. (2015), where spectroscopic binaries or multiples are present in large fractions, but they also do not observe tens or hundreds of spectroscopic companions to a central massive star. Nevertheless, our results show that companions produced by disk fragmentation can also exist at distances of the order of 1000 au astronomical units (although inward and outward migration is still possible in the long term). We also note in this comparison that the masses of the fragments given in the preceding sections are not necessarily an indication of the masses of the future companions, as accretion is still ongoing at the end of our simulations.

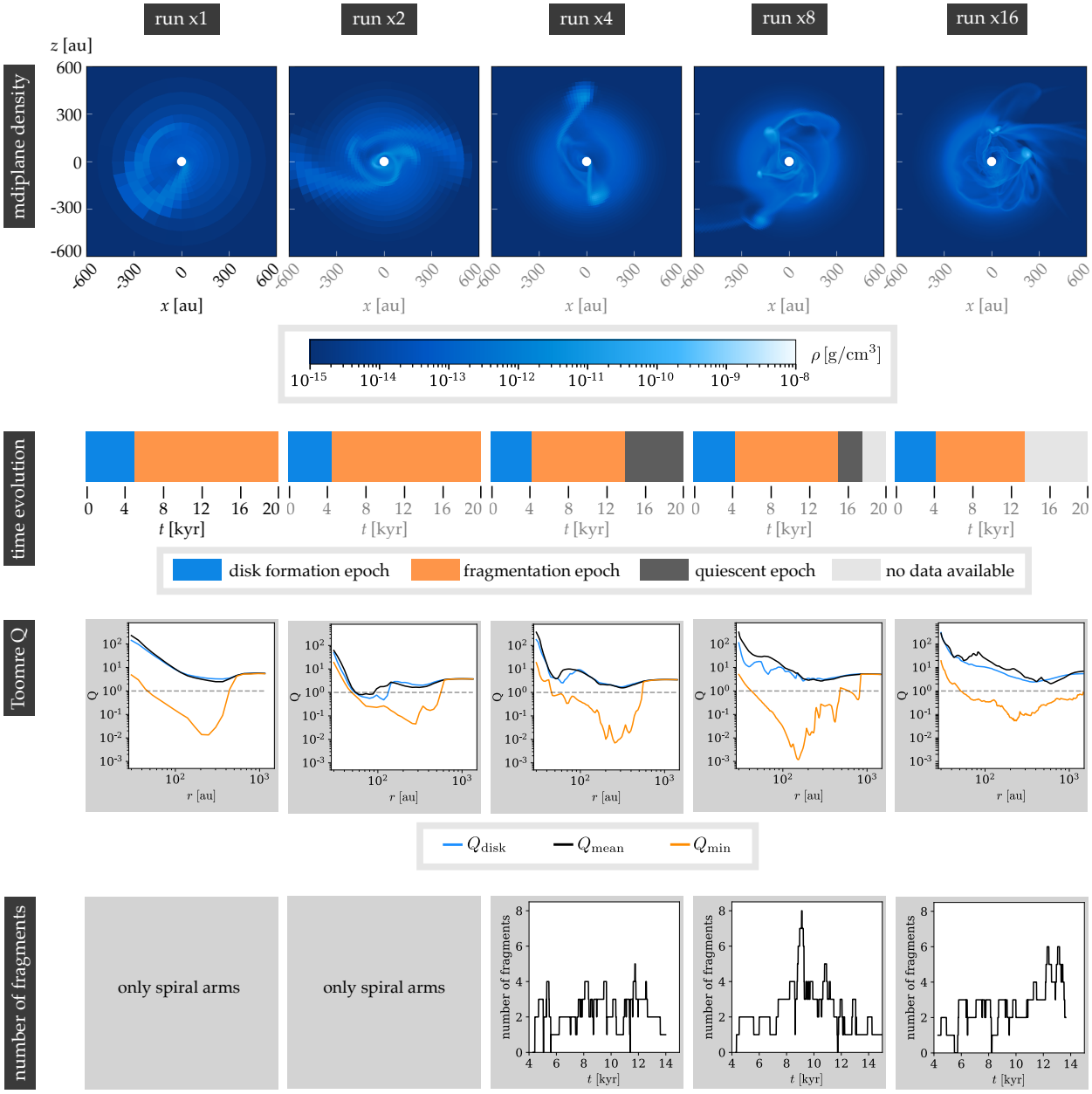



**Fig. 20.** Convergence of different quantities with resolution. The midplane density data were taken at $t = 7\,500$ yr for all the maps in the row. The Toomre Q was time-averaged during the fragmentation epoch.

## 8. Resolution effects

After describing the main results, the focus of the following section is to describe how these change with resolution by comparing five runs with different spatial resolution.

### 8.1. Convergence of fragmentation

Here, we refer to the panels in Fig. 20. The midplane density maps (Fig. 20) show that only spiral arms are produced in runs x1 and x2, but no fragments. By no fragments we mean that our conditions for fragment detection are not met, and that the shape of the substructures formed (regions of higher density than the background disk) is difficult to be recognized as a fragment because of resolution. Runs x4, x8, and x16 produce fragments and spiral arms. Runs x1, x2, and x4 show thicker spiral arms than runs x8 and x16, probably as a result of numerical diffusion. Substructure formation in runs x1 and x2 continues until the end of the simulated time, that is, the evolution of the system does not drastically change over time. In contrast, a quiescent epoch with no further fragmentation is observed in runs x4 and x8. Due to computational costs, data for run x16 are not available beyond $t = 13.5$ kyr, which prevents us from confirming the existence of a quiescent epoch in that run as well. In summary, only the runs with sufficiently high spatial resolution exhibit an end to the fragmentation epoch.

The Toomre $Q$ parameter shows a similar behavior for all resolutions. We see in Fig. 5 that the value of $Q$ for fragments

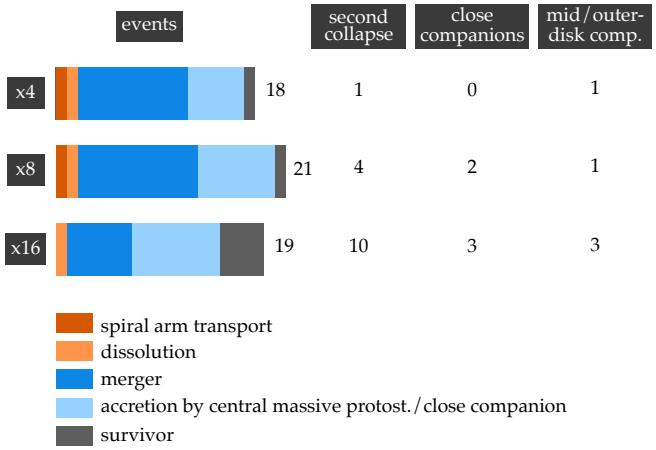



**Fig. 21.** Fragment statistics for the fragment-producing runs. The charts show the fate of the fragments with a life longer than 200 yr according to the simulation, that is without taking into account the effects of the inner boundary and hydrogen dissociation, as discussed in Sect. 7.2. The estimated number of these fragments that undergo second collapse is given in the right-hand column.

and spiral arms, corresponding to the $Q_{\rm min}$, reveals the susceptibility of these areas to fragmentation, but the background disk and mean values (expected to be dominant in underresolved observations) show the system as Toomre-stable.

The number of fragments present at a given time in the simulation that live longer than 200 yr is also similar, except for the peak of eight fragments seen in simulation x8, which is discussed above. The average number of fragments at a given time during the fragmentation epoch is around 2.2. The tendency of longer lived fragments to be created at larger radial positions with time is also observed in the other simulations, although not shown here.

### 8.2. Convergence in the properties of the fragments

The fate of the fragments without taking into account the effects of the inner boundary and hydrogen dissociation we discussed in Sect. 7.2 are shown in Fig. 21. Mergers and shear/accretion into the sink cell dominate the mechanisms of fragment destruction. Spiral arm matter transport and dissolutions are far more rare.

Comparing Figs. 15 and 16, the central temperature of fragments gets higher with resolution. From this, the number of fragments that get to the second collapse phase increases from run x8 to run 16, but remains in the same order of magnitude. In Bhandare et al. (2018) (Fig. 2c), the temperature profile of a first core shows that the maximum temperature is reached at a radius of ∼1 au. Run x16 has a resolution of $\lesssim$1 au at $r \lesssim 100$ au, which might indicate that the values of the central temperature for fragments in the inner disk are close to convergence.

The statistics of fragment interactions show that independently of resolution, fragments in a hydrostatic core stage are fragile, and it is not safe to include them in a particle sub-grid model if they do not reach second core status, for which the correct resolution is needed. As already discussed in Sect. 6.3, the masses of the fragments for runs x8 and x16 are similar, and although not shown here, the masses of the fragments produced in run x4 also have consistent values.

Fragments in the outer disk, as exemplified by fragment 94 of run x8, tend to have higher masses, and therefore higher probabilities of reaching the temperature required for a second collapse. However, the spatial resolution of the numerical grid is lower in the outer disk (for run x8, the cell size is ∼20 au at ∼1000 au); and although we show in Sect. 9.2 that, at that radial distance, this is enough to resolve the Jeans length and therefore the formation of fragments, it is not enough to resolve the substructure of the fragments. Therefore, fragments located at $r \gtrsim 1000$ au have radii that are artificially higher due to numerical diffusion, even when not considering the physics of the second collapse. A larger radius makes the fragment less gravitationally bound, and filaments and secondary spiral arms are developed between the fragment and the central massive protostar. These structures fragment and the fragments migrate rapidly inwards and produce accretion bursts in the late stages of runs x4 and x8 during the quiescent epoch; but we believe this effect to be mainly numerical. Thanks to better spatial resolution, we can see that fragments produced in run x16 have more consistent sizes across the disk.

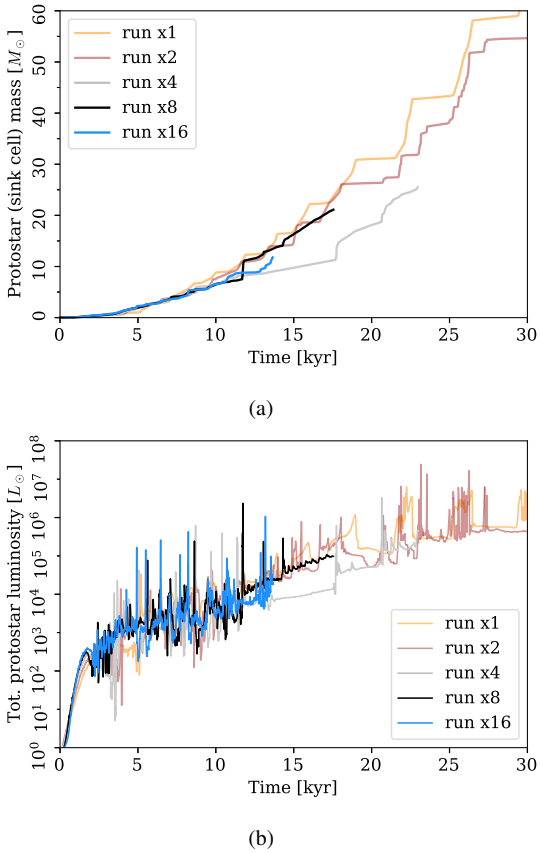



**Fig. 22.** Convergence of the properties of the formed protostar.

### 8.3. Convergence of the formed massive protostar

During the simulation, several properties of the central massive protostar are calculated under several assumptions. Figure 22 shows the mass and total luminosity. We remind the reader that the mass of the central protostar is simply the mass of the sink cell, and the total stellar luminosity is the sum of the accretion luminosity (total conversion of gravitational potential energy of the accreted material into radiation) and the stellar luminosity calculated following the evolutionary tracks of Hosokawa & Omukai (2009) (which depend on the mass of the protostar and the accretion rate).

Figure 22a shows only qualitative convergence in the protostellar mass after ∼11 kyr, because it depends heavily on how the material is accreted in each simulation, and this in turn depends on the fragmentation that is developed in time. Figure 22b shows that the total luminosity curves are similar for all simulations: all feature some accretion bursts and a general increase in time due to the contribution of stellar evolution. The plots for runs x4 and x8 also show a general reduction in accretion bursts at the end of the simulated time (quiescent epoch), except for some bursts caused by the effect discussed in Sect. 8.2, that is, triggered by fragments in the outer disk. There is no quiescence observed for runs x1 and x2. We also find that the central massive protostar starts burning hydrogen at ∼12 kyr for runs x16 and x8, ∼18 kyr for run x4, and ∼16 kyr for runs x1 and x2.

## 9. Comparison with previous studies

### 9.1. Overview

Several studies on massive star formation, including cloud and disk fragmentation, have been performed over the years. We summarize some of them in this section and compare their outcomes and main features in the following sections.

First, we discuss some studies on cloud fragmentation. Girichidis et al. (2012) performed several gravito-hydrodynamical simulations to study a collapsing cloud under the fragmentation-induced starvation scenario without radiation transport, an AMR grid of a minimum size of 13 au, and sink particles. In these simulations, various initial density profiles were used, together with a supersonically turbulent initial velocity profile but no rotation. These latter authors find between 161 and 429 sink particles in total; some of their simulations show filamentary accretion, and some the formation of an accretion disk.

Peters et al. (2010, 2011) used the code FLASH to study the effects of magnetic fields and ionizing radiation in a large-scale collapsing cloud of 1000 $M_\odot$, neglecting the thermodynamics of dust re-emission, that is, continuum radiation transport was not taken into account. Both studies used AMR with a minimum cell size of 98 au, and sink particles. However, according to our results, these sink particles could not be comparable to our fragments, since their accretion radius of ∼400 au is at least one order of magnitude bigger than the size of a fragment with the potential of forming a companion, and more comparable to the size of the whole primary accretion disk, that is ∼400 au in radius in the middle of the fragmentation epoch. With no magnetic field, around 25 sink particles were created; the presence of magnetic field reduced fragmentation by around a factor of two, and generated a more massive protostar due to magnetic braking. Similar results were obtained by Hennebelle et al. (2011), where the RAMSES code was used to study a cloud of initial mass 100 $M_\odot$ and radius of 1.35 pc. These latter authors used AMR with a minimum cell size of 8 and 2 au for their low- and high-resolution runs, respectively, and no sink particles, but used the barotropic equation of state. The number of fragments obtained is of the order of 50 without magnetic field.

The following studies also considered disk formation and fragmentation. In Krumholz et al. (2007, 2009), three-dimensional gravito-hydrodynamical simulations were performed, with a gray flux-limited diffusion approximation for stellar radiation as well as radiation by the dust. The first study dealt with the collapse of a core in initial supersonic shock-dominated turbulence, while the latter consiered solid-body rotation without any initial turbulence. Both studies used sink particles following the Jeans criterion only. In the turbulent case for an initial mass of 200 $M_\odot$ (Krumholz et al. 2007), the spherical cloud forms filaments that feed two clumps that ultimately become one massive protostar with an accretion disk that fragments into spiral arms, but no further fragmentation; however, three sink particles are independently formed at around 3000 au from the primary. With regards to fragmentation, in Krumholz et al. (2009), the disk forms earlier, and ultimately the system develops into a binary with a separation of ∼1500 au. Both simulations used the code Orion, with an AMR grid with a maximum resolution of 10 au.

Klassen et al. (2016) used the FLASH code with an improved treatment of radiation transport, and an AMR grid with a minimum cell size of 10 au. The cloud was initially in solid-body rotation, and masses of 30, 100, and 200 $M_\odot$ were considered. They used a stricter sink particle algorithm that, in addition to the Jeans criterion, checks for a convergent flow, a gravitational potential minimum, and a negative total energy. The use of this criterion with the resolution considered leads to no fragmentation at all; only the formation of spiral arms was observed.

Rosen et al. (2016) repeated the simulations for both the initially laminar and highly supersonic turbulent cases, including a hybrid radiation transfer method that properly treats the multi-frequency stellar irradiation and gray flux-limited diffusion thermal re-emission (Rosen et al. 2017), but the maximum resolution of their AMR grid was 20 au. Their sink particle algorithm detects 29 companions, 16 with masses >0.1 $M_\odot$ for the laminar case, and 3 companions for the turbulent case. In both cases, an accretion disk with spiral arms is formed around the massive protostar, but in the turbulent case the disk becomes eccentric. Contrary to Krumholz et al. (2009), the system does not form a binary (in part due to different sink particle merging criteria). Initially, in the turbulent case the massive protostar is fed primarily by filaments, but the accretion rate is not significantly different from that in the laminar case. A similar setup was used by Rosen et al. (2019) to study the role of turbulence in fragmenting cores with initially virial and subvirial initial conditions. These latter authors find that virialized cores undergo significantly more turbulent fragmentation at early times than subvirial cores. In both cases, a fragmenting accretion disk was formed.

Meyer et al. (2017, 2018) used Pluto with a similar setup to ours, that is, a fixed spherical grid with the radial coordinate increasing logarithmically. They also used the same radiation transport scheme, but lower spatial resolution. In Meyer et al. (2018), several initial angular velocity profiles were examined for fragmentation, specifically $\beta_\Omega = 0$, $-0.35$, and $-0.75$. These latter authors found formation of spiral arms followed by fragmentation; the highest number of fragments was obtained for $\beta_\Omega = -0.75$. It was proposed that fragmentation might explain the high spectroscopic binary fraction of massive stars. Accretion bursts were observed in Meyer et al. (2017, 2018, 2019). Meyer et al. (2019) also studied the effects of disk wobbling during the fragmentation epoch.

### 9.2. Resolution of the grid and the use of sink particles

In order to check whether or not a simulation is resolving the correct scales associated with the physical phenomena described, we computed the pressure scale height of the disk and the Jeans length using the data from run x16, averaged over the time period [6, 8] kyr, which corresponds to the fragmentation epoch. The pressure scale height gives an idea of the scale of the vertical structure of the disk, and it is defined in the midplane as

$$\frac{H_{\rm disk}}{r} = \frac{c_{\rm s}}{v_\phi}, \tag{16}$$

A&A 644, A41 (2020)

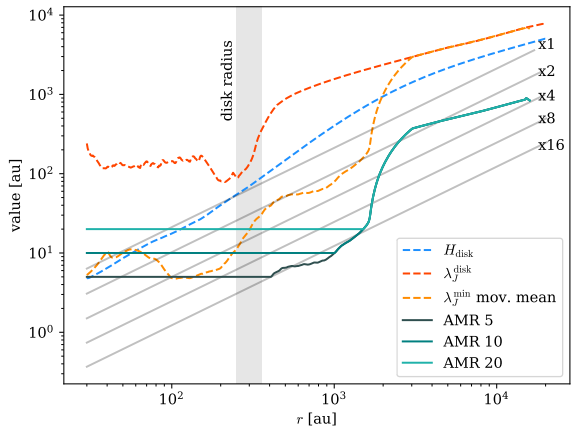



**Fig. 23.** Comparison of midplane grid cell sizes in our fixed grid and other studies that use AMR. The different relevant scales of the system are shown as dashed lines; these were calculated as averages for the time period [6,8] kyr, and the corresponding disk radius is shown in the gray box. The number following the label for the AMR curves indicates the minimum cell size in astronomical units.

where $c_{\rm s}^2 = \gamma\, \partial P/\partial\rho$ is the sound speed. The Jeans length $\lambda_{\rm J}$ indicates the size of a region that becomes gravitationally unstable at a certain density $\rho$ and temperature, and is calculated as

$$\lambda_{\rm J} = c_{\rm s}\sqrt{\frac{\pi}{G\rho}}. \tag{17}$$

In order to adequately study fragmentation numerically, the Jeans length has to be resolved properly. In order to study a Jeans length radial profile, we separate it into two values: the Jeans length of the background disk $\lambda_{\rm J}^{\rm disk}$, calculated with the median values (as described in Sect. 4), and the minimum Jeans length, $\lambda_{\rm J}^{\rm min}$, which corresponds to the value of the most fragmentation-prone areas of the disk, that is, the fragments and spiral arms.

Figure 23 contains the radial profiles of these quantities, which were calculated using the data from run x16 and time-averaged during the period between 6 and 8 kyr. The disk radius is also shown for reference. Additionally, the cell size of our simulations, $\Delta x(r)$, is shown for each run (gray lines).

The pressure scale height scales approximately linearly with distance, giving an ansatz on the required cell size needed to resolve the vertical structure of the disk. The cell size of our logarithmic grid also scales linearly with distance. As a result of the simulation, we obtain $H(r) \approx 0.12 r^{1.07}$ on the disk region, and a comparison with the different runs allows us to conclude that $H$ is resolved by all of them, but only partially by x1.

The Jeans length decreases with increasing density, which means that it increases with distance. Our choice of the coordinate grid then makes possible a better resolution of the Jeans length while saving computational power. The Jeans length for the background disk is resolved by all runs, and indeed we observe some sort of structure formation (spiral arms and/or fragments) in all runs. However, when observing the curve for the minimum value of the Jeans length, it is clear that only runs x8 and x16 are able to resolve fragmentation adequately, and run x4 only partially resolves fragmentation, which coincides with the results found in the convergence study presented in Sect. 8.

In order to compare the results from other studies, we establish approximate equivalences between the different grids used. In the case of the fixed grids used in Meyer et al. (2017, 2018, 2019): (a) Meyer et al. (2018) use approximately the same grid structure as our run x4 (except in their "Run 1-HR", where the grid used is almost our run x8); (b) Meyer et al. (2017, 2019) use a grid comparable with our run x4.

A direct comparison of our fixed grid with AMR implementations is not trivial, because they are dependent on the selected refinement criteria and the particular evolution of the system. In order to present a panorama of the resolution differences, we take the criteria given in for example Rosen et al. (2016), that is, a Jeans length should be resolved by at least eight cells. The resulting profiles are shown in green in Fig. 23, where if eight Jeans lengths cannot be resolved, the maximum refinement is plotted.

We now examine the disk region. According to our results, the minimum Jeans length is only marginally resolved by an AMR simulation that has a minimum cell size of 5 au. Even in that case, our simulations provide much more detail, especially in the region 100 au $\lesssim r \lesssim$ 600, where according to Fig. 7b we observe the biggest number of long-lived fragments being created. This choice has allowed us, as we have shown in the results, to study even the interactions between fragments and their internal structure, and not merely to resolve where a fragment should be created by the Jeans criterion.

Based on these considerations, we can establish that an AMR grid with a minimum cell size of 5 au provides a resolution between those of runs x16 and x8 for the outer disk, but with a resolution similar to or lower than that of run x4 for the inner disk ($r \lesssim 100$ au). A minimum cell size of 10 au corresponds to a resolution that is between those of runs x8 and x4 for the outer disk, but is equivalent to that of run x2 for the inner disk. A minimum cell size of 20 au provides a resolution that is between those of runs x4 and x2 for the outer disk, but that is similar to or lower than that of run x1 for the inner disk.

Studies that use a sink particle algorithm typically use the Jeans density as the main criterion for particle creation. This is the case in, for example, Krumholz et al. (2009, 2007), Rosen et al. (2016), Peters et al. (2010, 2011). As mentioned above, a self-consistent treatment of the fragmentation process – in contrast to a sink particle algorithm – provides more certainty in the number of fragments formed, and, as we show here, in the number of fragments that survive the fragmentation process and can become companions. We also show that fragments, while in the hydrostatic core phase, undergo several interactions that can lead to their destruction, and they need to reach a second core status in order to be safely replaced with a sink particle. The use of sink particles for hydrostatic cores additionally misses the formation of the smaller secondary disks, and the fact that their associated spiral arms can occasionally give rise to new fragments.

The fact that AMR grids with minimum cell sizes of 20 au and 10 au do not adequately resolve the Jeans length, in addition to the fact that we do not observe fragmentation in runs x1 and x2, suggests that sink particles created in simulations that use such grids, although representing regions of high density, do not (necessarily) represent physical local collapse. This means that companions produced in this way are due to purely numerical effects, and therefore we do not recommend the use of a sink particle algorithm in multiplicity studies if not used in conjunction with a grid of adequate resolution.

### 9.3. Additional physical effects

Contrary to our setup, the simulations from Krumholz et al. (2009), Rosen et al. (2016) (laminar), and Klassen et al. (2016) do not restrict the motion of the central massive protostar via a fixed sink cell. However, these studies show qualitatively that if the system forms a disk, the central massive protostar does not

excessively move from the center. This was studied in more detail and confirmed in Meyer et al. (2019), where the authors implemented disk wobbling and found no dramatic differences when treating the massive protostar as fixed during the fragmentation period.

With regards to the initial density profile, studies that consider a constant density profile (e.g., Peters et al. 2010, 2011; Girichidis et al. 2012) find that the cloud forms many disperse fragments, while clouds with power-law density profiles (e.g., Girichidis et al. 2012; Rosen et al. 2016; Meyer et al. 2018, and this work) are dominated by a central object, with increasingly less fragmentation as the profile steepens. Observational studies (e.g., Beuther et al. 2002; van der Tak & Menten 2005; Palau et al. 2014) typically find density slopes $\beta_\rho$ of between $-1.5$ and $-2.6$.

From the studies considered in Sect. 9.1, Girichidis et al. (2012), Rosen et al. (2016), Hennebelle et al. (2011), and Krumholz et al. (2007) performed simulations with supersonic initial turbulence, while Krumholz et al. (2009), Rosen et al. (2016), Peters et al. (2010, 2011), and Klassen et al. (2016) considered solid-body rotation. Furthermore, Meyer et al. (2018) offered a parameter scan for different initial angular velocity profiles, without turbulence. Highly supersonic turbulence leads to filamentary accretion that produces fragments with lower mass ratios to the most massive fragment, and are separated by longer distances than in a weakly turbulent cloud dominated by thermal Jeans fragmentation. The amount of turbulent fragmentation has been found to depend on the level of turbulence, with higher velocity dispersions leading to more fragmentation (Rosen et al. 2019; Fontani et al. 2018). Also, the most massive protostar moves considerably from the center of the cloud, although a (fragmenting) disk is formed in some cases (Rosen et al. 2016, 2019). The parameter scan in Meyer et al. (2018) revealed that a steep initial angular velocity profile such as the one used here produces more and earlier fragmentation.

Our choices for initial conditions are in agreement with the discussion in Beuther et al. (2018) and references therein. In that paper, observations of 20 high-mass star-forming regions showed that fragmentation is more consistent with the thermal Jeans fragmentation picture, and so low values of turbulence are expected.

Some of the studies mentioned in Sect. 9.1 consider the presence of magnetic fields. In general, the presence of magnetic fields is expected to reduce fragmentation. In Kölligan & Kuiper (2018), the effect of magnetic fields was studied in the context of high-resolution two-dimensional simulations of jet launching. Magnetic pressure was found to dominate the inner parts of the disk, and so we expect a more stable disk in these regions. This could also mean that fragmentation may be observed later in time, as the disk would need to reach a certain size to become unstable and fragment. Magnetic braking is also expected to reduce the size of the disk, and since we observe fragmentation in the outer disk, this can reduce the number of fragments. For more details on the role of magnetic fields on forming massive stars, see for example Commerçon et al. (2011b), Seifried et al. (2011) and Rosen & Krumholz (2020).

### 9.4. Accretion bursts

Meyer et al. (2017, 2019) describe the existence of accretion bursts, a phenomenon we have also observed in our simulations, in the same way. Nevertheless, our analysis of the mass of the fragments (see Sect. 7.3.1), their second collapse phase, and their possible final orbits leads us to conclude that strong accretion bursts of magnitudes $\gtrsim 4$ as described in Meyer et al. (2019) are unlikely to happen with the predicted frequency, because the masses needed for these events correspond typically to fragments that should have undergone second collapse and, because of the reduced collisional cross section, are less probable of being accreted directly by the central massive protostar, instead forming companions.

## 10. Summary and conclusions

We present the highest resolution, three-dimensional self-gravity-radiation-hydrodynamical simulations of a forming and fragmenting accretion disk around a forming massive star performed to date, incorporating stellar evolution, and dust sublimation and evaporation. The high resolutions achieved in this work mean that no sink particles are necessary to describe the fragments, which also has allowed us to study the fragmentation mechanisms, interactions, and the structure of fragments. A detailed analysis of the formation, interactions, and ultimate fate of the fragments is presented. For this analysis, sophisticated data post-processing techniques allowed us to track the masses and central temperatures of the fragments and their orbits. We also studied the further evolution of these fragments into companion stars by considering the conditions for the formation of second Larson cores.

The same simulation was run five times with varying resolutions. We studied convergence in our results, and verified that we properly resolve the disk pressure scale height and the Jeans length. Our findings can be summarized as follows:

- A growing accretion disk is formed around a central massive protostar.
- The disk forms spiral arms, and they in turn fragment.
- In the fragmenting disk, the Toomre parameter indicates that the disk is globally stable while being locally unstable, and therefore an insufficiently resolved disk may appear to be Toomre-stable while fragmentation is happening at lower scales.
- Fragments are highly dynamic; they form, interact, and can be destroyed, sometimes forming secondary disks with their own spiral arms.
- Secondary disks can also fragment.
- Fragments tend to have highly eccentric and chaotic orbits, which is due to their continuous interactions. However, they can also gain enough mass to be in more stable orbits and form companions in the middle or outer regions of the disk.
- The masses of the fragments are of the order of one solar mass once their central temperatures can reach the hydrogen dissociation limit (2000 K). Fragments that go beyond that temperature should form second Larson cores while others remain as hydrostatic cores.
- Fragments in general can migrate inwards; if they are hydrostatic cores, they might be accreted by the central massive protostar and create accretion bursts, and if they become second cores, they most likely would form spectroscopic companions.
- The number of fragments that survive the fragmentation epoch is $\lesssim 10$.
- Reducing resolution by a factor of two (run x8) does not significantly affect the overall picture of the results, except for the report of lower central temperatures in the fragments.
- When reducing resolution by a factor of four (run x4), the formation of secondary spiral arms is limited, and the fragments no longer achieve the required temperatures for secondary collapse.

– When reducing the resolution by a factor of eight (run x2), the formation of the primary disk and its spiral arms is recovered, but the fragmentation physics is no longer properly achieved.
– When reducing the resolution by a factor of sixteen (run x1), only the formation and growth of the primary disk is recovered, but its internal substructure can no longer be resolved.

With each level of higher resolution another aspect of the physics of disk fragmentation appears and remains for all simulations in even higher resolution. The two highest resolution runs agree on the disk properties, its morphology, and the onset of fragmentation, while showing only subtle differences in the central temperature of the forming fragments, which suggests convergence of the physical processes involved in fragmentation. However, only the highest resolution run shows the amount of detail in the smaller scales necessary to see the formation of hydrostatic cores, that may become future companions.

*Acknowledgements.* G.A.O. acknowledges financial support by the Deutscher Akademischer Austauschdienst (DAAD), under the program Research Grants - Doctoral Programmes in Germany. R.K. acknowledges financial support via the Emmy Noether Research Group on Accretion Flows and Feedback in Realistic Models of Massive Star Formation funded by the German Research Foundation (DFG) under grant No. KU 2849/3-1 and KU 2849/3-2. We thank the anonymous referee for their very valuable and helpful comments and suggestions.

## References

Ahmadi, A., Kuiper, R., & Beuther, H. 2019, A&A, 632, A50
Beuther, H., Schilke, P., Menten, K. M., et al. 2002, ApJ, 566, 945
Beuther, H., Henning, T., Linz, H., et al. 2015, A&A, 581, A119
Beuther, H., Walsh, A. J., Johnston, K. G., et al. 2017, A&A, 603, A10
Beuther, H., Mottram, J. C., Ahmadi, A., et al. 2018, A&A, 617, A100
Beuther, H., Ahmadi, A., Mottram, J. C., et al. 2019, A&A, 621, A122
Bhandare, A., Kuiper, R., Henning, T., et al. 2018, A&A, 618, A95
Caratti o Garatti, A., Stecklum, B., Garcia Lopez, R., et al. 2017, Nat. Phys., 13, 276
Cesaroni, R., Sanchez-Monge, A., Beltran, M. T., et al. 2017, A&A, 602, A59
Chen, X., Sobolev, A. M., Ren, Z.-Y., et al. 2020, Nat. Astron., in press, https://doi.org/10.1038/s41550-020-1144-x
Commerçon, B., Teyssier, R., Audit, E., Hennebelle, P., & Chabrier, G. 2011a, A&A, 529, A35
Commerçon, B., Hennebelle, P., & Henning, T. 2011b, ApJ, 742, L9
D'Angelo, G., & Bodenheimer, P. 2013, ApJ, 778, 77
Draine, B. T., Dale, D. A., Bendo, G., et al. 2007, ApJ, 663, 866
Dunstall, P. R., Dufton, P. L., Sana, H., et al. 2015, A&A, 580, A93
Fontani, F., Commerçon, B., Giannetti, A., et al. 2018, A&A, 615, A94
Ginsburg, A., Bally, J., Goddi, C., Plambeck, R., & Wright, M. 2018, ApJ, 860, 119
Girichidis, P., Federrath, C., Banerjee, R., & Klessen, R. S. 2012, MNRAS, 420, 613
Goodman, A. A., Benson, P. J., Fuller, G. A., & Myers, P. C. 1993, ApJ, 406, 528
Hennebelle, P., Commerçon, B., Joos, M., et al. 2011, A&A, 528, A72
Hosokawa, T., & Omukai, K. 2009, ApJ, 691, 823
Hunter, T. R., Brogan, C. L., MacLeod, G., et al. 2017, ApJ, 837, L29
Ilee, J. D., Cyganowski, C. J., Nazari, P., et al. 2016, MNRAS, 462, 4386
Ilee, J. D., Cyganowski, C. J., Brogan, C. L., et al. 2018, ApJ, 869, L24
Isella, A., & Natta, A. 2005, A&A, 438, 899
Johnston, K. G., Robitaille, T. P., Beuther, H., et al. 2015, ApJ, 813, L19
Johnston, K. G., Hoare, M. G., Beuther, H., et al. 2020, A&A, 634, L11
Klassen, M., Pudritz, R. E., Kuiper, R., Peters, T., & Banerjee, R. 2016, ApJ, 823, 28
Kobulnicky, H. A., Kiminki, D. C., Lundquist, M. J., et al. 2014, ApJS, 213, 34
Kölligan, A., & Kuiper, R. 2018, A&A, 620, A182
Kratter, K. M., Matzner, C. D., & Krumholz, M. R. 2008, ApJ, 681, 375
Kratter, K. M., Matzner, C. D., Krumholz, M. R., & Klein, R. I. 2010, ApJ, 708, 1585
Krumholz, M. R., Klein, R. I., & McKee, C. F. 2007, ApJ, 656, 959
Krumholz, M. R., Klein, R. I., McKee, C. F., Offner, S. S. R., & Cunningham, A. J. 2009, Science, 323, 754
Kuiper, R., Klahr, H., Beuther, H., & Henning, T. 2010a, ApJ, 722, 1556
Kuiper, R., Klahr, H., Dullemond, C., Kley, W., & Henning, T. 2010b, A&A, 511, A81
Kuiper, R., Klahr, H., Beuther, H., & Henning, T. 2011, ApJ, 732, 20
Laor, A., & Draine, B. T. 1993, ApJ, 402, 441
Laughlin, G. P., & Rozyczka, M. 1996, ApJ, 456, 279
Lichtenberg, T., & Schleicher, D. R. G. 2015, A&A, 579, A32
Maud, L. T., Cesaroni, R., Kumar, M. S. N., et al. 2019, A&A, 627, L6
Meyer, D. M. A., Vorobyov, E. I., Kuiper, R., & Kley, W. 2017, MNRAS, 464, L90
Meyer, D. M. A., Kuiper, R., Kley, W., Johnston, K. G., & Vorobyov, E. 2018, MNRAS, 473, 3615
Meyer, D. M. A., Vorobyov, E. I., Elbakyan, V. G., et al. 2019, MNRAS, 482, 5459
Mignone, A., Bodo, G., Massaglia, S., et al. 2007, ApJS, 170, 228
Palau, A., Estalella, R., Girart, J. M., et al. 2014, ApJ, 785, 42
Peters, T., Klessen, R. S., Mac Low, M.-M., & Banerjee, R. 2010, ApJ, 725, 134
Peters, T., Banerjee, R., Klessen, R. S., & Mac Low, M.-M. 2011, ApJ, 729, 72
Rosen, A. L., & Krumholz, M. R. 2020, AJ, 160, 78
Rosen, A. L., Krumholz, M. R., McKee, C. F., & Klein, R. I. 2016, MNRAS, 463, 2553
Rosen, A. L., Krumholz, M. R., Oishi, J. S., Lee, A. T., & Klein, R. I. 2017, J. Chem. Phys., 330, 924
Rosen, A. L., Li, P. S., Zhang, Q., & Burkhart, B. 2019, ApJ, 887, 108
Sana, H., de Mink, S. E., de Koter, A., et al. 2012, Science, 337, 444
Seifried, D., Banerjee, R., Klessen, R. S., Duffin, D., & Pudritz, R. E. 2011, MNRAS, 417, 1054
Sugiyama, K., Saito, Y., Yonekura, Y., & Momose, M. 2019, ATel, 12446, 1
Takahashi, S. Z., Tsukamoto, Y., & Inutsuka, S.-I. 2016, MNRAS, 458, 3597
Toomre, A. 1964, ApJ, 139, 1217
van der Tak, F. F. S., & Menten, K. M. 2005, A&A, 437, 947
Zhu, Z., Hartmann, L., Nelson, R. P., & Gammie, C. F. 2012, ApJ, 746, 110

Springer Nature 2021 LaTeX template

# Snapshot of a magnetohydrodynamic disk wind traced by water maser observations

Luca Moscadelli[1*], Alberto Sanna[2,3], Henrik Beuther[4], André Oliva[5,6] and Rolf Kuiper[7]

[1*]Osservatorio Astrofisico di Arcetri, Istituto Nazionale di Astrofisica, Largo E. Fermi 5, Firenze, 50125, Italy.
[2]Osservatorio Astronomico di Cagliari, Istituto Nazionale di Astrofisica, Via della Scienza 5, Selargius (CA), 09047, Italy.
[3]Max-Planck-Institut für Radioastronomie, Max Planck Gesellschaft, Auf dem Hügel 69, Bonn, D-53121, Germany.
[4]Max Planck Institute for Astronomy, Max Planck Gesellschaft, Königstuhl 17, Heidelberg, D-69117, Germany.
[5]Institut für Astronomie und Astrophysik, Universität Tübingen, Auf der Morgenstelle 10, Tübingen, D-72076, Germany.
[6]Space Research Center (CINESPA), School of Physics, University of Costa Rica, Ciudad Universitaria Rodrigo Facio, San José, 11501, Costa Rica.
[7]Faculty of Physics, University of Duisburg-Essen, Lotharstraße 1, Duisburg, D-47057, Germany.

*Corresponding author(s). E-mail(s): luca.moscadelli@inaf.it;
Contributing authors: alberto.sanna@inaf.it; beuther@mpia.de; astro@gandreoliva.org;
rolf.kuiper@uni-due.de;

**Keywords:** ISM: jets and outflows – ISM: kinematics and dynamics – Stars: formation – Masers – Techniques: interferometric

**The formation of astrophysical objects of different nature, from black holes to gaseous giant planets, involves a disk-jet system, where the disk drives the mass accretion onto a central compact object and the jet is a fast collimated ejection along the disk rotation axis. Magnetohydrodynamic disk winds can provide the link between mass accretion and ejection, which is essential to ensure that the excess angular momentum is removed and accretion can proceed. However, up to now, we have been lacking direct observational proof of disk winds. This work presents a direct view of the velocity field of a disk wind around a forming massive star. Achieving a very high spatial resolution of ≈ 0.05 au, our water maser observations trace the velocities of individual streamlines emerging from the disk orbiting the forming star. We find that, at low elevation above the disk midplane, the flow co-rotates with its launch point in the disk, in agreement with magneto-centrifugal acceleration. Beyond the co-rotation point, the flow rises spiraling around the disk rotation axis along a helical magnetic field. We have performed (resistive-radiative-gravito-) magnetohydrodynamic simulations of the formation of a massive star and record the development of a magneto-centrifugally launched jet presenting many properties in agreement with our observations.**

Magnetohydrodynamic (MHD) disk winds have been proposed to be the engines of the powerful jets observed at varying length scales in many diverse sources, from young stellar objects [1] (YSO) to black holes [2]. According to the classical model of an ideal MHD disk wind [2], in the reference frame co-rotating with the launch point, the flow streams along the magnetic field line anchored to the accretion disk. An observer at rest sees magneto-centrifugal acceleration: the magnetic field keeps the flow in co-rotation with its launch point while its radial distance increases, till reaching the Alfvén point where the poloidal kinetic and magnetic energies are equal. Beyond the Alfvén point, the flow spirals outward along the rotation axis with a stably increasing ratio of the streaming onto the rotational velocity, until it gets eventually collimated into a fast jet [3, 4]. So far, the best observational evidence for a MHD disk wind has been the finding of line of sight velocity gradients transversal to the jet axis, which are interpreted in terms of jet rotation and the imprint of the magneto-centrifugal acceleration [5–8]. However, that is an indirect evidence and the derivation of key parameters, as the launch radius and the magnetic lever arm, can be seriously affected by systematic biases [9]. On scales of ∼100 au, a few studies based on Very Long Baseline Interferometry (VLBI) maser observations have revealed rotating disk-like[10–12], conical[13] or cylindrical [14]

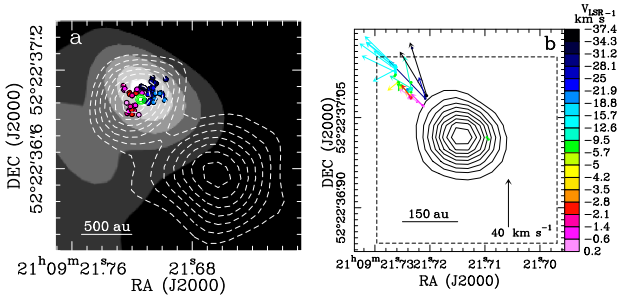



**Fig. 1 Previous NOEMA, JVLA and VLBA observations towards IRAS 21078+5211.** (a) The gray-scale (from 10 to 35 mJy beam$^{-1}$) map reproduces the NOEMA 1.37 mm continuum emission[17]. The colored dots represent the channel emission peaks of the $CH_3CN$ $J_K = 12_K$-$11_K$ ($K$ = 3–6) and $HC_3N$ $J$ = 24-23 lines, with colors denoting the channel $V_{LSR}$: blue for [−13.6, −10] and red [−2.5, 0.5] km s$^{-1}$. The green (70%, 80%, and 90% of 0.50 mJy beam$^{-1}$) and white (from 30% to 90%, in steps of 10% of 0.096 mJy beam$^{-1}$) contours show the JVLA A-Array continuum at 1.3 cm and 5 cm, respectively. (b) Colored dots and arrows give absolute positions and proper motions of the 22 GHz water masers determined with multi-epoch (2010–2011) VLBA observations[15], with colors denoting the maser $V_{LSR}$. The black contours (from 10% to 90%, in steps of 10% of 0.50 mJy beam$^{-1}$) indicate the JVLA A-Array continuum at 1.3 cm. The dashed rectangle delimits the field of view plotted in Fig.2a.

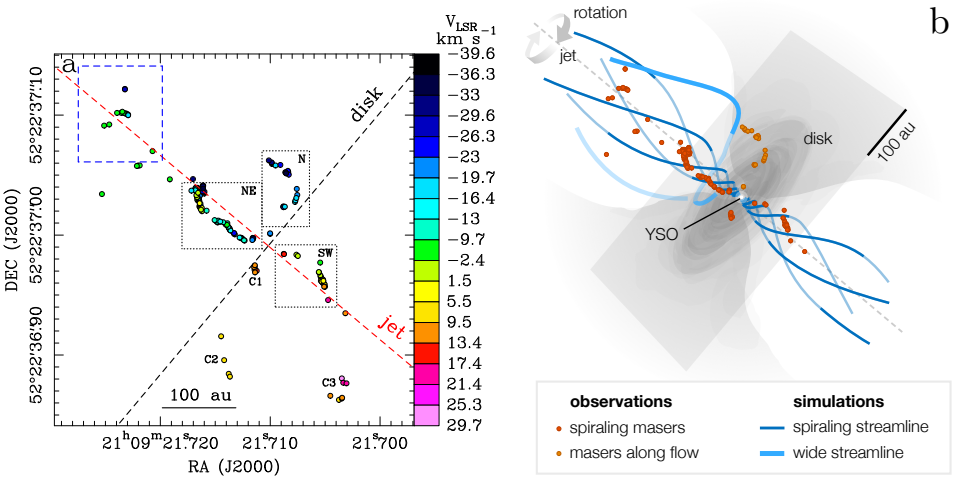



**Fig. 2 Global VLBI observations of the 22 GHz water masers and 3D view of the proposed kinematical interpretation.** (a) Colored dots give absolute positions of the 22 GHz water masers, with colors denoting the maser $V_{LSR}$. The black dotted rectangles encompass the three regions, to the N, NE and SW, where maser emission concentrate. The blue dashed rectangle delimits the area of maser emission in the previous VLBA observations, and three distinct maser clusters S of the YSO are labeled "C1", "C2", and "C3" (see 'Kinematics of the water masers further to NE and S' in Methods). The red and black dashed lines mark the sky-projected jet and disk axis, respectively. (b) Observed maser positions (red and orange dots) overlaid on top of streamlines (blue lines) computed from resistive-radiative-gravito-MHD simulations of a jet around a forming massive star (see 'Simulation snapshot of a forming massive star' in Methods). The streamlines close to the rotation axis show significant spiraling motion, in agreement with the kinematic signature of the masers observed in the NE and SW regions. The wide streamline from the simulation illustrates the outflowing trajectory of material from the outer disk, similar to the observed masers in the N region. For context, the protostar, the disk and the outflow cavity have been sketched in gray, based on the density structure obtained in the simulations (see Supplementary Figure 1).

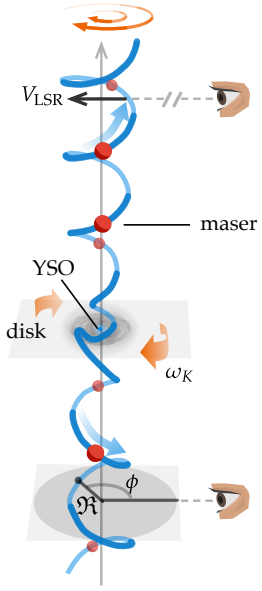



**Fig. 3 The geometry of the spiral motion.** Illustration of the spiral motion of the masers (small red balls) along a magnetic field line (blue) emerging from the YSO's disk. The rotation angle, $\phi$, and radius, $\mathfrak{R}$, are labeled. The field line is anchored to a point of the disk rotating at an angular velocity $\omega_K$. This plot is based on the data from (resistive-radiative-gravito-) MHD simulations of a jet around a forming massive star (see 'Simulation snapshot of a forming massive star' in Methods).

maser distributions at the jet root, but the streamlines of a disk wind have been never traced, up to now.

IRAS 21078+5211 is a star forming region of high bolometric luminosity, $5 \times 10^3$ $L_\odot$ [15] at a distance of 1.63±0.05 kpc [16], and harbors a cluster of forming massive stars. On scales of a few 100 au, by employing the NOrthern Extended Millimeter Array (NOEMA), a disk [17] is observed in high-density molecular tracers ($CH_3CN$ and $HC_3N$, see Fig.1a) rotating around a YSO of mass of $5.6 \pm 2$ $M_\odot$. Interferometric observations at radio wavelengths (5 cm) using the Jansky Very Large Array (JVLA) have revealed a jet [15] directed NE-SW (PA $\approx$ 44°) emerging from the YSO, whose position at the center of the disk is pinpointed by compact thermal emission observed with the JVLA at 1.3 cm. During 2010–2011 we have performed multi-epoch Very Long Baseline Array (VLBA) observations of the maser emission of the water molecule at 22 GHz. These observations have discovered a cluster of masers placed ≈100 au NE from the YSO, whose proper motions are collimated NE-SW (PA = 49°) and trace the base of the jet from the YSO [15] (see Fig.1b). The analysis of the three-dimensional (3D) maser motions, specifically the local standard of rest (LSR) velocity ($V_{LSR}$) gradient transversal to the jet axis and the constant ratio between the toroidal and poloidal velocities, suggested that the jet could be launched from a MHD disk wind.

In October 2020, we performed novel observations (see Fig.2a) of the water maser emission in IRAS 21078+5211 by including all telescopes available in the VLBI network, with the aim to simulate next-generation radio interferometers which will improve current sensitivities by more than an order of magnitude (see 'Observations' in Methods). In the following, we will show that these new observations prove that the water masers trace magnetized streams of gas emerging from the YSO's disk (see Fig.2b and 'Simulation snapshot of a forming massive star' in Methods). The maser emission concentrates in three regions to NE, N, and SW, inside the three dotted rectangles of Fig.2a. Along the jet axis (the dashed red line in Fig.2a), whose sky-projection is known from previous observations of the maser proper motions and radio jet (see 'Water

masers: shock type and corresponding flow kinematics' in Methods), we observe two elongated structures, blue- and red-shifted (with respect to the systemic $V_{\rm LSR}$ of the YSO: $V_{\rm sys} = -6.4$ km s$^{-1}$) to NE and SW, respectively. These structures are the opposite lobes of a collimated outflow from the YSO, located in between the two lobes; the disk axis (the black dashed line in Fig.2a) is the intercept of the jet axis at the YSO position. From previous VLBA observations we know that the jet axis has to lay close to the plane of the sky, with an inclination $\leq 30°$. According to the maser $V_{\rm LSR}$, the jet is inclined towards us to NE, and away from us to SW.

The jet and disk axes provide a convenient coordinate system to refer the maser positions to. In the following, we present the interpretation of the maser kinematics, which is based on the analysis of the three independent observables: $z$, the elevation above the disk plane (or offset along the jet), $R$, the radial distance from the jet axis (or transversal offset), and the maser $V_{\rm LSR}$. As discussed in 'Observations' in Methods, the accuracy of the maser positions is $\approx 0.05$ au, and that of the maser $V_{\rm LSR}$ $\approx 0.5$ km s$^{-1}$. Without loss of generality, we can express the maser velocities as the sum of two terms, one associated with the toroidal component or rotation around the jet axis, $V_{\rm rot}$, and the other associated with the poloidal component including all the contributions owing to non-rotation, $V_{\rm off}$. Since the jet axis is close to the plane of the sky and we observe the rotation close to edge-on (see Fig 3), we can write:

$$V_{\rm LSR} = V_{\rm off} + V_{\rm rot} = V_{\rm off} + \omega\ \mathfrak{R}\ \sin(\phi) \quad (1)$$

$$R = \mathfrak{R}\ \sin(\phi) \quad (2)$$

$$\phi = \omega\ t \quad (3)$$

where $\phi$ is the angle between the rotation radius $\mathfrak{R}$ and the line of sight, and $\omega$ and $t$ are the angular velocity and the time, respectively.

Fig. 4c shows the remarkable finding that the spatial coordinates $z$ and $R$ of the maser emission in the SW flow satisfy the relation:

$$R = C\ \sin(f_z(z - z_0)) \quad (4)$$

where $C$, the amplitude of the sinusoid, $f_z$, the spatial frequency, and $z_0$, the position of zero phase, are fitted constants (see Table 1). In 'Resolving the NE emission into three distinct streams' in Supplementary Information, we demonstrate that the masers in the NE flow can be separated in three different streams, each of them satisfying the relation 4 (see Fig. 5c and Table 1). The comparison of Eqs. 2 and 4 leads to a straightforward interpretation of the sinusoidal relation between the coordinates by taking: 1) $\mathfrak{R} = C$, and 2) $\phi = f_z\ \|z - z_0\|$. The former equation indicates that the rotation radius is the same for all the masers, the latter shows that the motions of rotation around and streaming along the jet axis are locked together, which is the condition for a spiral motion. Denoting with $V_z$ the streaming velocity along the jet axis, we can write $\|z - z_0\| = V_z\ t$ and, comparing with Eq. 3, we derive the relation between the rotation and streaming velocities:

$$f_z = \omega / V_z \quad (5)$$

According to Eq. 5, the observation of a well defined sinusoidal pattern requires that $\omega$ and $V_z$ are directly proportional, or constant. The constancy of $V_z$ implies that $V_{\rm off}$ is also constant, because, if the rotation radius does not change, $V_{\rm off}$ is the projection along the line of sight of $V_z$. Following Eqs. 1 and 2, the constancy of $\omega$ and $V_{\rm off}$ would result into a tight linear correlation between $V_{\rm LSR}$ and transversal offsets $R$. While a good linear correlation between $V_{\rm LSR}$ and $R$ is observed for the SW and NE-1 spiral motions (see Figs. 4b and 5b, black symbols), the scatter in velocity is considerable for the NE-2 spiral motion (see Fig.5b, red symbols). In 'Velocity scatter' in Methods we investigate the physical reason for the observation of well defined sinusoidal patterns despite the presence of a significant velocity scatter. Applying the equations of motions for an axisymmetric MHD flow, we find that the magnetic field configuration has to be helical over the maser emission region, and the motion along such an helical field line, in the reference frame co-rotating with the launch point, leads to the sinusoidal pattern of maser positions.

We consider now the N region (see Fig.2a) and show that, in this region as well, the maser kinematics is consistent with the predictions for a MHD disk wind. The N masers have a larger separation from the jet axis than the NE and SW masers. A few nearby masers show quite different $V_{\rm LSR}$, which could hint at distinct streams, as observed (see Fig. 5a) and discussed (see 'Resolving the NE emission into three distinct streams' in Supplementary Information) for the NE flow. In this case, however, only a single stream is reasonably well sampled in position and $V_{\rm LSR}$ with the masers, and we focus our kinematical analysis on that. The spatial distribution of this stream presents an arc-like shape: a subset of maser features draws a line at small angle with the disk axis and another group extends at higher elevations about parallel to the jet axis (see Fig.6a). Fig.6c shows that the maser $V_{\rm LSR}$ increases linearly with $R$ in the range $-95$ au $\lesssim R \lesssim -70$ au up to an elevation $z \approx 60$ au. The relatively large separation from the jet axis and radial extent, and the arc-like shape of the maser distribution lead us to think that the N emission is observed close to the plane of the sky. In this case, the maser $V_{\rm LSR}$ should mainly trace rotation, which is also expected to be the dominant velocity component at low elevations above the disk. Then, the good linear correlation between $V_{\rm LSR}$ and $R$ indicates that the masers co-rotate at the same angular velocity, $\omega_{\rm N} = 0.274 \pm 0.005$ km s$^{-1}$ au$^{-1}$, up to $R \approx -95$ au and $z \approx 60$ au. A simple interpretation is in terms of a magneto-centrifugally accelerated stream of gas emerging from a point of the disk. A disk in Keplerian rotation around an YSO of about 5.6 $M_\odot$ attains an angular velocity equal to $\omega_{\rm N}$ at $R \approx 40$ au. The line drawn by the masers at the lowest elevations intercepts the disk axis close to $-40$ au (see Fig.6a), as expected if the gas, launched from the disk, first streams approximately along a straight line and then progressively bends up along the jet axis. Note that, basing on Eqs. 1 and 2, the derivation of $\omega_{\rm N}$ does not depend on the maser geometry. Therefore, the finding that the masers lay along a line intercepting the disk at $\approx -40$ au provides an "a posteriori" test of the assumption that the N emission is observed close to the plane of the sky.

The masers found at elevation $z > 60$ au appear to set aside of the arc-like distribution (see Fig.6a) and their $V_{\rm LSR}$ are significantly more negative and do not follow the linear correlation with the radius (see Fig.6c). A natural interpretation is that the location at $R \approx -95$ au and $z \approx 60$ au is the Alfvén point of the stream, and beyond that the gas is not any longer co-rotating. The lever arm of the stream is $\approx (95\ {\rm au})/(40\ {\rm au}) = 2.4$, in agreement with the values of 2–3 predicted by theory

[18, 19]. The more negative $V_{\rm LSR}$ are explained if $V_z$ (and the absolute value of $V_{\rm off}$) increases with the elevation, as a consequence of the magneto-centrifugal launching. The linear correlation between $V_{\rm LSR}$ and $z$ ($\mathrm{d}V_{\rm LSR}/\mathrm{d}z = -0.195 \pm 0.002$ km s$^{-1}$ au$^{-1}$) shown in Fig.6b results from the combination of the two regimes: 1) sub-Alfvénic, where $V_{LSR} \propto R$ and the gas streams approximately along a straight line, that is $R \propto z$; 2) trans-Alfvénic, where $V_z$ increases fast with $z$ and $V_{\rm off}$ starts to be significant.

From the previous analysis, a MHD disk wind seems to be a natural frame to explain both the spiral motions traced by the masers close to the jet axis in the NE and SW regions and the gas co-rotation along the N stream. If some locations of the YSO's disk are perturbed, the flow emerging from those perturbed launch points should harbor internal shocks (see 'Water masers: shock type and corresponding flow kinematics' in Methods), which travel outward along spiraling trajectories. These internal shocks provide physical conditions suitable for the excitation of the water masers [20–22]. The spiral motions traced with the masers would correspond to portions of the trajectories beyond the Alfvén point where the rotation radius keeps about constant. An essential feature of the proposed model is that, as the launch point rotates, the maser emissions have to travel along spatially distinct, spiraling trajectories. These trajectories are invariant under rotation and nearby masers share the same orbital parameters. However, since the masers sample different trajectories, we need to make a distinction between the angular velocity of the trajectory, $\omega$, derived through the linear fit of the maser $V_{\rm LSR}$ versus $R$ (see Eqs. 1 and 2, and Figs. 4b and 5b), and the effective angular velocity of rotation, $\omega_{\rm e}$, the one to be used in Eqs. 3 and 5. Since the different trajectories are rigidly anchored to the launch point and water masers at higher (absolute) elevations have been launched earlier in time, the simple relation holds:

$$\omega_{\rm e} = \omega - \omega_{\rm K} \tag{6}$$

where $\omega_{\rm K}$ is the Keplerian angular velocity of the launch point. Eq. 6 shows that $\omega_{\rm e}$ is the angular velocity of the spiraling trajectory as observed in the reference frame co-rotating with the launch point. Based on axisymmetric MHD models [9, 23], the ratio $\omega_{\rm K}/\omega$ increases stably from 1 up to a value $\approx 4$ while the gas climbs from $z_{\rm A}$ to 10 $\mathfrak{R}_{\rm K}$, where $z_{\rm A}$ is the elevation of the Alfvén point and $\mathfrak{R}_{\rm K}$ is the launch radius. Being $\omega \leq \omega_{\rm K}$, the negative value of $\omega_{\rm e}$ indicates that the rotation angle of the maser positions decreases with $z$. Following the previous discussion, Eq. 5 has to be corrected by replacing $\omega$ with $\omega_{\rm e}$:

$$f_z = \|\omega_{\rm e}\|/V_z \tag{7}$$

A good test of the above considerations comes directly from our data. Assuming that all the masers move along a single trajectory and using the fitted values of $\omega$ and $f_z$ in Eq. 5, we obtain implausibly small values for $V_z$: 31, 37, 17 and 49 km s$^{-1}$, for the SW, NE-1, NE-2, and NE-3 spiral motions, respectively. There are two strong observational evidences that the derived streaming velocities are too small. First, comparing them with the values of $V_{\rm off}$ (see Table 1), the two velocities have similar amplitudes, and that is inconsistent with the expectation that $V_{\rm off}$ be the line of sight component of $V_z$ and the jet axis being close to the plane of the sky. Second, taking the ratio between the highest elevations reached by the masers, that is 100–130 au (see Figs. 4 and 5), and the above values of $V_z$, the derived traveling times of 15–40 yr exceed the separation of 10 yr since the previous VLBA observations, when no maser emission was detected at corresponding positions.

Since $V_{\rm off}$ corresponds to the line of sight projection of $V_z$, we can write:

$$V_z = \|V_{\rm off} - V_{\rm sys}\| \ / \ \sin(i_{\rm axi}) \tag{8}$$

where $V_{\rm off}$ is corrected for the systemic $V_{\rm LSR}$ of the YSO, and $i_{\rm axi}$ is the inclination angle of the jet axis with the plane of the sky. As we know that $i_{\rm axi} \leq 30°$, Eq. 8 allows us to derive a lower limit for $V_z$, reported in Table 2. Using the derived lower limit of $V_z$ and the corresponding value of $f_z$ (see Table 1), by means of Eq. 7 we can calculate a lower limit for $\omega_{\rm e}$. Finally, we use Eq. 6 and the fitted value of $\omega$ (see Table 1) to infer a lower limit for $\omega_{\rm K} = \omega + \|\omega_{\rm e}\|$ and, knowing the mass of the YSO, a corresponding upper limit for the launch radius $\mathfrak{R}_{\rm K}$ (see Table 2). The NE-1 stream, which extends the most in elevation (from 20 to 130 au, see Fig.5a), includes a group of maser features at elevation of $\approx 20$ au, which should be located closer to the Alfvén point. In 'Constraining the Alfvén point of the NE-1 stream' in Supplementary Information, we study the change of $V_{\rm LSR}$ versus $R$ internal to this cluster and obtain a lower limit for $\omega_{\rm K} \geq 2.4$ km s$^{-1}$ au$^{-1}$ that agrees well with the corresponding value reported in Table 2 for the NE-1 stream. The results shown in Table 2 are in general agreement with the theoretical predictions from MHD disk winds [18, 19]: the inferred lower limits on the streaming velocity $V_z$ increase steeply with decreasing launch radius; for the SW and NE-3 streams, which are those with relatively lower uncertainty in the measurement of both $\omega$ and $\mathfrak{R}$ (see Table 1), the ratio between $V_z$ and the rotation velocity $\omega\,\mathfrak{R}$ is $\geq$ 2–3.

In conclusion, our observations resolve the kinematics of a MHD disk wind on length scales of 1–100 au, allowing us to study the velocity pattern of individual streamlines launched from the disk. As represented in Fig. 2b, close to the disk rotation axis we observe flows spiraling outward along a helical magnetic field, launched from locations of the disk at radii $\leq$ 6–17 au. At larger separation from the rotation axis, we observe a stream of gas co-rotating with its launch point from the disk at radius of $\approx 40$ au, in agreement with the predictions for magneto-centrifugal acceleration. Our interpretation is supported by (resistive-radiative-gravito-) MHD simulations of the formation of a massive star that lead to a magneto-centrifugally launched jet whose properties agree with our maser and thermal (continuum and line) observations of IRAS 21078+5211. These results provide a clear evidence for a MHD disk wind. Since water maser emission is widespread in YSOs, sensitive VLBI observations of water masers can be a valuable tool to investigate the physics of disk winds.

–

# Methods

## Observations

We observed the $6_{16} - 5_{23}$ $H_2O$ maser transition (rest frequency 22.235079 GHz) towards IRAS 21078+5211 (tracking center: RA(J2000) = $21^h9^m21^s.720$ and Dec(J2000) = $+52°22'37''.08$) with global VLBI for 24 hr, starting on 2020 October 27, 13:30 UT. The antennae involved were 16 antennae of the European VLBI network (EVN): Yebes, Sardinia, Medicina, Jodrell_Bank, Effelsberg, Onsala, Metsahovi, Torun, Svetloe, Badary, Zelenchukskaya, KVN_Tamna, KVN_Ulsan, KVN_Yonsei, Urumqi, Tianma; plus the 10 antennae of the VLBA: Brewster, Fort Davis, Hancock, Kitt Peak, Los Alamos, Mauna Kea, North Liberty, Owens Valley, Pie Town, and Saint Croix. The observations were designed to achieve a relative and absolute position accuracy of $\sim 0.01$ mas and $\sim 1$ mas, respectively, and to reach a sensitivity in the maser line $\leq 1$ mJy beam$^{-1}$. While the EVN antennae observed continuously the target, interleaving calibration scans $\approx 8$ min long every hour, the VLBA performed also phase-referencing observations (over 10 hr), alternating scans on the target and the phase-reference calibrator every 45 s. During the phase-reference session, the target and the calibrators were always observed by the VLBA simultaneously with the EVN to ensure global VLBI baselines. The fringe-finder and bandpass calibrators were: J2202+4216, 2007+777, 3C84 and 3C48; the phase-reference calibrators were 2116+543 and 2051+528, both within 2.5° from the target and with a correlated flux of $\sim 0.1$ Jy beam$^{-1}$ at 22 GHz.

We recorded dual circular polarization through four adjacent bandwidths of 16 MHz, one of them centered at the maser $V_{\rm LSR}$ of $-6.4$ km s$^{-1}$. The four 16 MHz bandwidths were used to increase the signal to noise ratio (SNR) of the weak continuum (phase-reference) calibrators. The data were correlated with the SFXC correlator at the Joint Institute for VLBI in Europe (JIVE, at Dwingeloo, the Netherlands) in two correlation passes, using 1024 and 128 spectral channels to correlate the maser 16 MHz bandwidth and the whole set of four 16 MHz bandwidths, respectively. The spectral resolution attained across the maser 16 MHz band was 0.21 km s$^{-1}$. The correlator averaging time was 1 s.

Data were reduced with the Astronomical Image Processing System (AIPS) package following the VLBI spectral line procedures [24]. The emission of an intense and compact maser channel was self-calibrated, and the derived (amplitude & phase) corrections were applied to all the maser channels before imaging. To cover the whole maser emission, we produced images extending $0''.65$ in both RA $\cos\delta$ and DEC, and 84 km s$^{-1}$ in $V_{\rm LSR}$. Using natural weighting, the FWHM major and minor sizes of the beam are 0.7 mas and 0.3 mas, respectively, and the beam PA is $-49°$. In channel maps with (relatively) weak signal, the $1\sigma$ rms noise is 0.7 mJy beam$^{-1}$, close to the expected thermal noise.

Inverse phase-referencing [24] produced good SNR ($\geq 10$) images of the two phase-reference calibrators. Taking into account that the calibrators are relatively compact with size $\lesssim 1$ mas, and that the absolute position of the calibrators is known within a few 0.1 mas, we estimate that the error on the absolute position of the masers is $\lesssim 0.5$ mas.

Supplementary Table 1 reports the parameters (intensity, $V_{\rm LSR}$, position) of the 22 GHz water masers in IRAS 21078+5211. Individual maser features are a collection of quasi-compact spots observed on contiguous channel maps and spatially overlapping (within their FWHM size). The spot positions are determined by fitting a two-dimensional elliptical Gaussian to their spatial emissions. The uncertainty of the spot position relative to the reference maser channel is the contribution of two terms: $\Delta\theta_{\rm spot} = \sqrt{\Delta\theta^2_{\rm fit} + \Delta\theta^2_{\rm bandpass}}$. The first term depends on the SNR of the data, following [25]: $\Delta\theta_{\rm fit} = \theta_{\rm beam}/(2\,{\rm SNR})$, where $\theta_{\rm beam}$ is the resolution beam size, conservatively taken equal to the FWHM major beam size of 0.7 mas. The second term depends on the accuracy of the bandpass calibration through the expression [26]: $\Delta\theta_{\rm bandpass} = \theta_{\rm beam}\,(\Delta\Psi/360°)$, where $\Delta\Psi$ in degrees is the phase stability across the observing band. In our case $\Delta\Psi \lesssim 10°$ and $\Delta\theta_{\rm bandpass} \lesssim 0.02$ mas becomes the dominant error term for spot intensity $\geq 100$ mJy beam$^{-1}$. The maser feature position (and corresponding error) is estimated from the error-weighted mean of the spot positions (and corresponding errors), and the feature $V_{\rm LSR}$ from the intensity-weighted mean of the spots' $V_{\rm LSR}$. To be conservative, the uncertainty on the feature $V_{\rm LSR}$ is taken equal to 0.5 km s$^{-1}$, corresponding to the typical maser FWHM line width.

## Velocity scatter

Figures 4b and 5b show that the maser $V_{\rm LSR}$ are linearly correlated with $R$ in the SW and NE-1 streams. For the masers belonging to the NE-2 stream, the measurement scatter from the linear fit of $V_{\rm LSR}$ versus $R$ is considerable (with large fit errors, see Table 1), while, in the case of the NE-3 stream, the range in $R$ is too small (2 au only) to constrain the parameters of the linear fit. The noticeable deviation of $V_{\rm LSR}$ from the linear fits seems difficult to conciliate with the accuracy with which the maser positions reproduce the sinusoidal patterns (see Figs. 4c and 5c). The average scatters of maser $V_{\rm LSR}$ and positions (along the jet axis from the fitted sinusoid) are 2.4 km s$^{-1}$ and 1.9 au, 3.1 km s$^{-1}$ and 3.8 au, 6.9 km s$^{-1}$ and 2.1 au, and 2.7 km s$^{-1}$ and 1.7 au, for the SW, NE-1, NE-2 and NE-3 streams, respectively. Assuming that the $V_{\rm LSR}$ scatter reflects mainly the variation of the streaming velocity $V_z$, since the jet axis is within 30° from the plane of the sky, the change in $V_z$ has to be at least twice that observed in $V_{\rm LSR}$. Then, using the above values, the ratios of the corresponding scatters in position and $V_z$ give upper limits for the maser traveling times of $\leq$ 1–3 yr. These traveling times, for maximum (absolute) elevations of the maser streams of 100–130 au (see Figs. 4 and 5), imply $V_z \geq$ 200–500 km s$^{-1}$, which appears to be too large with respect to the observed maser $V_{\rm LSR}$. In the following, we investigate the physical reason for the observation of well defined sinusoidal patterns despite the co-occurrence of significant velocity scatters.

In a stationary, axisymmetric MHD flow, the two fundamental equations of motions [18, 19, 27] linking velocity and magnetic field along a field line are:

$$\rho V_{\rm p} = k B_{\rm p} \tag{9}$$

$$B_\phi = \frac{\rho}{k}\,(V_\phi - \omega_{\rm K}\mathfrak{R}) \tag{10}$$

where $V_{\rm p}$ and $V_\phi$, and $B_{\rm p}$ and $B_\phi$ are the poloidal and toroidal components of the velocity and magnetic field, respectively, $\rho$ is the gas mass volume density, $\omega_{\rm K}$ is the

Keplerian angular velocity at the launch point, $\mathfrak{R}$ is the rotation radius, and $k$ is the "mass load" of the wind, expressing the fixed ratio of mass and magnetic fluxes along a given magnetic field line. Since $V_\phi - \omega_{\rm K}\,\mathfrak{R}$ is the toroidal velocity in the reference frame co-rotating with the launch point, Eqs. 9 and 10 lead to the well-known result that the velocity and magnetic field vectors are always paralell in the co-rotating reference frame. Writing $V_\phi = \omega\,\mathfrak{R}$, where $\omega$ is the angular velocity of the trajectory at radius $\mathfrak{R}$, the two equations above can be combined into:

$$\frac{B_\phi}{B_{\rm p}} = \frac{(\omega - \omega_{\rm K})}{V_{\rm p}}\,\mathfrak{R} = \frac{\omega_{\rm e}}{V_{\rm p}}\,\mathfrak{R} \qquad (11)$$

where we have used the definition of $\omega_{\rm e}$ in Eq. 6. We can define the magnetic field helix angle $\alpha_B = \arctan(B_\phi/B_{\rm p})$, which is the angle with which a helical field line winds around the jet axis.

We have seen that the observation of well defined sinusoids in the plane of the sky requires that the rotation radius $\mathfrak{R}$, and the ratio of the effective angular velocity $\omega_{\rm e}$ on the streaming velocity $V_z$ keep constant (see Eq. 7). Since the polar velocity $V_{\rm p}$ is equal to $V_z$ if $\mathfrak{R}$ is constant, Eq. 11 implies that $\alpha_B$ does not vary along each of the observed maser streams. However, the reverse argument holds too. If the magnetic field is sufficiently stable and has a constant helix angle (that is, a helical configuration), the motion along the field line (in the co-rotating reference frame) requires a constant value of the ratio $\omega_{\rm e}/V_z$. That preserves the maser sinusoidal pattern despite the concomitant presence of a relatively large velocity scatter. From Eqs. 11 and 7, with $V_{\rm p} = V_z$, we have:

$$\frac{\|B_\phi\|}{B_{\rm p}} = f_z\,\mathfrak{R} \qquad (12)$$

Using the values reported in Table 1, we derive: $f_z\,\mathfrak{R} = 0.79 \pm 0.06$, $1.1 \pm 0.2$, $0.88 \pm 0.04$, and $0.70 \pm 0.05$ for the SW, NE-1, NE-2 and NE-3 streams, respectively. From Eq. 10, $B_\phi \approx 0$ within the Alfvén point when the flow co-rotates with the disk and $V_\phi \approx \omega_{\rm K}\,\mathfrak{R}$. Beyond the Alfvén point, the inertia of the matter in the flow forces the magnetic field to fall behind the rotation of the disk, which causes $\|B_\phi\|$ to increase. The derived values of the ratio $\|B_\phi\|/B_{\rm p}$ in the range 0.7–1.1 agree with the water masers tracing a region of the spiraling trajectory in between the Alfvén point and the fast magneto-sonic point, beyond which the toroidal magnetic field component should become the predominant component [18, 28].

Finally, we discuss briefly possible causes for the observed velocity scatter. For the SW, NE-1, and NE-2 spiral motions, the residual of the linear fit of $V_{\rm LSR}$ versus $R$ is plotted versus $z$ in Supplementary Figure 2. These plots indicate that the residual velocity is not correlated with position, contrarily to what it would be expected if the velocity scatter from the linear fit was caused by the smooth change with $z$ of the characteristic velocities, $\omega$ and $V_z$ (and consequently $V_{\rm off}$), of the spiraling trajectory. The residual velocities cannot be dominated by turbulence, too, since the latter would produce an independent variation of the toroidal and poloidal velocity components, which, as discussed above, is not consistent with the observation of the maser sinusoidal patterns. Moreover, it would be difficult to explain the observed different degree of turbulence between the NE-1 and NE-2 streams (see Supplementary Figure 2) over the same region of the sky.

The irregular change of the velocities can be naturally linked to our flow tracers, the water masers, which are excited in internal shocks of the flow emerging from perturbed locations of the disk. Eq. 9 and 10 show that the flow velocity depends critically on the mass load $k$, which, on its turn, depends on the physical conditions, including dissipative processes, near the disk surface. If the physical conditions of the perturbed launch points varied erratically on time scales so short as months, that would qualitatively explain the observed scatter of maser velocities. Emission variability over time scales of months is observed and theoretically expected in accretion bursts from high-mass YSOs [29–31], in such cases where an extended portion of the accretion disk gets perturbed.

## Water masers: shock type and corresponding flow kinematics

We propose that the water masers observed in IRAS 21078+5211 inside the NE, SW and N regions arise in internal shocks along streamlines of the YSO's disk wind. If observed at sufficiently high angular resolution, radio jets are often resolved into chains of compact emission centers (named "knots"), which are interpreted in terms of internal shocks owing to fluctuation in mass or velocity ejection[32]. Since the jets are the innermost (most collimated and fastest) portion of a disk wind, it is possible that the structure of more external streamlines, where the gas is weakly ionized and mainly molecular, is characterized by internal shocks, too. If the fluctuation responsible for the shocks is relatively small compared to the (time average) flow properties, the internal shocks are weak C-shocks and the shock (and maser) velocity is close to the flow velocity. In fact, the proper motions of radio knots are considered a reliable measurement of the jet speed[32]. In IRAS 21078+5211, the regular (arc-like) spatial and $V_{\rm LSR}$ distribution of the water masers indicate that the masers co-move with the flowing gas.

Models of water maser excitation predict them to arise in both strong dissociative J[21, 33]- and weak non-dissociative C[22]-shocks. While in J-shocks the masers form in the cooling post-shock gas at $T_{\rm kin} \approx 400$ K following the chemical re-formation of water, in C-shocks the masing molecules do not dissociate and reach a significantly higher temperature, $T_{\rm kin} \approx 1000 - 3000$ K. The presence of shocks is naturally expected in correspondence of the fast protostellar outflows, whose association with the 22 GHz water masers is well proved observationally[34]. The location of the 22 GHz masers, often found at the wall of the jet cavity or at the terminal bow-shock of the jet, and their speed (mainly $\leq$ 30 km s$^{-1}$)[17] significantly smaller that that of the jet (a few 100 km s$^{-1}$)[32], indicate that the large majority of the 22 GHz water masers arise in strong external (lateral or terminal) J-shocks of the fast flow against the dense ambient material. While the velocity of the internal shocks is close to the flow speed, external shocks travel at a reduced speed because of the density contrast between the lighter impinging flow and the denser surrounding material.

As exemplified by our observations in IRAS 21078+5211, the origin of the 22 GHz masers in internal shocks of the flow make them a formidable tool to trace individual streams of gas of the disk wind. In the following, we show that the alternative interpretation

for these masers as external shocks of a wide-angle wind or a jet impacting against the surrounding medium is much less plausible. Looking at Fig. 2a, the water masers could be found at the wall of a wind cavity, if the axis of this putative wind was oriented at PA $\approx 10°$–$20°$ and its opening angle was $\approx 30°$–$40°$. It is very difficult to conciliate this wide-angle wind with the jet geometry and precession rate estimated from previous (2010–2013) JVLA and VLBA observations (see Fig. 1). The elongation (PA $= 56°\pm12°$) of the slightly resolved (size $\approx$ 150 au) JVLA continuum at 1.3 cm, the collimated (PA $= 49°\pm18°$) proper motions of the water masers near (100–200 au) the YSO, and the direction (PA $\approx 44°$) of the non-thermal radio jet traced by the extended (size $\approx$ 1000 au) JVLA continuum at 5 cm, consistently indicate the presence of a jet oriented at PA $\approx 50°$. A distinct signature of precession[17] was the finding of a spur in the 5 cm continuum $\approx$ 7000 au NE from the YSO along the same direction, PA $= 60°$, of the red-shifted lobe of the SO outflow observed with NOEMA. Clearly, a precession rate of only $\approx (60°-50°) = 10°$ over a length scale of 7000 au cannot account for a change in orientation between the putative wind and the JVLA/VLBA jet of $\geq (50°-20°) = 30°$ over a length scale $\leq$ 100 au and a timescale $\leq$10 yr. On the other hand, if this inner wind and the jet co-existed, it would be even more difficult to explain an abrupt transition in orientation and opening angle from the former to the latter across a few 10 au (see Fig. 2a). The interpretation of the water masers in IRAS 21078+5211 as external shocks at the cavity wall of a wide-angle wind faces also the difficulty to account for the huge maser $V_{\rm LSR}$ gradients, $\geq$ 40 km s$^{-1}$ over $\leq$ 10 au, transversal to the NE stream at elevation $z \geq$ 90 au (see Fig.5a). If the masers, instead of delineating two streams at different velocities, traced shock fronts (seen close to edge-on) at the wind wall, it would be very difficult to explain such a large velocity difference for almost overlapping emissions.

We conclude this discussion on alternatives to the disk wind interpretation showing that it is improbable that we are observing multiple outflows from a binary system. Inspecting Fig. 1, our previous NOEMA/JVLA/VLBA observations consistently indicate a single disk/jet system on scales of 100–500 au. The NOEMA 1.37 mm and the JVLA 1.3 cm continuum emissions, tracing the hosting molecular core and YSO's ionization, respectively, are compact and well aligned in position. The rotating disk revealed by the $V_{\rm LSR}$ gradient of high-density molecular ($CH_3CN$ and $HC_3N$) lines is centered on the peak of the 1.3 cm continuum. The agreement in direction between the elongated (double-lobe) JVLA 5 cm continuum and the collimated water maser proper motions points to a single jet emerging from the YSO. Considering now the new, global VLBI observations, on scales of 1–100 au, Fig. 2a shows that the spatial distribution of the water masers is about symmetrical with respect to the YSO position. This further supports the interpretation that a single YSO is responsible for the excitation and motion of the water masers.

## Kinematics of the water masers further to NE and S

In the main text, we have considered only the filaments of maser emission inside the NE, SW and N regions, but more scattered maser features are also observed further to NE close to the jet axis and S of the YSO (see Fig. 2a). The outmost northeastern features are found approximately in the same region of the previous VLBA maser detections (see Fig. 2a). However the newly observed masers are fewer than before and their $V_{\rm LSR}$ is now within $\pm5$ km s$^{-1}$ from $V_{\rm sys}$ instead of covering the range $[-38, 0]$ km s$^{-1}$ as before. The directions of the VLBA maser proper motions are well collimated but their amplitudes (in the range [10, 50] km s$^{-1}$) scatter significantly in position (see Fig. 1b), which, as discussed in 'Water masers: shock type and corresponding flow kinematics', suggests that these masers arise in external shocks and do not trace the true flow speed. In our previous analysis[17], we have interpreted these outmost northeastern masers as external shocks at the wall of a cylindrical MHD jet interacting with the surrounding medium. Applying the equations for a MHD disk wind, we have derived a terminal jet speed of $\approx$ 200 km s$^{-1}$ and a launch radius of $\approx$ 2 au. These values agree with the trend of the calculations reported in Table 2, where higher streaming velocities correspond to smaller launch radii.

The southern features are distributed in three separated clusters (see Fig. 2a): C1) $z \leq$ 20 au and 9.5 km s$^{-1}$ $\leq V_{\rm LSR} \leq$ 17.4 km s$^{-1}$; C2) 20 $\leq z \leq$ 100 au and 5.5 km s$^{-1}$ $\leq V_{\rm LSR} \leq$ 9.5 km s$^{-1}$; C3) $z \geq$ 120 au and 5.5 km s$^{-1}$ $\leq V_{\rm LSR} \leq$ 29.7 km s$^{-1}$. Comparing the C1 & C2 clusters with the N region, maser positions and $V_{\rm LSR}$ are about symmetrical with respect to the YSO; beside, each of the two clusters presents an arc-like shape similar to the N streamline. Thus, it is possible that these clusters trace small portions of two co-rotating streamlines emerging at different disk radii. Finally, the maser cluster C3 has position and $V_{\rm LSR}$ approximately symmetrical to the emission previously observed with the VLBA further to NE (see Fig. 1b), which suggests that masers in C3 can emerge in shocks at the wall of the southeastern lobe of the jet.

## Simulation snapshot of a forming massive star

As part of a more extensive study we will describe in a forthcoming article, we performed an axisymmetrical simulation of the formation of a massive star starting from the gravitational collapse of a rotating cloud core threaded by a magnetic field (GAO, RK et al., in preparation). We used the methods of magnetohydrodynamics to model the weakly ionized gas and dust with the code Pluto[35], with an Ohmic resistivity model as a non-ideal effect[36], and additional modules for self-gravity[37] and the transport of the thermal radiation emitted by the gas and dust[38].

The cloud core has an initial mass of 100 $M_\odot$ and a radius of 0.1 pc. The assumed conditions for the onset of the gravitational collapse ($t = 0$) are as follows: the density is distributed according to $\rho \propto r^{-1.5}$, the cloud core rotates like a solid body with a rotational energy equivalent to 4% of its gravitational energy content, and the magnetic field is uniform. The initial magnitude of the magnetic field is determined by the mass-to-flux ratio, which we take as 20 times the critical (collapse-preventing) value[39] and corresponds to a relatively weak initial magnetic field. A constant value of the opacity of 1 cm$^2$ g$^{-1}$ was used to model the gas and dust, as well as an initial dust-to-gas mass ratio of 1%.

We used an axisymmetrical grid of 896×160 cells in spherical coordinates, with the radial coordinate increasing logarithmically with the distance to the center of the cloud. An inner boundary of 3 au was set up, inside of

which the protostar is formed through accretion. No flows are artificially injected from the inner boundary into the collapsing cloud.

The simulation starts with an initial gravitational collapse epoch. After $\sim 5$ kyr, enough angular momentum is transported to the center of the cloud to start forming an accretion disk that grows in size over time. Roughly at the same time, we observe the launch of magnetically-driven outflows. Magnetic pressure arising from the dragging of magnetic field lines by the rotating flow eventually overcomes gravity and seeds the formation of the outflow cavity, thrusting a bow shock in the process (Supplementary Figure 1d), which propagates outwards as the cavity grows in size. Previous observations of IRAS 21078+5211 have uncovered the presence of a bow shock located at distances of $\approx 36000$ au from the forming massive YSO[17]. The initial launch of the magnetically-driven outflows provides a possible formation mechanism for the observed bow shock and in return, the propagation of the bow shock provides an estimation for the age of the system.

In the simulation, the protostar reaches a mass of 5.24 $M_{\odot}$ (a value in the expected mass interval from observations) after 13.84 kyr of evolution. We estimate that the bow shock has propagated to a distance of $\approx$ 30000 au at that time, roughly in line with the observations. At the same time, the accretion disk has grown to about 180 au in radius, in agreement with the observational estimates[17], as well. The data reveal a magneto-centrifugally launched jet, in a similar way as reported by the literature [2, 40], however, we see that the launching region of the jet is narrowed by the ram pressure of the infalling material from the envelope and the presence of a thick layer of the accretion disk which is vertically supported by magnetic pressure. Material transported from large scales through the accretion disk reaches the launching region, located at $z \lesssim 100$ au (see Supplementary Figure 1b), where the centrifugal force is stronger than gravity, and simultaneously, where the flow becomes sub-Alfvénic in the co-rotating frame and the magnetic field lines are mostly poloidal. Under those conditions, a parcel of plasma is accelerated along the field lines until the flow becomes super-Alfvénic again, a point at which the magnetic field lines become mostly toroidal. This causes the parcel to acquire a helical trajectory (depicted previously in Fig. 2b). The geometry and kinematics of the region where the flow becomes helical in the simulation coincides roughly with the positions and velocities of the observed masers of the NE and SW regions. At larger rotation radii, the broader magnetic field lines present in the outflow cavity could give rise to the kinematic footprint detected in the masers in the N region.

At distances of $\sim 10000$ au, where the outflow material propagates through the cloud (Supplementary Figure 1c), we notice the existence of re-collimation zones that arise because of magnetic hoop stress and ram pressure from the envelope. The position of the re-collimation zones is similar to the zones where lobes of possible synchrotron emission have been previously observed around the YSO [17], thus providing a possible mechanism for their formation.

We provide this comparison as an example that a magneto-centrifugally launched jet around a forming massive star yields a consistent picture with the observations. However, the coincidences should be taken with caution, as different combinations of initial conditions may yield similar results, which means that a wider and deeper investigation is needed in order to determine the conditions of the onset of star formation from the observational data.

## Data Availability:

This letter makes use of the following EVN data: GM077 (EVN project code).

The calibrated datasets generated during and/or analyzed during the current study are available from the corresponding author on reasonable request.

## Correspondence and Request for Material:

Any request should be addressed to Luca Moscadelli

## Code Availability:

The custom parts of the code for producing the simulations and subsequent data analysis are not ready for public use, but they can be provided upon reasonable request. For the magnetohydrodynamics part of the software, we make use of the open-source code Pluto[35, 41]. The implementation method of the employed radiation transport module ("Makemake") is publicly accessible[38].

# Acknowledgments

We thank Christian Fendt and Daniele Galli for very useful discussion. GAO acknowledges financial support from the Deutscher Akademischer Austauschdienst (DAAD), under the program Research Grants - Doctoral Projects in Germany, and complementary financial support for the completion of the Doctoral degree by the University of Costa Rica, as part of their scholarship program for postgraduate studies in foreign institutions. HB acknowledges support from the European Research Council under the Horizon 2020 Framework Programme via the ERC Consolidator Grant CSF-648505. HB also acknowledges support from the Deutsche Forschungsgemeinschaft in the Collaborative Research Center (SFB 881) "The Milky Way System" (subproject B1). RK acknowledges financial support via the Emmy Noether and Heisenberg Research Grants funded by the German Research Foundation (DFG) under grant no. KU 2849/3 and 2849/9. The European VLBI Network is a joint facility of independent European, African, Asian, and North American radio astronomy institutes. Scientific results from data presented in this publication are derived from the following EVN project code: GM077.

## Author Contribution Statement:

L.M. led the project, analysis, discussion, and drafted the manuscript.

A.S, H.B., and R.K. commented on the manuscript and participated in the discussion.

G.A.O. and R.K. performed the numerical jet simulations described in 'Simulation snapshot of a forming massive star' in Methods.

G.A.O. performed the dynamical analysis of the simulations, compared the simulation results to the observations, and produced the illustrations of the magnetic field lines and streamlines.

## Competing Interests:

The authors declare no competing (financial and non-financial) interests.

# References

[1] Pudritz, R.E., Norman, C.A.: Centrifugally driven winds from contracting molecular disks. Astrophys. J. **274**, 677–697 (1983).

[2] Blandford, R.D., Payne, D.G.: Hydromagnetic flows from accretion disks and the production of radio jets. Mon. Not. R. Astron. Soc. **199**, 883–903 (1982).

[3] Ouyed, R., Pudritz, R.E.: Numerical Simulations of Astrophysical Jets from Keplerian Disks. I. Stationary Models. Astrophys. J. **482**(2), 712–732 (1997).

[4] Krasnopolsky, R., Li, Z.-Y., Blandford, R.: Magnetocentrifugal Launching of Jets from Accretion Disks. I. Cold Axisymmetric Flows. Astrophys. J. **526**(2), 631–642 (1999).

[5] Bacciotti, F., Ray, T.P., Mundt, R., Eislöffel, J., Solf, J.: Hubble Space Telescope/STIS Spectroscopy of the Optical Outflow from DG Tauri: Indications for Rotation in the Initial Jet Channel. Astrophys. J. **576**(1), 222–231 (2002).

[6] Hirota, T., Machida, M.N., Matsushita, Y., Motogi, K., Matsumoto, N., Kim, M.K., Burns, R.A., Honma, M.: Disk-driven rotating bipolar outflow in Orion Source I. Nature Astronomy **1**, 0146 (2017).

[7] Lee, C.-F., Ho, P.T.P., Li, Z.-Y., Hirano, N., Zhang, Q., Shang, H.: A rotating protostellar jet launched from the innermost disk of HH 212. Nature Astronomy **1**, 0152 (2017).

[8] Aalto, S., Falstad, N., Muller, S., Wada, K., Gallagher, J.S., König, S., Sakamoto, K., Vlemmings, W., Ceccobello, C., Dasyra, K., Combes, F., García-Burillo, S., Oya, Y., Martín, S., van der Werf, P., Evans, A.S., Kotilainen, J.: ALMA resolves the remarkable molecular jet and rotating wind in the extremely radio-quiet galaxy NGC 1377. Astron. Astrophys. **640**, 104 (2020).

[9] Tabone, B., Cabrit, S., Pineau des Forêts, G., Ferreira, J., Gusdorf, A., Podio, L., Bianchi, E., Chapillon, E., Codella, C., Gueth, F.: Constraining MHD disk winds with ALMA. Apparent rotation signatures and application to HH212. Astron. Astrophys. **640**, 82 (2020).

[10] Matthews, L.D., Greenhill, L.J., Goddi, C., Chandler, C.J., Humphreys, E.M.L., Kunz, M.W.: A Feature Movie of SiO Emission 20-100 AU from the Massive Young Stellar Object Orion Source I. Astrophys. J. **708**, 80–92 (2010).

[11] Moscadelli, L., Goddi, C.: A multiple system of high-mass YSOs surrounded by disks in NGC 7538 IRS1 . Gas dynamics on scales of 10-700 AU from $CH_3OH$ maser and $NH_3$ thermal lines. Astron. Astrophys. **566**, 150 (2014).

[12] Sanna, A., Surcis, G., Moscadelli, L., Cesaroni, R., Goddi, C., Vlemmings, W.H.T., Caratti o Garatti, A.: Velocity and magnetic fields within 1000 AU of a massive YSO. Astron. Astrophys. **583**, 3 (2015).

[13] Moscadelli, L., Cesaroni, R., Rioja, M.J., Dodson, R., Reid, M.J.: Methanol and water masers in IRAS 20126+4104: the distance, the disk, and the jet. Astron. Astrophys. **526**, 66 (2011).

[14] Burns, R.A., Imai, H., Handa, T., Omodaka, T., Nakagawa, A., Nagayama, T., Ueno, Y.: A 'water spout' maser jet in S235AB-MIR. Mon. Not. R. Astron. Soc. **453**(3), 3163–3173 (2015).

[15] Moscadelli, L., Sánchez-Monge, Á., Goddi, C., Li, J.J., Sanna, A., Cesaroni, R., Pestalozzi, M., Molinari, S., Reid, M.J.: Outflow structure within 1000 au of high-mass YSOs. I. First results from a combined study of maser and radio continuum emission. Astron. Astrophys. **585**, 71 (2016).

[16] Xu, Y., Li, J.J., Reid, M.J., Menten, K.M., Zheng, X.W., Brunthaler, A., Moscadelli, L., Dame, T.M., Zhang, B.: On the Nature of the Local Spiral Arm of the Milky Way. Astrophys. J. **769**, 15 (2013).

[17] Moscadelli, L., Beuther, H., Ahmadi, A., Gieser, C., Massi, F., Cesaroni, R., Sánchez-Monge, Á., Bacciotti, F., Beltrán, M.T., Csengeri, T., Galván-Madrid, R., Henning, T., Klaassen, P.D., Kuiper, R., Leurini, S., Longmore, S.N., Maud, L.T., Möller, T., Palau, A., Peters, T., Pudritz, R.E., Sanna, A., Semenov, D., Urquhart, J.S., Winters, J.M., Zinnecker, H.: Multi-scale view of star formation in IRAS 21078+5211: from clump fragmentation to disk wind. Astron. Astrophys. **647**, 114 (2021).

[18] Pudritz, R.E., Ouyed, R., Fendt, C., Brandenburg, A.: Disk Winds, Jets, and Outflows: Theoretical and Computational Foundations. In: Reipurth, B., Jewitt, D., Keil, K. (eds.) Protostars and Planets V, p. 277 (2007).

[19] Pudritz, R.E., Ray, T.P.: The Role of Magnetic Fields in Protostellar Outflows and Star Formation. Frontiers in Astronomy and Space Sciences **6**, 54 (2019).

[20] Elitzur, M., Hollenbach, D.J., McKee, C.F.: Planar H2O masers in star-forming regions. Astrophys. J. **394**, 221–227 (1992).

[21] Hollenbach, D., Elitzur, M., McKee, C.F.: Interstellar $H_2O$ Masers from J Shocks. Astrophys. J. **773**, 70 (2013).

[22] Kaufman, M.J., Neufeld, D.A.: Water Maser Emission from Magnetohydrodynamic Shock Waves. Astrophys. J. **456**, 250 (1996).

[23] Pesenti, N., Dougados, C., Cabrit, S., Ferreira, J., Casse, F., Garcia, P., O'Brien, D.: Predicted rotation signatures in MHD disc winds and comparison to DG Tau observations. Astron. Astrophys. **416**, 9–12 (2004).

[24] Sanna, A., Moscadelli, L., Cesaroni, R., Tarchi, A., Furuya, R.S., Goddi, C.: VLBI study of maser kinematics in high-mass star-forming regions. I. G16.59-0.05. Astron. Astrophys. **517**, 71 (2010).

[25] Reid, M.J., Schneps, M.H., Moran, J.M., Gwinn, C.R., Genzel, R., Downes, D., Rönnäng, B.: The distance to the center of the galaxy - h2o maser proper motions in sagittarius b2(n). Astrophys. J. **330**, 809 (1988).

[26] Zhang, Q., Claus, B., Watson, L., Moran, J.: Angular Momentum in Disk Wind Revealed in the Young Star MWC 349A. Astrophys. J. **837**(1), 53 (2017).

[27] Pelletier, G., Pudritz, R.E.: Hydromagnetic Disk Winds in Young Stellar Objects and Active Galactic Nuclei. Astrophys. J. **394**, 117 (1992).

[28] Staff, J., Koning, N., Ouyed, R., Pudritz, R.: Three-dimensional simulations of MHD disk winds to hundred AU scale from the protostar. In: European Physical Journal Web of Conferences. European Physical Journal Web of Conferences, vol. 64, p. 05006 (2014).

[29] Caratti o Garatti, A., Stecklum, B., Garcia Lopez, R., Eislöffel, J., Ray, T.P., Sanna, A., Cesaroni, R., Walmsley, C.M., Oudmaijer, R.D., de Wit, W.J., Moscadelli, L., Greiner, J., Krabbe, A., Fischer, C., Klein, R., Ibañez, J.M.: Disk-mediated accretion burst in a high-mass young stellar object. Nature Physics **13**, 276–279 (2017).

[30] Hunter, T.R., Brogan, C.L., MacLeod, G., Cyganowski, C.J., Chandler, C.J., Chibueze, J.O., Friesen, R., Indebetouw, R., Thesner, C., Young, K.H.: An Extraordinary Outburst in the Massive Protostellar System NGC6334I-MM1: Quadrupling of the Millimeter Continuum. Astrophys. J. Lett. **837**(2), 29 (2017).

[31] Oliva, G.A., Kuiper, R.: Modeling disk fragmentation and multiplicity in massive star formation. Astron. Astrophys. **644**, 41 (2020).

[32] Anglada, G., Rodríguez, L.F., Carrasco-González, C.: Radio jets from young stellar objects. Astron. Astrophys. Rev. **26**(1), 3 (2018).

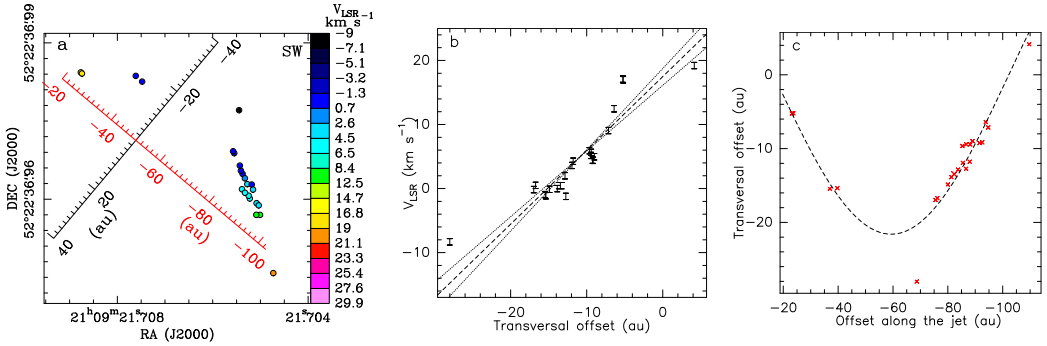



**Fig. 4 The SW spiral motion.** (a) Expanding view of the maser positions and $V_{\rm LSR}$ in the SW region. Colored dots have the same meaning as in Fig.2a. The distances along the jet (red) and disk (black) axes are indicated. (b) Plot of the maser $V_{\rm LSR}$ (and corresponding $2\sigma$ errors, denoted with errorbars) versus $R$. The black dashed and dotted lines show the best linear fit and the associated uncertainty, respectively. (c) Plot of the maser coordinates $R$ versus $z$. The positional error is smaller than the cross size. The black dashed curve is the fitted sinusoid, whose parameters are reported in Table 1.

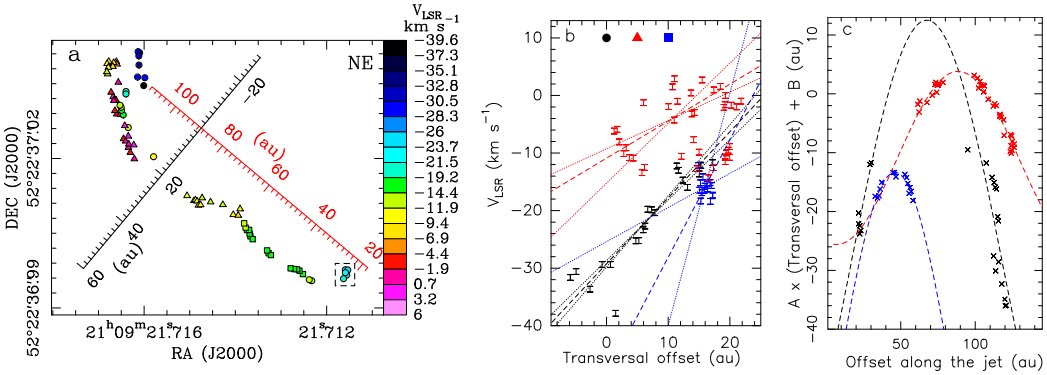



**Fig. 5 The NE spiral motions.** (a) Expanding view of the maser positions and $V_{\rm LSR}$ in the NE region. Different symbols are employed to identify the three spiral motions: dots for the NE-1, triangles for the NE-2, and squares for the NE-3 spiral motion. Colors denote the maser $V_{\rm LSR}$. The distances along the jet (red) and disk (black) axes are indicated. The black dashed rectangle encompasses the maser cluster closest to the YSO. (b) In this and following panel, black, red, and blue colors refer to masers belonging to the NE-1, NE-2, and NE-3 streams, respectively. Errorbars, dashed and dotted lines have the same meaning as in Fig.4b. Masers in the NE-2 stream with similar radii, 10 au $\leq R \leq$ 22 au, but different elevations, 60 au $\leq z <$ 90 au and $z \geq$ 90 au, have $V_{\rm LSR}$ different by $\approx$ 10 km s$^{-1}$ (see 'Velocity scatter' in Methods). For the NE-2 stream, the linear fit of the $V_{\rm LSR}$ has been performed considering only the masers with $z \geq$ 90 au. (c) Plot of the linear transformation of $R$ versus $z$. For each of the three streams, the coefficients $A$ and $B$ are taken equal to the corresponding values of $\omega$ and $V_{\rm off}$, respectively, in Table 1. We plot the linear transformation of the radii to reduce the overlap and improve the visibility of each of the three streams. The dashed curves are the fitted sinusoids. In Table 1, we report the parameters of the sinusoidal fits of the radii.

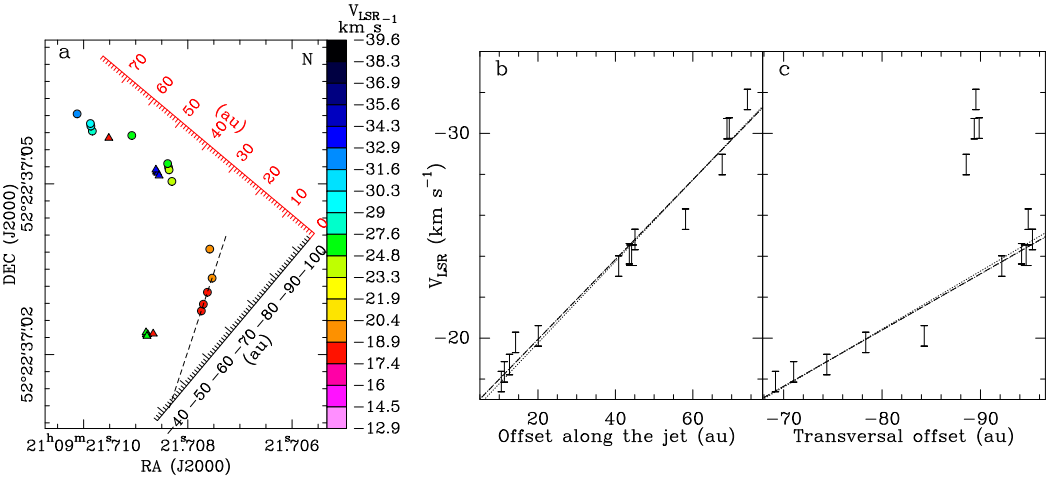



**Fig. 6 The co-rotating N stream.** (a) Expanding view of the maser positions and $V_{\rm LSR}$ in the N region. Colored dots and triangles give absolute positions of the 22 GHz water masers, with colors denoting the maser $V_{\rm LSR}$. The triangles mark a few masers with detached $V_{\rm LSR}$ excluded from the kinematical analysis. The distances along the jet (red) and disk (black) axes are indicated. The black dashed line shows the linear fit of the positions of the masers at elevation $z <$ 20 au. Plot of maser $V_{\rm LSR}$ versus $z$ (b) and $R$ (c). In both panels, errorbars denote the maser $V_{\rm LSR}$ and corresponding $2\sigma$ errors, and the black dashed and dotted lines show the best linear fit and the associated uncertainty, respectively. The linear fit of $V_{\rm LSR}$ versus $R$ has been performed considering only the masers with $V_{\rm LSR} \geq -27$ km s$^{-1}$.

**Table 1 Parameters of the linear and sinusoidal fits**

| | Linear fit | | Sinusoidal fit | | |
|---|---|---|---|---|---|
| Stream | $\omega$ (km s$^{-1}$ au$^{-1}$) | $V_{\rm off}$ (km s$^{-1}$) | $\mathfrak{R}$ (au) | $f_z$ (rad au$^{-1}$) | $z_0$ (au) |
| SW | $1.15 \pm 0.12$ | $17.5 \pm 1.3$ | $21.6 \pm 1.0$ | $0.0366 \pm 0.0012$ | $-16.5 \pm 1.9$ |
| NE-1 | $1.15 \pm 0.09$ | $-29.2 \pm 0.6$ | $36 \pm 5$ | $0.0307 \pm 0.0008$ | $16.3 \pm 2.0$ |
| NE-2 | $0.64 \pm 0.27$ | $-10.9 \pm 3.0$ | $22.9 \pm 0.5$ | $0.0386 \pm 0.0008$ | $47.8 \pm 1.2$ |
| NE-3 | $2.0 \pm 0.5^a$ | $-49 \pm 27$ | $17.2 \pm 0.3$ | $0.0405 \pm 0.0023$ | $7.3 \pm 2.3$ |

Column 1 denotes the maser stream; Cols. 2 and 3 provide the values of $\omega$ and $V_{\rm off}$ from the linear fit of maser $V_{\rm LSR}$ versus $R$; Cols. 4, 5 and 6 report the amplitude, the spatial frequency and the position of zero phase, respectively, of the sinusoidal fit of the maser coordinates $R$ versus $z$.

[a]The determination of this error, smaller than the value, 1.7 km s$^{-1}$ au$^{-1}$, from the linear fit, is discussed in 'The angular velocity of the NE-3 stream' in Supplementary Information.

**Table 2 Estimate of the stream parameters**

| Stream | $V_z$ (km s$^{-1}$) | $\omega_{\rm K}$ (km s$^{-1}$ au$^{-1}$) | $\mathfrak{R}_{\rm K}$ (au) |
|---|---|---|---|
| SW | $\geq 48$ | $\geq 2.9$ | $\leq 9$ |
| NE-1 | $\geq 46$ | $\geq 2.6$ | $\leq 10$ |
| NE-2 | $\geq 9$ | $\geq 1.0$ | $\leq 17$ |
| NE-3 | $\geq 85$ | $\geq 5.4$ | $\leq 6$ |

Column 1 indicates the maser stream; Col. 2 reports the estimated streaming velocity along the jet axis; Cols. 3 and 4 give the estimate of the angular velocity and the radius, respectively, at the launch point.

[33] Elitzur, M., Hollenbach, D.J., McKee, C.F.: H2O masers in star-forming regions. Astrophys. J. **346**, 983–990 (1989).

[34] Moscadelli, L., Sanna, A., Goddi, C., Krishnan, V., Massi, F., Bacciotti, F.: Protostellar Outflows at the EarliesT Stages (POETS). IV. Statistical properties of the 22 GHz $H_2O$ masers. Astron. Astrophys. **635**, 118 (2020).

[35] Mignone, A., Bodo, G., Massaglia, S., Matsakos, T., Tesileanu, O., Zanni, C., Ferrari, A.: PLUTO: A Numerical Code for Computational Astrophysics. Astrophys. J. Suppl. Ser. **170**(1), 228–242 (2007).

[36] Machida, M.N., Inutsuka, S.-i., Matsumoto, T.: Magnetic Fields and Rotations of Protostars. Astrophys. J. **670**(2), 1198–1213 (2007).

[37] Kuiper, R., Klahr, H., Beuther, H., Henning, T.: Circumventing the Radiation Pressure Barrier in the Formation of Massive Stars via Disk Accretion. Astrophys. J. **722**, 1556–1576 (2010).

[38] Kuiper, R., Yorke, H.W., Mignone, A.: Makemake + Sedna: A Continuum Radiation Transport and Photoionization Framework for Astrophysical Newtonian Fluid Dynamics. Astrophys. J. Suppl. Ser. **250**(1), 13 (2020).

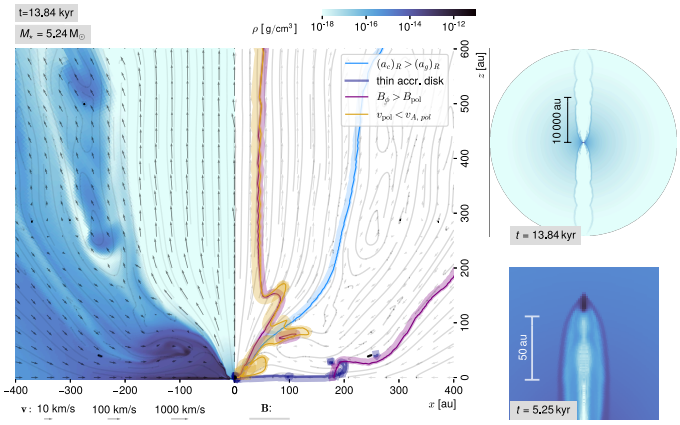
[39] Mouschovias, T.C., Spitzer, J. L.: Note on the collapse of magnetic interstellar clouds. Astrophys. J. **210**, 326 (1976).

[40] Kölligan, A., Kuiper, R.: Jets and outflows of massive protostars. From cloud collapse to jet launching and cloud dispersal. Astron. Astrophys. **620**, 182 (2018).

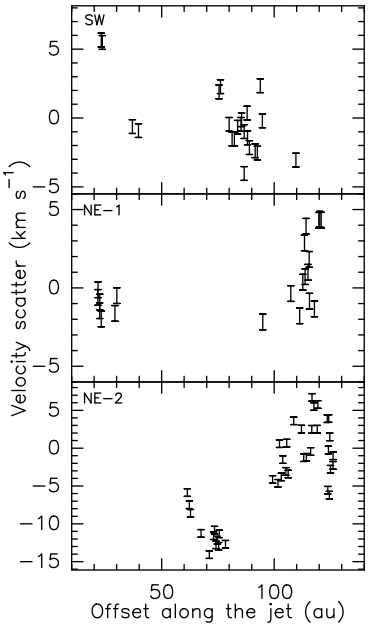
[41] Mignone, A., Tzeferacos, P., Zanni, C., Tesileanu, O., Matsakos, T., Bodo, G.: PLUTO: A Code for Flows in Multiple Spatial Dimensions. Astrophysics Source Code Library, record ascl:1010.045 (2010).

# Supplementary information

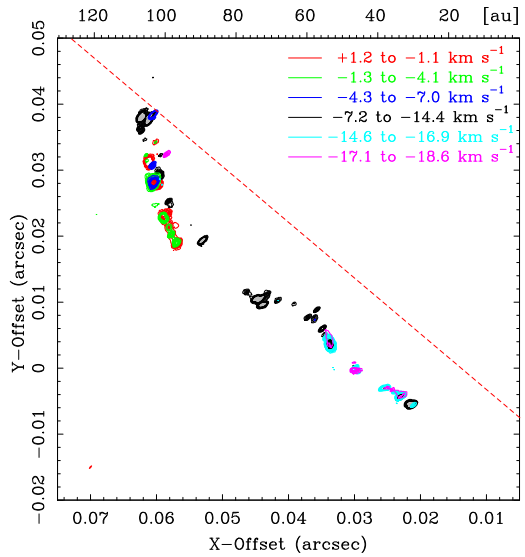




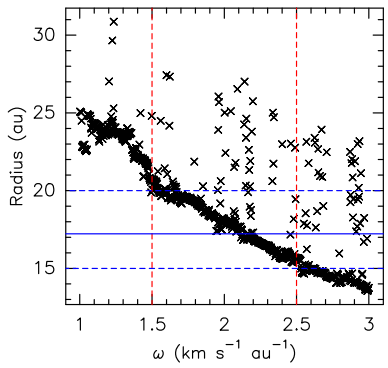

**Supplementary Fig. 1: Simulation snapshot of a forming massive star, surrounded by an accretion disk and magnetically-driven outflows:** (a) Density, velocity and magnetic field lines. (b) Contours that show the regions where: the material is sub-Alfvénic (yellow), the magnetic field lines are wound by rotation (purple), and the centrifugal acceleration is stronger than gravity (blue). The shadow that accompanies each contour indicates the region where the inequality listed in the legend holds true. The contour lines have been smoothened in order to filter out local and short-lived features. (c) Large-scale structure of the outflows. (d) Bow-shock produced in the simulation.




**Supplementary Fig. 2: Maser velocity scatter.** The residual velocity (and corresponding $2\sigma$ error, denoted with errorbar) from the linear fit of maser $V_{\rm LSR}$ versus $R$ (see Figs. 4b and 5b) is plotted versus $\|z\|$ for the masers in the SW (upper panel), NE-1 (central panel), and NE-2 (lower panel) streams.

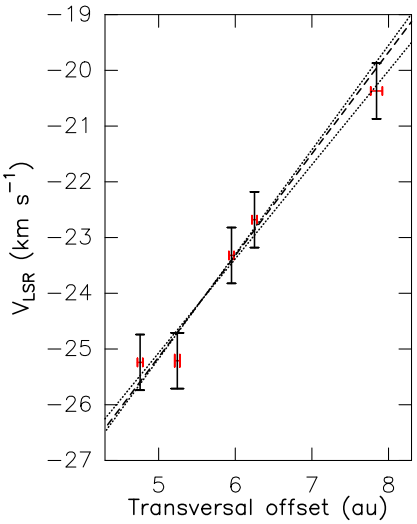



**Supplementary Fig. 3: Integrated emission map of the NE maser stream.** Emission summed over the whole velocity range $[-19, +1]$ km s$^{-1}$ by selecting groups of channels (top right) with similar noise thresholds. Colored contours correspond to a given velocity interval and increase at steps of 5 times the noise thresholds of each group (corresponding to $\approx 10\,\sigma$). Angular offsets correspond to Supplementary Table 1 and the linear scale is drawn in the top axis. The dashed red line denotes the jet axis and the synthesized VLBI beam is plotted in the bottom left corner.

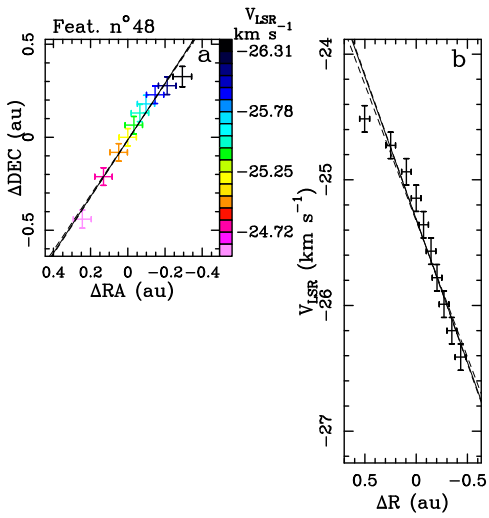



**Supplementary Fig. 4: Constraining $\omega$ for the NE-3 stream.** Plot of the rotation radius estimated from the ratio $\mathfrak{C}/\omega$ versus $\omega$, where $\mathfrak{C}$ is the amplitude of the sinusoidal fit of the rotational velocity, $\omega$ $R$, versus $z$ (see the analysis in 'The angular velocity of the NE-3 stream'). The blue continuous and dashed lines mark the observed value of the rotation radius and the corresponding range of uncertainty, respectively; the red dashed lines delimit the range of $\omega$ for which the fitted radius is consistent with the observations.

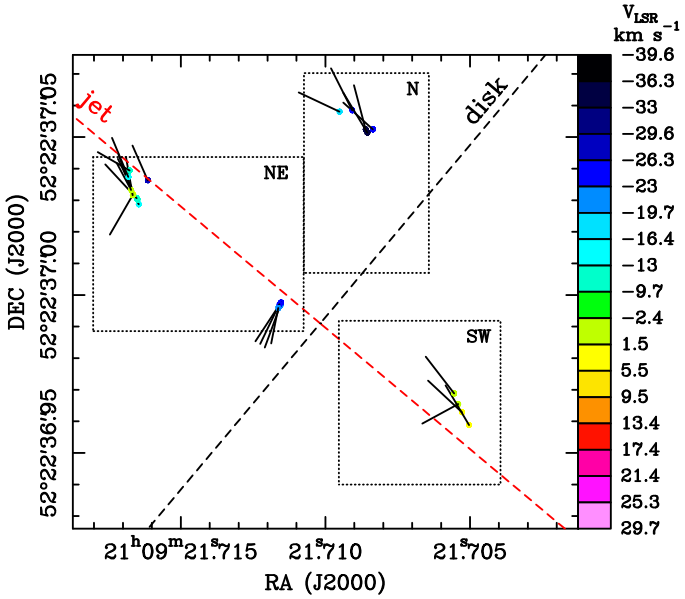
## Supplementary information 2




**Supplementary Fig. 5: Estimate of $\omega$ at the base of the NE-1 stream.** Plot of $V_{LSR}$ versus $R$ for the maser cluster at the base of the NE-1 stream, inside the dashed rectangle in Fig. 5a. Vertical black and horizontal red errorbars indicate velocities and radii (with corresponding $2\sigma$ and $1\sigma$ errors), respectively. The black dashed and dotted lines show the best linear fit and the associated uncertainty, respectively.




**Supplementary Fig. 6: Rotation inside individual maser features.** (a) Colored errorbars give positions (and corresponding $1\sigma$ errors) of the individual spots collected into the maser feature, with colors denoting the maser $V_{LSR}$. The black continuous and dashed lines give the best linear fit of the spot positions and the associated uncertainty, respectively. (b) Plot of the spot $V_{LSR}$ ($2\sigma$ errorbars) versus positions projected along the major axis of the spot distribution ($1\sigma$ errorbars). The black continuous and dashed lines show the best linear fit of the plotted values and the associated uncertainty, respectively.




**Supplementary Fig. 7: Spatial distribution of internal velocity gradients of 22 GHz water maser features.** Colored dots, black dotted rectangles, and the red and black dashed lines have the same meaning as in Fig. 2a. The black segments show the velocity gradient orientation. Only the maser features which yield correlation coefficients $\geq 0.7$ from the linear fits of both the spot positions (see Supplementary Fig. 6a) and $V_{LSR}$ versus projected positions (see Supplementary Fig. 6b), are plotted.

# Supplementary information



## Resolving the NE emission into three distinct streams

The masers in the NE emission are separated into three distinct streams identified with different symbols: dots, triangles and squares (see Fig. 5a). Each stream traces a sinusoid in the plane of the sky (see Fig. 5c), which is the signature for a spiral motion. The identification of the maser features belonging to each of the three sinusoids can be done with good confidence. First, we note that the masers at elevation $z \geq 90$ au can be unambiguously divided into two streams, dots and triangles, on the basis of the very different $V_{\rm LSR}$ of nearby emissions. Both dots and triangles at $z \geq 90$ au have $R$ decreasing with $z$, suggesting that they could trace the descending portion of a sinusoid, and one can argue that the corresponding ascending portion would be traced by masers with $z < 90$ au. Next, we note that the group of masers with 30 au $\leq z \leq 60$ au draw an arc, and, since they cannot be part of a sinusoid together with other masers at larger $R$, they have to trace a third sinusoid with maximum radius close to the radius, $R_{\rm apex} = 17.2$ au, of the apex of the arc. We have also verified that the blue-shifted cluster of masers located at elevation $z \approx 20$ au (inside the dashed rectangle of Fig. 5a) cannot be adjusted within this third sinusoid. We have fitted the expression:

$$R = (R_{\rm apex} - C) + C \ \sin(f_z(z - z_0)) \qquad (1)$$

with the maximum radius fixed to $R_{\rm apex}$ and the zero level given by $R_{\rm apex} - C$, with $C$ free parameter. When the masers at elevation $z \approx 20$ au and those drawing the arc at 30 au $\leq z \leq 60$ au are considered together, the fit of Supplementary Eq. 1 results into an implausible, very negative zero level at $\approx -60$ au. Thus, after putting all the masers with 30 au $\leq z \leq 60$ au (and only them) into a third spiral motion, it remains to deal only with the masers in the two separated ranges 20 au $\leq z < 30$ au and 60 au $\leq z < 90$ au. The sinusoidal fit of $R$ versus $z$ of the triangles at $z \geq 90$ au indicates that the ascending portion of the sinusoid has to extend from $\approx 50$ au to $\approx 90$ au, and, over that range of elevations, intercepts all the observed masers. Finally, the remaining masers at 20 au $\leq z < 30$ au trace the ascending portion of the sinusoid identified with dots in Fig. 5a.

Supplementary Figure 3 evidences the filamentary morphology of the maser emission in the NE region. First, we selected six velocity ranges (see Supplementary Fig. 3) of channel maps with similar noise thresholds. Then, we summed the emission of each group of channels, blanking pixels with emission below a typical threshold of $\approx 10\,\sigma$, and overplotted the six maps together. This method allows to appreciate the overall spatial structure traced by maser emission with very different brightness levels.

## The angular velocity of the NE-3 stream

The NE-3 stream is sampled by the masers only close to the positions where it attains the maximum radius. Because of the small radial range, 15 au $\lesssim R \lesssim 17$ au, the linear fit of $V_{\rm LSR}$ versus $R$ constrains very little the angular velocity, $\omega = 2.04 \pm 1.72$ km s$^{-1}$ au$^{-1}$. However, since $R$, and the rotational velocity $\omega\, R$, are sinusoidal functions of the elevation $z$, we can use the results of the sinusoidal fits to reduce the error in $\omega$. For plausible values of $\omega$ in the range 0–4, we have performed the sinusoidal fit of the rotational velocity, and estimated the radius from the ratio of the fitted amplitude, $\mathfrak{C}$, and $\omega$. For a given value of $\omega$, we have fitted the expression:

$$\omega\, R = (\omega\, R_{\rm apex} - \mathfrak{C}) + \mathfrak{C} \ \sin(f_z(z - z_0)) \qquad (2)$$

fixing the maximum velocity to $\omega\, R_{\rm apex}$ and fitting the zero level $\omega\, R_{\rm apex} - \mathfrak{C}$, with the amplitude $\mathfrak{C}$ as a free parameter. Supplementary Figure 4 shows that, apart a minor fraction of scattered results, the radius estimated from the sinusoidal fit decreases regularly with $\omega$, and attains a value consistent with the observations, $17.5 \pm 2.5$ au, for $\omega = 2.0 \pm 0.5$ km s$^{-1}$ au$^{-1}$, thus effectively reducing the uncertainty to 0.5 km s$^{-1}$ au$^{-1}$.

## Constraining the Alfvén point of the NE-1 stream

Supplementary Figure 5 shows that the $V_{\rm LSR}$ of the five masers at the base ($z \approx 20$ au) of the NE-1 stream (inside the dashed rectangle of Fig. 5a) changes linearly with $R$. The derived value of $\omega = 1.82 \pm 0.09$ km s$^{-1}$ au$^{-1}$ is significantly higher than the value, $1.15 \pm 0.09$ km s$^{-1}$ au$^{-1}$(see Table 1), determined at larger elevations. That can be interpreted as evidence that the gas closer to the Alfvén point rotates faster than that at higher elevations, in agreement with the MHD disk-wind theory. As described in 'Observations' in Methods, each maser feature is a collection of many compact spots for which we have accurately measured position and $V_{\rm LSR}$. For the maser feature (out of the five) nearest to the jet axis, Supplementary Fig. 6a shows that the spatial distribution of the spots is linear and elongated close to (7°away from) the disk axis, and Supplementary Fig. 6b shows that the spot $V_{\rm LSR}$ changes linearly with the position, $\Delta R$, along the major axis of the spatial distribution. Given its orientation, it is natural to interpret the $V_{\rm LSR}$ gradient internal to the maser feature in terms of rotation, and from the linear fit of $V_{\rm LSR}$ versus $\Delta R$ we derive a value of $\omega = 2.3 \pm 0.1$ km s$^{-1}$ au$^{-1}$. This should still be considered a lower limit for $\omega_{\rm K}$, the angular velocity at the Alfvén point. Beside the one just considered, other two maser features present a well defined, internal $V_{\rm LSR}$ gradient. In these two features, the linear distribution of the spots is directed at larger angles, 20–30°, from the disk axis, and the amplitudes of the $V_{\rm LSR}$ gradients are $1.8 \pm 0.1$ and $3.1 \pm 0.1$ km s$^{-1}$ au$^{-1}$. These two features have larger separation from the jet axis and the corresponding larger inclination of the spot distribution with the plane of rotation could indicate that the internal $V_{\rm LSR}$ gradient is influenced by non-rotation terms, as, for instance, the increase of the streaming velocity with the elevation. In any case, assuming that also for these two features the internal $V_{\rm LSR}$ gradient is dominated by rotation, we obtain a consistent average value for the in-feature angular velocity of $\omega = 2.4$ km s$^{-1}$ au$^{-1}$.

We stress that the internal motion of the maser features does not contribute to the features' $V_{\rm LSR}$ used in our analsys of the maser velocity pattern on larger scales (see Figs. 4, 5 and 6). In fact, the feature $V_{\rm LSR}$ is obtained by averaging the internal spots' $V_{\rm LSR}$ (see 'Observations' in Methods), with the result that any contribution from internal motions is averaged out. In the previous analysis, we have interpreted the maser internal motions, on scales of a few au, as a product of the larger scale (10–100 au) motions. Since we have considered only five features within a small area, this interpretation has to be better justified. Supplementary Figure 7 shows the internal gradient orientation for all the maser features in IRAS 21078+5211 with well defined internal gradients. Most of the gradients are directed close to either the jet or disk axis. That suggests that the maser internal motions trace mainly the large scale dynamics, dominated by either the streaming flow motion or rotation. Interestingly, a previous study[1] of a sample of 6.7 GHz methanol maser sources reached a similar conclusion. Finally, we note that, on the size (a few au) of the maser features, turbulent motions have to be significantly smaller than the typical maser line widths or $\leq 0.1$ km s$^{-1}$, otherwise they would destroy the velocity coherence along the maser amplification path.

## References

[1] Moscadelli, L., Sanna, A., Goddi, C.: Unveiling the gas kinematics at 10 AU scales in high-mass star-forming regions. Milliarcsecond structure of 6.7 GHz methanol masers. Astron. Astrophys. **536**, 38 (2011).

Monthly Notices of the ROYAL ASTRONOMICAL SOCIETY

MNRAS **505,** 2870–2885 (2021) https://doi.org/10.1093/mnras/stab1380
Advance Access publication 2021 May 17

# Effects of the treatment of the mass quadrupole moment on ray-tracing applications for rapidly rotating neutron stars

G. André Oliva [1,2]★ and Francisco Frutos-Alfaro [2]★

[1] *Institute for Astronomy and Astrophysics, University of Tübingen, Auf der Morgenstelle 10, D-72076 Tübingen, Germany*
[2] *Space Research Center (CINESPA), School of Physics, University of Costa Rica, 11501 San José, Costa Rica*

Accepted 2021 May 11. Received 2021 May 6; in original form 2020 August 17

## ABSTRACT

The Neutron Star Interior Composition Explorer (NICER) mission has provided a unique opportunity to constrain the equation of state of neutron stars by using the technique of pulse-profile modelling. This technique requires accurate and efficient ray-tracing, that in turn requires a robust representation of the space–time around a neutron star. Several exact and approximate metrics have been proposed, and used, to perform ray-tracing around neutron stars, with both moderate and fast rotation. In this paper, we perform a comparison between several of these metrics, when used for ray-tracing. We calculate the shape of the neutron star as seen by a distant observer using two different surface formulae, the thermal spectrum and pulse profiles from circular and crescent-shaped hotspots, for four configurations of pulsars with rotation rates ranging from 622 to 1000 Hz, and using both a moderate and a stiff equation of state to include realistic and extreme cases. We find small differences between the metrics for rotation frequencies starting at ∼700 Hz that could theoretically be used for constraining the quadrupole moment or the space–time models. We also determine the practicality of use of each metric in larger-scale applications such as pulse-profile modelling.

**Key words:** gravitation – methods: numerical – stars: neutron – pulsars: general – X-rays: stars.

## 1 INTRODUCTION

The problem of finding a solution of the Einstein field equations for a neutron star is still unsolved, in part because of the lack of sufficient knowledge about the equation of state of dense nuclear matter. With the advent of the Neutron Star Interior Composition Explorer (NICER) mission, it is now possible to perform high-precision measurements of the mass and radius of a neutron star, which also constraint its equation of state (Miller et al. 2019; Raaijmakers et al. 2019).

Hot emitting regions on the surface of a neutron star, or hotspots, are responsible for the periodic signal observed from pulsars. Pulse-profile modelling is a technique that uses the general relativistic effect on the X-ray thermal emission from hotspots in order to measure neutron star parameters (see e.g. Watts et al. 2016; Bogdanov et al. 2019). Isolated pulsars of rotation frequencies ∼200 Hz were selected by the NICER group in order to constrain the mass–radius relation of neutron stars with this technique, by fitting a large number of light-curve models produced with different parameters to the observational data (Miller et al. 2019; Riley et al. 2019). Rapidly rotating pulsars, however, are known to exist (PSR J1748-2446ad has a rotation frequency of 716 Hz), and their rotation causes deformation and frame dragging that in turn affect their emission, and these effects should be taken into account into future observational studies of such targets.

Pechenick, Ftaclas & Cohen (1983) used the Schwarzschild metric for modelling the light curve of the radiation emitted by a hotspot. In Miller & Lamb (1998), Poutanen & Gierliński (2003), and Poutanen & Beloborodov (2006), the approximate effects of the Doppler effect by rotation were added to the Schwarzschild metric to the pulse profiles. Cadeau et al. (2007) tried a completely numerical approach, by using a numerical metric to integrate the geodesic equations and calculate the light curves. Morsink et al. (2007), in the other hand, improved the Schwarzschild+Doppler approximation by adding an approximation to the oblateness of the neutron star.

Bauböck et al. (2012) used an approximate metric (developed by Glampedakis & Babak 2006, hereafter GB) that included quadrupole moment in order to study how it affects the apparent shape of a rapidly rotating neutron star as seen by a distant observer. They used values of the quadrupole moment fitted empirically by Laarakkers & Poisson (1999) for several equations of state. Using the same metric, Psaltis & Özel (2014) calculated the pulse profiles, and did extensive comparisons with the results obtained with the Schwarzschild+Doppler approximation and the oblate Schwarzschild+Doppler approximation. A similar comparison (among many other ray-tracing applications) was performed in Pihajoki et al. (2018), but using the metric of AlGendy & Morsink (2014), which is a fitted expansion of the metric of Butterworth & Ipser (1976). Bauböck et al. (2015a) used the GB metric in order to calculate corrections to the thermal spectrum due to rotation. In Nättilä & Pihajoki (2018), a theoretical framework for ray-tracing for rapidly rotating neutron stars was introduced. The effects of the atmosphere were incorporated to a numerical metric approach by Vincent et al. (2018).

Some of the studies mentioned above contain the classical model of two antipodal hotspots. In Riley et al. (2019) and Miller et al. (2019), however, more complex configurations were explored, like annuli,

★ E-mail: andree.oliva@uni-tuebingen.de (GAO); francisco.frutos@ucr.ac.cr (FF-A)

© 2021 The Author(s)
Published by Oxford University Press on behalf of Royal Astronomical Society

Downloaded from https://academic.oup.com/mnras/article/505/2/2870/6276752 by UB Tuebingen user on 16 June 2021

crescent-shaped and oval spots, with the result that the antipodal configuration was strongly disfavoured in the cases analysed.

Apart from the approximate space–time models mentioned already, there are additional exact and approximate metrics that have been proposed as a description of the exterior space–time of a spinning neutron star (among others, Quevedo 1990; Manko & Novikov 1992; Glampedakis & Babak 2006; Boshkayev, Quevedo & Ruffini 2012; Frutos-Alfaro 2016; Pappas 2017; Frutos-Alfaro 2019). Although such metrics converge for slow rotation and small deformation, an assessment and comparison of their practical use in ray-tracing applications for rapidly rotating neutron stars has not been performed until now. The expected small differences between them may give rise to small uncertainties when used in pulse profile modelling and fitting of the spectrum.

The present study aims to estimate these small differences for rapidly rotating neutron stars, and establish an optimal metric that minimizes computing resources while keeping an adequate accuracy. We also expand the parameter range presented in previous similar studies and explore the coupled effects of rotation and deformation on ray-tracing applications. The present paper is structured as follows. Section 2 gives a general introduction to the metrics used, Section 3 deals with the chosen physical objects for this study and their parameters. A direct comparison between a numerical solution of the Einstein field equations and the analytical metrics is presented in Section 4. In Sections 5–8, we present several ray-tracing applications: light scattering, determination of the shape of the neutron star, the thermal spectrum and pulse profiles. In each section, the methods and results are detailed. Section 9 offers a summary and general conclusions. Unless stated otherwise, we use geometrized units ($G = c = 1$) throughout the paper.

## 2 EXTERIOR KERR-LIKE METRICS

In the case of analytical solutions of the Einstein field equations, the problem is typically divided into an interior and an exterior solution. There are some exact exterior solutions, and some approximate analytical solutions, a subset of which we review in the following sections, and use throughout this study.

In Newtonian gravity, an expansion up to order $r^{-3}$ of the gravitational potential outside a static spheroid of equatorial radius $R$ and mass $M$ is given by (see e.g. Capderou 2014, section 3.3.4):

$$\Phi = -\frac{M}{r} + \frac{q}{r^3} P_2(\cos\theta), \tag{1}$$

where $q$ is the mass quadrupole (in this case, the difference between the moments of inertia along the polar and equatorial axes; with dimensions of $MR^2$), and $P_2(\cos\theta) = (3\cos^2\theta - 1)/2$ is the Legendre polynomial of second order.

In the general relativistic case, consider a neutron star modelled as a rotating spheroid of mass $M$, angular momentum $J \equiv Ma$, and mass quadrupole moment ($q > 0$ for an oblate object). In principle, the mass quadrupole could be determined from the mass, angular momentum and equation of state that describes the interior of the neutron star. The most general solution of the Einstein field equations for the exterior (vacuum) space–time around such an object has the general form

$$\begin{aligned} \mathrm{d}s^2 = &-V(r,\theta)\,\mathrm{d}t^2 + 2W(r,\theta)\,\mathrm{d}t\,\mathrm{d}\phi + X(r,\theta)\,\mathrm{d}r^2 \\ &+ Y(r,\theta)\,\mathrm{d}\theta^2 + Z(r,\theta)\,\mathrm{d}\phi^2, \end{aligned} \tag{2}$$

where the potentials $V$, $W$, $X$, $Y$, and $Z$ depend on $M$, $a$, and $q$ as well. In the limit $r \to \infty$, the potential $V$ might be expanded as (see e.g. Frutos-Alfaro 2019)

$$V \approx 1 - 2\Phi - 2\frac{Ma^2}{r^3}\cos^2\theta, \tag{3}$$

where the last term is due to rotation (matching with the Kerr solution when $q = 0$). The second-order moment (coefficient of the $r^{-3}$ terms) is then

$$M_2 = -q - Ma^2. \tag{4}$$

There are some exact solutions that contain the required parameters. In this study, we focus in particular on two exact metrics: the Quevedo–Mashhoon (QM) metric (Quevedo 1990) and the Manko–Novikov (MN) metric (Manko & Novikov 1992). The QM metric is a generalization of the Kerr and Erez–Rosen space–times, i.e. it reduces to these metrics when the mass quadrupole moment and rotation vanish, respectively. The MN metric is also a generalization of the Kerr metric, and it contains arbitrary mass multipole moments. Both metrics have a complex analytic representation (see the Appendix), and their practical use in applications of ray-tracing is explored in Section 5.

There are several approximate metrics that have a simpler analytical form. Hartle & Thorne (1968, hereafter HT) solved approximately the Einstein field equations for terms up to order $J^2$ and $q$. The Glampedakis–Babak (GB) metric (Glampedakis & Babak 2006), used in previous studies of ray-tracing applications, is a perturbed version of the Kerr metric using the corrected form of Abramowicz for the Hartle–Thorne metric. The approximate metric presented in Frutos-Alfaro (2016, hereafter Fru16) also contains the Kerr(-Newman) metric, and an approximation to the Erez–Rosen metric up to second order in quadrupole moment. A transformation to the expanded Hartle–Thorne metric was found, and more multipole moments can be added to the approximation (Frutos-Alfaro 2019).

The metric potentials $V$, $W$, $X$, $Y$, and $Z$ are given for each of these metrics in the Appendix, as well as a multipole analysis (given that not all the metrics use the same definitions of the quadrupole moment) and the necessary transformations to the definition given by equation (4).

## 3 CHOICE OF NEUTRON STAR PARAMETERS

We are interested in millisecond pulsars, since high rotation rates can produce high deformation, and therefore, higher quadrupole moment and a better opportunity to find disagreement between the results yielded by the use of different metrics. We used the programme Rapidly Rotating Neutron Star (`RNS`; Stergioulas & Friedman 1995) in order to model the parameters of several rapidly rotating neutron stars. `RNS` solves the Einstein field equations numerically by first computing a non-rotating equilibrium configuration (by solving the Tolman–Oppenheimer–Volkoff equation) and iteratively adding rotation with a Green function approach (for more details, see Komatsu, Eriguchi & Hachisu 1989; Cook, Shapiro & Teukolsky 1992).

We selected the following configurations: `BWFX` corresponds to the Black Widow pulsar (PSR B1957 + 20); `SHFT` corresponds to PSR J1748-2446ad, the fastest spinning pulsar known to date (rotation frequency: 716 Hz), and `KAFT` and `KALN`, that correspond to hypothetical pulsars that rotate with a frequency of 1000 Hz. The full parameters corresponding to those configurations are shown in Table 1.

Two classic equations of state were used: FPS (Lorenz, Ravenhall & Pethick 1993) and L (described in Arnett & Bowers 1977). The equation of state L is based on the mean-field approximation and is unrealistically stiff; it is used here only to consider an extreme case of

Downloaded from https://academic.oup.com/mnras/article/505/2/2870/6276752 by UB Tuebingen user on 16 June 2021

**Table 1.** Parameters of the pulsars considered in this study. From left to right, the columns indicate the name of the configuration, the (gravitational) mass of the neutron star in solar masses, the mass expressed in geometrized units of the equatorial radius $R$, the frequency of rotation, the specific angular momentum in units geometrized units of $R$, the ratio of the polar to equatorial radii, the mass quadrupole moment in geometrized units of the equatorial radius, the equatorial radius, the central density, the name of the equation of state used (following the convention in RNS and the condition on the mass that defines the model).

| Config. | Mass | | Rotation | | Deformation | | Model parameters | | | |
|---|---|---|---|---|---|---|---|---|---|---|
| | $[M_\odot]$ | $M/R$ | Freq. [Hz] | $a/R$ | $R_p/R$ | $q/R^3$ | $R$ (km) | $\rho_c$ (g cm$^{-3}$) | EoS | Condition |
| BWFX | 1.82 | 0.2836 | 622 | 0.054 24 | 0.9675 | 0.001 450 | 9.487 | $3.2 \times 10^{15}$ | FPS | Max. mass |
| SHFT | 1.44 | 0.1854 | 716 | 0.061 29 | 0.8972 | 0.002 829 | 11.43 | $1.25 \times 10^{15}$ | FPS | Typ. mass |
| KAFT | 1.41 | 0.1648 | 1000 | 0.086 64 | 0.7568 | 0.005 277 | 12.65 | $1.1 \times 10^{15}$ | FPS | Typ. mass |
| KALN | 2.72 | 0.2003 | 1000 | 0.1429 | 0.5703 | 0.010 016 | 20.05 | $6.1 \times 10^{14}$ | L | Min. mass |

deformation with a high rotation frequency. The equation of state FPS is more realistic because it produces more moderately stiff configurations, and it is therefore used for the other cases considered here.

The Black Widow pulsar has a rotation frequency of 622 Hz, and its mass has been constrained to $>1.66\,M_\odot$ (van Kerkwijk, Breton & Kulkarni 2011). For this reason, we chose the configuration that yielded the most massive neutron star using the equation of state FPS. The configurations SHFT and KAFT consider a typical neutron star mass of $1.4\,M_\odot$, and the extreme case of KALN was chosen with the minimum mass possible, which produced the maximum deformation. The equation of state L yields for the configuration KALN a value of the mass that is probably unrealistically high; however, we keep the configuration as an extreme case as a reference only.

## 4 DIRECT NUMERICAL COMPARISON OF THE METRIC COMPONENTS

We present here a comparison between the components of the exterior numerical metric produced by RNS with its analytical counterparts described in Section 2. The configuration KAFT was given as an input to RNS, as well as a grid of 401 cells in the radial direction and 201 cells in the polar direction.

### 4.1 Obtaining parameters and coordinates from the numerical solution

The Komatsu–Eriguchi–Hachisu scheme used by RNS uses the general form of a stationary and axisymmetric metric in quasi-isotropic coordinates. In order to compare the numerical solution with analytical metrics written in Boyer–Lindquist coordinates, we used the transformation provided by Brandt & Seidel (1996):

$$r_{\rm BL} = r_{\rm I}\left(1+\frac{M_{[g]}+a_{[g]}}{2r_{\rm I}}\right)\left(1+\frac{M_{[g]}-a_{[g]}}{2r_{\rm I}}\right), \tag{5}$$

where $r_{\rm I}$ is the radial coordinate in quasi-isotropic coordinates, $r_{\rm BL}$ is the radial coordinate in Boyer–Lindquist coordinates, and the subindex [g] emphasizes the use of geometrized units.

Given the angular frequency of rotation $\Omega$, the mass $M$, and the moment of inertia $\mathcal{I}$ computed by RNS, all in CGS units, the specific angular momentum $a$ in geometrized units of cm was computed as

$$a_{[g]} = \left(\frac{\mathcal{I}\Omega}{Mc}\right)_{[cgs]}. \tag{6}$$

For the mass quadrupole moment, we followed the discussion in, e.g. Pappas & Apostolatos (2012) and Doneva et al. (2014): RNS computes the second order multipole, and by an asymptotic expansion of the potentials that form the numerical solution, it is possible to isolate the contribution to the $r^{-3}$ terms that corresponds to the mass quadrupole moment, by subtracting the contribution of rotation, in a way that is analogous to equation (4).

### 4.2 Results of the comparison

Fig. 1 shows the fractional difference between each one of the metrics considered in this study (see Section 2) and the numerical solution by RNS, for the non-zero components of the metric evaluated at the equatorial plane (panels *a–e*), and the angular behaviour of some components evaluated at a fixed distance of $r = 20\,$km (panels *f–h*). As a reference, the Kerr solution is also shown.

In all cases, the solutions tend to agree more with increasing radial position. The asymptotic features in all the curves correspond to a change of sign in the fractional difference. The component $g_{t\phi}$ (panels *b* and *g*) show a clear distinction between the exact metrics with mass quadrupole moment (QM and MN) and the approximations. In the $g_{tt}$ component (panels *a*, *f*), QM, MN, HT and GB are very similar. The Fru16 metric becomes marginally better close to the surface of the neutron star, while the Kerr metric becomes insufficient in the same region. In the $g_{rr}$ component, HT is marginally worse than the rest of the metrics. We expect the differences in those three components to dominate over the other spacial components. These results are consistent with what Berti & Stergioulas (2004) found when comparing the components of the metric by Manko, Mielke & Sanabria-Gómez (2000) and the Kerr metric with the numerical metric by RNS, as well as the findings by Pappas (2017), who compared the numerical solution with another analytical solution and the HT metric.

Considering the information in the plots, and the expected numerical accuracy of the solution provided by RNS, we conclude that all the analytical metrics in Section 2 are consistent with the numerical solution. However, with this comparison, we cannot establish an order of accuracy between the metrics at large distances, or an order of accuracy at smaller distances other than the mentioned general distinction between exact and approximate metrics.

## 5 RAY-TRACING FOR LIGHT SCATTERING

### 5.1 Method

For the ray-tracing applications, we developed a software package called UJTI[1] that first calculates symbolically the geodesic equations given a axially symmetric metric, and then solves them numerically. We used an early version of the program in Oliva-Mercado et al. (2015). We start by calculating a general expression of the geodesic

[1] 'path' in Nawat language. The source code is available from http://cinespa.ucr.ac.cr.



Downloaded from https://academic.oup.com/mnras/article/505/2/2870/6276752 by UB Tuebingen user on 16 June 2021

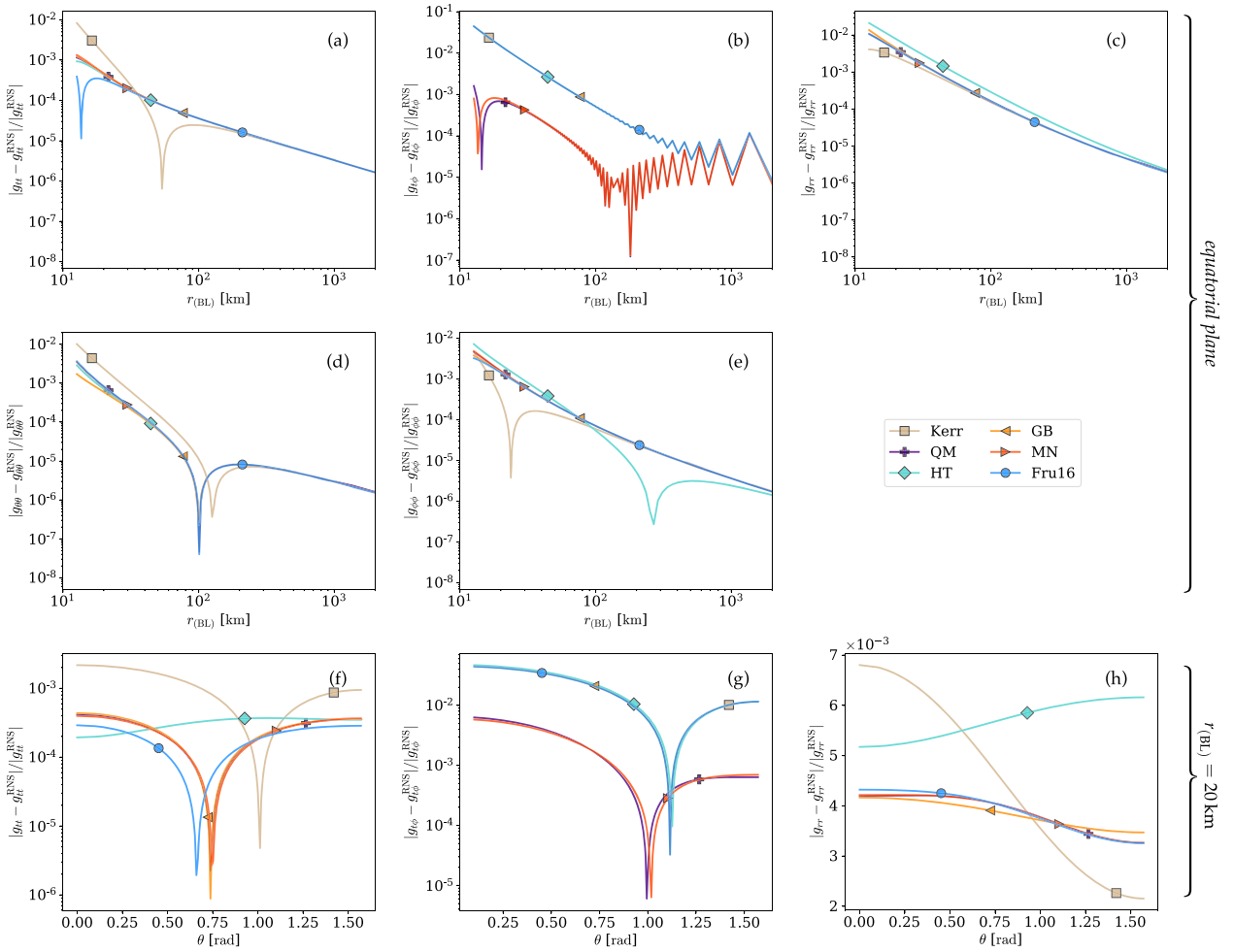



**Figure 1.** Direct numerical comparison of the metric components against the exterior numerical solution provided by RNS. Panels *a–e* show the radial behaviour and correspond to the equatorial plane ($\theta = 0$), while panels *f–h* show the angular behaviour and are evaluated at $r = 20$ km. All radii are expressed in Boyer–Lindquist (BL) coordinates. The configuration KAFT was used for this numerical comparison.

equations for the metric (2) in Boyer–Lindquist coordinates, yielding expressions that are dependent on the potentials $V$, $W$, $X$, $Y$, $Z$, and their derivatives. These expressions are then calculated for each metric, and numerically evaluated when solving the geodesic equations.

Using the Runge–Kutta–Fehlberg method (fourth order, with an error estimator of the fifth order) as described in Burden & Faires (2011), we compute the numerical solution of the geodesic equations

$$\frac{\mathrm{d}^2 x^\kappa}{\mathrm{d}\ell^2} = -\Gamma^\kappa_{\mu\nu}\frac{\mathrm{d}x^\mu}{\mathrm{d}\ell}\frac{\mathrm{d}x^\nu}{\mathrm{d}\ell}. \tag{7}$$

We set the wave vector $k^\mu$ of a photon that follows a null geodesic to $\mathrm{d}x^\mu/\mathrm{d}\ell$. The affine parameter $\ell$ can be fixed by considering the component $k^0 = \omega$ and then integrating to set $\ell \equiv t/\omega$, i.e. the affine parameter is taken as being proportional to the proper wavelength of the photon.

In all the applications considered in this paper, the geodesics are released parallel to each other from distant points. The null geodesic condition, $k^\mu k_\mu = 0$, is also imposed to the initial wave vector by normalizing it.

### 5.2 Light scattering results and discussion

#### *5.2.1 The relative importance of a and q*

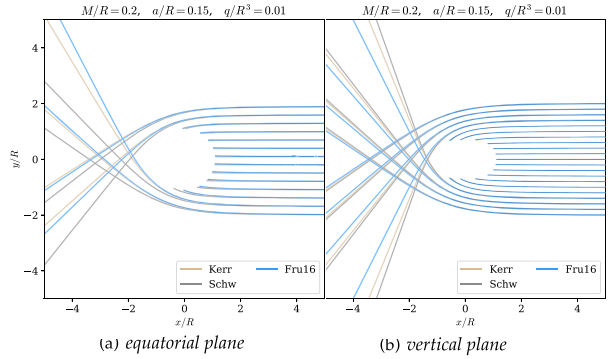
In order to explore the relative importance of $a$ and $q$ in light scattering, we trace rays with the Fru16 metric (that contains both parameters), the Kerr metric (which is the limit when $q = 0$), and the Schwarzschild metric (which is the limit when both $a$ and $q$ vanish). We took values of $M/R$, $a/R$, and $q/R^3$ that are consistent with the extreme values in Table 1, namely $M/R = 0.2$, $a/R = 0.15$, and $q/R^3 = 0.01$. The ratio of polar to equatorial radii $R_p/R$ was taken to be 0.9 for $q/R^3 = 0.003$.

Fig. 2 shows the results of this exercise. In the equatorial plane, the Schwarzschild metric yields, as expected, symmetric results, while the Kerr metric shows asymmetry product of frame dragging. The Fru16 metric also exhibits the same frame dragging as the Kerr metric, but the mass quadrupole moment increases slightly the deflection angle, so that the geodesics intersect at a slightly closer position from the neutron star.

The vertical plane in the same figure corresponds to the projection of the geodesics on to the $y/R = 0.2$ plane; the plane $y = 0$ was



Downloaded from https://academic.oup.com/mnras/article/505/2/2870/6276752 by UB Tuebingen user on 16 June 2021




(a) *equatorial plane* (b) *vertical plane*

**Figure 2.** Effect of the quadrupole moment as defined in the Fru16 metric.

not used because it contains the coordinate singularity of the $z$-axis in spherical-like coordinates. In the vertical plane, the situation is symmetrical respect to the mid-plane. The parameter $a$ in the Kerr metric has the effect of decreasing the deflection angle, which is decreased even further by the presence of $q$ in the Frutos metric.

#### *5.2.2 Differences between metrics in ray-tracing*

A parameter scan was performed for the rest of the metrics by considering $M/R = 0.2$, $a/R = \{0.06, 0.15\}$, and $q/R^3 = \{0.003, 0.01\}$. All four combinations of these parameters are shown in Fig. 3 for the equatorial plane, and only the more extreme cases in the vertical plane. $R_p/R$ (ratio of polar to equatorial radii) was taken as 0.9 for $q/R^3 = 0.003$, and 0.6 for $q/R^3 = 0.01$.

With the increase of $a$ (and fixed $q$), frame dragging is stronger and the geodesics in the equatorial plane tend to bend in the direction of rotation, as expected from the well-known behaviour of the null geodesics of the Kerr metric. Again, the vertical plane projections do not exhibit variation with $a$.

With the increase of $q$ (and fixed $a$), the deflection angle tends to increase in the equatorial plane, but this increase is metric-dependent. Fru16 and HT underestimate the effect of $q$ with respect to the exact solutions (MN and QM), while GB underestimates it for the geodesics that bend in favour of rotation but overestimates it in the geodesics that bend against rotation. We relate this result to the methods of approximation between metrics (GB uses a linear deviation from Kerr while Fru16 uses a multiplicative approach). In the vertical direction, GB slightly overestimates the effect of $q$, while Fru16 and HT underestimate it.

In general, the null geodesics of the expanded HT metric agree with the rest of the metrics, with the important exception of the case with high $a$ and low $q$, where the solutions are more similar to the Kerr metric and therefore, the Hartle–Thorne approximation starts not to be sufficient. According to Table 1, however, an increase in $a$ is accompanied with an increase in $q$ for the equations of state considered. The differences between the metrics quickly decay with increasing impact parameter, and, from the plots, they are more notable in the regions closer to the edge of the neutron star.

From these results, we conclude that the approximate metrics both underestimate and overestimate the results of the exact solutions. In most regions, the geodesics of the exact metrics lie in between the ones of GB and Fru16. Those metrics can then be used to do ray-tracing, and their difference can be used to estimate where the solution by the QM and MN metrics should lie. Based on these results as well, we believe that approximate analytical metrics provide better accuracy than a numerical integration of the geodesic equations that uses the numerical solution.

### 5.3 Numerical considerations

Fig. 4 shows a convergence study for the results in the preceding section. Specifically, we focus on the final positions of the photons that land on the surface of the neutron star for the equatorial plane in the case of $M/R = 0.2$, $a/R = 0.06$, $q/R^3 = 0.003$ (Fig. 3a), with increasing values of the tolerance in the Runge–Kutta–Fehlberg method, that defines the accuracy of the solution. The horizontal axis corresponds to the final $x$ position, and the vertical axis, to the difference between this final position and the lowest tolerance run ($\text{tol} = 10^{-16}$, i.e. the highest accuracy run). In general, this difference is higher in regions closer to the edge of the neutron star, in which the null geodesics are more affected by the general relativistic effects. The plot also shows the convergence characteristic of the Runge–Kutta–Fehlberg method. Similar plots for other metrics yield the same kind of convergence, and so, differences between metrics are mostly resolution-independent.

The next sections of this paper focus on several applications of ray-tracing that require the construction of a grid of initially parallel geodesics released from a long distance. We are interested in knowing the minimum accuracy (highest tolerance) required so that the initial and final positions of the photon converge within the size of a grid cell (hereafter, 'pixel'). In Fig. 4, dashed lines indicate the distance in $x$ between geodesics that land at the surface of the neutron star, i.e. how the size of one pixel is transformed (lensed) by space–time for a given grid size.

For the grids that we use in the next sections, a tolerance of $10^{-10}$ is enough to cover the neutron star with ∼106 pixels across (161 px grid) with at most one pixel of uncertainty; a tolerance of $10^{-12}$ is enough to cover it with ∼212 pixels across (321 px grid) with no uncertainty, or ∼424 pixels across (641 px grid) with one pixel of uncertainty. Finally, a tolerance of $10^{-14}$ is enough to cover it with ∼848 pixels across (1281 px grid) with no uncertainty.

Using a very low tolerance not only increases computing time but also requires too low values of the step size. This causes the numerical integration to stop in the regions close to the $z$ axis when the maximum numerical precision is reached. In the other hand, in determining the shape of hotspots, a too small grid introduces additional uncertainty merely by the discretization of the observer's plane. Considering these elements, we chose to use a tolerance of $10^{-10}$, and a grid of 1281 px across, which means that the uncertainty of the final positions of the photons is of ±4 px across, when comparing our results to observations.

Computing times are critical for ray-tracing applications, a fact that motivates the use of the oblate Schwarzschild+Doppler approximation for pulsars of rotation frequencies of ∼200 Hz (Bogdanov et al. 2019). For the metrics considered in this study, we crudely report the computing times of the (serial) execution of the light scattering applications in this section, in order to assess the practicality of use of each metric in more complex ray-tracing applications. If we call $\tau$ the computing time for tracing a geodesic for the expanded HT metric, the GB metric takes $\approx 1.15\tau$; the Fru16 metric, $\approx 2.7\tau$; the MN metric, $\sim 350\tau$; and the QM metric, $\sim 600\tau$, meanwhile, the Kerr metric takes $\sim 0.8\tau$, and the Schwarzschild metric, $\sim 0.3\tau$. The computing times for the exact solutions MN and QM are too high for practical application, which justifies the use of analytical approximations for studies that involve ray-tracing of rapidly-rotating neutron stars. Because of this, in the sections that follow, we restrict ourselves



Downloaded from https://academic.oup.com/mnras/article/505/2/2870/6276752 by UB Tuebingen user on 16 June 2021

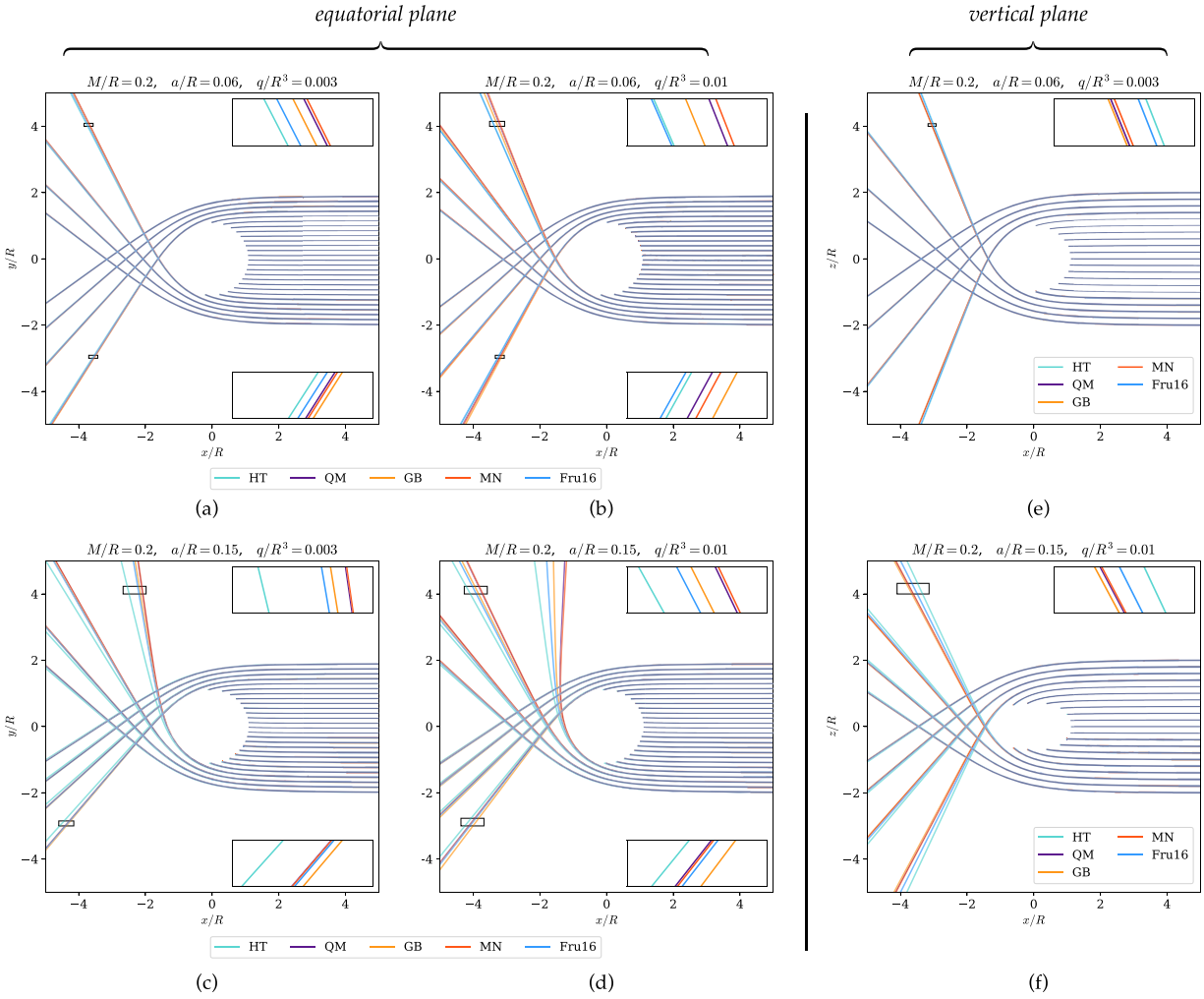



**Figure 3.** Light scattering for different metrics. The vertical plane considered in (e) and (f) is $y/R = 0.2$. Inset in each graph is a zoomed-in portion of the corresponding rectangle.

to study the applications of the approximate metrics (expanded HT, GB, and Fru16).

## 6 SHAPE OF THE NEUTRON STAR

For the rest of this paper, we consider some applications of ray-tracing for light emitted at the surface of a neutron star, as measured by a distant observer, for whom the rays arrive parallel (although in the code, we use a backwards-tracing algorithm that inverts this process). In this section, we determine the shape of the neutron star as seen by a distant observer. In Fig. 5, we describe our set-up. The observer is located at an inclination $i$ with respect to the equatorial plane of the neutron star.

### 6.1 Method: determination of the surface

We divide the observer's plane into a grid of null geodesics as previously discussed in Section 5.3, choosing a 1281 × 1281 px grid. Then, we backtrace null geodesics, focusing on the ones that originate from the surface of the neutron star. In a post-processing stage, the surface of the neutron star is also divided in regions of $\Delta\theta = \Delta\phi = 22.5°$, and the positions of the photons on the surface are classified; with the corresponding positions on the observer's plane forming the image.

We need a clear function for the surface of the neutron star, $r(\theta)$. A straightforward but computationally intensive approach would be a full search and fit from the numerical pressure or enthalpy field yielded by `RNS`, as explained in, e.g. Silva et al. (2021).

After examining the numerical pressure field, we can approximate the surface to an ellipsoid of a certain ratio of polar to equatorial radii ($R_p/R$) (see Lai, Rasio & Shapiro 1993, for a deeper look into this approximation). The equation $r(\theta)$ of an ellipsoid in polar coordinates (with $\theta = 0$ at the $z$-axis) is

$$\frac{r(\theta)}{R} = \left[1 + \left(\frac{R^2}{R_p^2} - 1\right)\cos^2\theta\right]^{-1/2}. \tag{8}$$

For small deformations, $R_p \sim R$ and so, we expand the right-hand side so that

$$\frac{r}{R} = 1 - \left(\frac{R}{R_p} - 1\right)\left(\frac{R}{R_p} + 1\right)\frac{\cos^2\theta}{2}. \tag{9}$$



Downloaded from https://academic.oup.com/mnras/article/505/2/2870/6276752 by UB Tuebingen user on 16 June 2021

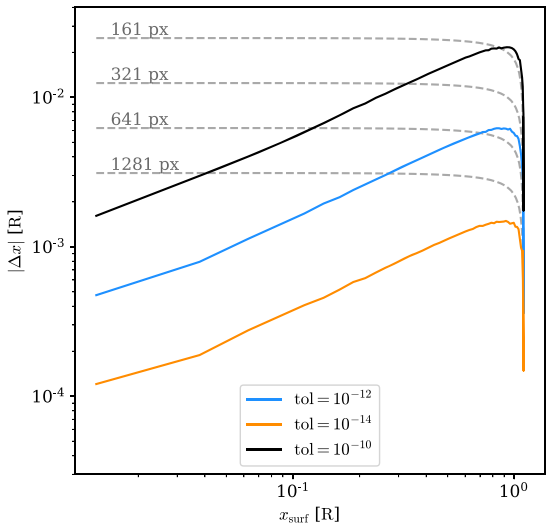



**Figure 4.** Convergence of the light-scattering results for the Fru16 metric. The horizontal axis is the final $x$ position of photons arriving at the surface of the neutron star, and the vertical axis is the difference between this final position and the lowest tolerance (maximum accuracy) run. Plots for the other metrics give a similar result.

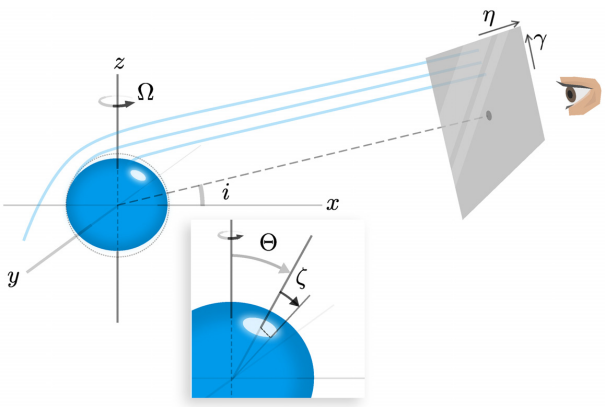



**Figure 5.** Set-up for ray-tracing. Geodesics are backwards-integrated to the observer, who is located at a long distance from the neutron star (hence, geodesics are parallel upon arrival), at an inclination $i$ with respect to the equatorial plane. The coordinates of the observation plane are $\eta$ and $\gamma$. In all the figures of this paper, the $x$-axis is chosen such that it coincides with the projection on to the equatorial plane of the line defined by the centre of the neutron star and the centre of the observation plane.

The second term in parenthesis can be approximated to 2. By using trigonometrical relations and considering the series expansion of $1/w := R_p/R$ around $w = 1$, we can put this relation in the form

$$\frac{r}{R} = \sin^2\theta + \frac{R_p}{R}\cos^2\theta, \tag{10}$$

which we use here to model the surface, given $R$ and $R_p/R$ from the RNS model. Equation (10) is the equation of state dependent form of the AlGendy–Morsink formula (AGM-EOSD; AlGendy & Morsink 2014). These authors also fitted the formula to several equations of state so that a relation is obtained, in terms of the angular momentum and the compactness of the neutron star only. This approach introduces further uncertainties due to the differences in shape produced by the equations of state, but it allows the bypass of the numerical computation of the interior solution, and it was used by the NICER mission (Riley et al. 2019). Other quasi-equation-of-state independent formulae have been built for this purpose (Silva et al. 2021; Morsink et al. 2007). In the rest of this article, we use both equations (10) and (8) and explore the differences in the most extreme cases. As the AlGendy–Morsink formula is widely used, we give priority to it in the analysis that follows, clearly marking the figures only if equation (8) is used instead of (10).

### 6.2 Results and comparison of the neutron star shape

Fig. 6 shows the surface of the neutron star as seen by a distant observer, for the configurations of Table 1. The shape of the neutron star becomes increasingly flattened with increasing rotation and quadrupole moment. The very high compactness shown in KALN greatly increases the area of the far side of the neutron star visible to the observer; this is also visible when comparing configurations BWFX and SHFT. By increasing rotation, the asymmetry of the image caused by frame dragging starts to become more apparent.

A caveat of these results is, upon close examination of Fig. 6, the existence of a missing region, one pixel wide, near the poles. This corresponds to the coordinate singularity of the $z$ axis. Due to the high resolution of the grid used, however, the effects of this singularity are minimized and can be neglected in the applications in the following sections.

The differences between the results yielded by the different metrics are negligible in configuration BWFX. They become barely visible in the configuration SHFT, i.e. with a pulsar of ∼700 Hz. Examining the differences in the image for KAFT and KALN, we see that the GB metric yields a more oblate object compared to the results yielded by the Fru16 metric. The biggest differences are concentrated in the rays that come to the observer from the edges and far side of the neutron star. For an inclination of 0°, this includes mainly the polar regions, precisely where the hotspots are expected to be located; for an inclination of 30°, the differences are concentrated in the rays that come from the Southern hemisphere and the top edge of the image, which includes the far side of the polar area. In Riley et al. (2019) and Miller et al. (2019), the models yielded a similar situation: an inclination of ≈54° with hotspots located in the Southern hemisphere.

We calculated the relative differences in the 'apparent area' or total subtended solid angle of the neutron star as seen by the distant observer. The rays in both the HT and GB metrics produce a slightly smaller total solid angle than the Fru16 metric (for KAFT, the differences are of about 0.25 and 0.5 per cent, respectively, while for KALN, around 0.6 and 1.2 per cent).

### 6.3 Effect of the surface formula on the shape

In configuration KALN, the ratio of polar to equatorial radius is 0.57, which is already too high for the approximations made in equation (10), and therefore explore the differences between the shapes obtained with equations (10) and (8). The result is shown in Fig. 7. For the configuration KALN, the differences are appreciable even in the non-relativistic plotting of the surface formulae. For both configurations KAFT and KALN, however, the differences are appreciable and of the same order as the differences between metrics. The ellipsoid formula has the general effect of increasing the sections of the far side of the neutron star that are visible to the observer, and to a lesser extent, reduce slightly the total solid angle subtended by



Downloaded from https://academic.oup.com/mnras/article/505/2/2870/6276752 by UB Tuebingen user on 16 June 2021

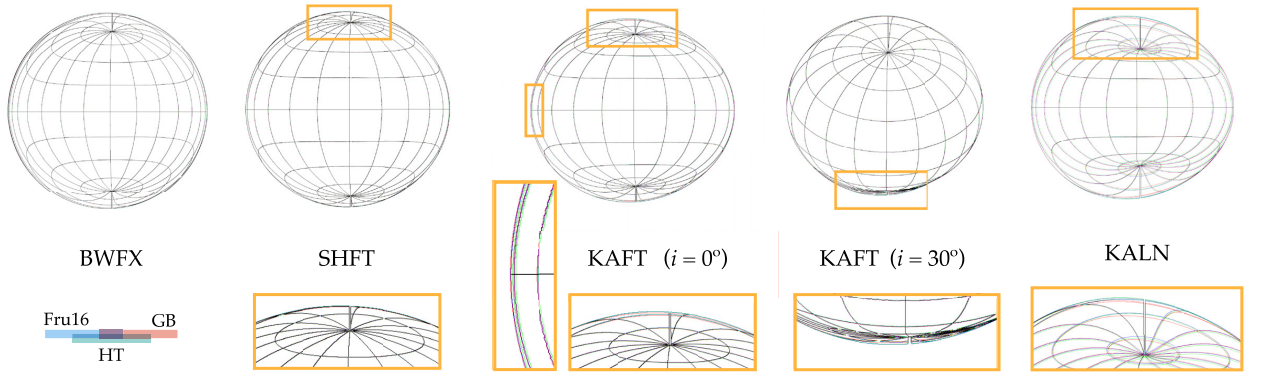



**Figure 6.** Shape of the neutron star as seen by a distant observer. For `BWFX`, `SHFT`, and `KALN`, the inclination angle is 0°. The parallels and meridians are drawn every 22.5°. The zoomed-in yellow rectangles show the regions with bigger differences between the metrics. The left side of the neutron star is receding from the observer, while the right side is approaching the observer. The observer's coordinates $(\eta, \gamma)$ have arbitrary scaling, but in this image, they have been normalized such that the *apparent* equatorial radii are the same; flattening can be compared across configurations.

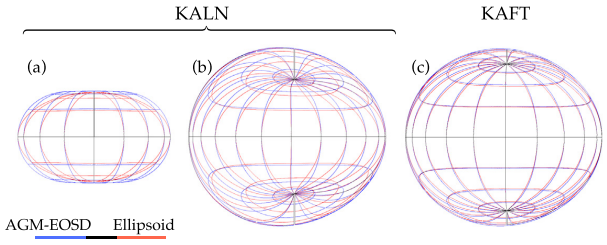



**Figure 7.** Comparison of surface formulae. For panel *a*, the non-relativistic shape of the neutron star according to the formulae is shown, while panels *b* and *c* use the Fru16 metric.

the neutron star. We refer to the consequences of these effects in the following sections.

## 7 THERMAL SPECTRUM

Observed thermal spectra of neutron stars can be used to constrain their masses and radii. In the approximation of a non-spinning, spherical neutron star, the Stefan–Boltzmann law can be used to calculate an apparent radius, given measurements of the bolometric flux and the effective temperature (see for example, Özel & Freire 2016). Then, the physical radius of the neutron star can be related to the apparent radius by considering lensing in the Schwarzschild space–time.

In a rapidly rotating neutron star, the effects of rotation and quadrupole moment have to be considered. With high-accuracy knowledge of the radii of the neutron stars (5–10 per cent, see Lattimer & Prakash 2001; Özel & Psaltis 2009), it is possible to constrain the equation of state of the neutron star. In a realistic system, however, the propagation of light through the stellar atmosphere and the environment has to be considered (see Heinke et al. 2006). Additionally, neutron stars with X-ray bursts require more complicated spectra, as discussed in detail in Suleimanov, Poutanen & Werner (2020). In Bauböck et al. (2015a), rotation and deformation were considered for rapidly rotating neutron stars (600 Hz) using the GB metric, and corrections were established for non-relativistic fits of the thermal spectrum. We investigate in this section the effects of higher spins and quadrupole moments, and the discrepancies between different approximate metrics, restricting ourselves to the simplest case of pure blackbody emission.

### 7.1 Method

#### 7.1.1 Gravitational and Doppler shift

First, the frequency shift due to rotation and the gravitational field has to be calculated, for which we follow Radosz, Augousti & Ostasiewicz (2008), and that we summarize as follows. The frequency $\omega$ of a photon as measured by an observer that moves with a four-velocity $U^\alpha$ is

$$\omega = -k_\alpha U^\alpha = -g_{\alpha\beta} k^\beta U^\alpha. \tag{11}$$

A static observer at infinity has a four-velocity $(U^\alpha_\infty) = (U^t_\infty, 0, 0, 0)$. The four-velocity can be normalized with the time-like geodesic condition so that $U_{t,\infty} U^t_\infty = -1$, yielding

$$U^t_\infty = \sqrt{-1/g_{tt}}. \tag{12}$$

An observer located at the surface of the neutron star, co-rotating with it at an angular frequency $\Omega \equiv 2\pi f_{\rm rot}$ has a four-velocity $(U^\alpha_{\rm surf}) = (U^t_{\rm surf}, 0, 0, U^\phi_{\rm surf})$. The definition of $\Omega$ also implies that

$$\Omega = \left(\frac{{\rm d}\phi}{{\rm d}t}\right)_{\rm surf} = \left(\frac{{\rm d}\phi}{{\rm d}\tau}\frac{{\rm d}\tau}{{\rm d}t}\right)_{\rm surf} = \frac{U^\phi_{\rm surf}}{U^t_{\rm surf}} \Rightarrow U^\phi_{\rm surf} = \Omega U^t_{\rm surf}, \tag{13}$$

where $\tau$ is the proper time measured by the observer. The normalization condition yields, for $U^t_{\rm surf}$,

$$U^t_{\rm surf} = \sqrt{\frac{-1}{g_{tt} + 2g_{t\phi}\Omega + g_{\phi\phi}\Omega^2}}. \tag{14}$$

The redshift $\mathbb{Z} = \omega_{\rm surf}/\omega_\infty - 1$ is then calculated for every geodesic that lands on the surface of the neutron star by making use of equations (11)–(14).

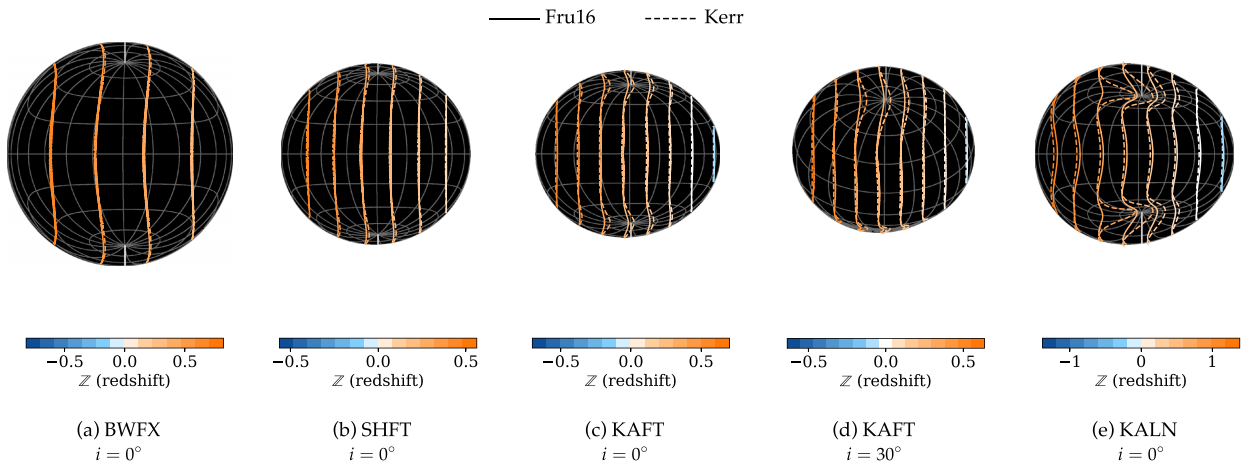
#### 7.1.2 Specific flux

Next, following the discussion in Bauböck et al. (2015a), we calculate the flux measured at infinity $F_\infty$ as

$$F_\infty(\omega_\infty) = \frac{1}{D^2}\iint I_\infty(\omega_\infty, \eta, \gamma)\,{\rm d}\eta\,{\rm d}\gamma, \tag{15}$$



Downloaded from https://academic.oup.com/mnras/article/505/2/2870/6276752 by UB Tuebingen user on 16 June 2021




(a) BWFX $i = 0°$ (b) SHFT $i = 0°$ (c) KAFT $i = 0°$ (d) KAFT $i = 30°$ (e) KALN $i = 0°$

**Figure 8.** Contours of equal redshift, as computed with the Fru16 and Kerr metrics, showing the effect of the mass quadrupole moment. The observer's coordinates $(\eta, \gamma)$ have arbitrary scaling, but here are normalized such that the neutron star equatorial (physical) radii are the same.

where $D$ is the distance from the observer at infinity to the neutron star. $I_\infty$ is the intensity, that we take as the blackbody intensity, as seen by an observer at the surface. The quantity $I/\omega^3$ is Lorentz invariant, so,

$$\frac{I_\infty(\omega_\infty)}{\omega_\infty^3} = \frac{I_{\rm surf}(\omega_{\rm surf})}{\omega_{\rm surf}^3} \tag{16}$$

and, defining $f_r := \omega_\infty/\omega_{\rm surf}$, we can finally evaluate the flux as

$$F_\infty(\omega_\infty) = \frac{1}{D^2}\iint f_r^3\, I_{\rm surf}\left(\frac{\omega_\infty}{f_r}\right) {\rm d}\eta\, {\rm d}\gamma. \tag{17}$$

The flux reported here has arbitrary units, and so, the choices of the distance to the observer and angular size of the neutron star are also arbitrary.

### 7.2 Results of gravitational redshift

In Fig. 8, we present the distribution of $\mathbb{Z}$ on the surface of the neutron star, calculated using the Fru16 and the Kerr metrics. For the configurations `KAFT` and `KALN` there is a net blueshift on the side of the neutron star approaching the observer. With increasing rotation, the Doppler shift due to rotation starts dominating over the purely gravitational redshift (which is axisymmetrical). This is the case despite the higher compactness of `KALN` relative to `KAFT`. The contour lines calculated with the Kerr metric and the oblate surface depart considerably from the Fru16 case around the poles with increasing rotation. In Fig. 2(b), we showed how the quadrupole moment reduces the deflection angle near the poles, which also has the effect of reducing the redshift.

### 7.3 Results and discussion of the thermal spectra

The thermal spectrum of `BWFX` (Fig. 9) was built with similar parameters than those used in Bauböck et al. (2015a). The inclination between the observer and the rotation axis is 0° in all cases. The spectrum is simultaneously broadened towards lower frequencies and redshifted due to the increase in apparent area and the presence of gravitational redshift, when comparing it to the (non-relativistic) surface spectrum (here calculated by using the Minkowski metric). When increasing the spin, however, the peak of the spectrum becomes closer to its surface value, although the whole curve continues to be broadened and redshifted. This is a result of the Doppler shift from rotation becoming more dominating compared to the purely gravitational redshift: when the integration over the solid angle is carried out, the blueshifted areas partially compensate the redshift. This means that in principle, the corrections to the peak temperature of a rapidly rotating neutron star become smaller compared to the necessary corrections for moderate rotation.

Each panel in Fig. 9 shows in the bottom the relative difference between the Kerr, HT, and GB metrics, and the Fru16 metric. These differences have their origin in both the total solid angle subtended by the neutron star and the gravitational redshift distribution.

In the case of the configuration `BWFX`, the GB metric and the Fru16 metric are virtually indistinguishable, while the difference in the peak specific flux between those metrics and the expanded HT metric remain below 0.5 per cent. That means that our results agree completely with those presented in Bauböck et al. (2015a). For the configuration `SHFT`, the differences in the peak between all the metrics account for less than 1 per cent, while in the configurations `KAFT` and `KALN` they are of about 0.5 per cent and 2 per cent, respectively.

Although a full interpretation of the origins of the differences between metrics with quadrupole moment becomes complicated because of the calculations involved, in general terms, the relative differences can be explained as follows. Following equation (17), the differences in redshift become increasingly important at high frequencies, where the flux suffers metric-dependent shifts. For low frequencies, the differences in the total subtended solid angle dominate (which explains the difference of a factor). Since HT produces a smaller total solid angle in comparison to Fru16, the flux is lower as well. The relative differences between the results for the Kerr metric, and GB or Fru16 increase for high frequencies in the most extreme cases. This can be explained by the differences in redshift shown in Fig. 8 due to the effect of the quadrupole moment.

We also computed the spectrum for configuration `KAFT` using the ellipsoid surface formula. The results are displayed in Fig. 10(a) and are very similar to Fig. 9(c). By comparing the curves yielded by both formulae using the Fru16 metric (Fig. 10b), a relative difference of about 2 per cent becomes apparent, which means that the use of a realistic surface formula can have a bigger impact than the use



Downloaded from https://academic.oup.com/mnras/article/505/2/2870/6276752 by UB Tuebingen user on 16 June 2021

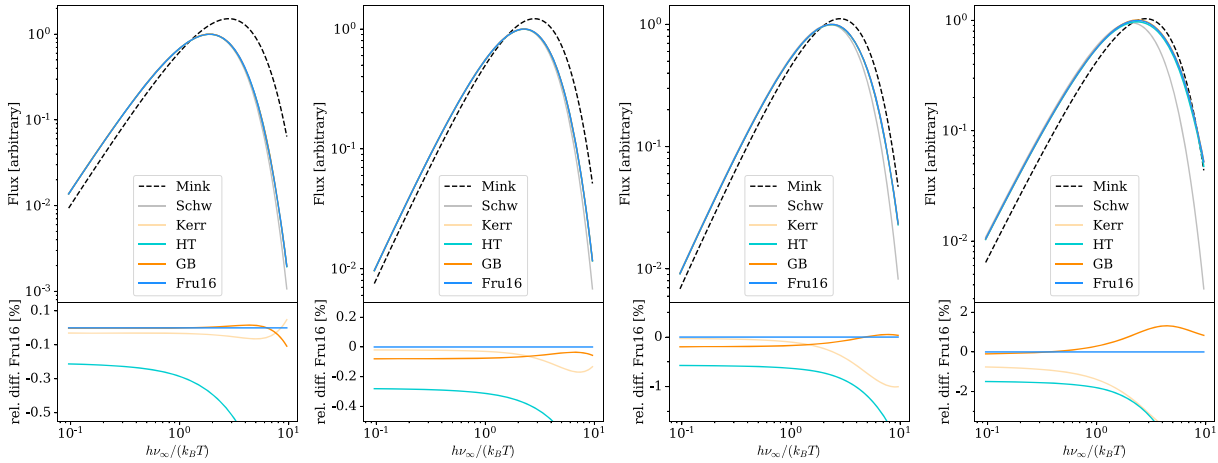



**Figure 9.** Thermal (blackbody) spectrum for different neutron stars. The relative difference with the Fru16 metric, $100 \times (F - F_{\rm Fru16})/F_{\rm Fru16}$, is shown in the bottom. The fluxes are normalized to the maximum of $F_{\rm Fru16}$.

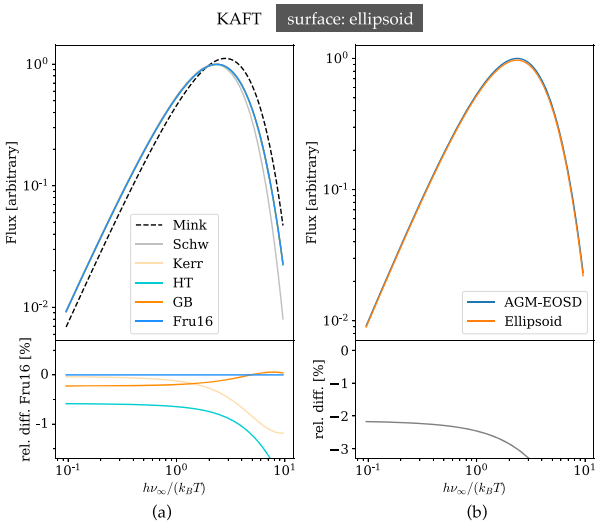



**Figure 10.** (a) Spectrum computed with the ellipsoid surface formula. (b) Difference between the spectra computed with both surface formulae, using the Fru16 metric.

of a realistic metric in calculating the thermal spectrum. Again, this difference arises from both the fact that the ellipsoid formula yields an observed smaller solid angle than the one yielded by the AGM-EOSD formula (cf. Fig. 7), and that the photons become more redshifted as they travel through regions closer to the origin and therefore with stronger space–time curvature.

These results mean that when calculating the effective temperature of a very rapidly rotating neutron star and fitting the spectrum to a blackbody, apart from the corrections given in Bauböck et al. (2015a), additional relative differences of a the order of 1 per cent have to be taken into account due to the approximation of space–time used, and similar, additional values for the use of different surface approximations. The biggest differences between space–time models appear at high frequencies, where there is a better opportunity to use them for constraining the value of the quadrupole moment only if a realistic surface formula is used.

## 8 PULSE PROFILES

As stated earlier, pulse profile modelling is an important technique in the determination of the neutron star parameters. In this section, we compute the light curve associated to a hotspot, and study the effects of the neutron star parameters and metrics used for performing the ray-tracing. According to the results reported in Riley et al. (2019) and Miller et al. (2019), the shape, number, and location of hotspots on the surface of a neutron star can be complex, and it does not necessarily conform to the classical picture of two antipodal sources. For this reason, we concentrate on the signal emitted by individual hotspots.

### 8.1 Method: modelling hotspot emission

For simplicity, we consider an individual hotspot of a given shape and location on the surface of the neutron star, and that emits monochromatically [so that only for one frequency, we set $I_{\rm surf}(\omega_{\rm surf}) \equiv$ const in equation (17)]. We focus on circular hotspots, but we also calculated the pulse profile of a crescent-shaped hot area, such as the ones obtained in the final models of Riley et al. (2019). A circular hotspot is characterized by its angular radius $\zeta$ and its colatitude $\Theta$, measured with respect to the rotation axis, as shown in the zoomed-in portion of Fig. 5.

First, we divide the observer's plane into a grid of pixels as explained in Section 6. We also discretize a full revolution of the neutron star into steps of $\Delta\phi_{\rm ns} = 0.5^\circ$.

We calculate the time that it takes for photons emitted from the hotspot to reach the observer as

$$t_{\rm arrival} = t_{\rm grav} + t_{\rm rot}. \tag{18}$$

Here, $t_{\rm grav}$ is the traveltime between the surface of the neutron star and the observer, and $t_{\rm rot} = \phi_h/(2\pi f)$ is the time at which the photons are emitted as the hotspot rotates; $\phi_h$ is the azimuth of the centre



Downloaded from https://academic.oup.com/mnras/article/505/2/2870/6276752 by UB Tuebingen user on 16 June 2021

of the hotspot measured with respect to the $x$-axis (i.e. the axis that coincides with the normal to the observer's plane when the inclination is zero). For simplicity, and given that the observer is located at an arbitrary distance from the hotspot, we use the time of arrival of the photon that lands in the center of the observer's plane when $\phi_h = 0$ as a reference time, so that we henceforth use $\Delta t_{\rm arrival}$, the difference in time of arrival. We calculate $\Delta t_{\rm arrival}$ for each discretized azimuthal position, and for every point of the hotspot that reaches the observer's discretized plane.

Then, we collect all photons that reach the observer's plane in an interval $\Delta t_{\rm expos} = \Delta\phi_{\rm ns}/(2\pi f)$, in analogy to the exposure time of a detector located there. These photons form the image of the hotspot. With the image of the hotspot, we calculate the total flux emitted from the hotspot, as done in Section 7, as a function of time (light curves).

Riley et al. (2019) and Miller et al. (2019) investigated not only circular hotspots, but also configurations of higher complexity, like crescent-shaped hotspots. Miller et al. (2019) also considered oval hotspots with allowed overlapping.

We decided to take the same parameters as reported in Riley et al. (2019) as a reference to study the light curve of a crescent-shaped hotspot of a kilohertz pulsar. In this case, the crescent is formed by subtracting two circular-shaped hotspots, the superseding member (subscript $s$) and the ceding member (subscript $c$). An additional parameter in this case is the difference in azimuthal position between the two members.

### 8.2 Results and comparison of the pulse shapes

#### *8.2.1 Effects of the neutron star and hotspot configurations*

Fig. 11 shows the light curves for a circular hotspot located at $\Theta = 45^\circ$, and an angular radius of $\zeta = 10^\circ$, viewed from an inclination of $i = 0^\circ$. The gravitational lensing of the surface causes the pulse to be visible at all times, in contrast to the dashed curve (that goes to zero), which corresponds to a non-relativistic treatment, and was calculated by ray-tracing with the Minkowski metric.

With increasing rotation and quadrupole moment, there are several clearly visible effects. A phase shift with respect to the non-relativistic light curve is due to the differences in time of arrival of the signal caused by the curvature of space–time (including frame dragging). The rising of the peak of the pulse compared to the non-rotating (Schwarzschild) case is product of the Doppler boost caused by rotation. These two effects were also seen in Poutanen & Beloborodov (2006) and Psaltis & Özel (2014). In configurations `KAFT` and `KALN`, the phase shift (with respect to Minkowski) is specially visible: the pulse is already descending when the Minkowski counterpart is ascending. The Doppler boost is increasingly more apparent with rotation when comparing the peaks of the profile across configurations. Additionally, we see that the flux is overall lower than its non-relativistic counterpart for configuration `BWFX`, and increasingly higher with rotation and quadrupole moment in the other configurations. This is simply due to the fact that a flat space–time produces no redshift, and so, $f_r = 1$ in (17), whereas for curved space–times, $f_r < 1$. High compactness and high-mass quadrupole moment increases the apparent area of the hotspot due to gravitational lensing and flattening. This can be seen when comparing the general relativistic profiles of configurations `KAFT` and `KALN` with their respective non-relativistic counterparts, as well as comparing the areas of the surface grids for the same configurations in Fig. 8.

We also tried varying the angular radius of the hotspot, with values of $5^\circ$, $10^\circ$, and $15^\circ$, finding essentially no difference between the profiles except for a different normalization due to the variation in area. These results are not shown in our figures, but are in agreement with the findings of Bauböck, Psaltis & Özel (2015b), who found that hotspots with angular radii of $\lesssim 18^\circ$ yield very similar profiles, leading to errors of $\lesssim 10$ per cent when used for determining the radius of the neutron star.

#### *8.2.2 Effects of the use of different metrics*

As with the other applications presented in this paper, the differences between metrics are only present in the configurations with higher spin. The lower panels in for each configuration plot in Fig. 11 show the absolute difference between each metric and the Fru16 metric. The presence of a grid introduces resolution-dependent noise in the curve, and so, a moving average and its corresponding standard deviation were calculated to show the overall behaviour of the difference (the flux is not averaged). For the configuration `BWFX`, the differences between metrics are negligible. For the configurations `KAFT` and `KALN`, the differences shown are bigger than their standard deviation, and for `SHFT`, they are of the same order of magnitude.

These differences between metrics are caused by differences in redshift, time of arrival and shape of the neutron star, which we discussed in the preceding sections. Therefore, hotspots that move close to the edge of the image as seen by the observer produce the biggest differences on the profile. In particular, the hotspot configuration selected in Fig. 11 ($\Theta = 45^\circ$, $\zeta = 10^\circ$) with an inclination of $i = 0^\circ$, goes into an area of high difference. By comparing the result yielded by the Kerr metric and the HT, GB, and Fru16 metrics, we determine that the difference arises due to the presence of the quadrupole moment. At that point, the hotspot is at the far side of the neutron star as seen by the observer, and close to the edge of the image, where the photons arriving to the observer are emitted more tangent to the surface, spend more time in the strong gravitational field and therefore are also deflected the most. Hotspots that move into those regions are therefore more likely to be strongly influenced by the quadrupole moment. In Fig. 12(a), a hotspot at same location is shown, but with an inclination of $i = 30^\circ$. As the hotspot moves into the far side of the neutron star with respect to the observer, the same differences arise, but upon comparison with Fig. 11(c), they are less important, because the hotspot is farther away from the edge of the image.

Apart from the differences close to the valley of the profile, there are some differences at the peak of the profile, but only significant in the most extreme configurations. These differences arise due to the differences in redshift as the quadrupole moment becomes increasingly important. In that region, the results from GB and Fru16 agree, while HT and Kerr underestimate the peak of the profile.

#### *8.2.3 Crescent-shaped hotspots*

Fig. 12(b) presents the results for a crescent shaped hotspot, observed with an inclination of $i = 0^\circ$. The shape of the pulse changes slightly (see e.g. the rounding of the valley for the Minkowski case, compared to Fig. 11c). The differences are similar for the region discussed in the previous paragraphs, but the narrower shape of the crescent increases the importance of the time of arrival and redshift (as a narrower range of frequencies and source locations are integrated at a time), resulting in the increase of the differences between metrics also in the peak of the profile.



Downloaded from https://academic.oup.com/mnras/article/505/2/2870/6276752 by UB Tuebingen user on 16 June 2021

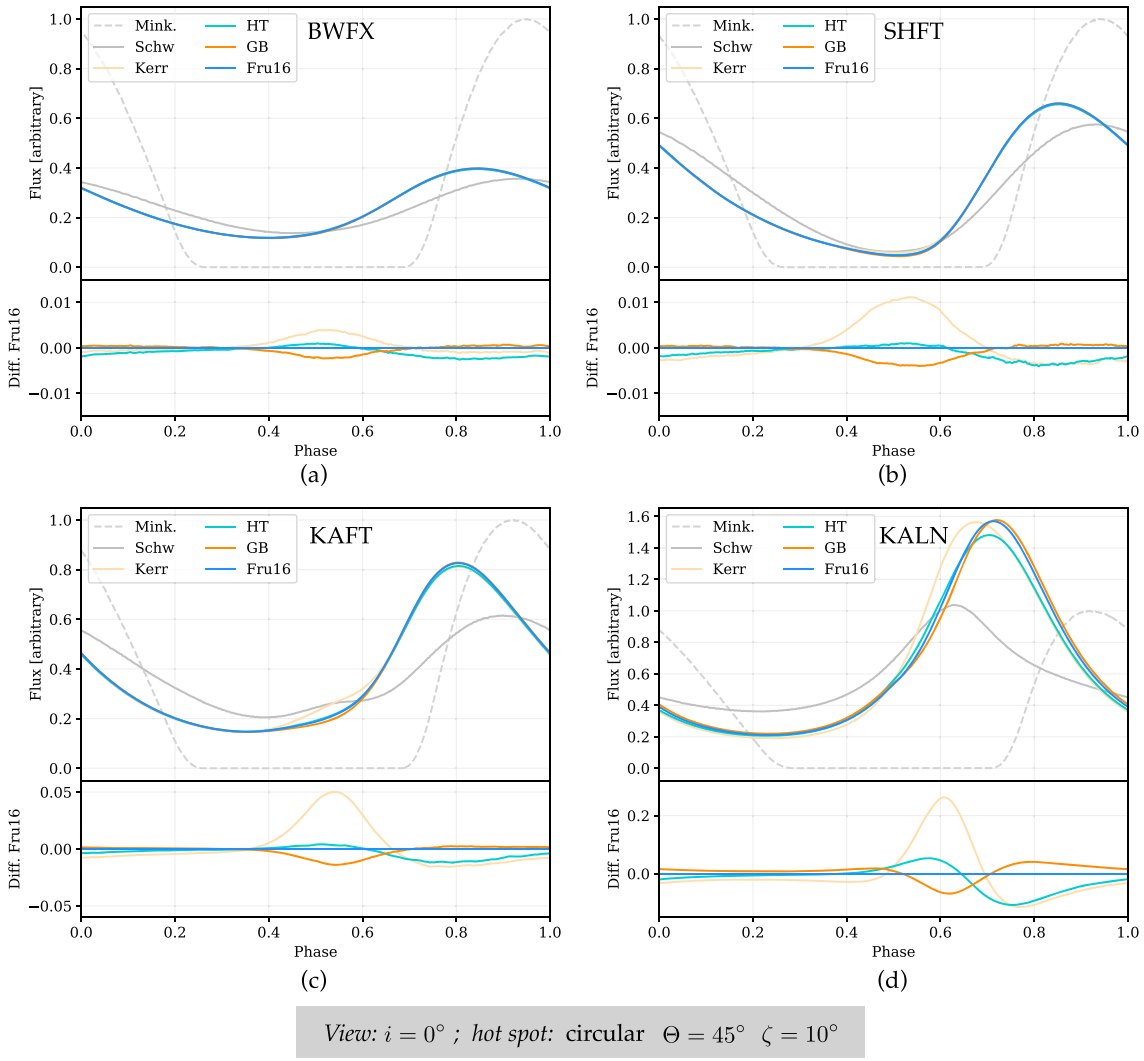



**Figure 11.** Light curves from hotspots: comparison of the neutron star configurations and metrics.

### *8.2.4 Comparison of surface formulae*

We also include the calculation of a profile for configuration KALN using the ellipsoid surface formula, the result of which is shown in Fig. 13(a). The differences between the results from the metrics increase slightly (the departure from the Kerr result is specially notable), but the general features discussed in the previous paragraphs are preserved. Fig. 13(b) shows the differences between the results yielded by the two surface formulae. There are marked differences at the peak of the profile, bigger than the differences between metrics at the peak, a result that highlights the need for choosing a realistic surface formula for modelling pulses under these circumstances. However, the pulse shape remains unchanged at the valley, which means that the differences caused by the treatment of the quadrupole moment between the different metrics are significant, independently from the surface formula used. Theoretically, this particular hotspot configuration could serve as a way of constraining the mass quadrupole moment or a way to probe the accuracy of approximations to the space–time around a neutron star.

### *8.2.5 Conclusions*

From the preceding discussion, we conclude that in the case of observationally known pulsars (rotation frequencies $\lesssim$700 Hz), the expanded HT metric yields sufficiently accurate pulse shapes. This is a consequence of the findings we discussed in Section 5.2, namely, that the HT metric yields accurate results if both $a$ and $q$ increase. The quadrupole moment is, however, dependent on the equation of state (we only examined two cases) and other factors like the internal magnetic field pressure. Studies that consider a wide range of values of $a$ and $q$ should use a more accurate approximation than HT. For rotation frequencies $\gtrsim$700 Hz also more accurate metrics than HT are needed. As discussed in Section 5, the results of GB and Fru16 shown here can be used to estimate the results that the exact solutions would yield without the increased computational cost. We showed that the differences between the results yielded by the metrics are relatively small but significant, and occur mostly when the hotspot is located near the edge of the neutron star image as seen by the observer (close to the valley of the light curve), but also at the peak, due to



Downloaded from https://academic.oup.com/mnras/article/505/2/2870/6276752 by UB Tuebingen user on 16 June 2021

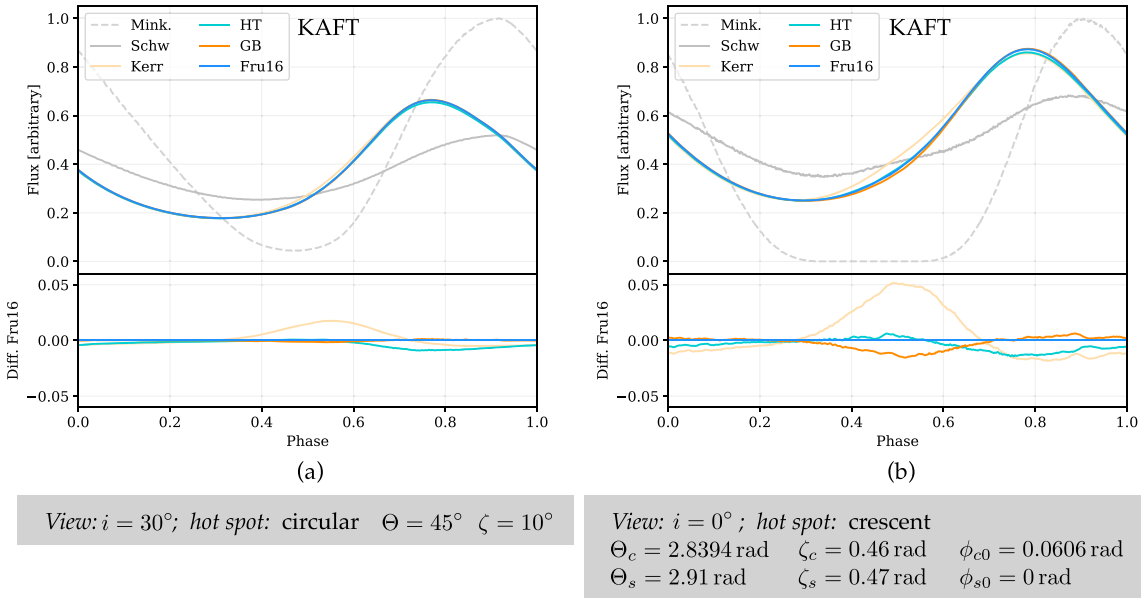



**Figure 12.** Light curves from hotspots: effect of the inclination with respect to the observer.

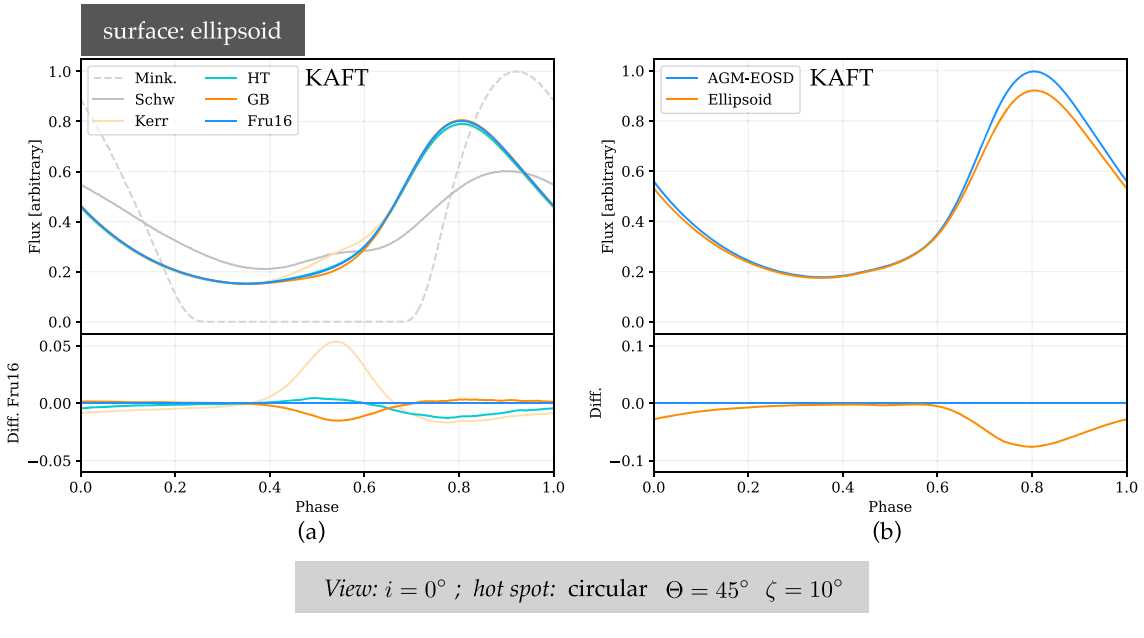



**Figure 13.** (a) Light curves computed with the ellipsoid surface formula. (b) Differences between formulae, for the Fru16 metric.

the differences in redshift. We also showed that surface formulae can also yield significant differences, more important when closer to the peak.

## 9 SUMMARY AND CONCLUSIONS

We have compared a catalogue of different metrics that describe the exterior space–time around a neutron star, including the numerical solution provided by the code RNS. For parameter ranges of mass, specific angular momentum and quadrupole moments that correspond to rapidly rotating neutron stars of rotation frequencies of $\lesssim$1 kHz, we found the following:

(i) All the metrics are consistent with the numerical solution, but we could not use it to discriminate between them.

(ii) The GB and Fru16 metrics provide excellent approximations compared to the exact solutions by Quevedo–Mashhoon and Manko–Novikov for ray-tracing, although the expanded Hartle–



Downloaded from https://academic.oup.com/mnras/article/505/2/2870/6276752 by UB Tuebingen user on 16 June 2021

Thorne metric provides a reasonable approximation and the lowest computing time.

(iii) The biggest differences between the results yielded by the metrics are found in the more extreme rotating configurations, and for regions closer to the edge of the neutron star as seen by the observer.

(iv) The differences between metrics start to be relevant at rotational frequencies of $\sim$700 Hz, they are negligible for frequencies of $\sim$600 Hz (which means that our results agree with previous studies) and they become more important at around $\sim$1000 Hz.

(v) Due to the dominance of the rotational Doppler shift, the corrections to the thermal spectrum of a rapidly rotating neutron star get smaller than in the slow rotation case, which is dominated by pure gravitational redshift.

(vi) The discrepancies between metrics in the determination of the peak of the thermal spectrum of a neutron star are of the order of 1 per cent for rapid rotation.

(vii) For pulsar profile modelling of observable pulsars (rotation frequencies of $\lesssim$700 Hz), the expanded Hartle–Thorne metric yields sufficiently accurate pulse shapes when compared to higher order approximations, while keeping the shortest computing time.

(viii) Hotspots that go through regions near the visible edges of the neutron star (corresponding to the valley of the pulse) are the most affected by the treatment of the mass quadrupole moment, and therefore could theoretically be used to constrain its value or discriminate between space–time models.

## ACKNOWLEDGEMENTS

GAO wishes to thank all the members of the Theoretische Astrophysik group of the University of Tübingen, in particular to Sourabh Nampalliwar, Arthur Suvorov, Daniela Doneva and Kostas Kokkotas, for their valuable suggestions for improving the ray-tracing applications. We wish to thank Javier Bonatti-González for the ideas and input during the development of this work and the anonymous referee for their valuable comments and suggestions.

## DATA AVAILABILITY

The data analysed in this article can be generated by means of the software package UJTI that we developed, the source code of which is publicly available at http://cinespa.ucr.ac.cr.

## REFERENCES

AlGendy M., Morsink S. M., 2014, ApJ, 791, 78
Arnett W. D., Bowers R. L., 1977, ApJS, 33, 415
Bauböck M., Psaltis D., Özel F., Johannsen T., 2012, ApJ, 753, 175
Bauböck M., Özel F., Psaltis D., Morsink S. M., 2015a, ApJ, 799, 22
Bauböck M., Psaltis D., Özel F., 2015b, ApJ, 811, 144
Berti E., Stergioulas N., 2004, MNRAS, 350, 1416
Bogdanov S. et al., 2019, ApJ, 887, L26
Boshkayev K., Quevedo H., Ruffini R., 2012, Phys. Rev. D, 86, 064043
Brandt S. R., Seidel E., 1996, Phys. Rev. D, 54, 1403
Burden R., Faires J., 2011, Numerical Analysis. Cengage Learning, Boston
Butterworth E. M., Ipser J. R., 1976, ApJ, 204, 200
Cadeau C., Morsink S. M., Leahy D., Campbell S. S., 2007, ApJ, 654, 458
Capderou M., 2014, Handbook of Satellite Orbits. Springer International Publishing, Cham
Cook G. B., Shapiro S. L., Teukolsky S. A., 1992, ApJ, 398, 203
Doneva D. D., Yazadjiev S. S., Stergioulas N., Kokkotas K. D., 2014, ApJ, 781, L6
Frutos-Alfaro F., 2016, Int. J. Astron. Astrophys., 6, 334 (Fru16)
Frutos-Alfaro F., 2019, Gen. Relativ. Gravit., 51, 46
Gair J. R., Li C., Mandel I., 2008, Phys. Rev. D, 77, 024035
Glampedakis K., Babak S., 2006, Class. Quantum Grav., 23, 4167
Hartle J. B., Thorne K. S., 1968, ApJ, 153, 807
Heinke C. O., Rybicki G. B., Narayan R., Grindlay J. E., 2006, ApJ, 644, 1090
Komatsu H., Eriguchi Y., Hachisu I., 1989, MNRAS, 237, 355
Laarakkers W. G., Poisson E., 1999, ApJ, 512, 282
Lai D., Rasio F. A., Shapiro S. L., 1993, ApJS, 88, 205
Lattimer J. M., Prakash M., 2001, ApJ, 550, 426
Lorenz C. P., Ravenhall D. G., Pethick C. J., 1993, Phys. Rev. Lett., 70, 379
Lukes-Gerakopoulos G., Apostolatos T. A., Contopoulos G., 2010, Phys. Rev. D, 81, 124005
Manko V. S., Novikov I. D., 1992, Class. Quantum Grav., 9, 2477
Manko V. S., Mielke E. W., Sanabria-Gómez J. D., 2000, Phys. Rev. D, 61, 081501
Miller M. C. et al., 2019, ApJ, 887, L24
Miller M. C., Lamb F. K., 1998, ApJ, 499, L37
Morsink S. M., Leahy D. A., Cadeau C., Braga J., 2007, ApJ, 663, 1244
Nättilä J., Pihajoki P., 2018, A&A, 615, A50
Oliva-Mercado G. A., Bonatti-González J., Cordero-García I., Frutos-Alfaro F., 2015, Rev. Mat. Teor. Apl., 22, 255
Özel F., Psaltis D., 2009, Phys. Rev. D, 80, 103003
Özel F., Freire P., 2016, ARA&A, 54, 401
Pappas G., 2017, MNRAS, 466, 4381
Pappas G., Apostolatos T. A., 2012, Phys. Rev. Lett., 108, 231104
Pechenick K. R., Ftaclas C., Cohen J. M., 1983, ApJ, 274, 846
Pihajoki P., Mannerkoski M., Nättilä J., Johansson P. H., 2018, ApJ, 863, 8
Poutanen J., Beloborodov A. M., 2006, MNRAS, 373, 836
Poutanen J., Gierliński M., 2003, MNRAS, 343, 1301
Psaltis D., Özel F., 2014, ApJ, 792, 87
Quevedo H., 1990, Fortschritte der Phys., 38, 733
Raaijmakers G. et al., 2019, ApJ, 887, L22
Radosz A., Augousti A. T., Ostasiewicz K., 2008, J. Phys. Conf. Ser., 104, 012008
Riley T. E. et al., 2019, ApJ, 887, L21
Silva H. O., Pappas G., Yunes N., Yagi K., 2021, Phys. Rev. D, 103, 063038
Stergioulas N., Friedman J. L., 1995, ApJ, 444, 306
Suleimanov V. F., Poutanen J., Werner K., 2020, A&A, 639, A33
van Kerkwijk M. H., Breton R. P., Kulkarni S. R., 2011, ApJ, 728, 95
Vincent F. H. et al., 2018, ApJ, 855, 116
Watts A. L. et al., 2016, Rev. Mod. Phys., 88, 021001

## APPENDIX: EXTERIOR SPACE–TIMES

### A1 Quevedo–Mashhoon (QM) metric

We present here the version of the Quevedo–Mashhoon metric with the parameters written as the mass ($M$), rotation ($J = Ma$), and mass quadrupole parameter

$$q_{\rm QM} := -\frac{15q}{2(\sigma^2/M^2)^{3/2}M^3}.$$

This space–time in prolate coordinates $(t,\ x,\ y, \phi)$ is given by

$$\begin{aligned} \mathrm{d}s^2 &= -f(\mathrm{d}t - \omega \mathrm{d}\phi)^2 \qquad \text{(A1)} \\ &\quad + \frac{\sigma^2}{f}\left[\mathrm{e}^{2\gamma}(x^2-y^2)\left(\frac{\mathrm{d}x^2}{x^2-1}+\frac{\mathrm{d}y^2}{1-y^2}\right)\right. \\ &\quad \left. + (x^2-1)(1-y^2)\mathrm{d}\phi^2\right] \\ &= -V\mathrm{d}t^2 + 2W\mathrm{d}t\mathrm{d}\phi + X\mathrm{d}x^2 + Y\mathrm{d}y^2 + Z\mathrm{d}\phi^2, \qquad \text{(A2)} \end{aligned}$$



Downloaded from https://academic.oup.com/mnras/article/505/2/2870/6276752 by UB Tuebingen user on 16 June 2021

where

$$
\begin{aligned}
f &= \frac{\mathcal{R}}{\mathcal{L}} e^{-2\psi}, \\
\omega &= -2\left(a + \sigma \frac{\mathcal{M}}{\mathcal{R}} e^{2\psi}\right), \\
\mathrm{e}^{2\gamma} &= \frac{1}{4}\left(1 + \frac{M}{\sigma}\right)^2 \frac{\mathcal{R}}{(x^2-1)} e^{2\chi}, \\
\mathcal{R} &= a_+ a_- + b_+ b_-, \\
\mathcal{L} &= a_+^2 + b_+^2, \\
\mathcal{M} &= \left[x(1-y^2)(\lambda+\eta)a_+ + y(x^2-1)(1-\lambda\eta)b_+\right], \\
\psi &= q_{\rm QM} P_2 Q_2, \\
\chi &= \frac{1}{2}(1+q_{\rm QM})^2 \ln\left[\frac{x^2-1}{x^2-y^2}\right] \\
&\quad + 2q_{\rm QM}(1-P_2)Q_1 + q_{\rm QM}^2(1-P_2)[(1+P_2)(Q_1^2 - Q_2^2) \\
&\quad + \frac{1}{2}(x^2-1)(2Q_2^2 - 3x\,Q_1 Q_2 + 3Q_0 Q_2 - Q_2')],
\end{aligned}
\tag{A3}
$$

with

$$
\begin{aligned}
a_\pm &= x(1-\lambda\eta) \pm (1+\lambda\eta), \\
b_\pm &= y(\lambda+\eta) \mp (\lambda-\eta), \\
\lambda &= \alpha \mathrm{e}^{2\delta_+}, \\
\eta &= \alpha \mathrm{e}^{2\delta_-}, \\
\delta_\pm &= \frac{q_{\rm QM}}{2} \ln\left[\frac{(x\pm y)^2}{x^2-1}\right] + q_{\rm QM}(P_2 - P_0)Q_1 \pm q_{\rm QM} P_1 (Q_2 - Q_0).
\end{aligned}
\tag{A4}
$$

The functions $P_l(y)$ and $Q_l(x)$ are Legendre polynomials of the first and second kind, respectively. They are given by

$$
\begin{aligned}
P_0 &= 1, \\
P_1 &= y, \\
P_2 &= \frac{1}{2}(3y^2 - 1), \\
Q_0 &= \frac{1}{2}\ln\left[\frac{x+1}{x-1}\right], \\
Q_1 &= \frac{x}{2}\ln\left[\frac{x+1}{x-1}\right] - 1, \\
Q_2 &= \frac{1}{4}(3x^2-1)\ln\left[\frac{x+1}{x-1}\right] - \frac{3x}{2}, \\
Q_2' &= \frac{\mathrm{d}Q_2}{\mathrm{d}x}.
\end{aligned}
\tag{A5}
$$

The metric potentials are given by

$$
\begin{aligned}
V &= f, \\
W &= f\omega, \\
X &= \sigma^2 \frac{\mathrm{e}^{2\gamma}}{f}\left(\frac{x^2-y^2}{x^2-1}\right), \\
Y &= \sigma^2 \frac{\mathrm{e}^{2\gamma}}{f}\left(\frac{x^2-y^2}{1-y^2}\right), \\
Z &= \frac{\sigma^2}{f}(x^2-1)(1-y^2) - f\omega^2.
\end{aligned}
\tag{A6}
$$

The mapping to transform from prolate coordinates to spherical coordinates is

$$
\sigma x = (r - M), \qquad y = \cos\theta. \tag{A7}
$$

The constants $\alpha$ and $\sigma$ are related with $a$, and $M$ by means of

$$
\alpha a = \sigma - M, \qquad \sigma = \sqrt{M^2 - a^2}. \tag{A8}
$$

The relativistic multipoles of this metric are

$$
\begin{aligned}
M_0 &= M, \\
S_1 &= J = Ma, \\
M_2 &= q_{\rm QM}\left(1 - \frac{a^2}{M^2}\right)^{3/2} - Ma^2.
\end{aligned}
\tag{A9}
$$

### A2 Manko–Novikov (MN) metric

This spacetime in prolate coordinates $(t,\ x,\ y, \phi)$ has the following potentials:

$$
\begin{aligned}
f &= \frac{A}{B}\mathrm{e}^{2\psi}, \\
\omega &= -2k\left(\frac{2\alpha}{1-\alpha^2} - \frac{C}{A}\mathrm{e}^{-2\psi}\right), \\
\mathrm{e}^{2\gamma} &= \frac{A\mathrm{e}^{2\chi}}{(1-\alpha^2)^2(x^2-1)}, \\
A &= (x^2-1)(1+ab)^2 - (1-y^2)(b-a)^2, \\
B &= [x+1+(x-1)ab]^2 + [(1+y)a + (1-y)b]^2, \\
C &= (x^2-1)(1+ab)[b-a-y(a+b)] \\
&\quad + (1-y^2)(b-a)[1+ab+x(1-ab)], \\
\psi &= q_{\rm MN}\frac{P_2}{R^3}, \\
\chi &= \frac{1}{2}\ln\left[\frac{x^2-1}{x^2-y^2}\right] + \frac{9}{6}\frac{q_{\rm MN}^2}{R^6}(P_3 P_3 - P_2 P_2) \\
&\quad + 2q_{\rm MN}\left[x\frac{P_0}{R} - y\frac{P_1}{R^2} + x\frac{P_2}{R^3} - 1\right], \\
a &= a(x,\ y) = -\alpha \mathrm{e}^{-2q_{\rm MN}\chi_1}, \\
b &= b(x,\ y) = \alpha \mathrm{e}^{2q_{\rm MN}\chi_2}, \\
\chi_1 &= -1 + \frac{(x-y)}{R}\left(P_0 + \frac{P_1}{R} + \frac{P_2}{R^2}\right), \\
\chi_2 &= 1 - \frac{(x+y)}{R}\left(P_0 - \frac{P_1}{R} + \frac{P_2}{R^2}\right), \\
R &= \sqrt{x^2+y^2-1}, \\
P_n &= P_n\left(\frac{xy}{R}\right),
\end{aligned}
\tag{A10}
$$

with $P_n$ as the Legendre polynomials.

The metric potentials are given by

$$
\begin{aligned}
V &= f, \\
W &= f\omega, \\
X &= k^2 \frac{\mathrm{e}^{2\gamma}}{f}\left(\frac{x^2-y^2}{x^2-1}\right), \\
Y &= k^2 \frac{\mathrm{e}^{2\gamma}}{f}\left(\frac{x^2-y^2}{1-y^2}\right), \\
Z &= \frac{k^2}{f}(x^2-1)(1-y^2) - f\omega^2.
\end{aligned}
\tag{A11}
$$

The mapping to transform from prolate coordinates to spherical coordinates is the same as in (A7), and the constants $\alpha$ and $k$ are related with $a$, and $M$ by means of the same expressions as in (A8), because $k \equiv \sigma$ in the QM metric.



Downloaded from https://academic.oup.com/mnras/article/505/2/2870/6276752 by UB Tuebingen user on 16 June 2021

The first three relativistic multipoles are given by

$$M_0 = M = k\left(\frac{1+\alpha^2}{1-\alpha^2}\right),$$
$$S_1 = -2\alpha k^2\left(\frac{1+\alpha^2}{1-\alpha^2}\right) = J = Ma,$$
$$M_2 = -k^3\left(q_{\rm MN} + 4\alpha^2\frac{(1+\alpha^2)}{(1-\alpha^2)^3}\right) = -k^3 q_{\rm MN} - Ma^2, \quad \text{(A12)}$$

from which we see that $q_{\rm MN} := q/k^3$

This version of the metric incorporates the corrections done by Gair, Li & Mandel (2008) and Lukes-Gerakopoulos, Apostolatos & Contopoulos (2010).

### A3 Expanded Hartle–Thorne (HT) metric

The metric as given in Hartle & Thorne (1968) was not expanded to the correct orders of accuracy (terms up to $J^2$ and $q$). Here, we use the expanded version from Frutos-Alfaro (2019):

$$V = 1 - 2\frac{M}{r} + 2\frac{q}{r^3}P_2 + 2\frac{Mq}{r^4}P_2 - \frac{2}{3}\frac{J^2}{r^4}(2P_2+1),$$
$$W = -2\frac{J}{r}\sin^2\theta - \frac{Jq}{r^4}P_3^1\sin\theta,$$
$$X = \left(1-2\frac{M}{r}\right)^{-1}\left[1 - 2\frac{q}{r^3}P_2 - 6\frac{Mq}{r^4}P_2 + 2\frac{J^2}{r^4}(8P_2-1)\right],$$
$$Y = r^2\left[1 - 2\frac{q}{r^3}P_2 - 5\frac{Mq}{r^4}P_2 + \frac{J^2}{r^4}P_2\right],$$
$$Z = r^2\sin^2\theta\left[1 - 2\frac{q}{r^3}P_2 - 5\frac{Mq}{r^4}P_2 + \frac{J^2}{r^4}P_2\right], \quad \text{(A13)}$$

where $P_3^1$ is the associated Legendre polynomial $P_3^1 = (5P_2 + 1)\sin\theta$. We discovered that the second term in $W$ can be omitted without any significative differences in the results for the configurations tested, while gaining a 13 per cent speed up in execution time.

### A4 Metric in Frutos-Alfaro (2016) (Fru16)

With the mass quadrupole moment $q_{\rm F} := -q$, the metric potentials are given by

$$V = -\frac{e^{-2\psi}}{\rho^2}[a^2\sin^2\theta - \Delta],$$
$$W = \frac{a}{\rho^2}[\Delta - (r^2+a^2)]\sin^2\theta + \frac{Jq_{\rm F}}{r^4}P_3^1\sin\theta,$$
$$X = \rho^2\frac{e^{2\chi}}{\Delta},$$
$$Y = \rho^2 e^{2\chi},$$
$$Z = \frac{e^{2\psi}}{\rho^2}[(r^2+a^2)^2 - a^2\Delta\sin^2\theta]\sin^2\theta, \quad \text{(A14)}$$

where

$$\Delta = r^2 - 2Mr + a^2, \quad \text{(A15)}$$

$$\rho^2 = r^2 + a^2\cos^2\theta, \quad \text{(A16)}$$

$$\psi = \frac{q_{\rm F}}{r^3}P_2 + 3\frac{Mq_{\rm F}}{r^4}P_2, \quad \text{(A17)}$$

$$\chi = \frac{q_{\rm F}P_2}{r^3} + \frac{Mq_{\rm F}}{r^4}\left(-\frac{1}{3} + \frac{5}{3}P_2 + \frac{5}{3}P_2^2\right) + \frac{q_{\rm F}^2}{r^6}\left(\frac{2}{9} - \frac{2}{3}P_2 - \frac{7}{3}P_2^2 + \frac{25}{9}P_2^3\right). \quad \text{(A18)}$$

The first three relativistic multipoles are giving by

$$M_0 = M,$$
$$S_1 = J = Ma,$$
$$M_2 = q_{\rm F} - Ma^2, \quad \text{(A19)}$$

in a similar way than the Hartle–Thorne metric, the second term in $W$ can be omitted, resulting in a small gain in performance without significant losses in accuracy.

### A5 Glampedakis–Babak (GB) metric

This metric was given in Glampedakis & Babak (2006) in the form $g_{\alpha\beta} = g^{\rm Kerr}_{\alpha\beta} + \epsilon h_{\alpha\beta}$, with the second term being the corrections from the Abramowicz form of the Hartle–Thorne metric. However, in the paper, only the contravariant components of the metric were given. We inverted them up to the correct order, obtaining the potentials

$$V = \left(1 - 2\frac{Mr}{\rho^2}\right) + 2\epsilon P_2 F_1\left(1 - 2\frac{M}{r}\right),$$
$$W = -2\frac{Jr}{\rho^2}\sin^2\theta,$$
$$X = \frac{\rho^2}{\Delta} - 2\epsilon P_2 F_1\left(1-2\frac{M}{r}\right)^{-1},$$
$$Y = \rho^2 + 2\epsilon r^2 P_2 F_2,$$
$$Z = \left(r^2 + a^2 + 2\frac{Ma^2 r}{\rho^2}\sin^2\theta\right)\sin^2\theta + 2\epsilon r^2 P_2 F_2\sin^2\theta, \quad \text{(A20)}$$

with

$$\Delta = r^2 - 2Mr + a^2,$$
$$\rho^2 = r^2 + a^2\cos^2\theta,$$
$$P_2 = \frac{1}{2}(3\cos^2\theta - 1). \quad \text{(A21)}$$

The function $P_2$ is a Legendre polynomial. The parameter $\epsilon$ is related with the quadrupole moment through $\epsilon = -q/M^3$. The functions $F_1$ and $F_2$ are given by

$$F_1 = -5(r-M)\frac{(2M^2+6Mr-3r^2)}{(8Mr(r-2M))} + \frac{15}{16}\frac{r(r-2M)}{M^2}\ln\left(1-2\frac{M}{r}\right), \quad \text{(A22)}$$

$$F_2 = \frac{5}{8}\frac{(2M^2-3Mr-3r^2)}{Mr} - \frac{15}{16}\frac{(r^2-2M^2)}{M^2}\ln\left(1-2\frac{M}{r}\right). \quad \text{(A23)}$$

This paper has been typeset from a TEX/LATEX file prepared by the author.

Downloaded from https://academic.oup.com/mnras/article/505/2/2870/6276752 by UB Tuebingen user on 16 June 2021

*Astronomy & Astrophysics* manuscript no. 43835
November 12, 2022
©ESO 2022

# Modeling disks and magnetic outflows around a forming massive star: I. Investigating the two-layer structure of the accretion disk

André Oliva[1] and Rolf Kuiper[2, 1]

[1] Institute for Astronomy and Astrophysics, University of Tübingen, Auf der Morgenstelle 10, 72076, Tübingen, Germany
e-mail: andree.oliva@uni-tuebingen.de

[2] Faculty of Physics, University of Duisburg–Essen, Lotharstraße 1, 47057, Duisburg, Germany
e-mail: rolf.kuiper@uni-due.de

Accepted: October 28, 2022

**ABSTRACT**

*Context.* Similar to their lower mass siblings, massive protostars can be expected to: a) be surrounded by circumstellar disks, and b) launch magnetically driven jets and outflows. The disk formation and global evolution is thereby controlled by advection of angular momentum from large scales, the efficiency of magnetic braking and the resistivity of the medium, and the internal thermal and magnetic pressures of the disk.
*Aims.* We determine the dominant physical mechanisms that shape the appearance of these circumstellar disks, their sizes, and aspect ratios.
*Methods.* We performed a series of 30 simulations of a massive star forming from the gravitational collapse of a molecular cloud threaded by an initially uniform magnetic field, starting from different values for the mass of the cloud, its initial density and rotation profiles, its rotational energy content, the magnetic field strength, and the resistivity of the material. The gas and dust was modeled with the methods of resistive magnetohydrodynamics, also considering radiation transport of thermal emission and self-gravity. We checked for the impact of spatial resolution in a dedicated convergence study.
*Results.* After the initial infall phase dominated by the gravitational collapse, an accretion disk was formed, shortly followed by the launching of magnetically driven outflows. Two layers can be distinguished in the accretion disk: a thin layer, vertically supported by thermal pressure, and a thick layer, vertically supported by magnetic pressure. Both regions exhibit Keplerian-like rotation and grow outward over time. We observed the effects of magnetic braking in the inner $\sim$ 50 au of the disk at late times in our fiducial case. The parameter study reveals that the size of the disk is mostly determined by the density and rotation profiles of the initial mass reservoir and not by the magnetic field strength. We find that the disk size and protostellar mass gain scale with the initial mass of the cloud. Magnetic pressure can slightly increase the size of the accretion disk, while magnetic braking is more relevant in the innermost parts of the disk as opposed to the outer disk. From the parameter study, we infer that multiple initial conditions for the onset of gravitational collapse are able to produce a given disk size and protostellar mass.

**Key words.** stars: massive – stars: formation – accretion, accretion disks – magnetohydrodynamics (MHD) – stars: jets

## 1. Introduction

Observations and numerical magnetohydrodynamical (MHD) models of the formation of massive protostars along with their accretion disks and collimated jets have made undeniable progress over the last decade. Even though there are several observational examples of jets from massive protostars (see e.g., Purser et al. 2016), direct observations and estimations of the radii of their associated accretion disks are rarer. The source for the HH 80-81 radio jet, for example, has an accretion disk with an estimated radius of 950–1300 au, and an inner radius of $\lesssim$ 170 au, with the mass of the protostar in the range of 4–18 $M_\odot$ (Girart et al. 2017; Carrasco-González et al. 2010).

Recently, a new generation of multiscale observations of the star-forming region IRAS 21078+5211 (Moscadelli et al. 2021, 2022) have revealed the existence of a disk-jet system around a protostar of $5.6 \pm 2\,M_\odot$. Emission peaks from molecular rotational transitions of $CH_3CN$ and $HC_3N$ trace the kinematical footprint of a Keplerian-like accretion disk of around 400 au in diameter surrounding the protostar. For the first time, the direct study of the launching mechanism of the jet has been possible, thanks to water maser observations performed with very long base interferometry (VLBI) (Moscadelli et al. 2022), which traced individual streamlines in the jet and reached a resolution of 0.05 au.

In Moscadelli et al. (2022), we modeled the disk-jet system in IRAS 21078+5211 with a resistive-radiation-gravito-magnetohydrodynamical simulation of a forming massive star starting from the collapse of a cloud core. We followed the evolution of the protostar, the formation of the accretion disk, and the launching, acceleration, collimation, propagation, and termination of the magnetically driven outflows, which self-consistently form within the computational domain. Thanks to the use of an axisymmetrical grid, we were able to reach unprecedented resolutions in the regions surrounding the forming massive star (up to 0.03 au), allowing for the comparison with the VLBI data (which has a resolution of 0.05 au). We found good agreement between the simulated and observed disk size (given the protostellar mass) as well as the main features of the jet. The simulation was part of a larger study that examines the effects of the natal environment on the formation of a massive star. We present the full series of simulations in this article, with a special focus

on the dynamics of the accretion disk, while the dynamics of the magnetically driven outflows are the focus of an upcoming article (Oliva & Kuiper 2022, hereafter Paper II).

Previously, the numerical simulations performed by Kölligan & Kuiper (2018) showed the self-consistent magneto-centrifugal launching of the jet and a tower flow driven by magnetic pressure in the context of massive star formation. The present study builds on their work by improving the treatment of the thermodynamics of the gas and dust with the inclusion of radiation transport with the gray flux-limited diffusion approximation (Kuiper et al. 2020), and increasing the resolution of the grid. Those changes enable us to examine the vertical structure of the accretion disk. Previous numerical studies of the formation of a massive star in an environment with magnetic fields did not consider magnetic diffusion (e.g., Myers et al. 2013 and Seifried et al. 2011) or approximate the thermodynamics of the system with the use of a barotropic (e.g., Machida & Hosokawa 2020) or isothermal (Kölligan & Kuiper 2018) equation of state, instead of solving the radiation transport equations. Recent studies by Mignon-Risse et al. (2021) and Commerçon et al. (2022), which include ambipolar diffusion as the nonideal MHD effect and as well as radiation transport, find indications of a magneto-centrifugally launched jet (although the grid used in that study does not properly resolve the launching region), and smaller disks with stronger magnetic fields. The question of the size of the disk is explored in more detail in the present article, as we find an opposite trend in our results. For a further literature review, we refer the reader to Sect. 7.

Because of computational costs, previous efforts have focused on only a select number of natal environmental conditions for the massive (proto)star. Our setup, in turn, allows us to explore a wide range of natal environmental conditions and their impact on the outcome of the formed massive star and its disk-jet system. In section 2 we describe the model, physical effects considered, and the parameter space of the simulations. We present an overview of the evolution of the system based on the fiducial case of the parameter space in 3. In section 4, we focus on the dynamical processes observed in the accretion disk, that is to say the effect of the magnetic field, Ohmic dissipation, and radiation transport. In section 5 we explore the dependence of the disk size and evolution with the initial conditions for the gravitational collapse, and finally in section 7 we offer a comparison of our results with previous numerical studies.

## 2. Model and method

### 2.1. Description of the model

We model axisymmetrically the gravitational collapse of a cloud core of mass $M_C$ and a radius of $R_C = 0.1$ pc (cf. Fig. 1), which has an initial density profile of the form

$$\rho(r, t = 0) = \rho_0 \left(\frac{r}{r_0}\right)^{\beta_\rho}. \tag{1}$$

The constant $r_0$ is chosen to be 1 au and $\rho_0$ is determined by computing the mass of the cloud with the integral of the density profile over $0 < r < R_C$. The cloud is in slow initial rotation, given by an initial angular velocity profile of the form

$$\Omega(R, t = 0) = \Omega_0 \left(\frac{R}{R_0}\right)^{\beta_\Omega}, \tag{2}$$

where $R$ is the cylindrical radius and $R_0$ is chosen to be 10 au. The constant $\Omega_0$ is fixed by computing the ratio of rotational to gravitational energy $\zeta \equiv E_r/E_g$ from the initial density and rotation profiles; $\zeta$ is then a parameter of the simulation.

The cloud core is threaded by an initially uniform magnetic field directed parallel to the rotation axis. Its magnitude $B_0$ is determined by the normalized mass-to-flux ratio $\bar{\mu}$,

$$\bar{\mu} \equiv \frac{M_C/\Phi_B}{(M_C/\Phi_B)_{\rm crit}}. \tag{3}$$

The denominator of the previous expression represents the critical value of the mass-to-flux ratio, that is the value for which the gravitational collapse is halted by the magnetic field under idealized conditions. We take the value from Mouschovias & Spitzer (1976). The magnetic flux $\Phi_B$ is simply computed as the flux across the midplane, $B_0 \cdot \pi R_C^2$, which in magnitude is the same flux that enters or leaves the spherical cloud.

### 2.2. Physics

The simulations solve for the equations of magnetohydrodynamics, with the addition of Ohmic resistivity as a nonideal effect, self-gravity, the gravitational force from the forming massive star, and radiation transport for the thermal emission from the gas and dust, on an axisymmetric grid. Next, we describe the set of equations solved.

The dynamics of the gas and dust are followed by numerically solving the following system of conservation laws, using the Pluto code (Mignone et al. 2007):

$$\partial_t \rho + \boldsymbol{\nabla} \cdot (\rho \boldsymbol{v}) = 0, \tag{4}$$

$$\partial_t (\rho \boldsymbol{v}) + \boldsymbol{\nabla} \cdot \left[\rho \boldsymbol{v} \otimes \boldsymbol{v} - \tfrac{1}{4\pi} \boldsymbol{B} \otimes \boldsymbol{B} + P_t \mathrm{I}\right] = \rho \boldsymbol{a}_{\rm ext}, \tag{5}$$

$$\partial_t \boldsymbol{B} + \boldsymbol{\nabla} \times (c\boldsymbol{\mathcal{E}}) = 0, \tag{6}$$

$$\partial_t (E^K + E^{\rm th} + E^B) + \boldsymbol{\nabla} \cdot \left[(E^K + E^{\rm th} + P)\boldsymbol{v} + c\boldsymbol{\mathcal{E}} \times \boldsymbol{B}\right] = \rho \boldsymbol{v} \cdot \boldsymbol{a}_{\rm ext}, \tag{7}$$

which correspond to the continuity equation, momentum equation, induction equation and energy conservation equation, respectively. The gas is weakly ionized and has density $\rho$, velocity $\boldsymbol{v}$ and magnetic field $\boldsymbol{B}$. The magnetic field must also satisfy the solenoidality condition $\boldsymbol{\nabla} \cdot \boldsymbol{B} = 0$. The total pressure $P_t = P + \frac{1}{8\pi} B^2$ is composed of the thermal and magnetic pressures. The electric field $\boldsymbol{\mathcal{E}}$ can be directly substituted by the expression

$$c\boldsymbol{\mathcal{E}} = -\boldsymbol{v} \times \boldsymbol{B} + \eta \boldsymbol{\nabla} \times \boldsymbol{B}, \tag{8}$$

where $\eta(\rho, T)$ is the Ohmic resistivity. The energy density of Eq. 7 is separated into its components: kinetic ($E^K$), thermal or internal ($E^{\rm th}$) and magnetic ($E^B$). The acceleration source term $\boldsymbol{a}_{\rm ext}$ is a sum of the gravity of the forming star $\boldsymbol{a}_{g\star} = -GM_\star/r^2\, \boldsymbol{e}_r$, the self-gravity of the gas $\boldsymbol{a}_{\rm sg}$ and the viscosity source term $\boldsymbol{a}_\nu$.

The self-gravity acceleration source term is given by $\boldsymbol{a}_{\rm sg} = -\nabla\Phi_{\rm sg}$. The self-gravity potential $\Phi_{\rm sg}$ is found by solving Poisson's equation $\nabla^2\Phi_{\rm sg} = 4\pi G\rho$ with a diffusion Ansatz, according to Kuiper et al. (2010). Self-gravity is inherently a three-dimensional effect, and a cloud with the characteristics we consider here is expected to produce an accretion disk with spiral

arms. Since we perform the simulations on a two-dimensional axisymmetric grid, we mimic the missing angular momentum transport by the gravitational torques with the addition of a shear viscosity source term $\boldsymbol{a}_\nu = \boldsymbol{\nabla}\Pi/\rho$, where the viscosity tensor $\Pi$ is fixed with the $\alpha$-parametrization of Shakura & Sunyaev (1973) and no bulk viscosity is considered. This approach was extensively studied in Kuiper et al. (2011), and we refer the reader to that article for more details on the computation of the viscosity tensor, as well as comparisons of the efficacy of angular momentum transport using this approach in comparison to nonviscous 3D models.

We treat radiation transport with the gray flux-limited diffusion approximation, by using the module Makemake described in ample detail in Kuiper et al. (2020). Specifically, we point the reader to sections 2.3.2 and 2.3.4 in that reference. In a nutshell, two equations are solved simultaneously for treating radiation transport. The first one is the zeroth-moment of the radiation transport equation within a given volume, which essentially says that the net emitted energy density (emission minus absorption) that is not lost through the boundary as a radiative flux, has to be stored as a local radiative energy density. This equation is simplified by assuming that the radiative flux can be written as a diffusion term in terms of the radiation energy density (hence flux-limited diffusion). The second equation describes the changes to $E^{\rm th}$: the net absorbed energy density (absorption minus emission) has to be stored as internal energy in the gas. Both energy fields are solved without previous assumption of equilibrium between them; this is the so-called two-temperature approach Commerçon et al. (2011). In all but one of the simulations (see Sect. 5.2 for details), a constant value of the opacity for the dust and gas of $1\,\mathrm{cm^2\,g^{-1}}$ was used. The initial dust-to-gas mass ratio is set to 1%. The irradiation from the forming massive star is not considered in this study.

We use the resistivity model by Machida et al. (2007) (which is based on a numerical study by Nakano et al. 2002)

$$\eta = \frac{740}{X_e}\left(\frac{T}{10\,\mathrm{K}}\right)^{1/2}\left[1-\tanh\left(\frac{n_H}{10^{15}\,\mathrm{cm^{-3}}}\right)\right]\,\mathrm{cm^2\,s^{-1}}, \tag{9}$$

where we use for simplicity $n_H = \rho/\mu_H$ as the number density of hydrogen nuclei ($\mu_H$ being the molecular weight of hydrogen) and the ionization fraction $X_e$ is given by

$$X_e = 5.7\cdot 10^{-4}\left(\frac{n_H}{\mathrm{cm^{-3}}}\right)^{-1}. \tag{10}$$

At all moments in time, the properties of the formed massive star are computed using the evolutionary tracks for high-mass stars calculated by Hosokawa & Omukai (2009) and the instantaneous values of the stellar mass and accretion rate.

### 2.3. Boundary conditions

The computational domain assumes symmetry with respect to the rotation axis and equatorial symmetry with respect to the midplane. This means that scalar quantities and the velocity are simply reflected across the $z$-axis and the midplane. In the case of the magnetic field, it is reflected across the $z$-axis, but across the midplane, the parallel component switches sign instead of the normal component. The same symmetries imply that the boundaries across the azimuthal direction are periodic. Both the inner and outer boundaries (i.e., the sink cell and the outermost part of the cloud) impose a zero gradient condition for the magnetic field and the azimuthal and polar components of the velocity; for the radial component of the velocity and the density, only outflow but no inflow is allowed. Therefore, all matter that goes inside of the sink cell is considered as accreted.

Table 1: Grid resolutions

| Grid | $N_r$ | $N_\theta$ | $\Delta x_{\rm min}$ [ au] | $\Delta x_{1000}$ [ au] |
|---|---|---|---|---|
| x1 | 56 | 10 | 0.51 | 160 |
| x2 | 112 | 20 | 0.25 | 80 |
| x4 | 224 | 40 | 0.12 | 40 |
| x8 | 448 | 80 | 0.06 | 20 |
| x16 | 896 | 160 | 0.03 | 10 |

### 2.4. Initial conditions: Parameter space and numerical configuration

We present an extensive parameter study of the system, with the express aim of aiding in the understanding of the physical processes that intervene in the formation and evolution of the disk and the magnetically driven outflows. In total, we present results from 31 different runs. Instead of describing all the parameters in multiple tables, we show a summary of the parameter space as a diagram in the right panel of Fig. 1.

We used five different axisymmetrical grids with increasing resolution, that we name x1, x2, x4, x8 and x16. The grid for the radial coordinate $r$ increases logarithmically with distance, starting from the radius of the inner boundary (3 au in the fiducial case), to the radius of the cloud core (0.1 pc). We often refer to the inner boundary as the sink cell. Using the assumed symmetries of the system, the colatitude $\theta$ extends from 0 to $\pi/2$ radians, and it is divided linearly into cells such that they have approximately the same dimensions in both the radial and polar directions for each distance to the center of the cloud. Table 1 details the number of cells in each direction, the minimum cell size and a reference cell size at 1000 au for all the grids used in this study, and assuming the sink cell size of the fiducial case.

The parameters with direct relation to physical quantities we considered are: the mass of the cloud core $M_C$, the resistivity model used, the normalized mass-to-flux ratio $\bar{\mu}$, the initial density profile exponent $\beta_\rho$, the initial rotation profile exponent $\beta_\Omega$, and the ratio of the rotational-to-gravitational energy $\zeta$. The values for each parameter in the fiducial case are highlighted in blue in Fig. 1. The fiducial case was run on all the grids. Modifications of the fiducial case are then investigated while keeping the rest of the parameters constant. Because of this, we refer in the paper to each simulation by the modified parameter followed by the grid it was run on; for example, $M_C = 150\,\mathrm{M_\odot}$ [x8] refers to a cloud of $150\,\mathrm{M_\odot}$, with the rest of the parameters as in the fiducial case for grid x8. The full set of values with direct relation to physical quantities was run on the base grid x4, and some selected values, which are underlined in Fig. 1, were run on grid x8 as well. During the preparation of this study, we also ran a part of this physical parameter space on the lower resolution grids, however, we do not include the results here because they are redundant. Details of the choice of the parameters, as well as the comparison of results obtained, are presented in Sect. 5.

The numerical convergence of the results was studied by changing the values of the sink cell radius, the strength of the $\alpha$ shear viscosity and the Alfvén limiter using the grid x2 as a base. A more detailed explanation of these latter parameters, as well as the results of the convergence study can be found in Appendix A.

A&A proofs: manuscript no. 43835

## 3. Overview of the evolution of the system

Figure 1 shows a schematic overview of the features observed during the evolution of the system, based on the results of the fiducial case but generally present in most of the simulations of the study. We describe these characteristic features and processes in the following subsections case-by-case.

### 3.1. Gravitational infall epoch

As soon as the simulation begins, the cloud starts collapsing under its own gravity. The flow quickly becomes super-Alfvénic (the kinetic flow velocity is larger than the Alfvén speed), and the magnetic field lines are dragged by the infall accordingly. The result of this collapse is that the configuration of magnetic field lines adopts an "hourglass" shape, as described in Galli et al. (2006), and that has been observed in Beltrán et al. (2019).

### 3.2. Protostar

A massive (proto)star is formed at the center of the cloud, which reaches a mass of $\sim 20\,M_\odot$ after 30 kyr. The luminosity of the (proto)star is dominated by the conversion of gravitational energy into radiation during the first 20 kyr, and only after that time the stellar luminosity becomes comparable to the accretion luminosity. We point out that both the stellar and accretion luminosities are not taken into account in this study, but we will report on these radiative feedback effects in future work.

### 3.3. Magneto-centrifugal epoch

Due to the conservation of angular momentum, gas coming from large scales rotates faster as it reaches the center of the cloud. At $t \sim 5$ kyr, enough angular momentum is transported onto the center of the cloud to form a Keplerian-like accretion disk as a result. The disk grows in time due to the continued infall of material from large scales.

The accretion disk can be morphologically divided into a thin and a thick layer. The thin layer of the disk is a region of the midplane consisting of material in rotation with speeds close to the Keplerian speed. The density of the thin layer increases toward the center of the cloud $10^{-16}$ to $10^{-11}\,\mathrm{g\,cm^{-3}}$. Enclosing the thin layer, there is a less dense thick layer (with typical densities of $10^{-14}\,\mathrm{g\,cm^{-3}}$) that is also rotating.

Roughly at the same time as the disk forms, magnetically driven outflows are launched, which we classify according to their speeds and driving mechanisms. The jet is launched by the magneto-centrifugal mechanism (in a way similar to the model of Blandford & Payne 1982) and it reaches typical speeds higher than $100\,\mathrm{km\,s^{-1}}$. Rotation drags the magnetic field lines, as it has been observed in Beuther et al. (2020) and Girart et al. (2013). This creates a magnetic pressure gradient that drives a slower and broader tower flow (cf. the model of Lynden-Bell 2003). Its typical speeds are on the order of $10\,\mathrm{km\,s^{-1}}$, and it broadens with time. A discussion of the dynamical processes present in the launching of outflows is offered in Paper II.

On the interface between inflow along the thick layer of the disk and outflow along the cavity, an additional structure is identified, which we refer as the *cavity wall*. Densities at the cavity wall are higher than those in the cavity, but also higher than the surrounding infalling envelope and the thick layer of the disk. In terms of its dynamics, material from the cavity wall contributes episodically to both the inflow and the outflow.

### 3.4. Magnetic braking epoch

As magnetic field lines are dragged by rotation, the resulting magnetic tension exerts a torque on the gas that brakes it, infalling as a consequence of the angular momentum loss. The inclusion of Ohmic dissipation makes magnetic braking negligible at early times in the simulation, but at around $t \sim 15$ kyr, magnetic braking starts to affect the innermost region of the disk and the cavity wall ($r \lesssim 30$ au). As a result, a magnetically braked region is formed, where the material is mostly infalling but where the disk densities are kept because of constant replenishment through material from the cavity wall.

The extraction of angular momentum from the inner region of the cloud by magnetic braking modifies or even interrupts the magneto-centrifugal mechanism that drives the jet, but not the tower flow, which is mostly present at large scales. The tower flow broadens over time because the continuous dragging of magnetic field lines by rotation increases the magnetic pressure gradient on top of the disk, which is itself growing in time as well. This outflow broadening mechanism offers an explanation for the earliest outflow broadening observed and discussed in Beuther & Shepherd (2005). An analysis and discussion of the effects of magnetic braking in outflows, as well as their propagation over time into the large scales of the cloud is offered in Paper II, which focuses on the outflow physics of the same simulation data analyzed here.

## 4. Dynamics of the disk

After giving an overview on the general evolution of the system, we aim at understanding the dynamical processes present in the disk in detail by taking the fiducial case and examining selected terms of the equations of motion. With the identification of these processes, we are able to perform a more effective and comprehensive comparison of results for the full parameter space, which we present in Sect. 5.

### 4.1. Radial dynamics in the disk

The forming massive star accretes mass through the accretion disk, which implies that the velocity in the disk must have a component in the radially inward direction. The torque necessary for the angular momentum transport in the disk is provided by gravitational torques of forming spiral arms, which is modeled here through the use of the $\alpha$ shear viscosity model. Nevertheless, $v_\phi \gg v_R$ in the disk, and so, it is useful to examine the effects of the different forces that act in the disk under the assumption of radial equilibrium.

In cylindrical coordinates $(R, \phi, z)$, the radial component of the MHD momentum equation, setting $\theta = \pi/2$ (midplane), assuming axisymmetry, is given by

$$\frac{\partial(\rho v_R)}{\partial t} + \nabla\cdot\left(\rho v_R \boldsymbol{v} - \frac{B_R \boldsymbol{B}}{4\pi}\right) + \frac{\partial P_t}{\partial R} = \rho g_R + \frac{\rho v_\phi^2 - B_\phi^2/(4\pi)}{R}, \quad (11)$$

where the divergence operator $\nabla\cdot$ acts according to

$$\nabla\cdot\boldsymbol{f}(R,z) = \frac{1}{R}\frac{\partial(R f_R)}{\partial R} + \frac{\partial f_z}{\partial z} \quad (12)$$

onto the vector fields $\boldsymbol{f}(R,z) \in \{\rho v_R \boldsymbol{v}, B_R \boldsymbol{B}\}$; $\boldsymbol{g}$ is the total gravitational force from the star and self-gravity, and $P_t$ is the sum of the thermal and magnetic pressures.

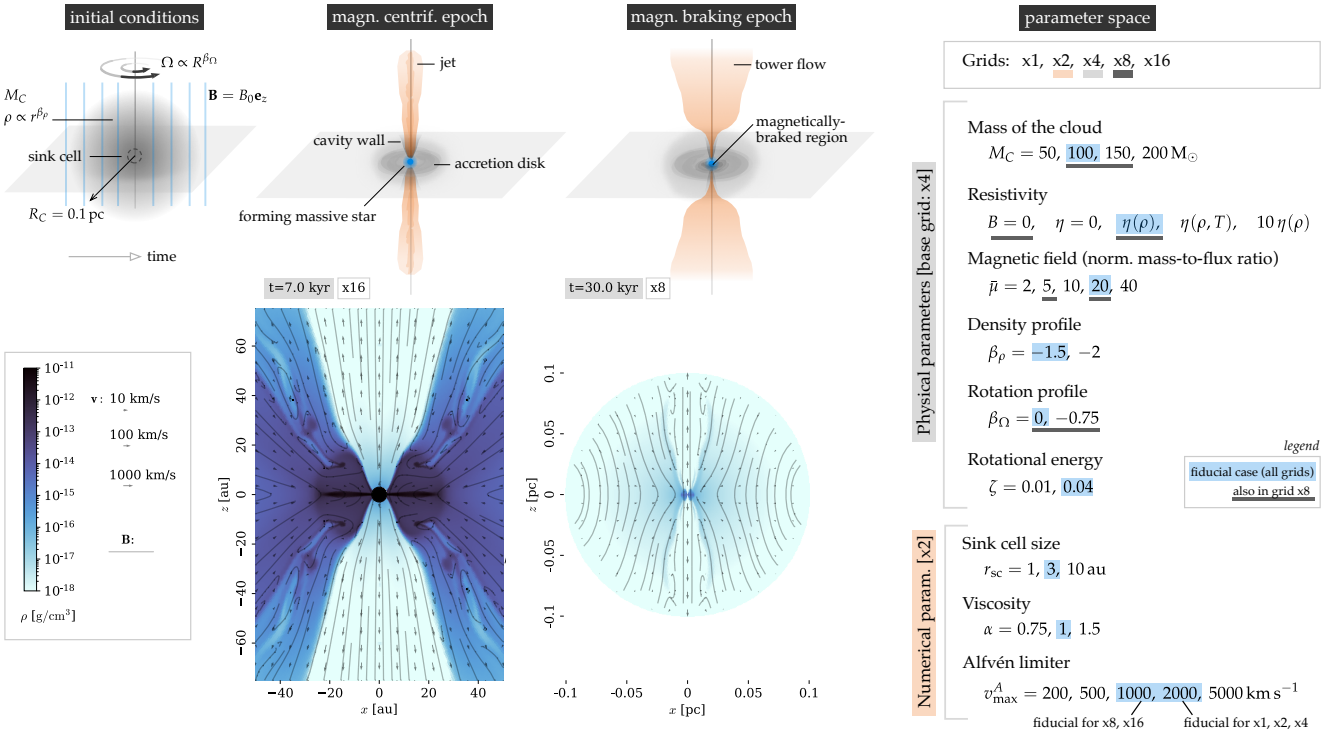



Fig. 1: Initial conditions, overview of the evolution of the system, and summary of the parameter space presented in this study.

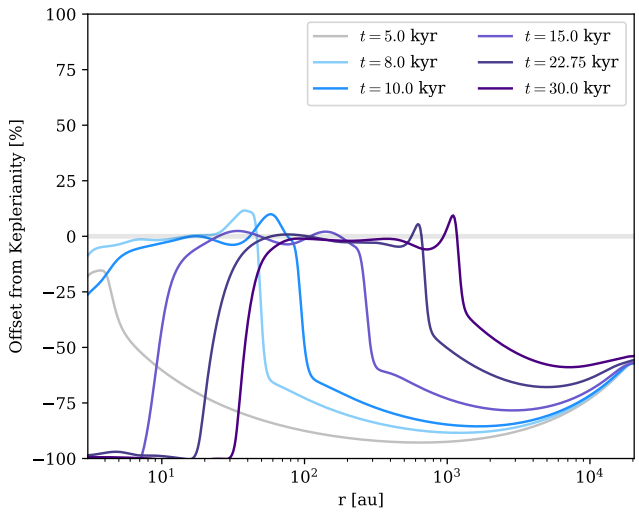



Fig. 2: Keplerianity on the midplane, computed with the fiducial simulation on grid x8.

In order to examine the forces that define radial equilibrium in the disk, we consider a parcel of gas moving in a circular orbit, for which we set $v_R = 0$ in eq. 11 and obtain

$$\frac{\rho v_\phi^2 - B_\phi^2/(4\pi)}{R} = -\rho g_R + \frac{\partial P}{\partial R} + \frac{\partial}{\partial R}\left(\frac{B^2}{8\pi}\right) - \nabla\cdot(B_R\boldsymbol{B}). \tag{13}$$

For $\boldsymbol{B} = \boldsymbol{0}$, $P = 0$, and considering the midplane, one recovers the well-known condition for gravito-centrifugal equilibrium (on the corotating frame), which defines the Keplerian velocity, $v_K = \sqrt{GM(r)/R}$; $M(r)$ being the enclosed mass (dominated by the mass of the protostar for small $r$). The use of the enclosed mass is an approximation to the use of the full potential given by the Poisson equation.

### 4.1.1. Keplerianity

The degree of gravito-centrifugal equilibrium in the whole disk can be measured by computing the ratio of the centrifugal force density to the gravitational force density:

$$\frac{a_R^c}{\rho g_R} = \frac{\rho v_\phi^2}{r\sin\theta}\cdot\frac{r^2}{\rho GM(r)\sin\theta} = \frac{v_\phi^2}{v_K^2\sin^3\theta}. \tag{14}$$

This motivates us to define the offset from Keplerianity as

$$\text{offset from Keplerianity} = \left|\frac{v_\phi}{v_K\sin^{3/2}\theta}\right| - 1, \tag{15}$$

which in the midplane corresponds to the fractional difference of the azimuthal velocity with respect to the Keplerian value.

Figs. 2 and 4 show the offset from Keplerianity presented as a percentage, in such a way that the negative values indicate sub-Keplerianity, and the positive values, super-Keplerianity. In the midplane, there is a Keplerian region within ±25% for all times, which corresponds to the thin accretion disk. The Keplerianity drops outside of the disk, which corresponds to the infalling envelope. At the exterior boundary of the disk, the mostly rotating material encounters the mostly-infalling material from the region of the envelope, creating a centrifugal barrier that is seen as a slight super-Keplerianity in Fig. 2. Even though we ignore the effect of viscosity in the analysis of this section, we note that, as it transports angular momentum outward, its effect is to increase

A&A proofs: manuscript no. 43835

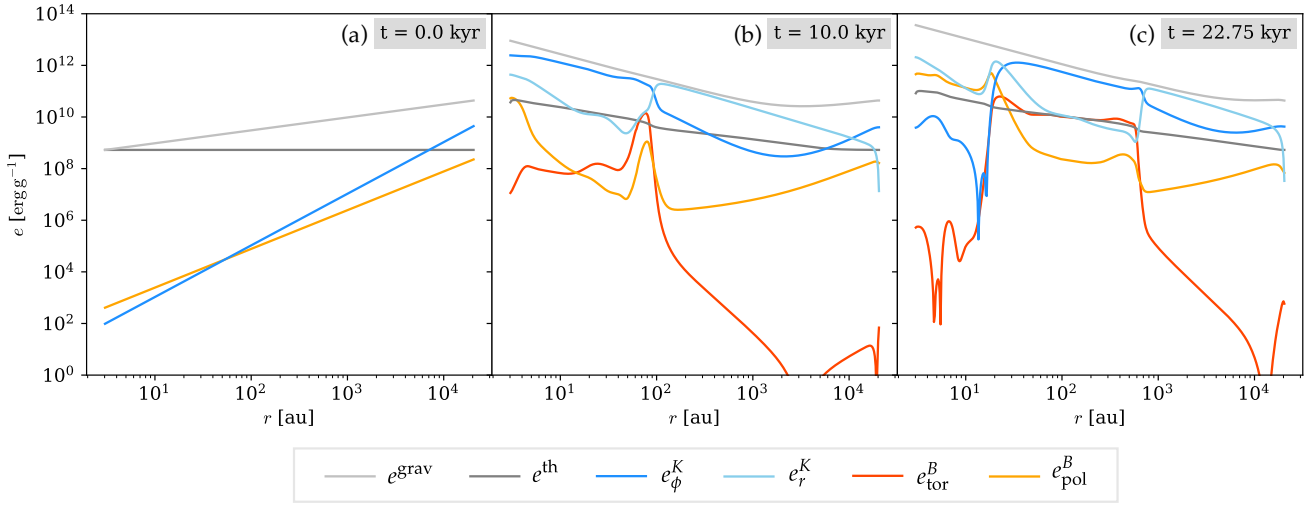



Fig. 3: Contributions to the specific energy in the thin layer of the disk, calculated with the fiducial simulation on grid x8.

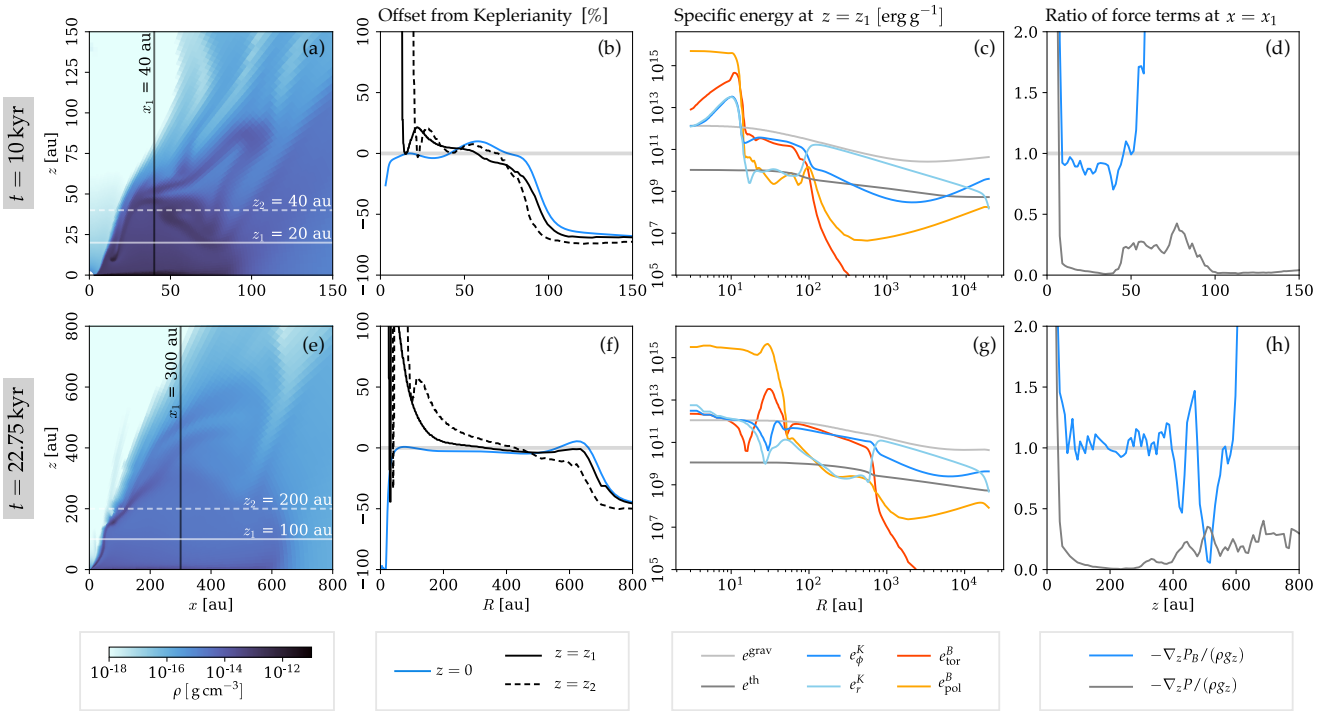



Fig. 4: Dynamics of the thick layer of the disk. The panels of the figure are grouped in columns such that they show: the density structure of the thick layer (*a* and *e*), the offset from Keplerianity at three different heights in the thick layer (*b* and *f*), the contributions to the specific energy (*c* and *g*), and the vertical balance of forces (*d* and *h*). Data from the fiducial simulation on grid x8 was used for this figure.

positively the deviation from Keplerianity. The rest of the deviations from Keplerianity in the disk are discussed in the following sections.

Panels *b* and *f* of Fig. 4 contrast the values of the offset from Keplerianity in the midplane with values in planes parallel to it, which slice through the thick layer of the disk and reveal its dynamical structure. In general, the thick layer also shows Keplerianity within ±25%, but it decreases with altitude because the cylindrical-radial component of gravity also decreases with altitude. The regions close to the cavity become increasingly super-Keplerian, while the regions close to the infalling envelope become increasingly sub-Keplerian.

### 4.1.2. Specific energies

We study the dynamics of the thin and thick layers of the disk by computing the terms of the Bernoulli equation, that is, the contributions to the specific energy of the material. This allows us to isolate the role of each term in the equations of magnetohydrodynamics and compare its relative importance. The results of

the energy calculations are available in Fig. 3 for the midplane, and Fig. 4 for the plane $z = z_1$. The contributions to the specific energy we considered are:

- the gravitational specific energy

$$e^{\rm grav} = \frac{GM(r)}{r}, \tag{16}$$

- the thermal specific energy

$$e^{\rm th} = \frac{P}{\rho(\Gamma - 1)}, \tag{17}$$

- the contribution to the specific kinetic energy by the azimuthal component of velocity

$$e^K_\phi = \frac{v^2_\phi}{2}, \tag{18}$$

- the contribution to the specific kinetic energy by the spherical-radial component of velocity

$$e^K_r = \frac{v^2_r}{2}, \tag{19}$$

- the contribution to the specific magnetic energy by the toroidal component of the magnetic field

$$e^B_{\rm tor} = \frac{B^2_\phi}{8\pi\rho}, \tag{20}$$

- the contribution to the specific magnetic energy by the poloidal component of the magnetic field

$$e^B_{\rm pol} = \frac{B^2_r + B^2_\theta}{8\pi\rho}. \tag{21}$$

Initially, the specific gravitational energy increases as a function of $r$ because it is given by the enclosed mass (see Fig. 3a). As the collapse progresses (Fig. 3b), the gravity of the forming massive star becomes more important, which means that the curve for $e^{\rm grav}$ has a point-source-like behavior close to the center of the cloud. At large scales, the enclosed mass of the envelope becomes important. As expected, the infalling envelope has $e^K_r > e^K_\phi$, but the advection of angular momentum from large to small scales causes $e^K_\phi$ to increase until $e^K_\phi > e^K_r$, forming the disk. When the magnetic field lines are dragged by rotation in the disk, the toroidal contribution to the magnetic energy increases.

#### 4.1.3. Thermal and magnetic pressure

The following two sections examine the contributions of the remaining terms of eq. 13 to the equilibrium of cylindrical radial forces in the disk and their impact to the values of the deviation of Keplerianity shown in Fig. 2. First, we only consider the additional radial support that the thermal pressure gradient $\partial P/\partial R$ gives to the material in the disk, which be inferred by using eq. 17 and Figs. 3 and 7. In agreement with the theory, we find that the thermal pressure gradient provides an additional small support against gravity and therefore makes material in radial equilibrium to appear to be slightly sub-Keplerian.

In Gaussian units, the magnetic pressure and magnetic energy density correspond to the same quantity, which means that we can use the specific energy density to study the magnetic pressure support in the disk. In the infalling envelope, the poloidal component of the magnetic field contributes the most to magnetic pressure (see, e.g., Fig. 3b), given that the initial magnetic field distribution is parallel to the rotation axis. When the disk is formed, the toroidal component of the magnetic field increases in general because the magnetic field lines are dragged by rotation. The toroidal magnetic field becomes dominant over the poloidal component, which additionally allows us to neglect the magnetic tension term $\nabla \cdot (B_R \boldsymbol{B})$ from eq. 13 in most parts of the disk.

The magnetic pressure $P_B = \rho(e^B_{\rm tor} + e^B_{\rm pol})$ decreases with distance in the infalling envelope (compare Figs. 3b and 7a), and overall in the disk as well, although the more complex structure of the magnetic field in the thin and thick layers of the disk means that there are regions of local increase with distance. Similarly to our argument with the thermal pressure gradient, $v_\phi < v_K$ for a negative magnetic pressure gradient. Therefore, the radius of the disk should be slightly larger compared to the nonmagnetic case, given that $v_\phi$ decreases with distance and the angular momentum contained at larger $R$ becomes sufficient to support a circular orbit. This argument is revisited in Sect. 5.3 after considering the effects of magnetic braking (Sect. 4.3) and magnetic diffusion (Sect. 4.2).

Additionally to magnetic pressure, the second term of the left-hand side of eq. 13 reveals that the azimuthal component of the magnetic field reduces the effectiveness of the centripetal force required to keep a circular orbit. This can be measured by comparing the azimuthal component of the kinetic and magnetic energies:

$$\frac{B^2_\phi}{4\pi R} \cdot \frac{R}{\rho v^2_\phi} = \frac{e^B_{\rm tor}}{e^K_\phi}. \tag{22}$$

In the thin layer of the disk, the contribution of this term is negligible, but in the thick layer, they are comparable. In terms of Keplerianity, this term can cause the material to be slightly super-Keplerian; this can be observed when comparing panels $f$ and $g$ of Fig. 4.

### 4.2. Ohmic dissipation

According to the model of Ohmic resistivity by Machida et al. (2007), which we use, the resistivity increases progressively with density for the number densities we obtain here ($n_H \lesssim 10^{13}\,{\rm cm}^{-3}$). We computed the ratio of the magnitude of the induction and diffusion terms in the induction equation, which is analogous to the magnetic Reynolds number, as

$${\rm Re}_m = \frac{|\boldsymbol{\nabla} \times (\boldsymbol{v} \times \boldsymbol{B})|}{|\eta \boldsymbol{\nabla} \times (\boldsymbol{\nabla} \times \boldsymbol{B})|}, \tag{23}$$

and show the results in Fig. 5, which are computed for two instants of time from the fiducial case. At $t = 10\,{\rm kyr}$, the plasma is fully diffusive in most regions of the thin layer of the disk; the thick layer is dominated by advection but it experiences magnetic diffusion in around one part per hundred; and the cavity wall is also partially diffusive. Later in time, at $t = 22.75\,{\rm kyr}$, only the highest density regions close to the massive protostar are dominated by diffusion, the thin layer experiences magnetic diffusion of around one part per hundred, and the thick layer is almost completely dominated by advection.

Ohmic resistivity acts mostly on the toroidal component of the magnetic field, as it can be seen by comparing the energy curves in Figs. 3 and 4. In the thick layer of the disk at late times (Fig. 4g) $e^B_{\rm tor}$ roughly follows $e^K_\phi$. This sets the picture for the case where magnetic diffusion is low. On the other hand, in the thin

A&A proofs: manuscript no. 43835

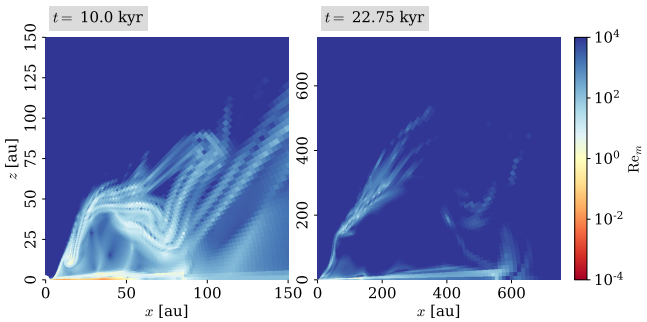



Fig. 5: Magnetic Reynolds number, computed with the fiducial simulation on grid x8. For $t = 10$ kyr, the radius of the disk is around 80 au, while for $t = 22.75$ kyr, the exterior radius is $\approx 700$ au and the interior radius is $\approx 20$ au.

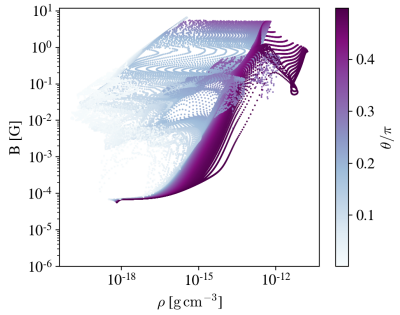



Fig. 6: Distribution of the magnetic field strength as a function of density. This histogram was computed with the fiducial simulation run on grid x16, for time $t = 7$ kyr. The color scale indicates the polar angle: the dark purple colors correspond to the midplane (with the disk corresponding to $\rho \gtrsim 10^{-15}$ g cm$^{-3}$) and the light blue colors correspond to the rotation axis (where the jet is located).

layer of the disk, at early times (Fig. 3b), $e^B_{\rm tor}$ and $e^K_\phi$ are clearly decoupled: the toroidal magnetic field component becomes low inside of the disk, corresponding to the region where diffusion dominates over advection. In the outer disk, where the density is lower, the resistivity is lower as well, and the toroidal component of the magnetic field is allowed to increase.

### 4.3. Magnetic braking

The momentum equation in the azimuthal direction, considering axisymmetry and circular motion, reduces to

$$\frac{\partial(\rho v_\phi)}{\partial t} = \frac{1}{R^2}\frac{\partial}{\partial R}(R^2 B_\phi B_R) + \frac{\partial}{\partial z}(B_\phi B_z). \tag{24}$$

The right-hand side of this equation is equal to zero if there are no magnetic fields, and it leads to the conservation of angular momentum. The terms on the right-hand side constitute the azimuthal component of the magnetic tension force, which exerts a torque that reduces angular momentum locally. This process is known as magnetic braking, and it can be understood as a consequence of the dragging of magnetic field lines by rotation (Galli et al. 2006).

Even though Ohmic resistivity reduces the toroidal component of the magnetic field (cf. $e^B_{\rm tor}$ in Fig. 3b), it does not completely suppress it. Over time, the magnetic field lines are wound enough so that magnetic braking happens in the innermost parts of the disk. In Fig. 3c, which corresponds to $t = 22.75$ kyr, $e^B_{\rm tor}$ is higher in the disk than when it is measured at $t = 10$ kyr, while $e^K_\phi$ decreases over the same interval of time in the inner 20 au; those quantities show the reduction of angular momentum due to magnetic tension. In the face of the reduction of angular momentum, the material falls toward the protostar, as evidenced by the increase in $e^K_r$; this creates the magnetically braked region. The cavity wall and the thick layer of the disk are also affected by magnetic braking; material from several directions is then delivered to the magnetically braked region.

### 4.4. Vertical support

In the vertical direction (i.e., parallel to the rotation axis), the momentum equation reads

$$\frac{\partial(\rho v_z)}{\partial t} + \nabla\cdot\left(\rho v_z \boldsymbol{v} - \frac{B_z \boldsymbol{B}}{4\pi}\right) + \frac{\partial P_t}{\partial z} = \rho g_z \tag{25}$$

with the same definition of the divergence as given in eq. 12. Considering a parcel of gas moving in a circular orbit ($v_z = 0$), and given that in the disk region $B_z \ll B_\phi$, eq. 25 becomes

$$\frac{\partial P}{\partial z} + \frac{\partial}{\partial z}\left(\frac{B^2}{8\pi}\right) = \rho g_z. \tag{26}$$

The ratio of the thermal to magnetic pressure is equivalent to the ratio of the specific thermal energy to the total magnetic energy. In the thin layer of the disk (Fig. 3), thermal pressure dominates over magnetic pressure, from which we conclude that the thin layer is supported mainly by thermal pressure (at late times, magnetic pressure becomes comparable but not much higher than thermal pressure). On the contrary, the thick layer of the disk is supported by magnetic pressure, as evidenced by Figs. 4d and 4h, where we present a direct comparison of both pressure gradients to gravity in a vertical slice that crosses the disk. As the vertical component of gravity vanishes at the midplane, both curves increase toward $z = 0$. In the thick layer of the disk, thermal pressure decreases, while the magnetic pressure gradient compensates gravity. At the cavity wall, thermal pressure increases because it has a higher density than the thick layer of the disk. Finally, in the cavity, magnetic pressure dominates over gravity in the vertical direction, which is expected in the case of a magnetically driven outflow.

### 4.5. Effects of other forms of magnetic diffusion

In this study, the effects of ambipolar diffusion and the Hall effect are not considered, and this formally constitutes a caveat of our approach which we plan to address in a future study. In this section, we discuss the expected effects that other forms of magnetic diffusivity might have on the results reported in the previous sections, with a focus on the fiducial case. We examine every region of interest for the discussion: the accretion disk, the infalling envelope and the outflow cavity. The simulation catalog also includes an investigation of the effects of the resistivity model; the results can be used to further assess the missing magnetic diffusivity and are presented in Sect. 5.2.

First, we consider only the accretion disk. The curves for ambipolar diffusivity and Ohmic resistivity given in, for example, Marchand et al. (2022, 2016) and Tsukamoto et al. (2021) reveal that, at least for the range of number densities $10^8 \lesssim n_H \lesssim$

$10^{13}\,\mathrm{cm}^{-3}$, which are found in the thin layer of the accretion disk, the values of the diffusivities are similar within the uncertainties of the dust models considered for their derivation, differing by about a factor of ten. The distribution of the magnetic field strength with density is presented in Fig. 6, where we use a color scale that highlights with darker colors the midplane. For the densities of the accretion disk ($\rho > 10^{-14}\,\mathrm{g\,cm}^{-3}$), the magnetic field strength increases with density, until it reaches between 0.1 and 1 G. When comparing the magnetic field distribution to the results of a recent study by Commerçon et al. (2022), who considered the effects of ambipolar diffusion but not Ohmic dissipation, we find consistent results for the thin layer of the disk. In the thick layer, however, the addition of higher, more realistic magnetic diffusivities might reduce the vertical magnetic pressure support. This means that thinner accretion disks than those reported here would be expected in a more realistic setting.

As for the effects of magnetic braking, we expect that ambipolar diffusion and the Hall effect reduce the magnetic Reynolds number, that is, the material would become more diffusive. Contrary to Ohmic dissipation, ambipolar and Hall diffusivities depend on magnetic field, and so the reduction could be of particular importance at later times, when considerable magnetic flux has been transferred to the central regions of the cloud core. This would cause a delay in the formation of the magnetically braked region in the inner disk (see also the discussion in Sect. 5.2). On the other hand, magnetic braking could play an important role in determining the total angular momentum transferred to the forming massive star, as well as the growth of HII regions by terminating the magnetically driven outflows (Martini et al., in prep.). An investigation of the role of all forms of magnetic diffusivity in the long-term evolution of the accretion disk and the jet is necessary. However, at least for early times ($t \lesssim 20\,\mathrm{kyr}$) in the formation of the massive star, our results fit observational constraints (see Sect. 6).

As a second region of interest, we consider the infalling envelope. According to the curves by Marchand et al. (2022), ambipolar diffusivities tend to be higher at lower densities ($n_H < 10^8\,\mathrm{cm}^{-3}$). This suggests that we are missing key magnetic diffusion during the early phases of gravitational collapse, where densities are low. However, there are theoretical and observational results that suggest that the collapse phase is still reasonably modeled in our simulations. In this simulation series, we consider the case of weak magnetic fields (see the discussion on this assumption in Sect. 5.3). Because ambipolar diffusivities increase with magnetic field strength, we expect magnetic diffusion to play a stronger role in cases when the magnetic fields are initially strong. In the studies by Commerçon et al. (2022) and Mignon-Risse et al. (2021), who considered $\bar{\mu} = 5$ and ambipolar diffusion but no Ohmic dissipation, the magnetic field distribution for low densities coincides well with what is depicted in Fig. 6. Based on this, we would not expect a strong qualitative divergence of our results for the gravitational collapse epoch ($t \lesssim 5\,\mathrm{kyr}$) upon the addition of ambipolar diffusion to our models. From the observational point of view, the role of ambipolar diffusion as a necessary enabler for gravitational collapse in a magnetized cloud core was recently questioned in Ching et al. (2022). These latter authors found a supercritical low-mass prestellar core, which is not yet self-gravitating. This means that the magnetic field was diffused before the gravitational collapse takes place, that is, earlier than predicted by the classical picture of ambipolar diffusion turning a subcritical core supercritical and in a consistent way with our simplification.

Lastly, we take a look at the magnetic diffusivities in the outflow cavity, which is the focus of Paper II. Observations of protostellar jets have found evidence of ionized material (see e.g., Moscadelli et al. 2021; Rodríguez-Kamenetzky et al. 2017; Carrasco-González et al. 2021; Guzmán et al. 2010), possibly from shock ionization. As discussed in Marchand et al. (2016, 2022), ionization leads to a general decrease in the magnetic diffusivities. So far, the models of ambipolar diffusion and the Hall effect done in, for example, Marchand et al. (2016, 2022) and Tsukamoto et al. (2021) do not consider the shock ionization in the outflow cavity. Material in the outflow cavity and close to the massive protostar is very low density and is in presence of strong magnetic fields, which means that neglecting shock ionization would overestimate magnetic diffusivities coming from the ambipolar diffusion and Hall effect terms, when comparing to the curves by Marchand et al. (2022). By only considering Ohmic dissipation (for which the resistivity is low for low densities and independent of magnetic field strength), the material in the cavity behaves closer to ideal MHD theory, in agreement to what has been found from observational evidence (see Sect. 6 and Moscadelli et al. (2022)). This can be seen in Fig. 6, where the magnetic field strengths in the cavity (light-colored dots) are able to increase while keeping the values constrained in the disk (dark-colored dots). A realistic treatment of the problem, however, would require the consideration of all forms of magnetic diffusivity (which would probably impact the disk dynamics) and the effect that thermal ionization and shock ionization have on the magnetic diffusivities corresponding to the outflow cavity.

### 4.6. Density and temperature profiles

Figure 7 presents the density and temperature profiles for the midplane. The thin layer has densities over $10^{-16}\,\mathrm{g\,cm}^{-3}$, and they reach over $10^{-11}\,\mathrm{g\,cm}^{-3}$ at the inner boundary. For $t \lesssim 15\,\mathrm{kyr}$, the density profile of the thin layer follows an approximate power law. Later, the magnetically braked region is formed, corresponding to the high density feature observed for $r \lesssim 30\,\mathrm{au}$ in Fig. 7a. Some of the material of the magnetically braked region is drawn from the thin layer of the disk: the density profile of the thin layer reveals the existence of a plateau close to its magnetic braking radius, which coincides as well with the decrease in the azimuthal contribution to the specific kinetic energy due to magnetic braking (Fig. 3c). However, another part of the material in the magnetically braked region corresponds to the inflows from the cavity wall and thick layer of the disk, both of which also experience magnetic braking and continuously replenish it.

The temperature profile of the thin layer follows roughly a power law of the form $T \propto r^{-1/2}$, and it experiences a general increase over time. The transition between the disk and the envelope is accompanied by a change in the temperature gradient; the transition between the magnetically braked region and the thin layer of the disk is subtler. We remind the reader that the present simulations do not include the effect of irradiation from the star, for which we anticipate two additional features not present in Fig. 7b, namely, an increase in temperature due to the flux from the forming massive star, and the existence of the dust evaporation front (see Kuiper et al. 2010). Those features are only relevant for $t \gtrsim 20\,\mathrm{kyr}$.

Fig. 8a presents the density profile at two different altitudes crossing the thick layer of the disk at the time $t = 10\,\mathrm{kyr}$ (when $M_\star = 3\,\mathrm{M}_\odot$), accompanied by a comparison with the density in the midplane. Differently than the thin layer of the disk, the thick layer has a nearly uniform density of $\sim 10^{-14}\,\mathrm{g\,cm}^{-3}$. The density drop for $r \lesssim 10\,\mathrm{au}$ corresponds to the outflow cavity. The mean density in the thick layer decreases slightly with time,

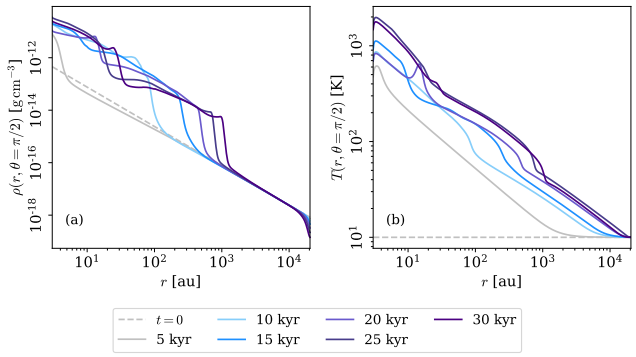



Fig. 7: Density (Panel *a*) and temperature (Panel *b*) profiles on the midplane, for the fiducial simulation on grid x8.

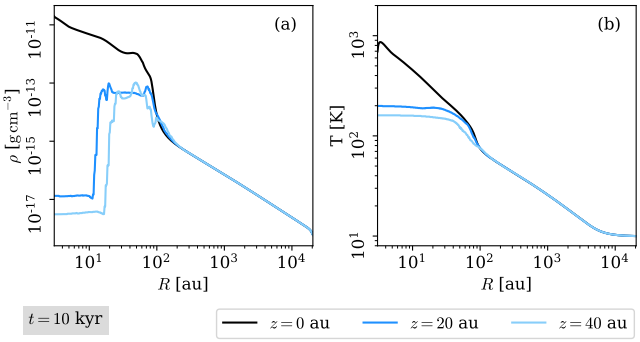



Fig. 8: Density (Panel *a*) and temperature (Panel *b*) for two different altitudes in the thick layers of the disk (blue lines), and the corresponding profile for the thin layer (black). The data corresponds to the fiducial simulation on grid x8.

however, it roughly remains within the same order of magnitude throughout the simulation.

Because the density is nearly uniform, the temperature of the thick layer of the disk remains also relatively uniform, at around 200 K in comparison to the power-law temperature of the thin layer. This means that it should be possible in principle to observe the vertical stratification of the disk by distinguishing the line emission from each layer.

## 5. Dependence of the resulting disk properties on initial cloud properties

We perform a series of simulations to explore the large parameter space of initial conditions. We vary the fiducial model model described above in terms of the initial mass of the cloud core, its density and rotation profiles, its rotational-to-gravitational energy ratio, its initial magnetic field strength and probe the effect of different models of Ohmic resistivity. In this section, we discuss how those changes affect the processes discussed in Sect. 4. As a probe, we use the radial extent of the Keplerian-like disk (between the magnetic braking radius and the [outer] radius), defined as the region where the material is within ±25% Keplerianity, and the results of which are presented in Fig. 9 for the whole parameter space. Similarly, the mass of the forming massive star is presented in Fig. 10 for the whole parameter space. We also examine differences in the density structure of the disk for selected values of the parameters, and relate them to the dynamical information revealed by the specific energy; the results are shown in Fig. 11.

### 5.1. Dependence on cloud core mass

Cloud cores of masses of 50, 100, 150 and 200 $M_\odot$ were considered, which form stars ranging masses from 6 to 75 $M_\odot$ after 30 kyr of evolution (see Fig. 10a). Further evolution and additional physical effects which are not considered here would be necessary to determine the final mass of the star. When changing the initial core mass of the fiducial model, we also change the normalization of the rotation profile in order to keep the rotational-to-gravitational energy ratio as in the fiducial model. The mass and size of the cloud core determines its free-fall timescale

$$t_{\rm ff} = \left( \frac{\pi^2 R_C^3}{8 G M_C} \right)^{1/2}, \tag{27}$$

which is 52.4 kyr for the fiducial case of $M_C = 100\,M_\odot$ and $R_C = 0.1$ pc. Panels A1 and A2 of Fig. 9 show that the disk and the magnetically braked region are smaller for the lower-mass cases when plotted against time, however, when investigated as a function of the stellar mass as a fraction of the initial mass of the cloud (panels A3 and A4), both the size of the disk and the magnetic braking radius coincide well. We find that resulting curves roughly follow the empirical linear relation

$$R_{\rm disk}(m) \approx R_{\rm onset} + R_\infty\,(m - m_{\rm onset})\,, \tag{28}$$

where we define

$$m \equiv \frac{M_\star}{M_C}. \tag{29}$$

We note that $R_{\rm onset} \equiv 3$ au is the minimum radius of the disk we can detect in the simulation data (the size of the sink cell), $m_{\rm onset} = 0.016$ is the corresponding normalized mass of the protostar for $R_{\rm onset}$, and $R_\infty = 6380$ au can be interpreted as the approximate value of the radius of the disk at the hypothetical end of the collapse where $m \sim 1$. This latter value will never be reached in reality because of stellar feedback: Kuiper & Hosokawa (2018), for example, found that the disk lifetime is expected to be of only a few $10^5$ yr (see also Kee & Kuiper 2019 for the conditions for limiting accretion through the disk). A similar empirical disk size formula was previously offered in Kuiper et al. (2011).

We also verified that the mass of the protostar, expressed as a fraction of the mass of the cloud, scales with time presented as fraction of the free-fall timescale (cf. panels *a* and *b* of Fig. 10). This result indicates that despite the differences in the scale-dependent microphysics, namely, the radiative transfer, resistivity and self-gravity, the disk scales well with the free-fall timescale, which allows our results to be used with a more ample range of cloud masses than what is presented here. Defining $\tau \equiv t/t_{\rm ff}$, we also find an approximate fit for the mass of the protostar with a power law:

$$m(\tau) \approx k_1\,\tau^{k_2}, \tag{30}$$

where $k_1 \approx 0.56$ and $k_2 \approx 1.8$.

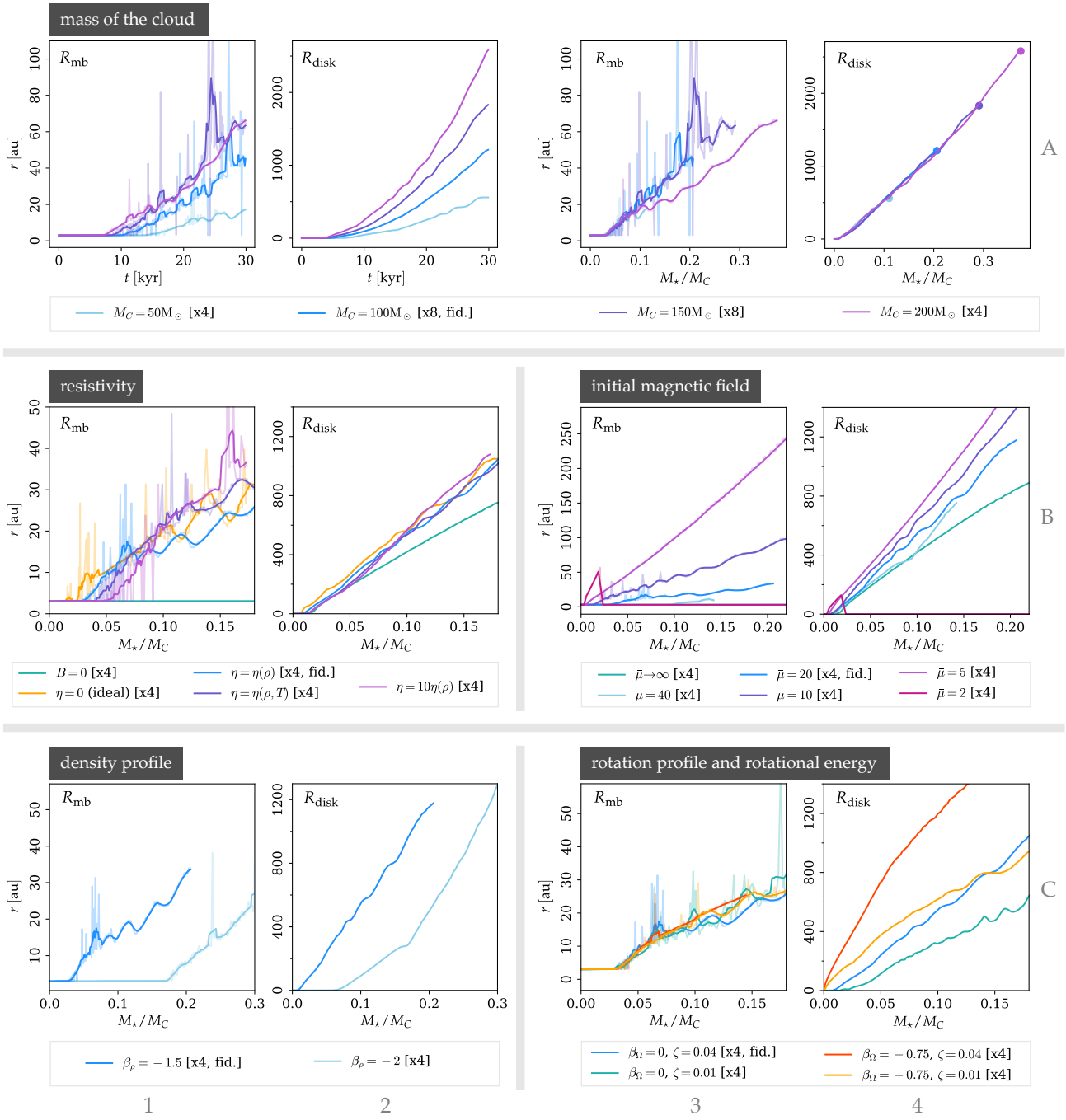



Fig. 9: Radius of the disk ($R_{\rm disk}$) and its magnetic braking radius ($R_{\rm mb}$) for different initial values of the mass of the cloud, magnetic field, density profile, rotational profile, rotational energy and resistivity models. The transparent lines in the panels that show $R_{\rm mb}$ indicate the full data, while the solid lines show the moving average. The colored dots in panel A4 indicate $t = 30$ kyr in each simulation. For all the panels in rows B and C, $M_C = 100\,{\rm M}_\odot$ was used.

### 5.2. Ohmic resistivity

The Ohmic resistivity model controls the diffusivity of the plasma, and therefore it has an impact on magnetic braking. We studied the effects of using the resistivity model of Machida et al. (2007) in two versions: the full expression dependent on both density and temperature, and the same expression but with a fixed temperature of ${}^{\rm o}T = 10\,{\rm K}$, as it was used in the isothermal study of Kölligan & Kuiper (2018). We denote the first one as $\eta(\rho, T)$ and the second one as $\eta(\rho)$ given the near linear behavior of the resistivity in the range of densities for which we are interested. We estimate that the version that considers the temperature dependence differs at most by a factor of 100 in regions close to the protostar with respect to the version with the fixed temperature. We compare our results as well with the ideal MHD case ($\eta = 0$) and the nonmagnetic (hydrodynamical) case ($\eta \to \infty$). In order to mimic the magnetic diffusivity

A&A proofs: manuscript no. 43835

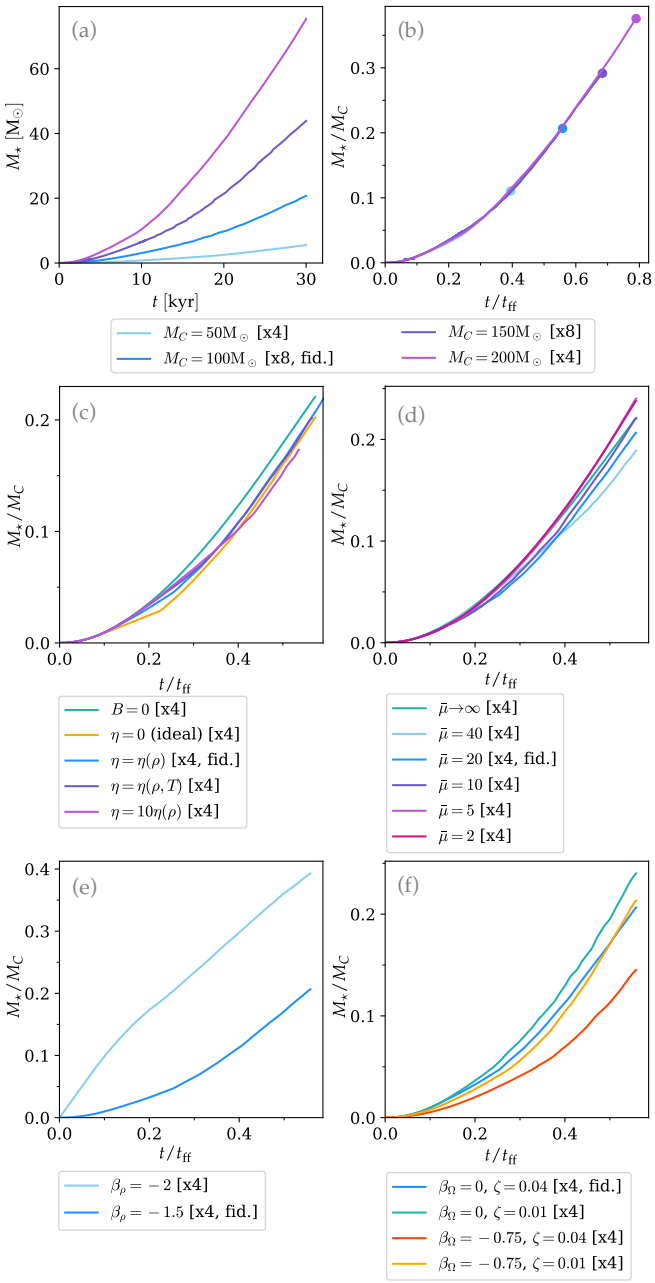



Fig. 10: Mass of the protostar, corresponding to the mass in the sink cell, for several values of the (*a*–*b*) mass of the cloud, (*c*) resistivity model, (*d*) mass-to-flux ratio, (*e*) density profile, and (*f*) rotation profile and rotational energy. Panel *b* shows the same results as panel *a*, but normalized in such a way that scalability can be readily seen. For panels (c)–(f), $M_C = 100\,M_\odot$ and $t_{\rm ff} = 53.73$ kyr.

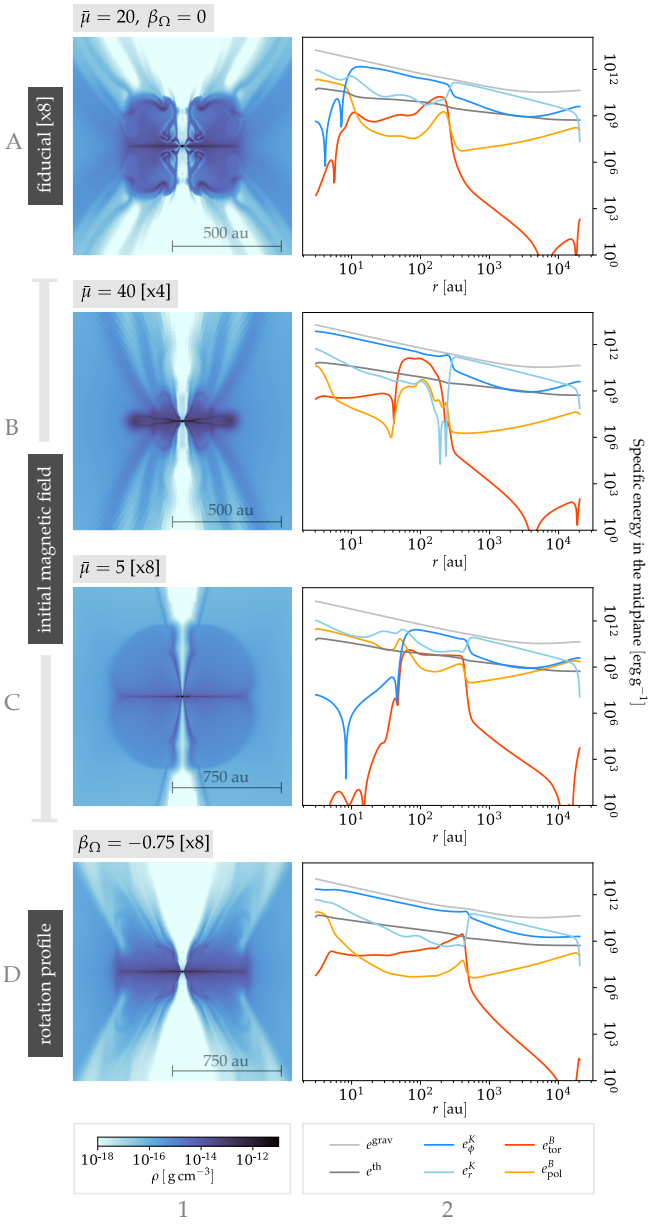



Fig. 11: Density structure (column 1) and specific energies (column 2) of the disk for selected values of the normalized values of the mass-to-flux ratio (rows B and C), and rotation profile (column D). All the snapshots were taken at $t = 15$ kyr of evolution. All cases consider a rotational-to-gravitational energy of 4%.

expected in the disk region if ambipolar diffusion were taking into account, we also include a simulation with an artificially high Ohmic resistivity (ten times the temperature-independent value, denoted as $10\eta(\rho)$). This factor is motivated by the difference in the curve for ambipolar diffusivity and Ohmic resistivity in Marchand et al. (2022), for disk densities. There is an additional difference between the simulations of this series: while most simulations of this study consider a constant dust and gas opacity of 1 cm$^2$ g$^{-1}$, the simulation with $\eta(\rho, T)$ uses the dust opacity table from Laor & Draine (1993) and a constant gas opacity of $10^{-2}$ cm$^2$ g$^{-1}$.

For the rest of Sect. 5, we present the size of the disk as a function of the stellar mass as a fraction of the cloud mass, instead of time, because the calculation of the offset from Keplerianity (which defines the disk) is dependent on the gravity of the (proto)star, and by fixing it we are able to compare and assess the effects of the other terms that influence the radial equilibrium of the disk, namely, the angular momentum and pressure support. Additionally, our results can be scaled as a result of the discussion in Sect. 5.1.

In the panel B1 of Fig. 9, we observe that the magnetically braked region develops earlier (when the mass of the star is lower, cf. Fig. 10c) in the ideal MHD case, as compared to the corresponding curves for the simulations that consider resistivity. The case with $\eta(\rho)$ requires a more massive protostar (more time evolution) for the magnetic braking radius to appear, a trend that is confirmed with the simulations that consider higher resistivity: the temperature-dependent resistivity delays the appearance of magnetic braking, while the simulation with the artificial factor of ten in resistivity delays it even further. As expected, the disk in the case with no magnetic fields does not develop a magnetic braking radius. A disk is able to form at all in the ideal MHD case because the relatively weak magnetic field considered for this parameter scan.

From this evidence, we infer that the presence of resistivity delays the action of magnetic braking compared to the results only considering ideal MHD. Higher resistivities delay magnetic braking more, however, as discussed in Sect. 4.3, because magnetic diffusion does not completely suppress the toroidal magnetic field, the Lorentz force continues to grow until enough magnetic tension force is built to decelerate the material. As a result, the innermost parts of the disk lose their centrifugal support.

The disk radius (Fig. 9B2) is in general larger in the magnetic cases in comparison to the nonmagnetic case. Moreover, the disk radius of the run with no resistivity (ideal MHD) is marginally larger than the ones with resistivity. Magnetic braking removes angular momentum from the disk because of the torque produced by magnetic tension; therefore, a smaller disk would be expectable. However, magnetic tension is highest in the inner disk, where the magnetic field lines are wound the most, and not in the outer disk. As discussed in Sect. 4.1.3, magnetic pressure can provide an additional radial support for the disk. This means that in the ideal MHD case, where the toroidal magnetic field is high in the disk, the additional magnetic pressure supports a larger disk. Magnetic diffusion lowers the toroidal magnetic field, and therefore the disk does not have radial magnetic pressure support: this can be seen at early times (where $M_\star < 5\,\mathrm{M}_\odot$ or $m = 0.05$) where the simulations with $\eta(\rho, T)$ and $10\eta(\rho)$ yield a disk radius that almost matches the one obtained in the nonmagnetic case. As the toroidal magnetic field increases over time due to the winding of magnetic field lines, the magnetic pressure support also increases and the disk becomes larger than the nonmagnetic case.

Given that magnetic braking delivers mass onto the protostar, we investigate the role of resistivity in the mass of the forming massive star. The corresponding curves for the mass of the protostar as a function of time are shown in Fig. 10c. The results for the resistive and nonresistive cases are very similar. The stellar mass, however, increases more in the nonmagnetic case in comparison to the magnetic cases. This happens because the protostar in the nonmagnetic case accretes material not only through the disk, but also through the infalling envelope along the bipolar directions. On the contrary, in the magnetic cases, there are magnetic outflows that impede accretion through the axis, resulting in a slightly lower mass.

### 5.3. Initial magnetic field strength

We study values of the normalized mass-to-flux ratio ranging from $\bar{\mu} = 2$ (strongest magnetic field) to $\bar{\mu} = 40$ (weakest magnetic field). The results of the radial extent of the centrifugally supported disk are shown in the panels B1 and B2 of Fig. 9. The curve for $\bar{\mu} = 2$ goes quickly to zero, which means that the structure formed is strongly sub-Keplerian and it is not classified as a Keplerian-like disk according to our criterion. A more detailed study of the specific energies revealed that the structure has a comparable radial and azimuthal velocities. Our result of no disk for $\bar{\mu} = 2$ should be taken with caution, because we do not include ambipolar diffusion in our calculations. As ambipolar diffusivities increase with magnetic field (contrary to Ohmic dissipation), the cases with strong magnetic fields are missing magnetic diffusivity that may allow the disk to form (see the discussions in Sects. 4.5 and 7.3).

The other values of the mass-to-flux ratio confirm that magnetic braking is responsible for the formation of the magnetically braked region because higher initial magnetic fields build enough magnetic tension earlier. Additionally, the magnetically braked region is larger for stronger magnetic fields. The radius of the disk, on the other hand, is larger for stronger magnetic fields, which supports the hypothesis that higher magnetic pressure provides additional support against gravity and allows material from larger radii (with lower angular momentum) to be part of the disk. As for the accretion onto the protostar, Fig. 10d reveals that higher magnetic fields do tend to deliver more mass onto the protostar, due to stronger magnetic braking at late stages.

The rows A–C of Fig. 11 present a comparison of the morphological differences of the disk when it has evolved for $t = 15\,\mathrm{kyr}$ under different values of the mass-to-flux ratio. For $\bar{\mu} = 40$, the weaker magnetic field produces a disk with a thick layer that is smaller than the thin layer. Both regions of the disk are of the same size for $\bar{\mu} = 20$, which confirms magnetic pressure as the nature of the vertical support in the thick disk. However, the part of the thin layer that is not enveloped by the thick layer of the disk becomes inflated by magnetic pressure, as the curve for the toroidal contribution to the specific magnetic energy reveals in Fig. 11B2: in the outer disk ($r \sim 100\,\mathrm{au}$), $e^B_{\mathrm{tor}}$ becomes higher than $e^{\mathrm{th}}$. Nevertheless, a similar analysis of the specific energies at later times reveals that the thick layer of the disk grows over time until it completely envelops the thin layer (which happens at around $t \sim 19\,\mathrm{kyr}$). At $t \approx 25.5\,\mathrm{kyr}$, the thin and thick disk layers of the disk of the case with $\bar{\mu} = 40$ become morphologically and dynamically similar to the results shown in panels A1 and A2 corresponding to the $\bar{\mu} = 20$ at 15 kyr; the difference being the size of the disk and the mass of the protostar. For a stronger initial magnetic field ($\bar{\mu} = 5$, row C of Fig. 11), the thick layer becomes thicker because of the increased magnetic pressure.

### 5.4. Initial density profile

A steeper initial density profile accelerates the accretion onto the protostar at early times because of the increased concentration of mass (and therefore gravity) in the center of the cloud. Apart from a density profile with $\beta_\rho = -1.5$, we also tried a profile with $\beta_\rho = -2$. The mass of the protostar (Fig. 10e) increases rapidly at early times with $\beta_\rho = -2$, but the accretion rate decelerates over time, which is the opposite behavior observed for $\beta_\rho = -1.5$. This behavior can be readily seen from the power-law fits to those curves: the normalization constant is similar in both cases, but while the fiducial case is described by $m \propto \tau^{1.80}$, the steeper initial density profile exhibits $m \propto \tau^{0.94}$. The radius of the disk (Fig. 9C2) is larger in the case of the shallower density profile when seen as a function of the stellar mass and its behavior is longer linear. However, given that the stellar mass increases more rapidly in the case of the steeper density profile, in this latter case, a disk of a given size is observed earlier in

A&A proofs: manuscript no. 43835

time. A similar comparison of stellar masses and time reveals that magnetic braking happens at roughly the same time for both simulations, because the magnetic field is wound by rotation in a similar way in both cases. While the magnetically braked region appears at $M \approx 3\,\mathrm{M}_\odot$ when $\beta_\rho = -1.5$, it appears at $M \approx 17\,\mathrm{M}_\odot$ for $\beta_\rho = -2$; however, the protostar reaches both masses at the same time, $t \approx 0.2 t_{\rm ff} \approx 10.7\,$kyr. As a result, we conclude that a disk that does not exhibit a magnetically braked region at a given time can be obtained for a range of protostellar masses by adjusting the initial density profile.

### 5.5. Initial rotation profile

We investigated the effect of two scenarios: initial solid-body rotation and a rotation profile that scales with the cylindrical radius at $\Omega \propto R^{-\beta_\Omega}$, with $\beta_\Omega = \beta_\rho/2 = -0.75$. This choice of $\beta_\Omega$ keeps the initial ratio of rotational to gravitational energy independent of the radius of the cloud. Additionally, the particular value of $-0.75$ produces a cloud for which the offset from Keplerianity is uniformly negative. We complemented this parameter scan with an investigation of the effects of using a lower initial rotational-to-gravitational energy ratio $\zeta$ of 1% instead of 4% as in the fiducial case.

An inspection between panels D1 and A1 of Fig. 11 reveals that the thick layer of the disk is flatter in the cloud with the steep rotation profile. The higher angular velocity at the center of the cloud allows for the formation of a larger accretion disk earlier in the simulation, in comparison with the cloud initially rotating as a solid-body. Panel C4 of Fig. 9 confirms this: the curves for the disk radius for $\beta_\Omega = -0.75$, $\zeta = \{0.01, 0.04\}$ are in general higher than the corresponding curves for $\beta_\Omega = 0$, and resemble a power law rather than a linear function as it is the case for solid-body rotation. For a fixed value of $\beta_\Omega$, the disk becomes larger with more content of initial rotational energy. Additionally, both curves for $\beta_\Omega = -0.75$ show that the disk forms at very early times during the simulation compared to $\beta_\Omega = 0$: for the solid-body case, angular momentum conservation during the gravitational collapse provides the necessary increase of angular momentum in the center of the cloud in order to build up a disk, while the steep rotation profile already provides some of this angular momentum from the start. Interestingly, the cases $\beta_\Omega = -0.75$, $\zeta = 0.01$ and $\beta_\Omega = 0$, $\zeta = 0.04$ produce a similar disk radius. The mass of the formed protostar (Fig. 10f) is lower in the cases with a steep rotation profile and higher initial rotational energy. This is consequence of the earlier formation of a disk that is also larger (and therefore more massive), at it reduces the efficiency of accretion onto the protostar (in Oliva & Kuiper 2020, we utilized this fact to study disk fragmentation in the absence of magnetic fields). The magnetic braking radius of the disk is very similar for all cases when plotted as a function of the protostellar mass, however, given that the masses grow different in time, magnetic braking appears later in the case with $\beta_\Omega = 0$, $\zeta = 0.04$.

From the dynamical point of view, a comparison between panels D2 and A2 of Fig. 11 reveals that in general, the different contributions to the specific energy have a more uniform radial gradient. Given that the offset from Keplerianity in the midplane can also be computed as $1 - 2e^K_\phi/e^{\rm grav}$, the disk formed with the steep rotation profile is more uniformly Keplerian. This is also manifested when comparing the curves for $e^K_r$ inside of the disk in both cases.

## 6. Comparison to observations

### 6.1. Natal environment of massive star formation

The parameter space in our simulation set was motivated by observational typical values found in regions of massive star formation. Surveys of cloud cores in the early stages of massive star formation have found power-law density profiles with exponents ranging in $1.5 \lesssim -\beta_\rho \lesssim 2.6$ (see, for example, Gieser et al. 2022; Beuther et al. 2018, 2002; Mueller et al. 2002; Hatchell & van der Tak 2003), with fragmenting cores having typical values of around $\beta_\rho \approx -1.5$. We take values in the extremes of this interval.

For the initial angular momentum, we start from the results of the survey by (Goodman et al. 1993), who found that the ratio of rotational to gravitational energy of cloud cores ($\zeta$) is of a few per cent, with typical values of around 2%. Those authors fit linear gradients to the cloud cores that had signs of rotation, and found solid-body profiles. Our second choice for the initial rotation profile, $\beta_\Omega = \beta_\rho/2$, is motivated by keeping $\zeta$ independent of the radius of the cloud core, as explained in Sect. 5.5.

The values of the mass-to-flux ratio are motivated by the supercriticality in star-forming cloud cores (e.g., Beuther et al. 2020; Girart et al. 2013) and the following analysis. In low-mass prestellar cores, the magnitudes of the magnetic field have been found to be on the order of a few to tens of micro Gauss (Ching et al. 2022; Troland & Crutcher 2008). As the precollapse conditions in the massive star formation case are currently not known, we consider two scenarios (see also the discussion in Machida & Hosokawa 2020) as follows. The first scenario assumes that the normalized mass-to-flux ratio is independent of mass, which means that magnetic field strengths of 100 to $1000\,\mu$G are required in the cloud prior to the gravitational collapse. On the other hand, the second scenario considers that the magnetic field strength of the high-mass star formation case is similar to the low-mass counterpart, which implies that the mass-to-flux ratio must be high.

The first case is investigated by using the low mass-to-flux ratios in our parameter space ($\bar{\mu} \sim 5$), while the second case corresponds to high mass-to-flux ratios, including our fiducial case ($\bar{\mu} = 20$).

### 6.2. Size of the disk

The analysis in Sect. 5 has shown that the radius of the disk is more strongly determined by the initial density and rotation (angular momentum) profiles of the large scale initial condition, as compared to the magnetic field and resistivity models, within the ranges of those values expected from observations. Panel B4 of Fig. 9 shows that when $M_\star/M_C \sim 0.15$, the average $R_{\rm disk}$ for the values of $\bar{\mu}$ we considered is around 850 au, with a variation on the order of $\pm 200$ au. However, the radius of the disk and its growth rate vary much more with the density profile and the rotation profile (panels C2 and C4 of Fig. 9). Smaller disks are produced with a lower and flatter initial distribution of angular momentum, and with shallower initial density profiles. This conclusion is crucial for the comparison of our results with previous studies, which is done in Sect. 7.

With regards to the available observational evidence of disk-jet systems around forming massive stars, we see that in principle it is possible to obtain a variety of disk sizes that are not only dependent on the age of the system but also on the initial distribution of matter and angular momentum, and not so strongly determined by magnetic braking in the outer regions of the disk.

For example, assuming that the molecular cloud has the typical values of $M_C = 100\,\mathrm{M}_\odot$ in a sphere of radius 0.1 pc of our fiducial case, we obtain a disk of radius $\sim 1200$ au when the mass of the protostar is $M_\star \sim 10\,\mathrm{M}_\odot$, if we assume a steep and fast initial rotation profile ($\beta_\Omega = -0.75$, $\zeta = 0.04$), which would provide a possible initial configuration for the observations of HH 80-81 (Girart et al. 2017).

In Moscadelli et al. (2022), we utilized the fiducial simulation run on grid x16 to model the accretion disk and jet of IRAS 21078+5211. For that particular system, observations of molecular rotational transitions had revealed the existence of a Keplerian-like accretion disk of around 200 au in size (Moscadelli et al. 2021). In order to find a model of our catalog that was consistent with the observations, in Moscadelli et al. (2022) we used the mass of the protostar, the radius of the disk, and the morphology of the ejected material to constrain the parameter space and the time elapsed. In that study, we found strong agreement between the velocity field of the observed water masers and the velocity streamlines predicted by the chosen model from our catalog. This good agreement in turn constitutes evidence that the results for the size of the disk as a function of the precollapse conditions –which we present in Sect. 5– are in line with what is expected from observations. We note, however, that the wide streamline traced by the maser points (Fig. 2 of Moscadelli et al. 2022) is slightly closer to the assumed disk plane compared to the reference wide streamline from the simulations. This can be caused by a number of factors, for example, a slightly different assumed perspective between the simulations and the observations, but a possible explanation is that the disk in IRAS 21078+5211 is thinner than what is predicted in the simulations.

## 7. Comparison with previous numerical studies

The present study is a continuation of the work started by Kölligan & Kuiper (2018). Their simulations correspond to our fiducial case but with a grid equivalent to our x2 grid, and used an isothermal equation of state. An isothermal equation of state yields a much smaller pressure scale height of the disk or thinner disk, respectively. In combination with the rather coarse grid resolution, the thickness of the disk could not be resolved on the numerical grid, making an in-depth convergence study problematic. In that sense, the addition of radiation transport and higher resolutions has enabled us to resolve the thin layer of the disk, and clearly differentiate it from the surrounding region that we call the thick layer of the disk. Also, they do not report about the existence of the magnetically braked region; however, it is visible upon close examination of their Fig. 21 as a region where the vertical velocity is negative close to the center of the disk. This was originally thought to be a numerical effect caused by the additional mass created by the Alfvén limiter, however, we performed a parameter scan with several values of the Alfvén limiter, the highest values of which produce negligible artificial mass, and found a magnetically braked region in all of them.

### 7.1. Studies with ideal MHD

Banerjee & Pudritz (2007), Seifried et al. (2011), Myers et al. (2013) and Rosen & Krumholz (2020) conducted simulations of the formation of massive stars under the assumption of ideal MHD. Although Banerjee & Pudritz (2007) observed magnetically driven outflows, their disk is always sub-Keplerian. Myers et al. (2013) started from a cloud of $300 M_\odot$, an initial velocity profile with supersonic turbulence and no rotation, and $\bar{\mu} = 2$ with $B_z \propto R^{-1/2}$. They included gray radiative transfer and radiative protostellar feedback, and used a 3D AMR grid with a maximum resolution of 10 au, as well as an additional isothermal high resolution run ($\Delta x = 1.25$ au). They only find a disk in their high resolution run; it has a radius of 40 au when $t \sim 0.2 t_{\mathrm{ff}}$, for which $M_\star \sim 3.5 M_\odot$. It is not trivial to compare their results to ours because of the difference in initial velocity fields, and the use of an isothermal equation of state. Using the scalability of our results with the mass of the cloud, we find the radius of the disk to be 128 au for $t = 0.2 t_{\mathrm{ff}}$ in the simulation for $\bar{\mu} = 2$. However, if we take $M_\star / M_C$ and compute the corresponding fraction of the free-fall timescale, we get $t/t_{\mathrm{ff}} \approx 0.104$, for which our disk has a radius of $\sim 30$ au, which is in line with the fact that supersonic turbulence delays the formation of an accretion disk as enough angular momentum has to assemble close to the forming star. Rosen & Krumholz (2020) also considered a cloud core with supersonic turbulence and radiation transport, however their coarse grid (minimum cell size of 20 au) only allows them to partially resolve a disk-like structure and therefore a direct comparison to our results is not possible.

Seifried et al. (2011) considered a setup similar to ours in terms of the mass and radius of the cloud, as well as its initial density and rotation profiles, but used a cooling function instead of radiation transport, and only considered the ideal MHD approximation. The code FLASH with an AMR grid of maximum resolution of 4.7 au was used. The authors explored several values of $\bar{\mu}$ ranging from 2.6 to 26, but with a uniform plasma $\beta$, and obtained a Keplerian-like accretion disk for $\bar{\mu} = 26$. They observe a drop in Keplerianity for the inner parts of the disk in the case of $\bar{\mu} = 10.4$, and credit it to magnetic braking, in agreement with our results; however, they do not observe a disk for $\bar{\mu} < 5.2$ because the high density of the thin layer of the disk decouples the gas from the magnetic field im resistive MHD runs.

### 7.2. Studies including Ohmic resistivity

Matsushita et al. (2017) and Machida & Hosokawa (2020) use the same Ohmic resistivity model as we do (Machida et al. 2007), but both consider a barotropic equation of state instead of solving for radiation transport. In Matsushita et al. (2017), a disk was formed, however, their analyses are strongly focused on the magnetic outflows. Machida & Hosokawa (2020) consider cloud cores of radius 0.2 pc with masses ranging from 11 to 545 solar masses, an enhanced Bonnor-Ebert density profile, and slow initial solid-body rotation. If we expand our cloud to 0.2 pc, keeping the same density profile as in the fiducial case, the mass of the cloud becomes $283\,\mathrm{M}_\odot$, which means that our setup is similar to their simulation series E. The authors also make a parameter scan with the normalized mass-to-flux ratio with values ranging from 2 to 20, and use a three-dimensional AMR grid with a maximum resolution of 0.62 au. After 10 kyr of evolution, they find disk radii of a few hundred astronomical units, which develop spiral arms and fragments for some configurations.

### 7.3. Studies including ambipolar diffusion

Mignon-Risse et al. (2021) and Commerçon et al. (2022) studied the formation of massive stars from $100\,\mathrm{M}_\odot$ cloud cores of radius 0.2 pc, with a centrally condensed initial density profile; which roughly correspond to our configuration $M_C = 50\,\mathrm{M}_\odot$. The cloud cores are initially in solid body rotation and are threaded by a uniform magnetic field determined from the normalized mass-to-flux ratio $\bar{\mu} = 5$ and 2. They treated radiation transport with the

A&A proofs: manuscript no. 43835

flux-limited diffusion approach and gray stellar irradiation; for magnetic diffusivity, they considered ambipolar diffusion using the model from Marchand et al. (2016) but no Ohmic resistivity, and ran their simulations on a three-dimensional AMR grid with the code RAMSES down to a maximum resolution of 5 au. In a nutshell, those studies constitute the ones which include the most similar physical ingredients but to our setup but with ambipolar diffusion instead of Ohmic dissipation as the resistive effect and utilizing a different grid method.

Both studies report on thin accretion disks which are vertically supported by thermal pressure, in agreement with our results; however, they do not observe a surrounding thick layer of the disk supported by magnetic pressure. Opposite to our findings, the authors find smaller disks with stronger magnetic fields, however, they do find a bigger disk for their ideal MHD run compared to the runs with ambipolar diffusion. In that case, the disk is not only bigger, but also inflated and therefore less dense, in agreement with our results. They attribute the finding of smaller disks to higher ionization in the outer disk, and therefore more magnetic braking. In turn, our results indicate that magnetic braking is highest in the inner disk, where the fluid and the magnetic field lines are dragged faster by rotation, although resistivity causes the dragging to be partial and delayed because of the dominance of magnetic diffusion. Moreover, in our results for the ideal MHD case we observe simultaneously the largest disk and the strongest magnetic braking, because it mostly affects the inner disk.

A comparison of the radius of the disk that we report here and the disk size reported in Commerçon et al. (2022) can only be made qualitatively and with several considerations in mind, apart from the difference in the nonideal MHD effect considered. First, the density profiles in both studies are different because of the presence of an initial density plateau in the inner $\sim 4125$ au in Commerçon et al. (2022) and Mignon-Risse et al. (2021), in contrast to our continuous power-law slope down to the smallest scales. This density plateau affects the gravitational collapse and therefore, the elapsed time and mass of the protostar cannot be directly compared. Second, the initial rotational to gravitational energy ratio of the cloud is not the same in the fiducial cases of both studies, but we can roughly compare our $\zeta = 0.04$ case to the "fast" case studied in Commerçon et al. (2022), which has $\zeta = 0.05$. This is of special importance because of what is shown in Fig. 9C4: the radius of the disk is strongly influenced by the initial rotation of the cloud, even more than the initial magnetic field (cf. Fig. 9B4) or resistivity (Fig. 9B2). Finally, the disk identification criterion is not the same in both studies: while Commerçon et al. (2022) use a set of criteria that involves the radial and vertical dynamics of the disk as well as a density threshold, we consider a purely dynamical criterion (radial equilibrium between gravity and centrifugal force) as it is more usual in observational studies. With this in mind, we note that in our simulation $M_C = 50$ M$_\odot$ [x4], the radius of the disk is around 470 au after 27 kyr, while their disk is around the same value after 51 kyr. However, the mass of the protostar at that time is lower in our case (4.6 M$_\odot$) than theirs (9.1 M$_\odot$); both the difference in time and mass can be reasonably attributed to the initial density profile. Additionally, while we find that the disk grows in size with time, most of the nonideal MHD simulations by Commerçon et al. (2022) find disks that stop growing at around 100 au.

Commerçon et al. (2022) and Mignon-Risse et al. (2021) do not report the existence of a magnetically braked region, for which we offer the following explanations, apart from the different criteria for disk identification we already discussed. First, ambipolar diffusion adds magnetic diffusivity, which may have the effect of delaying the formation of the magnetically braked region. In more detail: we report on the fact that higher Ohmic resistivities delay the onset of magnetic braking and with it, the formation of the magnetically braked region. Ambipolar diffusion also decouples the magnetic field from the flow (even though it may act in a different direction than Ohmic resistivity), which leads us to assume that a similar delaying effect on magnetic braking could be obtained upon the inclusion of ambipolar diffusion in our calculations. We note, however, that if this delay in the onset of magnetic braking is longer than the timescale of gravitational collapse of the cloud, the massive star and the disk may form without ever developing a magnetically braked region. Second, spatial resolution: their 3D AMR grid has a minimum cell size (maximum spatial resolution) of 5 au, while our grid has minimum cell sizes on the order of $10^{-1}$ au close to the sink cell for the simulation series x1, x2 and x4, and $10^{-2}$ au for the simulation series x8 and x16. Third, their sink particle algorithm requires the definition of an accretion radius, set to four times the minimum cell size, that is 20 au, which is the size of the magnetically braked region for most of the time in our fiducial case. As a consequence, gas orbiting the massive protostar within the accretion radius or in the forming magnetically braked region cannot be resolved on their finest AMR level while it is resolved on our spherical grid.

Finally, we mention the study by Masson et al. (2016), who carried out simulations of low-mass star formation considering both ideal MHD and ambipolar diffusion. Although we cannot compare our results quantitatively with theirs, there are several qualitative similarities. The authors observe an accretion disk vertically supported by thermal pressure, with magnetic pressure dominating above the disk. Their figure 14 shows a structure with relatively high angular momentum enveloping the disk for both the diffusive and ideal cases, which is reminiscent of the thick layer of the disk we observe, however, due to the different definitions of the disk used in both studies, we cannot establish a direct correspondence. The same figure also shows that in the ideal MHD case, the inner parts of the disk are destroyed by magnetic braking at late times. Nevertheless, their corresponding run that considers ambipolar diffusion also exhibits for late times a region of low angular momentum (probably due to magnetic braking) in a conical region around the inner disk and that could deliver material to it, in a way that is reminiscent of the early stages of magnetic braking we observe in our simulations. Those results seem to support the idea that increasing the diffusivity leads to a delay but not complete suppression of magnetic braking in a magnetized disk embedded in a collapsing cloud.

## 8. Summary and conclusions

We have modeled the formation of a massive star with a series of 30 magnetohydrodynamical simulations including Ohmic resistivity, radiation transport from thermal emission of the dust and gas, and self gravity. The series of simulations covered a wide range of cloud masses, magnetic field strengths, density profiles, rotation profiles, and ratios of rotational to gravitational energy, which is in line with the currently estimated values from observations. We also performed a convergence study to test the robustness of our results.

After analyzing the fiducial case of our parameter study in depth, we found the following general features of the system:

– After the initial gravitational collapse, a Keplerian-like accretion disk was formed.

- The accretion disk is divided into two layers: a thin layer supported vertically by thermal pressure, and a surrounding thick layer supported by magnetic pressure. The thin layer of the disk appears only in simulations with sufficiently high resolution.
- At early times magnetic diffusion due to Ohmic resistivity is strong in the inner parts of the disk and it greatly reduces magnetic braking there during the magneto-centrifugal epoch ($5\,\mathrm{kyr} \lesssim t \lesssim 15\,\mathrm{kyr}$). As time progresses, and the magnetic field lines are continuously dragged by rotation, magnetic braking is observed in the innermost $\sim 50$ au of the disk for the fiducial case in our parameter space.
- Magnetic pressure can increase the size of the accretion disk.

When examining the full parameter space of initial conditions for the onset of gravitational collapse, we find that:

- Our results for the size of the disk and the mass gain of the protostar scale with the initial mass of the cloud, despite the nonscalability of self-gravity and the thermodynamics considered.
- The thickness of the thick layer of the disk is controlled by the initial magnetic field strength.
- For a cloud with an initial density profile $\rho \propto r^{-1.5}$ and in solid-body rotation, the disk grows roughly linearly in size as $R_{\mathrm{disk}} \approx [6380 M_\star/M_C - 98]$ au. The stellar mass grows approximately as $M_\star \propto (t/t_{\mathrm{ff}})^{1.5..1.9}$.
- The size of the disk is more strongly determined by the initial distribution of density and rotational energy in the cloud than by the strength of the magnetic field.
- Multiple initial configurations of the cloud can produce a given disk size and (proto)stellar mass. This means that observations of disk-jet systems constrain (as opposed to determine) the possible conditions for the onset of gravitational collapse, and more measurements (distribution and strength of magnetic fields, for example) are needed to break the degeneracies.

These results indicate that the initial conditions of massive star formation determine the features of the system composed of the disk, jet and protostar. In the second part of this study (Paper II), we perform a dynamical analysis of the magnetically driven outflows of the same dataset we present here.

*Acknowledgements.* We thank Richard Nies for his contributions to the analysis of part of the dataset at the early stages of the project. GAO acknowledges financial support from the Deutscher Akademischer Austauschdienst (DAAD), under the program Research Grants - Doctoral Projects in Germany, and complementary financial support for the completion of the Doctoral degree by the University of Costa Rica, as part of their scholarship program for postgraduate studies in foreign institutions. RK acknowledges financial support via the Emmy Noether and Heisenberg Research Grants funded by the German Research Foundation (DFG) under grant no. KU 2849/3 and 2849/9.

## References

Banerjee, R. & Pudritz, R. E. 2007, ApJ, 660, 479
Beltrán, M. T., Padovani, M., Girart, J. M., et al. 2019, A&A, 630, A54
Beuther, H., Mottram, J. C., Ahmadi, A., et al. 2018, A&A, 617, A100
Beuther, H., Schilke, P., Menten, K. M., et al. 2002, ApJ, 566, 945
Beuther, H. & Shepherd, D. 2005, in Astrophysics and Space Science Library, Vol. 324, Astrophysics and Space Science Library, ed. M. S. N. Kumar, M. Tafalla, & P. Caselli, 105
Beuther, H., Soler, J. D., Linz, H., et al. 2020, ApJ, 904, 168
Blandford, R. D. & Payne, D. G. 1982, MNRAS, 199, 883
Carrasco-González, C., Rodríguez, L. F., Anglada, G., et al. 2010, Science, 330, 1209
Carrasco-González, C., Sanna, A., Rodríguez-Kamenetzky, A., et al. 2021, ApJ, 914, L1
Ching, T. C., Li, D., Heiles, C., et al. 2022, Nature, 601, 49
Commerçon, B., González, M., Mignon-Risse, R., Hennebelle, P., & Vaytet, N. 2022, A&A, 658, A52
Commerçon, B., Teyssier, R., Audit, E., Hennebelle, P., & Chabrier, G. 2011, A&A, 529, A35
Galli, D., Lizano, S., Shu, F. H., & Allen, A. 2006, ApJ, 647, 374
Gieser, C., Beuther, H., Semenov, D., et al. 2022, A&A, 657, A3
Girart, J. M., Estalella, R., Fernández-López, M., et al. 2017, ApJ, 847, 58
Girart, J. M., Frau, P., Zhang, Q., et al. 2013, ApJ, 772, 69
Goodman, A. A., Benson, P. J., Fuller, G. A., & Myers, P. C. 1993, ApJ, 406, 528
Guzmán, A. E., Garay, G., & Brooks, K. J. 2010, ApJ, 725, 734
Hatchell, J. & van der Tak, F. F. S. 2003, A&A, 409, 589
Hosokawa, T. & Omukai, K. 2009, ApJ, 691, 823
Kee, N. D. & Kuiper, R. 2019, MNRAS, 483, 4893
Kölligan, A. & Kuiper, R. 2018, A&A, 620, A182
Kuiper, R. & Hosokawa, T. 2018, A&A, 616, A101
Kuiper, R., Klahr, H., Beuther, H., & Henning, T. 2010, ApJ, 722, 1556
Kuiper, R., Klahr, H., Beuther, H., & Henning, T. 2011, ApJ, 732, 20
Kuiper, R., Yorke, H. W., & Mignone, A. 2020, ApJS, 250, 13
Laor, A. & Draine, B. T. 1993, ApJ, 402, 441
Lynden-Bell, D. 2003, MNRAS, 341, 1360
Machida, M. N. & Hosokawa, T. 2020, MNRAS, 499, 4490
Machida, M. N., Inutsuka, S.-i., & Matsumoto, T. 2007, ApJ, 670, 1198
Marchand, P., Guillet, V., Lebreuilly, U., & Mac Low, M.-M. 2022, arXiv e-prints, arXiv:2202.11625
Marchand, P., Masson, J., Chabrier, G., et al. 2016, A&A, 592, A18
Masson, J., Chabrier, G., Hennebelle, P., Vaytet, N., & Commerçon, B. 2016, A&A, 587, A32
Matsushita, Y., Machida, M. N., Sakurai, Y., & Hosokawa, T. 2017, MNRAS, 470, 1026
Mignon-Risse, R., González, M., Commerçon, B., & Rosdahl, J. 2021, A&A, 652, A69
Mignone, A., Bodo, G., Massaglia, S., et al. 2007, ApJS, 170, 228
Moscadelli, L., Beuther, H., Ahmadi, A., et al. 2021, A&A, 647, A114
Moscadelli, L., Sanna, A., Beuther, H., Oliva, A., & Kuiper, R. 2022, Nat. Astron., https://doi.org/10.1038/s41550-022-01754-4
Mouschovias, T. C. & Spitzer, L., J. 1976, ApJ, 210, 326
Mueller, K. E., Shirley, Y. L., Evans, Neal J., I., & Jacobson, H. R. 2002, ApJS, 143, 469
Myers, A. T., McKee, C. F., Cunningham, A. J., Klein, R. I., & Krumholz, M. R. 2013, ApJ, 766, 97
Nakano, T., Nishi, R., & Umebayashi, T. 2002, ApJ, 573, 199
Oliva, A. & Kuiper, R. 2022, A&A, accepted (Paper II)
Oliva, G. A. & Kuiper, R. 2020, A&A, 644, A41
Purser, S. J. D., Lumsden, S. L., Hoare, M. G., et al. 2016, MNRAS, 460, 1039
Rodríguez-Kamenetzky, A., Carrasco-González, C., Araudo, A., et al. 2017, ApJ, 851, 16
Rosen, A. L. & Krumholz, M. R. 2020, AJ, 160, 78
Seifried, D., Banerjee, R., Klessen, R. S., Duffin, D., & Pudritz, R. E. 2011, MNRAS, 417, 1054
Shakura, N. I. & Sunyaev, R. A. 1973, A&A, 24, 337
Troland, T. H. & Crutcher, R. M. 2008, ApJ, 680, 457
Tsukamoto, Y., Machida, M. N., & Inutsuka, S. 2021, ApJ, 913, 148

A&A proofs: manuscript no. 43835

## Appendix A: Numerical convergence

As part of the parameter scan performed for this study, we investigated the effects of the grid and other numerically relevant parameters on our findings. Here, we focus on checking the effect on the extent of the disk, that is its inner and outer radii, which we present in Fig. A.1.

### *Appendix A.1: Sink cell size*

We tried sink cell radii of $r_{\rm sc} = 1, 3$, and 10 au as our inner boundary. As shown in panels A1 and A2 of Fig. A.1, the results for the radius of the disk and the magnetic braking radius are very consistent for $r_{\rm sc} = 1$ and 3 au, but larger inner and outer radii at late phases of the simulation for $r_{\rm sc} = 10$ au. Of special interest is the fact that for the smaller sink sizes, both the size and the time of formation of the magnetically braked region region does not change, which supports the idea that the effect is physical and not due to the inner boundary conditions.

During the formation of the massive star starting from the $100\,{\rm M}_\odot$ cloud, the stellar radius computed with the stellar evolutionary tracks increases up to a maximum of 150 solar radii, which correspond to approx. 0.7 astronomical units. The use of a smaller sink cell would not be accurate because it would require the solution of the full set of stellar structure equations, which we do not do. With this in mind, we conclude that a sink cell size of 1 au is close to the reasonable limit for the approximations considered in this study, and a sink cell size of 3 au is enough to replicate the results of the smaller sink.

### *Appendix A.2: Resolution*

We conducted the study of the fiducial case in five different resolutions, each one doubling the amount of cells in each one of the directions (radial and polar). The simulation x16 was only run until $t = 13.45$ kyr due to the high computational cost. The radius of the disk is very similar in all of the simulations. The magnetic braking radius appears somewhat later in the high resolution simulations and it shows more variability for the grid x8. This could be due to the increased resolution of the effects of the outflows, which will be discussed in Paper II. However, during the comparison of the disk radii, it is important to consider that our definition of the size of the disk, based on a simple threshold to Keplerianity, is affected by the size of the cells, rounding to the nearest cell that satisfies the criterion.

### *Appendix A.3: Viscosity*

The $\alpha$-viscosity model to gravitational torques produced by spiral arms in the self-gravitating disk introduces an additional parameter. For this reason, we investigated what happens if the value of $\alpha$ is changed to 0.75 and 1.5 from its fiducial value of 1. Panels B1 and B2 in Fig. A.1 show relatively consistent results in all cases, even though with some local differences. The magnetic braking region appears when the star is of the same mass in all cases, and the radius of the disk averages approximately to the same value over time. Even though viscosity transports angular momentum, the qualitative behavior is different than the effect of resistivity and initial magnetic field, both of which significantly alter the formation time of the magnetically braked region and its size. This marks the difference between magnetic braking and angular momentum transport by viscosity.

### *Appendix A.4: Alfvén limiter*

We employed an upper limit to the Alfvén speed

$$v_A = \frac{B}{\sqrt{4\pi\rho}}, \tag{A.1}$$

by introducing a locally variable density floor such that the Alfvén speed never exceeds the limit, which is defined a priori. This limiter was introduced to avoid having the Alfvén speed increase indefinitely. The time step remains within limits that allow us to cover the desired timescales in a reasonable computing time. This approach has the disadvantage that artificial mass is created in the process, which in theory could affect the dynamics of the gas. A more detailed discussion of the effects of the Alfvén limiter will be offered in Paper II on jet physics, however, we mention here that with the values chosen for the simulation series x4 and x8, 2000 and $1000\,{\rm km\,s^{-1}}$ respectively, artificial mass below $0.002\,{\rm M}_\odot$ is generated at the end of the simulation. This value is very small compared to the mass of the cloud and should not change the dynamics of the disk and the outflows. In turn, for simulation series x2, an Alfvén limiter of $2000\,{\rm km\,s^{-1}}$ produces an additional $0.2\,{\rm M}_\odot$ of artificial mass, with lower values yielding over $1\,{\rm M}_\odot$, i.e., more than one per cent of the initial mass of the cloud. With these values of the limiter and the artificial mass in mind, we examine the extent of the disk in panels B3 and B4 of Fig. A.1 as a probe for effects in the dynamics of the disk and find that only in the case of an exceptionally low Alfvén limiter of $200\,{\rm km\,s^{-1}}$ there are appreciable changes to the inner and outer radii of the disk for late times.

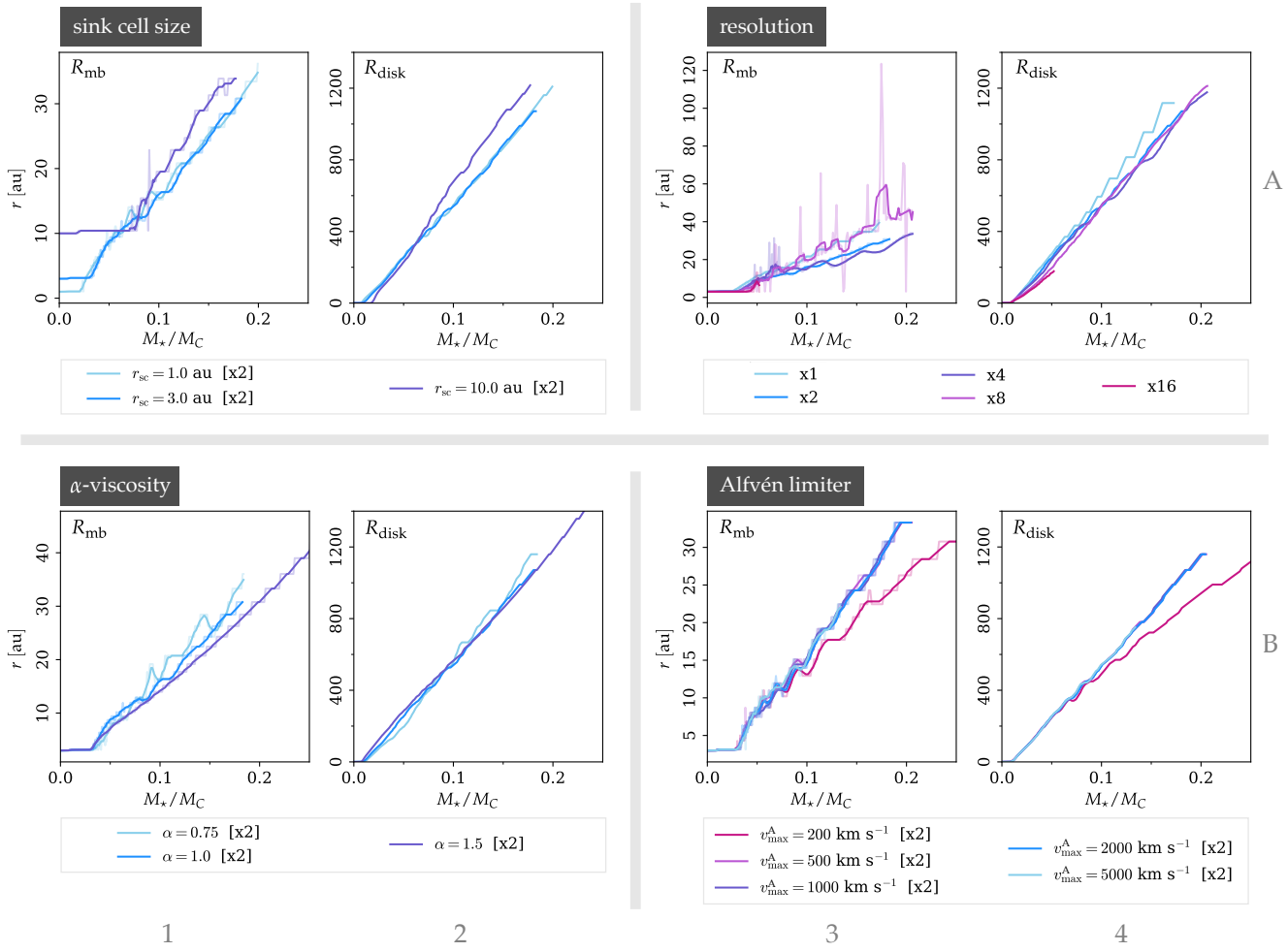



Fig. A.1: Variation of the radius of the disk and the magnetic braking radius for different the inner boundary (sink cell size), resolution of the grid, the $\alpha$-viscosity used to model gravitational torques and the Alfvén limiter.

*Astronomy & Astrophysics* manuscript no. 44434
November 12, 2022
©ESO 2022

# Modeling disks and magnetic outflows around a forming massive star: II. Dynamics of jets from massive protostars

André Oliva[1] and Rolf Kuiper[2, 1]

[1] Institute for Astronomy and Astrophysics, University of Tübingen, Auf der Morgenstelle 10, D-72076, Tübingen, Germany
e-mail: andree.oliva@uni-tuebingen.de

[2] Faculty of Physics, University of Duisburg–Essen, Lotharstraße 1, D-47057, Duisburg, Germany
e-mail: rolf.kuiper@uni-due.de

Accepted: September 21, 2022

**ABSTRACT**

*Context.* Forming massive stars launch outflows of magnetic origin, which in fact serve as a marker for finding sites of massive star formation. However, both the theoretical and observational study of the mechanisms that intervene in the formation and propagation of such magnetically driven outflows has been possible only until recent years.
*Aims.* With this work, we aim to study the mechanisms that drive highly collimated outflows from early stages of the formation of a massive star, in detail, and how those processes are impacted by the properties of the natal environment of the forming massive star.
*Methods.* We performed a series of 31 simulations with the aim of building a unified theoretical picture of these mechanisms, and determined how the impact of different environments alter their morphology and momentum output. The magnetohydrodynamical simulations also consider Ohmic dissipation as a nonideal effect, self-gravity, and diffusive radiation transport for thermal absorption and emission by the dust and gas. We started from a collapsing cloud core that is threaded by an initially uniform magnetic field and which is slowly rotating. We utilized a two-dimensional axisymmetric grid in spherical coordinates.
*Results.* In the simulations, we can clearly distinguish a fast, magneto-centrifugally launched and collimated jet (of speeds $\gtrsim 100\,\mathrm{km\,s^{-1}}$), from a wider magnetic tower flow driven by magnetic pressure which broadens in time. We analyze the acceleration of the flow, in detail, and its recollimation by magnetic forces happening at distances of several hundreds of astronomical units. We quantify the impact of magnetic braking in the outflows, which narrows the outflow cavity for the late evolution of the system. We find that despite the nonscalability of self-gravity and the thermodynamics of the medium, our results scale with the mass of the cloud core and can, in principle, be used with a range of values for such mass. We observe the presence of the same jet-driving mechanisms for a wide range of assumptions on the natal environment of the massive protostar, but with changes to their morphology and mechanical feedback into larger scales over time.

**Key words.** stars: massive – stars: formation – magnetohydrodynamics (MHD) – stars: jets

## 1. Introduction

During the formation of massive stars, collimated bipolar outflows are launched, which become a marker of star formation and a source of mechanical feedback into their natal environment. They transport angular momentum into large scales, enhancing accretion through their accompanying disk. There is mounting observational and theoretical evidence, especially in recent years, that highly collimated protostellar outflows are driven by magnetic processes.

The presence of collimated jets around young massive stellar systems is well documented: Purser et al. (2021, 2016), for example, used radio continuum observations to build catalogs of candidates of jets around massive protostars, and McLeod et al. (2018) were able to even detect a jet around a massive young star from an extragalactic source. Guzmán et al. (2010) and Sanna et al. (2019) performed radio observations of jets around massive protostars for the star-forming regions IRAS 16562-3959 and G035.02+0.35, respectively. Synchrotron emission has been observed coming from the massive protostellar jets HH 80-81, Cep A HW2, and IRAS 21078+5211 (see Carrasco-González et al. 2010; Carrasco-González et al. 2021 and Moscadelli et al. 2021) in regions not close to the protostar (at least a few hundred astronomical units away). The origin of this nonthermal emission has been attributed to a recollimation of the jet due to magnetic forces (Carrasco-González et al. 2021). In Carrasco-González et al. (2021), two components of the magnetically driven outflows are observed: a fast jet (with speeds of at least $500\,\mathrm{km\,s^{-1}}$) and a wide-angle wind. Substructures with proper motions have been observed in the outflow ejecta (Obonyo et al. 2021), indicating nonsmoothness in the ejection process.

A new generation of observations that combine data from new or upgraded (sub)millimiter interferometers such as the Northern Extended Millimeter Array (NOEMA), the Atacama Large Millimeter/submillimeter Array (ALMA), the Very Long Baseline Interferometry network (VLBI), and the Jansky Very Large Array (JVLA) have enabled an unprecedented resolution of the innermost $\sim$ 100 au around the forming massive star, such that the direct study of the dynamical processes that intervene in the launching (Moscadelli et al. 2022) and collimation (Carrasco-González et al. 2021) of the jet is now possible. However, previous numerical studies of massive protostellar outflows (for example, Rosen & Krumholz 2020; Machida & Hosokawa 2020 or Mignon-Risse et al. 2021; a more detailed literature review is offered in Sect. 5) have not been able to spatially resolve

A&A proofs: manuscript no. 44434

the launching mechanisms of the fast component of the magnetically driven collimated jets. The study by Kölligan & Kuiper (2018) has shown that a self-consistent launching of a fast magnetic outflow driven by the magneto-centrifugal mechanism was possible.

Thanks to observations of water masers done in Moscadelli et al. (2022), the innermost $\sim$ 100 au region where the jet is launched can now be observed with a resolution of up to 0.05 au. In that article, we presented a simulation of a forming massive star surrounded by a disk-jet system that was able to reach those resolutions and reproduced the observed jet kinematics reasonably well. That simulation was part of a larger set of 31 simulations in total, and subjected to a deeper analysis of the physical processes and evolution of the disk and the magnetically driven outflows.

In a previous article (Oliva & Kuiper 2022, hereafter Paper I), we focused on the study of the effects of magnetic fields in the dynamics of the disk. We found that the disk can be distinguished into two vertical layers supported by thermal and magnetic pressure, respectively. Additionally, we extensively studied the size of the disk and the impact of magnetic braking under several star-forming environments. In this article, we focus on the dynamics of the magnetically driven outflows: their launching processes, acceleration, propagation, and termination. The use of the full parameter space we introduced in Paper I enables us to deepen our understanding of how those processes develop, and how the initial conditions for the gravitational collapse influence the resulting outflow, its structure, and propagation.

In section 2, we summarize the setup and methods we used in Paper I. Section 3 deals with a dynamical analysis of the launching, acceleration, propagation, and termination of the magnetically driven outflows, focused on the fiducial case of our simulation catalog. In Section 4, we study how the conditions for the onset of gravitational collapse affect the protostellar outflows produced by the forming massive star. In Section 5, we offer a literature review and a comparison of our results with previous numerical studies. Section 6 contains a summary and the major conclusions of our work. Finally, we examine the numerical convergence of our results in Appendix A.

## 2. Methods and parameter space

Here, we summarize the methods and configuration of the simulation catalog already presented in Paper I. For a more in-depth discussion of the equations solved, and the solution methods used, we point the reader to that reference.

We simulate the formation of a massive star by following the gravitational collapse of a slowly rotating cloud core of 0.1 pc in radius, threaded by an initially uniform magnetic field, until the formation of a disk-jet system around the massive (proto)star. At the onset of gravitational collapse (initial configuration), the cloud core has a mass $M_C$, distributed along a density profile $\rho \propto r^{\beta_\rho}$ ($r$ being the spherical radius), a rotational-to-gravitational energy ratio $\zeta$, an angular velocity distribution according to $\Omega \propto R^{\beta_\Omega}$ (with $R$ the cylindrical radius), and a uniform magnetic field parallel to the rotation axis whose strength is determined by the mass-to-flux ratio $\bar{\mu}$ in units of the critical (collapse-preventing) value. We used the Machida et al. (2007) resistivity model (both with the full temperature and density dependence and with a fixed temperature to save computational power and to allow for a direct comparison with the models by Kölligan & Kuiper 2018), and two other cases for comparison: neglecting the resistivity (ideal MHD) and neglecting magnetic fields.

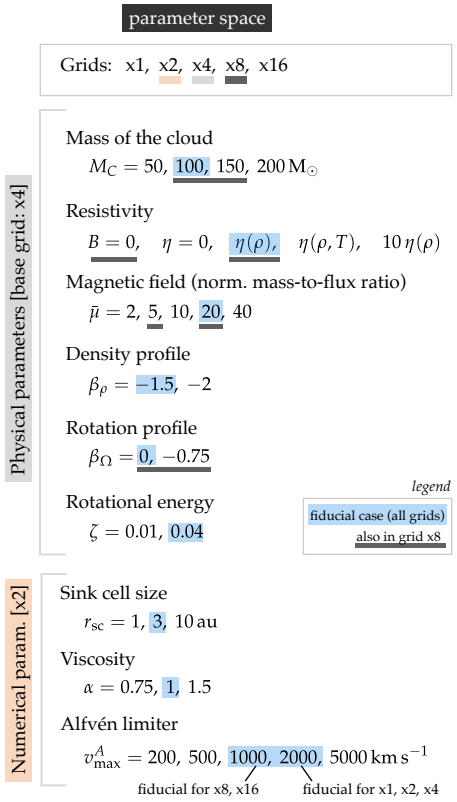



**Fig. 1.** Schematic overview of the parameter space covered by the simulation series.

For modeling the weakly ionized gas, we used the methods of magnetohydrodynamics with the code Pluto (Mignone et al. 2007), with additional modules for Ohmic resistivity (with the model by Machida et al. 2007), self-gravity (Kuiper et al. 2010), and the radiation transport of thermal emission from the dust and gas (Kuiper et al. 2020) with the gray flux-limited diffusion approximation. We assume axisymmetry and equatorial symmetry in the simulations. The inner boundary of the simulation domain, which we refer as the sink cell, models the (proto)star. Matter that flows into the sink cell is considered as accreted by the protostar and cannot escape. The magnetic field lines are prolonged across the sink cell with a zero-gradient boundary condition. No flows are artificially injected into the cloud from the protostar; the outflow launching occurs self-consistently within the computational domain. The accretion disk is massive and is expected to form spiral arms and fragment (Oliva & Kuiper 2020). In order to model the gravitational torque from the spiral arms in the azimuthal direction, we use shear $\alpha$-viscosity, following the setup and results of Kuiper et al. (2011). Inside the outflow cavity, the Alfvén speed increases significantly due to the low densities and strong magnetic fields. In order to avoid extremely small numerical time steps, a limit to the Alfvén speed was used (a detailed discussion of its effects on the outflows is offered in Appendix A.2).

Convergence of the results was studied in the parameter space by using five different grids of increasing resolution, as well as several sizes for the inner boundary (which we refer as the sink cell, and which models the forming protostar). Grid x16, the highest resolution one in our series, consists of 896 logarithmically spaced cells in the radial direction, and 160 linearly spaced cells along the polar angle. This translates to a minimum

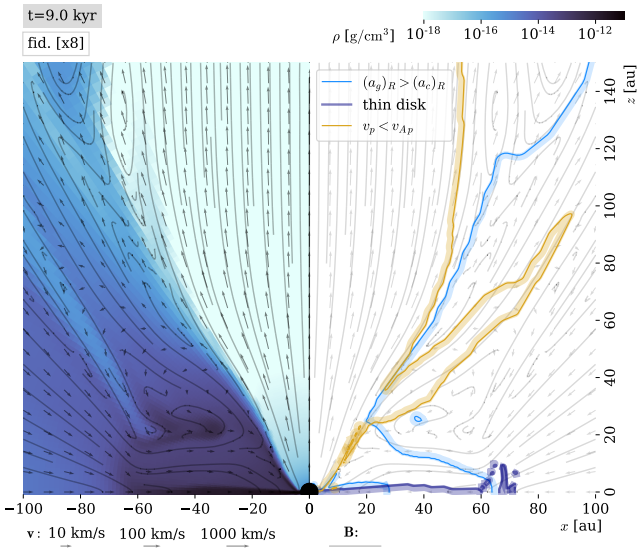



**Fig. 2.** Magneto-centrifugal mechanism for the fiducial case in x8

grid cell size is 0.03 au at 3 au from the forming massive star and 10 au at $r = 1000$ au. The rest of the grid sizes in the series are obtained by dividing by two the number of cells of each direction. Figure 1 presents a schematic summary of the parameter space considered in this study. The values of each parameter corresponding to the fiducial case are highlighted in blue. To simplify nomenclature, we use the following convention: modifications of the fiducial values are written followed by the name of the corresponding grid. For example, $\bar{\mu} = 5$ [x8] means a cloud of a mass-to-flux ratio of 5, with the rest of the parameters as in the fiducial case run on the grid x8.

## 3. Physical processes in the outflows

This section is focused on a detailed examination of the outflows produced in the fiducial simulation of our series. We compute several force terms from the magnetohydrodynamical equations and compare their relative strength with the aim of understanding the physical processes that intervene in the launching, acceleration, propagation and termination of the different components of the magnetically driven massive protostellar outflows.

### 3.1. Magneto-centrifugal launching

The low-density, bipolar jet cavity starts to appear close to the protostar shortly after the formation of the disk at around $t \sim 5$ kyr, in a process described in more detail in Sect. 3.7, which results in an initial bow shock being thrust out. Once the high-speed component of the outflow has established, (and similarly to Kölligan & Kuiper 2018) we find evidence for the magneto-centrifugal mechanism described in Blandford & Payne (1982) inside of the cavity, although with some key geometrical differences which we explain below.

A brief note on the visualizations that make use of directed contours throughout the article: an understanding of the launching mechanisms for outflows requires the simultaneous visualization of several intervening forces, morphological features, and other quantities that carry dynamical information. With this end, and taking advantage of the axial symmetry of our models, we present here a system of plots containing contour lines which aided the interpretation of our results and the drawing of our conclusions. The first instance of such visualizations is given in the right panel of Fig. 2. Each solid contour line is followed by an adjacent shadow of the same color, which indicates the direction on which the inequality listed in the legend holds true. Throughout the article, we refer to both the contour and its corresponding shadow as a *directed contour* [1].

First, we perform a dynamical examination of the launching mechanism of the fast jet. Figure 2 displays a typical scenario during the magneto-centrifugal phase of the simulation. The left panel provides a joint view of the gas mass density (background color map), poloidal velocity (as a vector field with arrows) and magnetic field (as field lines in solid color), and the right panel presents the directed contours that separate the fulfillment of conditions on two quantities of dynamical interest. The blue directed contour indicates the equilibrium between the (corotating) centrifugal acceleration

$$(a_g)_R = \frac{v_\phi^2}{R}, \tag{1}$$

and the cylindrical radial component of the gravitational acceleration

$$(a_c)_R = \frac{GM(r)}{r^2} \sin\theta, \tag{2}$$

where $M(r)$ is the mass enclosed in a spherical radius $r$ (including the mass of the protostar), and which constitutes an approximation to the use of the full gravitational potential of stellar gravity and gas self-gravity. In the shadowed blue region, the gravitational force dominates over the centrifugal force along the cylindrical radial direction. A disadvantage of the use of contours to visualize a ratio of forces is the poor handling of regions where equilibrium holds, as opposed to regions with clear dominance of a force over another. This is the case in the thick and thin layers of the disk, for which the contour is no longer adequate. The equilibrium of forces in the disk was studied in detail in Paper I: in a nutshell, both the thick and thin disks are roughly Keplerian, with thermal and magnetic pressure causing small local regions of sub- and super-Keplerianity, but with the material always being transported inward.

The yellow directed contour delimits the Alfvén surface, that is the surface where the speed of the plasma is lower than the Alfvén speed

$$v_A = \frac{|\boldsymbol{B}|}{\sqrt{4\pi\rho}}, \tag{3}$$

where the magnetic field strength $|\boldsymbol{B}|$ is expressed in Gauss. For the purpose of our analysis, we use the corotating frame of reference, which means that we take only the magnitudes of the poloidal components of the velocity and magnetic field[2]. Outside of the Alfvén surface, perturbations to the originally vertical magnetic field (in this case, caused by the gravitational collapse) occur faster than the restoring force of magnetic tension,

[1] Directed contours are computed with respect to the boundaries of the grid cells, making them appear unnecessarily complex in high-resolution simulations. A smoothing filter has been applied to all the directed contours in this article in order to improve clarity in the explanations. As a caveat, this smoothing process causes some parts of certain contours to appear open.

[2] Given that we assume axisymmetry and the simulations were performed on a grid in spherical coordinates, we decompose a given vector $\boldsymbol{A}$ into two perpendicular vector components: toroidal $A_\phi \boldsymbol{e}_\phi$, and poloidal $\boldsymbol{A}_p = A_r \boldsymbol{e}_r + A_\theta \boldsymbol{e}_\theta$, with $\boldsymbol{e}_i$ denoting unit vectors.

resulting in the typical hour-glass morphology of gravitational collapse of a gaseous cloud in rotation (for an observational example, see Beuther et al. 2020). The contrary happens inside the Alfvén surface: the gas flow is forced to follow the magnetic field lines thanks to the restoring magnetic forces. The sub-Alfvénic regime is reached because of the strong magnetic fields close to the protostar (caused by the gravitational drag of the magnetic field) and the low density in the cavity.

The simulations presented include magnetic diffusion in the form of Ohmic resistivity, which acts mostly in the thin and thick disks (see Paper I) but its action is severely limited in the cavity due to its low density (and therefore, low resistivity). This implies that in the cavity, the plasma is essentially flux-frozen. This can be readily seen while comparing the directions of the velocity field and magnetic field lines in the cavity as presented in Fig. 2. We note, however, that while the plasma is flux-frozen in the simulations, this might not be fully the case in reality because other forms of magnetic diffusion (ambipolar diffusion and the Hall effect) are not considered in this study.

We can summarize the magneto-centrifugal mechanism as seen in our results in the following way. Consider a parcel of gas that has fallen in from large scales onto the thick disk. It is then transported through the accretion disk until it reaches the cavity wall. If the parcel enters the cavity, it experiences $(a_c)_R > (a_g)_R$, and the parcel would tend to move cylindrical-radially outward in the absence of magnetic fields. However, the parcel enters simultaneously the sub-Alfvénic regime, which means that the flow must follow the magnetic field lines resulting in the parcel being launched radially outward. The acceleration of the parcel inside the cavity is detailed in Sect. 3.2.

The model by Blandford & Payne (1982) was proposed in the context of accretion disks surrounding black holes, that is, an infalling envelope was not included, which is necessary in the study of the early stages of protostellar jets. Even though we find general agreement in the launching mechanism of the high-velocity jet, we observe that the jet launching area is not located on top of the full accretion disk. The ram pressure from the infalling envelope, and the effect of magnetic pressure on the disk (the existence of a thick layer in the disk) constrain the formation of the cavity to a conic region in the innermost scales, which means that the launching surface of the jet is located on the portion of the cavity wall that is in contact with the incoming material from the thick accretion disk. The densities found in the envelope and the thick disk impede the flow to become sub-Alfvénic except in the cavity, close to the launching area. The Alfvén surface does not occupy the full cavity, but it is restricted to a narrow region close to the rotation axis and reaches sizes of $\sim 1000$ au, after which the magnetic field becomes too weak. Beyond the Alfvén surface, the flow is collimated in a process described in Sect. 3.6.

### 3.2. Acceleration of material in the jet

In this section, we continue the discussion of the trajectory of a parcel of plasma as it accelerates throughout the cavity and is expelled into larger scales. The right panel of Fig. 3 provides a view of the gravito-centrifugal equilibrium and the Alfvén surface as discussed above, but also presents a directed contour (in purple) that delimits the region where the magnetic field lines are mostly wound by rotation. In the launching area (marked as $a$), the magnetic field lines are mostly poloidal, and a (sub-Alfvénic) parcel of plasma is then forced to follow a mostly radial trajectory until it reaches the Alfvén surface.

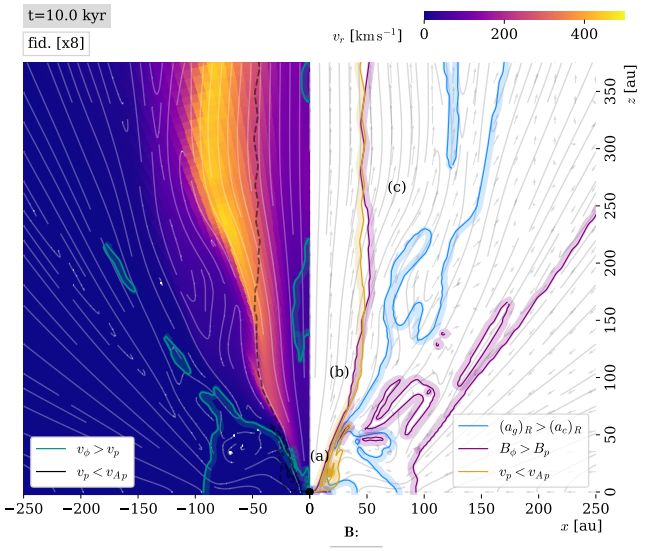



**Fig. 3.** Acceleration of material along the magnetic field lines

To see this explicitly, we take the energy equation of the plasma that, ignoring radiation transport and considering a stationary state, reduces to

$$\boldsymbol{\nabla} \cdot \left[ (E^g + E^K + E^{\rm th} + P)\boldsymbol{v} + c\boldsymbol{\mathcal{E}} \times \boldsymbol{B} \right] = 0, \tag{4}$$

with the first terms inside the parenthesis being the gravitational, kinetic and thermal energy densities, and $\boldsymbol{\mathcal{E}}$ being the electric field. The presence of the gravitational energy density as stated is possible because it does not change significantly over time during the acceleration process. Given that in the cavity we can ignore Ohmic dissipation, $c\boldsymbol{\mathcal{E}} = -\boldsymbol{v} \times \boldsymbol{B}$. As discussed, the sub-Alfvénicity of the flow close to the launching area causes $\boldsymbol{B} \parallel \boldsymbol{v}$, which implies $c\boldsymbol{\mathcal{E}} \times \boldsymbol{B} = -(\boldsymbol{v} \times \boldsymbol{B}) \times \boldsymbol{B} = \boldsymbol{0}$ and allows us to conclude from Eq. 4 that

$$E^g + E^K + E^{\rm th} + P = \text{constant} \tag{5}$$

along the flow in the cavity. This expression enables us to study the process of acceleration of material in the jet, illustrated in the left panel of Fig. 3. The background map represents the radial velocity (for which the color scale ignores the negative values), and the directed contour highlights the region where the azimuthal component of the velocity is higher in magnitude than its poloidal value. Outside of the disk and in the outer parts of the cavity, the velocity turns from mostly azimuthal to mostly poloidal. As the parcel is forced to follow the magnetic field lines from the position marked as $a$ to $b$ in Fig. 3, it travels to larger $r$, where the gravitational energy is lower. Then, according to Eq. 5, the kinetic energy of the parcel has to increase, given our result from Paper I that the contribution of the thermal energy and pressure are negligible. The parcel accelerates $v_r \sim 0$ to $\sim 400$ km/s along the spherical-radial direction. As a consequence of this process, the highest velocities of the jet at small scales are not found close to the rotation axis.

Once the parcel of plasma leaves the Alfvén surface (mark $c$ in Fig. 3), it enters the region where the magnetic field lines are mostly wound. The trajectory of the flow becomes helical as the flow partially follows the magnetic field lines, but an additional upward acceleration is experienced by the parcel because of magnetic pressure (more details of this process are offered in

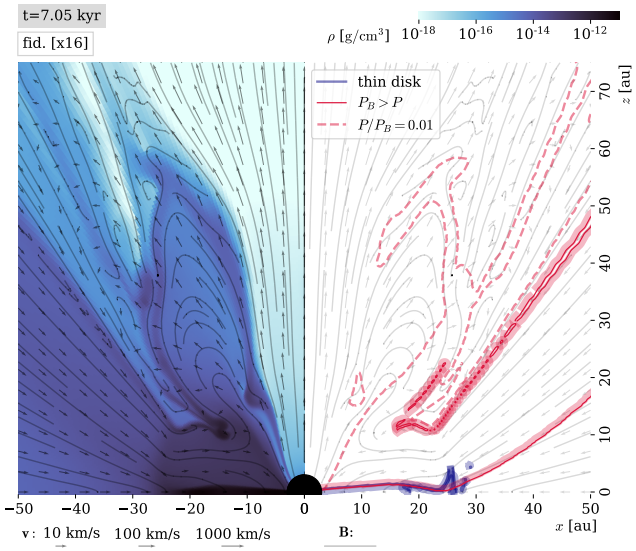



**Fig. 4.** Cavity wall ejection

Sect. 3.4). The jet now propagates away from the protostar and into larger scales of the cloud core.

A more thorough examination of the jet speeds across the whole simulation series reveals that speeds of at least 100 km s$^{-1}$, and over 1000 km s$^{-1}$ are reached in certain regions. However, the maximum speed reached by the jet is not a fully converged value for the reasons discussed in Appendix A.

The most direct observational evidence of the magneto-centrifugal mechanism and the acceleration of the jet as described here is provided by the recent observations of the most massive young stellar object ($M_\star = 5.6 \pm 2.0 M_\odot$) in the star-forming region IRAS 21078+5211 (Moscadelli et al. 2022, 2021). In Moscadelli et al. (2022), 22 GHz water maser observations (which trace internal shocks of the gas), were able to uncover the helical trajectories of the plasma as it is magneto-centrifugally ejected. In that article, we used the simulation corresponding to the fiducial case with grid x16 to produce a snapshot comparison when the protostellar mass is similar to the observed value, and found that the geometry and kinematics of the transition region where the flow abandons the Alfvén surface and becomes helical coincide very well with the observed masers. Furthermore, the high velocities of the water masers observed in IRAS 21078+5211 ($\sim 200$ km s$^{-1}$) are fully compatible with the values found in the numerical simulations.

### 3.3. Cavity wall ejections

The cavity wall contributes to both inflows and outflows episodically. When a section from the cavity wall enters the region where centrifugal forces dominate over gravity, the section starts to move outward, forming a toroidal prominence, as illustrated in Fig. 4. This prominence grows quickly and develops a neck, thanks to the material infalling from larger scales that provides an inward flow that narrows the neck. The densities present on the cavity wall are sufficient for magnetic diffusion to take place, allowing magnetic field lines to reconnect. This in turn allows the protuberance to decouple from the rest of the cavity wall and it is ejected through the cavity thanks to the magneto-centrifugal mechanism.

The solid pink directed contour in the right panel of Fig. 4 shows the regions where magnetic pressure dominates over thermal pressure, that is, it delimits the region where

$$\beta_p \equiv \frac{P}{P_B} = \frac{E^{\rm th}}{E^B} < 1. \tag{6}$$

The contour confirms that the thin disk is thermally supported while the thick disk is magnetically supported in the vertical direction, as it was concluded from Paper I. The densest parts of the cavity wall become thermally dominated, as magnetic diffusion becomes high enough in those regions and then magnetic energy is dissipated into thermal energy. We also display the contour for $\beta_p = 0.01$, which temporarily includes the protuberance and shows that some magnetic energy is dissipated into thermal energy as the magnetic field lines are reconnected. After the ejection event takes place, the magnetic field lines are quickly reconfigured in the cavity wall in a similar way to Fig. 2. We remark, however, that the ejection mechanism for the cavity wall ejections is the magneto-centrifugal mechanism and not the energy released by magnetic diffusion during reconnection. The reconnection of magnetic field lines provides a way for the mass to be released into the cavity.

The cavity wall ejections provide not only a mechanism for episodic ejection, but also a mechanism for episodic accretion, as the infall from the envelope onto the protostar is temporarily halted while the ejection event takes place. The observed timescale for the formation and ejection of the protuberance is $\sim 10$ yr, with the reconnection event happening in $\lesssim 1$ yr, although those values increase with the elapsed time as the disk grows in size.

We remind the reader that the simulations are performed under the assumption of axisymmetry, and therefore, a three-dimensional study that resolves similar scales would be required to know the role that a turbulent flow would have on ejected material from the cavity wall. For example, turbulent reconnection might make cavity wall ejections more frequent, asymmetric and smaller in size, instead of episodic and large in size, as we find. Additionally, the inclusion of ambipolar diffusion and the Hall effect may affect the reconnection process or not allow the formation of the prominence at all.

### 3.4. Magnetic tower flow

We observe a different kind of magnetically driven outflow which we refer to as the magnetic tower flow, and corresponds to the outflow mechanism described in Lynden-Bell (2003). As time progresses, the dragging of magnetic field lines by rotation increase magnetic pressure until its gradient is eventually larger than the local gravitational force. At large scales, outside of the Alfvén surface, this force drives the magnetic tower flow.

An example of the tower flow is given in Fig. 5, taken from late stages ($t = 28$ kyr $= 0.59 t_{\rm ff}$) and large scales (the cavity reaches the radius of the cloud). Again, the purple directed contour delimits the region where the magnetic field lines are wound by the rotational drag (i.e., where $|B_\phi| > |B_p|$). We observe that the magnetic field lines are mostly toroidal in most parts of the cavity at large scales, with the exception of the regions close to the rotation axis and also inside of the Alfvén surface, where the magnetic field is mostly poloidal.

The $z$-component of the momentum equation, considering a steady-state flow, reads

$$\nabla \cdot \left( \rho v_z \boldsymbol{v} - \tfrac{1}{4\pi} B_z \boldsymbol{B} \right) + \partial_z P_t = \rho a_{g\,z}, \tag{7}$$

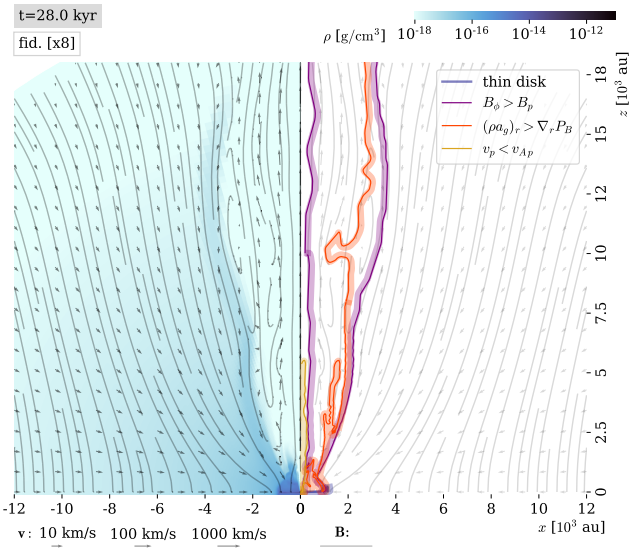



**Fig. 5.** Magnetic tower flow

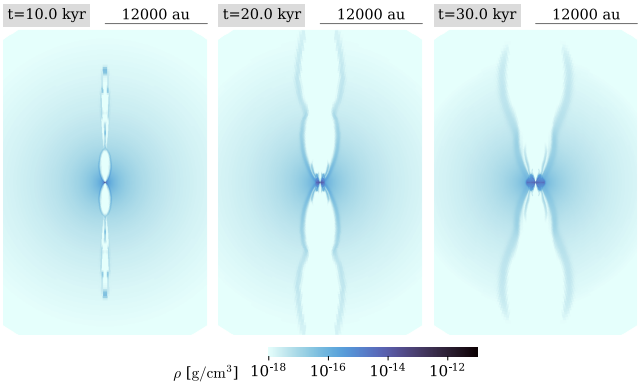



**Fig. 6.** Magnetic broadening of the cavity due to the tower flow.

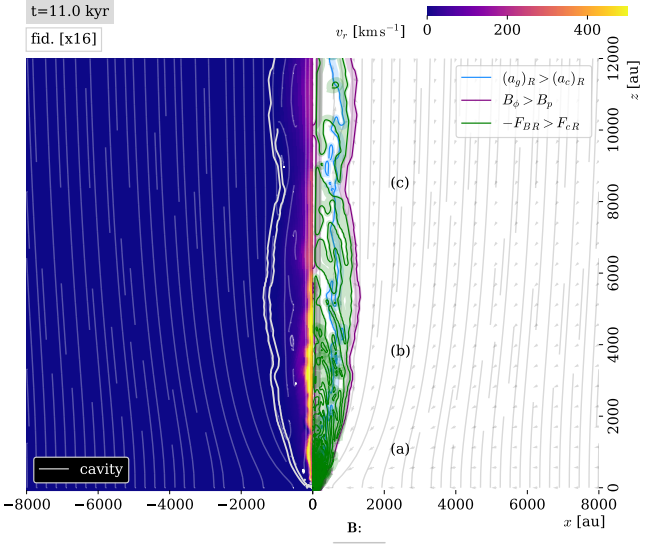



**Fig. 7.** Recollimation of the jet. The color scale for the radial velocity is saturated at $v_r = 500\,\mathrm{km\,s^{-1}}$. For a fuller picture of the speeds reached over time, we refer the reader to Fig. 10.

where the divergence $\nabla \cdot \boldsymbol{f}$ of a each vector field $\boldsymbol{f}(R,z)$ is $\nabla \cdot \boldsymbol{f} = (1/R)\partial_R(Rf_R) + \partial_z f_z$. Given that the magnetic field lines are strongly toroidal in the tower flow, we can neglect the contribution from magnetic tension, which only involves the poloidal components. The low thermal pressures at large scales and in the cavity allow us to consider only the contribution of the magnetic pressure to the total pressure gradient. With these approximations, Eq. 7 becomes

$$\nabla \cdot (\rho v_z \boldsymbol{v}) = \rho a_{g\,z} - \tfrac{1}{8\pi}\partial_z B^2 \tag{8}$$

The $z$-component of the gravitational force is negative in the upper hemisphere. In general, the magnetic field strength increases toward the center of the cloud because it is being dragged there by gravity, and so, the $z$-component of the pressure gradient is generally negative in the same region. Therefore an outward momentum flow is obtained if

$$\left|\tfrac{1}{8\pi}\partial_z B^2\right| > |\rho a_{g\,z}|. \tag{9}$$

The condition of Eq. 9 is calculated and shown in Fig. 5 as the nonshadowed part of the orange directed contour. That directed contour was computed with the spherical-radial components of both quantities for simplicity, given that $z \sim r$ for $\theta \to 0$. Indeed, in the tower flow, the magnetic pressure gradient is larger than gravity, and since $B$ is toroidal in the same region, we conclude that the tower flow is driven by the winding of magnetic field lines by rotation.

The speeds obtained in the tower flow are slower than the magneto-centrifugally driven jet. Typical values are on the order of $10\,\mathrm{km\,s^{-1}}$. The morphology and velocity structure of the tower flow can vary significantly with the initial conditions chosen for the cloud core. This is explored in more detail in Sect. 4.

### 3.5. Magnetic broadening of the outflow cavity

We observe (Fig. 6) that the tower flow increases its thickness over time. As the accretion disk grows in size with time (cf. Oliva & Kuiper 2022), so does the region of the cloud where the magnetic field lines are wound by rotation. Magnetic pressure keeps increasing in the cavity, strengthening the tower flow and broadening it as a consequence. Additionally, the slow depletion of the envelope means that the ram pressure from large scales in the cloud core decreases over time, allowing further growth of the cavity. The broadening of the tower flow offers an additional component for the earliest outflow broadening (before the driving of HII regions) around early O and B-type stars (see Beuther & Shepherd 2005). According to our results, very collimated outflows are indicative of the earliest stages of star formation (fiducial case $t \sim 10\,\mathrm{kyr}$ or $0.2t_{\mathrm{ff}}$). A first broadening comes as a result of the broadening of the tower flow ($t \gtrsim 20\,\mathrm{kyr}$), and we expect a second broadening due to the growth of the HII region ($t \gtrsim 100\,\mathrm{kyr}$, see Kuiper & Hosokawa 2018) before other forms of radiative feedback (e.g., stellar winds and radiation pressure) take over.

### 3.6. Jet recollimation

At the launching region, the jet is accelerated along the spherical-radial direction, which means that the highest speeds are not reached along the rotation axis. However, at scales of a few thousand astronomical units along the propagation of the jet, and fully outside of the Alfvén surface, we find evidence that

magnetic hoop stress and the ram pressure from the infalling envelope exert forces that recollimate the flow and yield high radial velocities at the rotation axis. In Fig. 7, we observe those recollimation points marked as $a$, $b$, and $c$, where the cavity appears narrower. The left panel of Fig. 7 presents the positive radial velocity, which peaks particularly strongly around the recollimation points $a$ and $b$. The right-hand panel of the figure provides a visualization of the forces involved in the recollimation. Similarly to the previous analysis, the region where the magnetic field lines are wound is shown in the shadowed area of the purple directed contour. Additionally, the green directed contour displays the regions where the cylindrical-radial component of the Lorentz force density

$$F_{BR} = (\boldsymbol{J} \times \boldsymbol{B})_R / c = \tfrac{1}{4\pi}[(\nabla \times \boldsymbol{B}) \times \boldsymbol{B}]_R \quad (10)$$

is negative (i.e., directed inward; $\boldsymbol{J}$ is the current density) and in magnitude larger than the cylindrical-radial component of the centrifugal force density $F_{cR}$, that is, the regions where the Lorentz force tends to bring the flow closer to the rotation axis. The overlapping of the green and purple contours shows that the inwardly directed Lorentz force constitutes an example of magnetic hoop stress.

Recollimation in massive protostellar outflows has been observed in the form of jet knots in, for example, IRAS 21078+5211 (Moscadelli et al. 2021) and the radio jet HH 80-81 (Rodríguez-Kamenetzky et al. 2017). In those systems, nonthermal synchrotron emission originated in the knots is observed, where the particles are accelerated until they reach relativistic speeds. We find velocities on the order of $\sim 1000\,\mathrm{km\,s^{-1}}$ in the jet material, however, the highest speed of the ejecta cannot be determined from our results because of the Alfvén limiter we set up in order to be able to avoid extremely small time steps. Even though we cannot fully recover the kinematics that produce the nonthermal emission observed in jet knots, the recollimation mechanism we observe provides an explanation and a model for the production of the knots themselves. For a concrete example, the recollimation point $a$ in Fig. 7, located at around 1000 au away from the massive protostar, and where such high speeds are seen in the simulation data, coincides reasonably well in position with the nonthermal emission lobe (JVLA observations at 5 cm) observed in IRAS 21078+5211 (Moscadelli et al. 2021, fig. 5). The recollimation of the outflow, which restricts the width of the cavity, is also visible in the shape of the radio lobes at scales of $\sim 10\,000$ au, taken from SO molecular transitions which trace external shocks of the flow (e.g., coming from the cavity wall; see Moscadelli et al. 2021).

Three-dimensional effects could potentially intervene in the production of jet knots and the propagation of the outflow. These effects should be studied with three-dimensional simulations of a disk-jet system, where the assumption of axisymmetry is relaxed. Material from fragments formed in the accretion disk could potentially be ejected along the jet cavity, producing jet knots or bow shocks (however, this has not been reported in three-dimensional simulations in the literature; see Sect. 5). Additionally, episodic accretion might cause small precession in the jet axis, as suggested by the different regions of the red- and blueshift in the ejected material at large and small scales in IRAS 21078+5211 (Moscadelli et al. 2021, 2022).

### 3.7. Bow shock and the formation of the cavity

Given that the magneto-centrifugal mechanism requires the existence of the cavity, the natural question to ask is how is this cavity formed in the first place. The formation of the cavity is captured in Fig. 8. The disk starts to appear shortly before the instant of time depicted (where it is only a few astronomical units in size). In the thick disk, the magnetic field is dragged by rotation and gravity, and magnetic pressure increases rapidly, until it eventually overcomes gravity and the outflow is launched. This is evidenced with the fact that the magnetic field in the cavity (excluding the region surrounding the rotation axis) is toroidal, and that the magnetic pressure gradient is larger in magnitude than gravity in the spherical radial direction. The velocities achieved in this stage are on the order of $10\,\mathrm{km\,s^{-1}}$, so they are in line with the values observed in the tower flow stage. The formation of the cavity produces a bow shock, marked in the figure with the label $a$, which propagates outward as the cavity expands over time. At $t \sim 5.4$ kyr in the fiducial simulation for the x16 grid, the cavity is broad enough such that the magneto-centrifugal mechanism is able to start from the cavity wall, as described in Sect. 3.1. Then, the velocities of the jet increase to more than $100\,\mathrm{km\,s^{-1}}$.

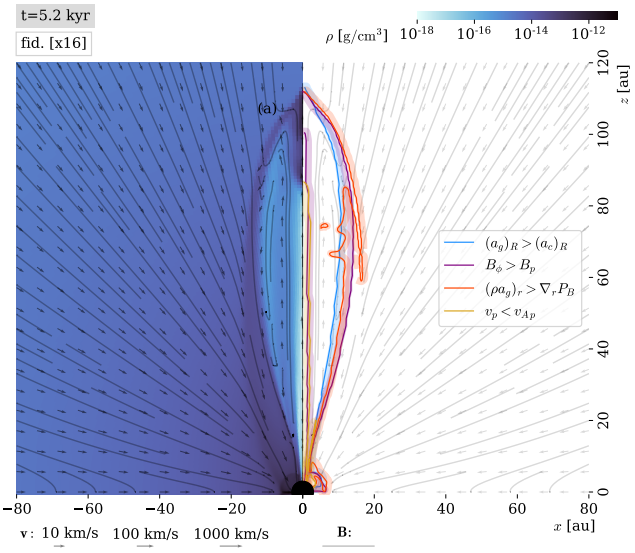



**Fig. 8.** Production of the bow shock that gives rise to the jet cavity.

Bow shocks are often observed in protostellar outflows (e.g., Moscadelli et al. 2021; Lefloch et al. 2015). Even though we expect bow shocks to be originated by multiple causes (for example, episodic accretion), the formation of the cavity provides a production mechanism for bow shocks that are highly symmetrical and appear distant in the ejected material. Moreover, the position and propagation velocity of the bow shock could serve as a crude estimate for the age of a given protostellar disk-jet system, as we suggested in Moscadelli et al. (2022). In that particular case, we estimated from the fiducial simulation on grid x16 that the propagation of the bow shock is of about $3\,300\,\mathrm{au\,kyr^{-1}}$, and with this, that when the protostar is $\approx 5.24\,\mathrm{M_\odot}$, the bow shock has propagated at around $\sim 30\,000$ au. This coincides reasonably well with the observed position of the bow shock at $\approx 36\,000$ au away from the forming massive star.

### 3.8. Magnetic braking: Effects on the outflows

The rotational dragging of magnetic field lines creates magnetic tension, which tends to locally remove angular momentum very efficiently from the small scales in a process called magnetic

A&A proofs: manuscript no. 44434

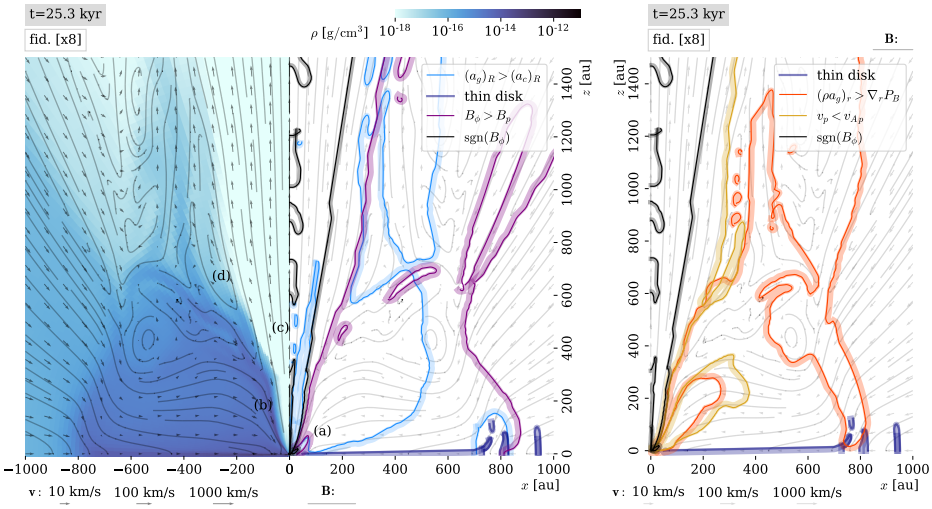



**Fig. 9.** Effects of magnetic braking on the magnetically driven outflows.

braking Galli et al. (2006). We discussed magnetic braking in the disk region in Paper I, and showed that its effects are stronger as time passes and the magnetic field lines are progressively more wound. When enough angular momentum is removed from the innermost parts of the disk and cavity wall (which in our fiducial case happens at $t \sim 15$ kyr), those regions lose centrifugal support and the flow becomes mostly infalling. Figure 9 shows an extensive morphological and dynamical analysis of the situation. The blue directed contour (gravito-centrifugal equilibrium) reveals the lack of centrifugal support for the inner parts of the disk (mark *a*) and the cavity wall (mark *b*), which corresponds to the magnetically braked flow region.

The magnetic field is mostly toroidal in the thin and thick layers of the disk, however, in the magnetically braked region of the disk it becomes mostly poloidal, following the flow. As time progresses, magnetic tension continues to transport angular momentum outward from the braking radius of the disk until the full depletion of angular momentum in the braked region. When this happens, sections in the low-density cavity are observed to counter-rotate (with the corresponding sign reversal in the toroidal magnetic field; see black directed contour in Fig. 9). The counter-rotation is intermittent in the early stages. Counter-rotation in jets has previously been studied as a theoretical possibility (Sauty et al. 2012; Cayatte et al. 2014; Staff et al. 2015), and some observational evidence has been gathered (see, e.g., Coffey et al. 2011; Louvet et al. 2016) although it is not conclusive (Tabone et al. 2020).

The removal of angular momentum from the innermost scales interferes with the magneto-centrifugal mechanism as discussed in Sect. 3.1. The center and right panels of Figure 2 show that the lack of angular momentum in the inner parts of the thick disk and cavity wall (marker *b*) impedes the magneto-centrifugal launching of material despite being in the sub-Alfvénic regime. As a consequence, the cavity becomes narrower close to the protostar. An outflow driven by magnetic pressure (marker *c*) can still be launched from the innermost parts of the cavity (cf. orange contour, that shows dominance of magnetic pressure over gravity in the vertical direction). Despite the loss of angular momentum in the innermost scales, the magneto-centrifugal mechanism and cavity wall ejections are able to continue from higher points in the disk (marker *d*), where the conditions of centrifugal support and sub-Alfvenicity are still satisfied. The tower flow, on the other hand, remains unaffected as the rotation of the disk continues to wind the magnetic field lines outside of the Alfvén surface, and therefore, magnetic pressure continues to be generated over time.

In this work, we did not include the effects of ambipolar diffusion and the Hall effect (see also the discussion in §4.2). In particular, we expect ambipolar diffusion to have the following effects. Because ambipolar diffusivities increase with decreasing density (Marchand et al. 2022) gravitational collapse would be promoted specially at its earliest stages. However, at the number densities found in the accretion disk ($10^9 \lesssim n \lesssim 10^{12}$ cm$^{-3}$), the diffusivity curves from Marchand et al. (2022) show that the ambipolar and Hall effect diffusivities behave similarly to Ohmic resistivity. Because of this, we would not expect a strong impact in the disk physics, although additional diffusivities might cause the thick layer of the disk to be thinner because of the decreased magnetic pressure. From Paper I, we expect higher diffusivities to delay the effects of magnetic braking (see also Masson et al. 2016 for an example study in the low-mass case where the interplay between ambipolar diffusion and magnetic braking is present).

Inside of the cavity, however, the situation is different. Even though ambipolar diffusivities increase with low densities and strong magnetic fields (such as inside the cavity), all magnetic diffusivities (Ohmic resistivity, ambipolar diffusivity and the Hall diffusivity) strongly drop when the material becomes ionized (Marchand et al. 2022; Machida et al. 2007). The ejected material from collimated outflows from massive (proto)stars has been found to be shock-ionized (Moscadelli et al. 2021; Rodríguez-Kamenetzky et al. 2017), so we expect our treatment of the jet physics in the cavity to be correct, especially at early times when magnetic braking effects are not yet present.

As the main focus of this article is the study of the mechanisms that mediate the production, propagation and termination of outflows, we point out that magnetic braking is nevertheless a mechanism capable of terminating a jet. Magnetic braking could then be the mechanism responsible for setting the timescale of collimated protostellar jets, and regulating the expansion of HII regions, although this conclusion must be confirmed by the addition of more physical effects to the model.

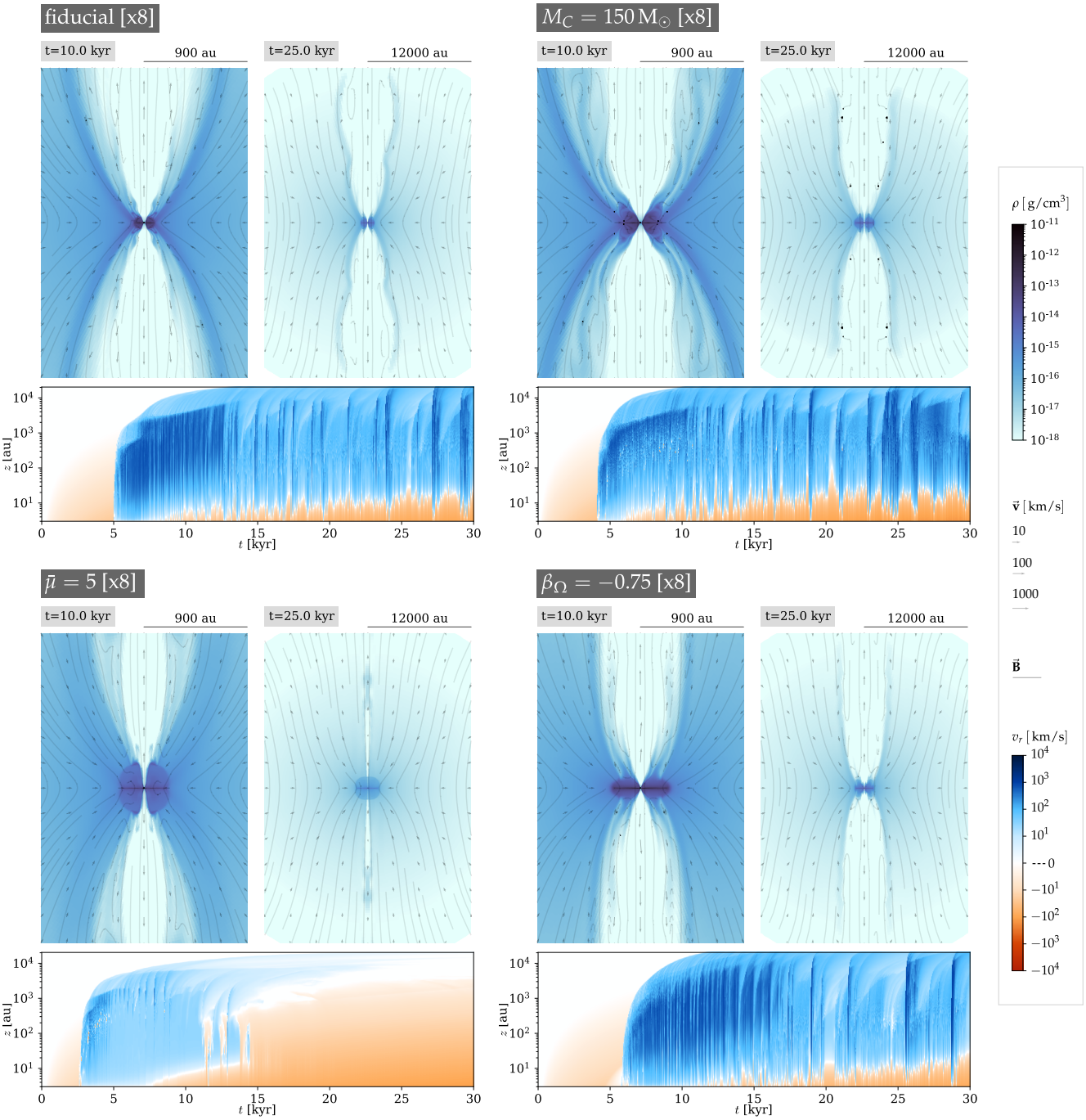



**Fig. 10.** Morphology and kinematics of the outflows for different initial conditions, using the grid x8. The velocities shown as a function of time correspond to the maximum radial velocity within an angle of 22.5° from the rotation axis, and the logarithmic scale has a cutoff of ±1 (velocities in the interval $-1 \leq v_r \leq 1\,\mathrm{km\,s^{-1}}$ are shown as zero).

## 4. Variation of the outflow properties with initial conditions

In this section, we utilize the analysis from Sect. 3 and the results from other simulations in our series in order to investigate how the physical processes of the outflows are impacted by the conditions of the natal environment of the protostar. For comparisons between simulations, we use three kinds of graphics, which we present next.

Each panel of Fig. 10 displays the morphology of the outflows at early and late times (with a corresponding adjustment to the spatial scale) accompanied by a velocity profile as a function of time. The velocity profile is taken along a cone of 22.5° around the rotation axis, using the maximum value of the radial velocity at a given radial distance, and it permits us to study the kinematical signature of the jet and its propagation through the cloud core. In order to produce an effective morphological comparison, we used only the results for the high resolution grid (x8) because coarser grids in our series are not able to fully resolve

A&A proofs: manuscript no. 44434

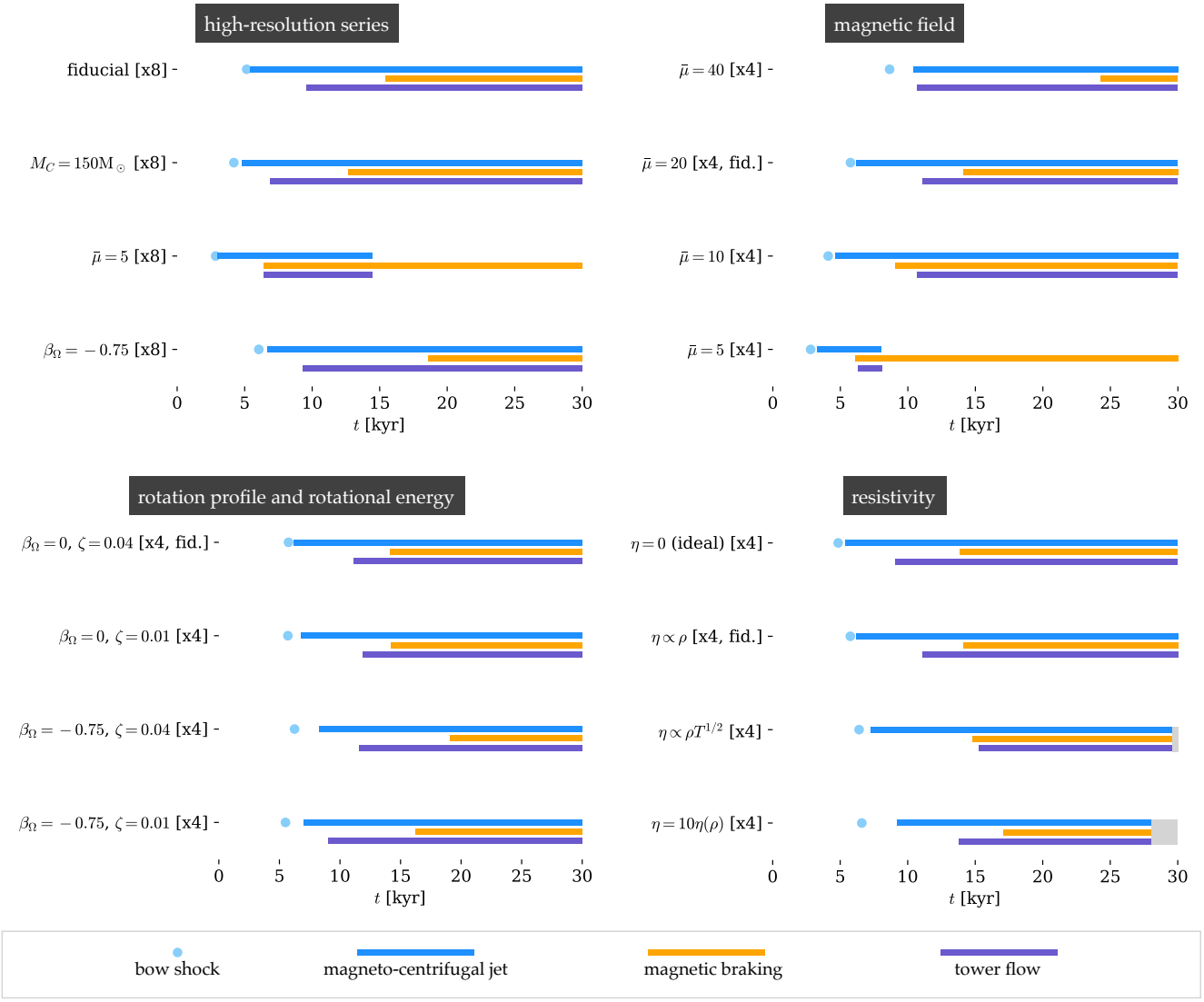



**Fig. 11.** Comparison of the processes present in the jet for different initial magnetic field strengths, rotation profiles, rotational energies and resistivity models. For all the simulations except $M_C = 150\,M_\odot$ [x8], the free-fall timescale is 52.4 kyr. The gray boxes denote that the simulation was not run until 30 kyr.

all the scales of interest (see Appendix A), although the basic physical processes are still present.

Figure 11 exhibits a comprehensive overview of the temporal evolution of the dynamical processes discussed in Sect. 3, namely, the formation of the cavity (leading to a bow shock), the magneto-centrifugal mechanism, magnetic braking and the magnetic tower flow. The time of launching of the bow shock is simply computed as when $v_r > 0$ for the first time at a reference altitude of $z = 100$ au. The interval of presence of the magneto-centrifugal jet requires additionally that $(a_c)_R > (a_g)_R$ and $v_p < v_{Ap}$ at the same altitude. Magnetic braking, in the other hand, is graphed by using the magnetic braking radius computed in Paper I. Finally, the presence of the tower flow is fixed by simultaneously enforcing the conditions $|B_\phi| > |B_p|$, $\nabla_r P_B > (\rho a_g)_r$, and $v_r > 0$ at an altitude of $z = 5\,000$ au.

Finally, Figure 12 aims to aid in the understanding of the effects of the jet in their environment with time, using only the data from the high-resolution series x8. We calculate the momentum flux (panel $c$) of the jet through a hemisphere of radius 15 000 au, which gives an idea of the mechanical feedback that the magnetically driven outflows impart to their natal environment at larger scales. In terms of mass, panel $d$ presents the accretion-to-ejection rate for the fiducial case, computed using the mass flux through spheres at different scales. The time average of the accretion-to-ejection rate at large scales in the cloud core remains within 10%. Both quantities are characterized by a strong variability over time, due to the episodic ejection events (specially at late times) caused by the cavity wall ejections; for this reason, a time average is necessary to study their overall behavior. A smoother quantity is the total radially-outward momentum contained in a hemisphere (i.e., the total momentum expelled by one branch of the jet), and it is presented in panels $a$ and $c$.

### 4.1. Mass of the cloud core

Morphologically, the fiducial case ($M_C = 100\,M_\odot$) and the higher mass cloud core ($M_C = 150\,M_\odot$) are very similar, ex-

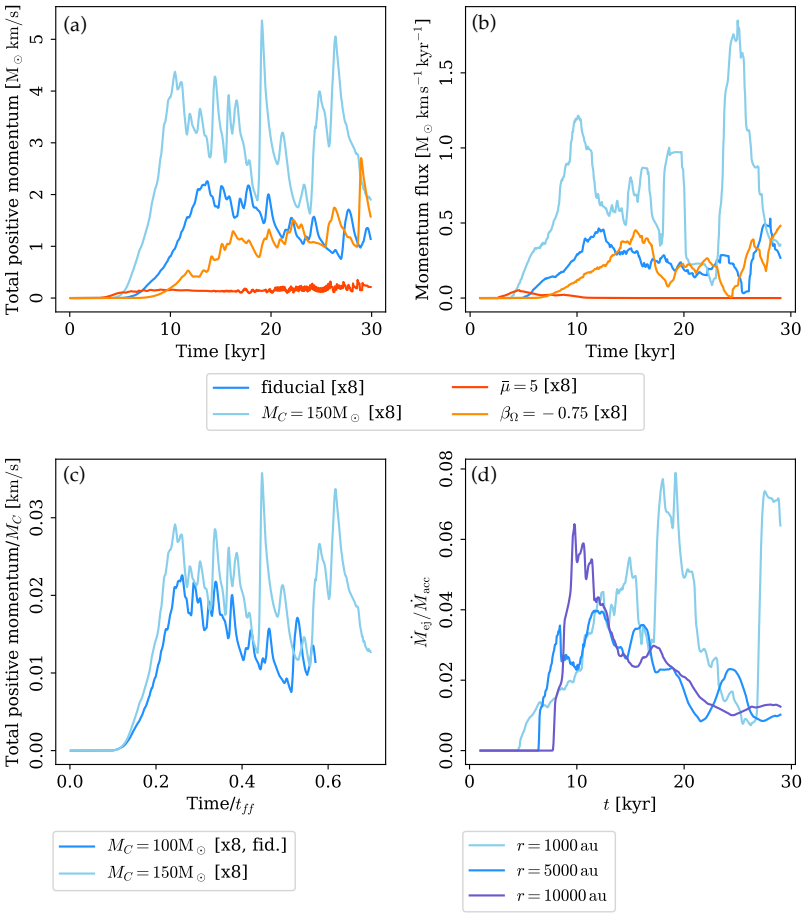



**Fig. 12.** Mechanical feedback from the outflow. Panel *a*: momentum ejected by the magnetically driven outflows within the cloud core, for the high-resolution series on grid x8. Panel *b*: time-averaged momentum flux through a hemisphere of radius $r$ = 15 000 au for the same simulation series. Panel *c*: total momentum ejected by the magnetic outflows, normalized to the mass of the cloud core, as a function of the fraction of the free-fall timescale elapsed, for two different masses of the cloud core. Panel *d*: ejection-to-accretion rate measured using spheres of three different radii.

cept that the cavity is "pinched" in the former case compared to the latter, which indicates that the jet recollimation does not occur in the same place for both simulations. The velocity profile along the rotation axis shows different stages of evolution of the system in the fiducial case: the initial gravitational infall before $t \approx 5$ kyr, the formation of the cavity and the launching of the magneto-centrifugal jet (velocities on the order of 100 km s$^{-1}$ after $t \approx 5$ kyr). The velocity profile does not show the acceleration of the jet on the smallest scales because it occurs radially outward (Sect. 3.2) and therefore it is not enclosed in the conical region used to compute the profile. However, the profile does capture the recollimation of the jet at scales of $10^2$–$10^3$ au (Sect. 3.6), where the velocity reaches values on the order of 1000 km s$^{-1}$.

All the dynamical mechanisms related to the outflows (Fig. 11) are present in both simulations, although they start earlier in time for the more massive case. The same can be seen when examining the total linear momentum carried out by the outflows (Fig. 12a), with the additional remark that the mechanical feedback from the magnetic outflows is stronger for more massive cloud cores. In Paper I, we concluded that the disk dynamics scale with the mass of the cloud core, when examining the wider range of cloud core masses of 50–200 $M_\odot$ using the lower resolution grid x4. Motivated by that result, we scaled the curves of the higher resolution results for the linear momentum by dividing by the mass of the cloud and expressed the time as a fraction of the free-fall timescale (Fig. 12c). We find that the momentum scales well with the mass of the cloud, and so, despite the nonscalable nature of the thermodynamics and magnetic diffusivities of the system and its self-gravity, the results reported in this article can be reasonably used for cloud cores in a wider interval of masses, possibly including low-mass star formation.

Taking into account the respective free-fall timescales for the two clouds (52.4 kyr for $M_C = 100\,M_\odot$ and 42.8 kyr for $M_C = 150\,M_\odot$), we corroborate the scalability of the outflow dynamics as follows. The bow shock and subsequent magneto-centrifugal jet start at $t = 5.2$ kyr $= 0.1 t_{\rm ff}$ for $M_C = 100\,M_\odot$, which corresponds to $t = 4.2$ kyr for $M_C = 150\,M_\odot$ and is in agreement with the respective simulation result. Similarly, the tower flow reaches the height of $z = 5\,000$ au at $t = 0.18 t_{\rm ff}$ in the fiducial case and at $t = 0.16 t_{\rm ff}$ in the more massive cloud core. We had checked the scalability of magnetic braking with the fraction of free-fall timescale in Paper I already.

The curve for the outflow total linear momentum is explained as follows. At $t \sim 0.1 t_{\rm ff}$, the magneto-centrifugal jet is launched, and the total linear momentum increases as the ejecta propagates throughout the cloud core. The outflow reaches a distance of 0.1 pc at around $0.2 t_{\rm ff}$. Once this happens, the total momentum reaches a maximum value, with variations caused by changes in the recollimation zone and episodic ejection events (cavity wall ejections). We see from Fig. 10 that the high velocities associated with recollimation and jet launching become less frequent at late stages, because of the effects of magnetic braking. This, together with the slower tower flow (which broadens the cavity at late stages), cause the total linear momentum to decline slightly over time for $t \gtrsim 0.35 t_{\rm ff}$.

### 4.2. Magnetic field

Our parameter space for the magnetic field responds to two different assumptions on the environmental conditions for massive star formation. In low-mass star formation, supercriticality has been observed in prestellar cores not yet under gravitational collapse, with measured magnetic field strengths on the order of a few tens of microgauss (see, e.g., Ching et al. 2022; Crutcher 2012), which mean mass-to-flux ratios on the order of a few. In the case of massive star formation, the precollapse conditions of the magnetic field are not well-known, and because of this, we assume cases of lower and higher magnetization. The lower magnetization case assumes that the same order of magnitude of the magnetic field strength observed in low-mass star formation is also present in the massive case and it constitutes our fiducial case. The higher magnetization case assumes that a similar mass-to-flux ratio as observed in the low-mass star formation would be present in the high-mass scenario.

In what follows, we compare the outcome of the fiducial run (normalized mass-to-flux ratio $\bar{\mu} = 20$, which corresponds to an initial magnetic field of $68\,\mu$G) and a simulation with a stronger initial magnetic field ($\bar{\mu} = 5$, corresponding to 0.27 mG). Stronger magnetic fields cause stronger and earlier magnetic braking as already discussed in Paper I, and the additional support from magnetic pressure allows for the formation of a larger accretion disk. The outflow cavity is narrower at early times (Fig. 10) with strong magnetic fields, which can be attributed to the additional magnetic pressure which makes the observed thick layer of the disk thicker, constraining the cavity close to the protostar.

In Sect. 3.7, we presented our finding that the outflow cavity is initially formed by magnetic pressure, launching a bow shock in the process. A comparison of the points and bars that indicate the bow shock and the magneto-centrifugal phase in Fig. 11 confirms that, with more magnetic pressure, the cavity is able to form earlier in time, followed by the jet. However, the magneto-centrifugal jet is shorter-lived in the case with $\bar{\mu} = 5$ (cf. its velocity profile, Fig. 10). Magnetic braking for a cloud core with $\bar{\mu} = 5$ acts earlier in time compared to when $\bar{\mu} = 20$. The extraction of angular momentum in the inner disk becomes very strong after $t \gtrsim 15$ kyr, which impedes the magneto-centrifugal mechanism to continue. Additionally, the magnetic braking starts to act in the thick disk as well (but not in the thin disk, see Paper I) turning the flow into sub-Keplerian and the tower flow cannot form because the magnetic pressure derived from the rotational dragging of magnetic field lines is not enough to overcome gravity. The magnetic pressure originated from the dragging of magnetic field lines by gravity, on the other hand, makes the thick disk thicker. We conclude from those results that very strong magnetic fields have the power to terminate magnetically driven outflows. Because of the lower jet speeds, the momentum output (Fig. 12a) of the outflows is considerably weaker in the case of stronger initial magnetic fields.

Because ambipolar diffusivities increase with magnetic field strength, we expect the higher magnetization case to be the most affected by the noninclusion of ambipolar diffusion in the present study. However, we remark that we still see the formation of a disk-jet system, and that magnetic braking, dependent on the initial magnetic field strength, would set a timescale for the formation and duration of the magneto-centrifugal phase of the outflows. For example, for low-mass star formation (where the $\bar{\mu}$ is on the order of a few) the jet duration (as a fraction of the freefall time) could be shorter. The interplay between jet termination, magnetic braking and angular momentum transport should be examined in future studies.

### 4.3. Angular momentum content

We performed simulations of various ratios of rotational to gravitational energy ($\zeta = 0.01, 0.04$) and initial distributions of angular velocity $\Omega \propto R^{\beta_\Omega}$, where $\beta_\Omega = 0$ (solid body rotation) and $\beta_\Omega = \beta_\rho/2 = -0.75$ (steep initial rotation profile, as we considered in our simulations of a fragmenting accretion disk in Oliva & Kuiper 2020). The fiducial case is $\beta_\Omega = 0$, $\zeta = 0.04$. In the high-resolution series, we only investigated the case where the rotational-to-gravitational energy ratio was kept the same but the angular momentum is initially more concentrated in the center of the cloud (steep rotation profile instead of the solid body assumption). In Paper I, we found that the accretion disk becomes larger thanks to the greater initial availability of angular momentum close to the protostar, and that the thick disk is flatter. As a result of a larger accretion disk for $\beta_\Omega = -0.75$, we find an initially wider tower flow (Fig. 10), which translates into a more cylindrical outflow in both small and large scales compared to solid body rotation.

Both the velocity profile in Fig. 10 and the total linear momentum (Fig. 12a) indicate that the propagation speed of the bow shock and the jet material is slower for the steep angular velocity profile compared to solid body rotation, although the recollimation speeds are similar in both cases. From Paper I, we know that the mass of the protostar does not increase the same way in both cases. For a steep initial angular momentum profile, the early formation of the accretion disk slows down the accretion rate onto the protostar. As an example, at $t = 10$ kyr, $M_\star = 3.1\,M_\odot$ for the fiducial case, but only $1.77\,M_\odot$ for $\beta_\Omega = -0.75$. Even though the magnetic field lines are dragged more by rotation with more availability of angular momentum, and therefore magnetic pressure should increase, the lower radial mass flux onto the protostar translates into a reduced dragging of magnetic field lines by gravity, which means that magnetic pressure actually decreases and the propagation of the outflow becomes slower. This difference can also be seen in the formation of the accretion disk: while in the fiducial case the magnetic outflows and the disk are formed almost simultaneously, in the case with $\beta_\Omega = -0.75$, the jet is launched with a delay with respect to the formation of the accretion disk (cf. Fig. 11 and Fig. 8 of Paper I). The differences in protostellar mass are also responsible for the delay in magnetic braking (see Paper I).

Overall, the total outward momentum reaches similar values for both cases. After examining the full parameter space including the results for the lower resolution series x4, we find that even though the initial angular momentum can cause differences in the launching and propagation of the jet, all the dynamical processes seen in the fiducial case are also seen in cloud cores with a lower ratio of rotational to gravitational energy.

### 4.4. Ohmic resistivity

As a final exploration, we look at the effect of resistivity in the dynamical processes present in the outflows (Fig. 11). We found in Paper I that the presence of resistivity delays magnetic braking compared to the ideal MHD case (the delay is more noticeable when comparing against the protostellar mass as opposed to time). Apart from our standard case, that considers resistivity only as a function of density, we included the full resistivity formula by Machida et al. (2007), which also depends on tempera-

ture and can cause an increase of a factor of 10–100 compared to our standard case. Additionally, we included a simulation where Ohmic resistivity is artificially high by a factor of 10. These four simulations provide insight to what happens when the resistivity model is varied, that is to say when more magnetic diffusivity is added. From Fig. 11, we see that the jet and the tower flow are launched slightly later for the case with higher resistivity. This is expected, because the jet launching mechanism depends on flux freezing inside of the Alfvén surface and the dragging of magnetic field lines by rotation. However, Fig. 11 shows the presence of all processes in all cases.

## 5. Comparison to previous numerical studies

In Paper I, we presented a comparison of our results for the accretion disk dynamics with several studies in the literature. Here we continue the comparison of our results for the dynamics of the magnetic outflows against the results found in the same studies.

Kölligan & Kuiper (2018) performed simulations of a forming massive star starting from the collapse of a cloud core with magnetic fields, but considering an isothermal equation of state (in contrast to our treatment of radiation transport with the flux-limited diffusion approximation). We base our fiducial case on the setup proposed in that study, except that they use a rotational to gravitational energy ratio of 2% (our fiducial case is of 4%). The study by Kölligan & Kuiper (2018) was the first to be able to clearly distinguish a fast, magneto-centrifugally launched jet from the slower magnetic tower flow in the context of massive star formation. They found evidence of the magneto-centrifugal launching of the jet, however, they applied a series of analytical criteria from the classic bead-on-a-wire jet theory from Blandford & Payne (1982) (for which the effects of the infalling envelope are missing) to identify the jet launching area both at early and late times (when it moves upward). Our explicit identification of the Alfvén surface and the gravito-centrifugal contour (cf. Fig. 2) enabled us to identify the launching region more accurately for all times and determine the effects of the ram pressure of the infalling envelope on the geometry of jet launching, which cause departures from the classic theory. Kölligan & Kuiper (2018) performed a convergence study using grids with increasing resolution, but their highest resolution grid is equivalent to our x2 grid, which means that in this study we are able to resolve more structures in the plasma. The insufficient resolution of the outer regions in the cloud core in their convergence study meant that the authors were not able to find convergence in several quantities, including the jet duration and the momentum transported by the magnetic outflows. In contrast, we find outflow momenta that tend to converge for the two highest resolution grids (x8 and x16), and the minimum cell size required for the adequate resolution of the tower flow at large scales (see Appendix A.1). In Kölligan & Kuiper (2018), the artificial mass generated by the Alfvén limiter grew to unrealistic limits for some simulations. The higher resolution grids used in our study and fine tuning of the Alfvén limiter allow us to keep the artificial mass generated by the limiter to negligible levels (cf. Appendix A.2).

### 5.1. Studies with ideal MHD

The study conducted by Banerjee & Pudritz (2007) consisted in 3D ideal MHD simulations of a slowly rotating Bonnor-Ebert sphere of $168\,M_\odot$ on 1.62 pc a combination of cooling and radiation diffusion for the gas thermodynamics and using the code FLASH with an adaptive mesh refinement (AMR) grid. Despite only obtaining a sub-Keplerian disk (probably due to strong magnetic braking due to the lack of magnetic diffusivity), they observe early pseudo-disk-driven magnetic winds of typical velocities of $4\,\mathrm{km\,s^{-1}}$, whose launching is credited to the tower flow mechanism.

A setup more comparable to ours is used in Seifried et al. (2012) ($100\,M_\odot$ within a radius of 0.125 pc and initial solid body rotation), where the effects of different mass-to-flux ratios was investigated. They find outflow velocities of $\sim 5\,\mathrm{km\,s^{-1}}$, which are both very collimated (weakly magnetized runs) and poorly collimated (strong magnetization). The authors point to the existence of a "fast" outflow component launched by the magneto-centrifugal mechanism, which is detected by a launching criterion based on the energy equation (cf. Eq. 4). However, the velocities of the fast outflow are still on the order of $10\,\mathrm{km\,s^{-1}}$, which we credit to the coarse grid used (3D AMR grid with a minimum cell size of 4.7 au) and the unconstrained effects that magnetic braking causes when no magnetic diffusivity is considered. They also observe an outflow driven by magnetic pressure, although the authors do not call it a tower flow, even though the whole cavity is dominated by the toroidal component of the magnetic field. The ejection-to-accretion rates at large scales are somewhat larger than our findings (they find $\dot{M}_\mathrm{ej}/\dot{M}_\mathrm{acc} \lesssim 0.4$).

The study of Myers et al. (2013) considers a denser cloud core ($300\,M_\odot$ within a radius of 0.1 pc) and $\bar{\mu} = 2$, but supersonic turbulence instead of rotation. They include a gray flux-limited diffusion approximation to radiation transport. Even though the authors report on the existence of magnetically driven outflows of up to $40\,\mathrm{km\,s^{-1}}$, they do not discuss their origin. A similar approach was taken by Rosen & Krumholz (2020), but with masses of the cloud core of $150\,M_\odot$. However, the coarse spacial grid used (minimum cell size of 20 au) impedes them to resolve the launching mechanisms of the magnetic outflows, adopting a subgrid outflow injection approach instead. This means that we cannot directly compare our results with theirs.

### 5.2. Studies including Ohmic resistivity

The three-dimensional studies by Matsushita et al. (2017) and Machida & Hosokawa (2020) use the same Ohmic resistivity model by Machida et al. (2007) as we do. However, while we use treatment of radiation transport based on the flux-limited diffusion approximation, both studies model the thermodynamics of the dust and gas with a barotropic equation of state. Matsushita et al. (2017) start from a Bonnor-Ebert sphere of several masses that range from 32 to $1542\,M_\odot$ and radius 0.28 pc which rotate as a solid body and that are threaded with an initially uniform magnetic field determined by normalized mass-to-flux ratios of $\bar{\mu} = 2$, 5 and 10. The authors report on outflows of magnetic origin associated with the outer disk, but do not discuss their origin in detail. The speeds obtained in the outflows are on the order of $10\,\mathrm{km\,s^{-1}}$. Machida & Hosokawa (2020) start from a similar setup, but expand the parameter space of the cloud core masses (from 11 to $525\,M_\odot$) and normalized mass-to-flux ratios (from 2 to 20). Additionally, they introduce an enhancement factor to the density profile to promote gravitational collapse and their cloud core radius is 0.2 pc. The authors classify their outflows into successful, delayed and failed. They observe protostellar outflows failing to evolve and collapse by the strong ram pressure when a massive initial cloud is weakly magnetized; a similar preliminary finding was reported in Matsushita et al. (2017) with the conclusion that only strongly magnetized cloud cores can drive protostellar outflows. This trend is opposite to our findings: we

see that a relatively weak initial magnetic field ($\bar{\mu} = 20$) is sufficient to produce a magneto-centrifugally launched jet, while strong magnetic fields launch shorted-lived jets because of the increased action of magnetic braking over time. In Matsushita et al. (2017) and Machida & Hosokawa (2020), the origin of the outflows is not thoroughly discussed, but given the magnitudes of the velocities obtained (a few tens of kilometers per second), it is reasonable to think that they are launched by magnetic pressure and not the magneto-centrifugal mechanism. The propagation of the failed outflows reported in Machida & Hosokawa (2020) are reported to be stopped by ram pressure from the infall, a direct consequence of the interplay between gravity and magnetic forces. We have seen both in this article and in Paper I that the initial density and angular momentum distribution are crucial to determine the features of the accretion disk and the magnetically driven outflows. For this reason, we speculate that the differences in the initial cloud mass distribution (they consider higher cloud masses which means stronger ram pressure) and the launching mechanisms for the outflows could be responsible for the contradictory conclusions obtained in our study and Matsushita et al. (2017) and Machida & Hosokawa (2020).

### 5.3. Studies including ambipolar diffusion

Finally, we turn our attention to studies that include the effects of ambipolar diffusion but no Ohmic dissipation. Mignon-Risse et al. (2021) found magnetically driven outflows of velocities on the order of $30\,\mathrm{km\,s^{-1}}$ in simulations that start from a cloud core of $100\,\mathrm{M_\odot}$ within a radius of 0.2 pc (roughly equivalent to $M_C = 50$ in our setup), a density profile increasing toward the center of the cloud but with a plateau, solid body rotation, a rotational-to-gravitational energy ratio of 1% and a mass-to-flux ratio of 5. Cloud cores with subsonic and supersonic turbulence were also considered in that study. The authors use the code RAMSES with an AMR grid of maximum resolution of 5 au, including radiation transport using the flux-limited diffusion approximation and gray irradiation from the protostar(s). Commerçon et al. (2022) start from a similar setup, but consider additional configurations with a rotational-to-gravitational energy ratio of 5% and a normalized mass-to-flux ratio of 2. The characteristics of the outflows obtained in both studies correspond mostly to our wide tower flow rather than the fast jet. In Mignon-Risse et al. (2021), the authors determine that the origin of the outflows is indeed magnetic (as opposed to produced by irradiation from the protostar), and that they are driven by the magnetic pressure gradient. The authors argue that the magneto-centrifugal mechanism might be responsible for some of the high velocity flow present in their simulations, but do not perform an in-depth confirmation of this possibility. We show that very high resolution is needed close to the massive protostar in order to obtain a fast jet. On the other hand, their consideration of ambipolar diffusion might mean that the early stages of gravitational collapse and the late stages of the outflow dynamics are better represented in their simulations for low values of the mass-to-flux ratio.

### 5.4. Sink particles and the launching region

When comparing our results against studies that make use of subgrid sink particle algorithms, such as the ones mentioned in this section with the exception of Kölligan & Kuiper (2018), it is important to take into account that those algorithms usually require the definition of an accretion radius. For example, the accretion radius in Commerçon et al. (2022) is four times the minimum cell size, that is to say $\sim$ 20 au. This means that the dynamics of the gas are only expected to be fully consistent with the system of equations beyond that radius. The use of a sink cell of 3 au in radius and a logarithmically spaced grid permitted us to resolve the launching region of the magneto-centrifugal jet in a more consistent way in the regions very close to the protostar. Additionally, the definition of an accretion radius when using sink particles affects any comparisons of the effects of magnetic braking, because we observe magnetic braking only in the innermost tens of astronomical units in the disk, within the size of the accretion radius of several of the studies above.

The minimum cell sizes of the simulations run in grids x8 and x16, of 0.06 and 0.03 au respectively, have enabled us to directly compare our results to the VLBI observations of IRAS 21078+5211, which have a resolution of 0.05 au (Moscadelli et al. 2022). This level of detail, in both observations and simulations, had not been obtained so far. The recent advances in observational techniques for studying protostellar jets evidences the need for future numerical studies to accurately describe the processes in the innermost $\sim$ 100 au from the forming massive star.

## 6. Summary and conclusions

We have paved the path toward a more complete theory of magnetically driven massive protostellar outflows by performing simulations that self-consistently generate them, by analyzing their dynamics and evolution over time, and by relating the conditions of the onset of gravitational collapse with their production and propagation into larger scales. We performed a set of 31 axisymmetric magnetohydrodynamical simulations, including Ohmic dissipation as a nonideal effect, and radiation transport of the thermal emission and absorption of the dust and gas. We summarize our findings as follows:

- The outflow cavity is originally formed by the increase in magnetic pressure as a product of the dragging of the magnetic field by the gravitational collapse and rotation. In the process, a bow shock is thrust outward. Once the cavity is formed and the Alfvén velocity increases inside, the magneto-centrifugal mechanism starts.
- The fast ($\gtrsim 100\,\mathrm{km\,s^{-1}}$) and highly collimated component of the outflow is launched by the magneto-centrifugal mechanism. Ram pressure from the infalling envelope and the thick layer of the accretion disk constrain the geometry of the launching region into a narrower configuration compared to the predictions of classical jet theory.
- The jet material is accelerated along the magnetic field lines while its flow is sub-Alfvénic. Once it leaves the Alfvén surface, it enters a helical trajectory along the cavity.
- We observe episodic ejection events originating in the innermost parts of the cavity wall that are in contact with the thick layer of the accretion disk.
- Magnetic pressure originating from the rotational dragging of magnetic field lines by the accretion disk drives a slower ($\sim 10\,\mathrm{km\,s^{-1}}$) magnetic tower flow that broadens over time.
- Magnetic hoop stress and the ram pressure from the infalling envelope recollimate the jet in regions that are, in principle, compatible with jet knots observed in protostellar jets, where the material reaches relativistic velocities and nonthermal radiation is produced.
- Magnetic braking modifies the innermost regions of the disk and the jet, narrowing the cavity, and it is capable of terminating the magnetically driven outflows.

– Our results indicate that the ejected momentum scales with the mass of the initial cloud core and its free-fall timescale.
– The morphology and dynamics of the magnetically driven outflows are affected by the initial conditions for the gravitational collapse. More centrally concentrated distributions of angular momentum, which produce a larger disk, drive a more cylindrical jet. Stronger initial magnetic fields launch jets and produce narrower jets that last shorter periods of time.

By assuming axisymmetry and taking maximum advantage of a grid in spherical coordinates that is able to resolve the phenomena of interest on both large and small scales, we were able to obtain unprecedented detail in the inner $\sim 100$ au around the protostar. This region is uncovered by a new generation of observational evidence (Carrasco-González et al. 2021; Moscadelli et al. 2021, 2022), which brings new challenges for theoretical predictions on massive protostellar outflows.

*Acknowledgements.* We thank Richard Nies for his contributions to the analysis of part of the dataset at the early stages of the project. AO acknowledges financial support from the Deutscher Akademischer Austauschdienst (DAAD), under the program Research Grants - Doctoral Projects in Germany, and complementary financial support for the completion of the Doctoral degree by the University of Costa Rica, as part of their scholarship program for postgraduate studies in foreign institutions. RK acknowledges financial support via the Emmy Noether and Heisenberg Research Grants funded by the German Research Foundation (DFG) under grant no. KU 2849/3 and 2849/9.

## References

Banerjee, R. & Pudritz, R. E. 2007, ApJ, 660, 479
Beuther, H. & Shepherd, D. 2005, in Astrophysics and Space Science Library, Vol. 324, Astrophysics and Space Science Library, ed. M. S. N. Kumar, M. Tafalla, & P. Caselli, 105
Beuther, H., Soler, J. D., Linz, H., et al. 2020, ApJ, 904, 168
Blandford, R. D. & Payne, D. G. 1982, MNRAS, 199, 883
Carrasco-González, C., Rodríguez, L. F., Anglada, G., et al. 2010, Science, 330, 1209
Carrasco-González, C., Sanna, A., Rodríguez-Kamenetzky, A., et al. 2021, ApJ, 914, L1
Cayatte, V., Vlahakis, N., Matsakos, T., et al. 2014, ApJ, 788, L19
Ching, T. C., Li, D., Heiles, C., et al. 2022, Nature, 601, 49
Coffey, D., Bacciotti, F., Chrysostomou, A., Nisini, B., & Davis, C. 2011, A&A, 526, A40
Commerçon, B., González, M., Mignon-Risse, R., Hennebelle, P., & Vaytet, N. 2022, A&A, 658, A52
Crutcher, R. M. 2012, ARA&A, 50, 29
Galli, D., Lizano, S., Shu, F. H., & Allen, A. 2006, ApJ, 647, 374
Guzmán, A. E., Garay, G., & Brooks, K. J. 2010, ApJ, 725, 734
Kölligan, A. & Kuiper, R. 2018, A&A, 620, A182
Kuiper, R. & Hosokawa, T. 2018, A&A, 616, A101
Kuiper, R., Klahr, H., Beuther, H., & Henning, T. 2010, ApJ, 722, 1556
Kuiper, R., Klahr, H., Beuther, H., & Henning, T. 2011, ApJ, 732, 20
Kuiper, R., Yorke, H. W., & Mignone, A. 2020, ApJS, 250, 13
Lefloch, B., Gusdorf, A., Codella, C., et al. 2015, A&A, 581, A4
Louvet, F., Dougados, C., Cabrit, S., et al. 2016, A&A, 596, A88
Lynden-Bell, D. 2003, MNRAS, 341, 1360
Machida, M. N. & Hosokawa, T. 2020, MNRAS, 499, 4490
Machida, M. N., Inutsuka, S.-i., & Matsumoto, T. 2007, ApJ, 670, 1198
Marchand, P., Guillet, V., Lebreuilly, U., & Mac Low, M.-M. 2022, arXiv e-prints, arXiv:2202.11625
Masson, J., Chabrier, G., Hennebelle, P., Vaytet, N., & Commerçon, B. 2016, A&A, 587, A32
Matsushita, Y., Machida, M. N., Sakurai, Y., & Hosokawa, T. 2017, MNRAS, 470, 1026
McLeod, A. F., Reiter, M., Kuiper, R., Klaassen, P. D., & Evans, C. J. 2018, Nature, 554, 334
Mignon-Risse, R., González, M., & Commerçon, B. 2021, A&A, 656, A85
Mignone, A., Bodo, G., Massaglia, S., et al. 2007, ApJS, 170, 228
Moscadelli, L., Beuther, H., Ahmadi, A., et al. 2021, A&A, 647, A114
Moscadelli, L., Sanna, A., Beuther, H., Oliva, A., & Kuiper, R. 2022, Nat. Astron., https://doi.org/10.1038/s41550-022-01754-4
Myers, A. T., McKee, C. F., Cunningham, A. J., Klein, R. I., & Krumholz, M. R. 2013, ApJ, 766, 97
Obonyo, W. O., Lumsden, S. L., Hoare, M. G., Kurtz, S. E., & Purser, S. J. D. 2021, MNRAS, 501, 5197
Oliva, A. & Kuiper, R. 2022, A&A, accepted (Paper I)
Oliva, G. A. & Kuiper, R. 2020, A&A, 644, A41
Purser, S. J. D., Lumsden, S. L., Hoare, M. G., & Kurtz, S. 2021, MNRAS, 504, 338
Purser, S. J. D., Lumsden, S. L., Hoare, M. G., et al. 2016, MNRAS, 460, 1039
Rodríguez-Kamenetzky, A., Carrasco-González, C., Araudo, A., et al. 2017, ApJ, 851, 16
Rosen, A. L. & Krumholz, M. R. 2020, AJ, 160, 78
Sanna, A., Moscadelli, L., Goddi, C., et al. 2019, A&A, 623, L3
Sauty, C., Cayatte, V., Lima, J. J. G., Matsakos, T., & Tsinganos, K. 2012, ApJ, 759, L1
Seifried, D., Pudritz, R. E., Banerjee, R., Duffin, D., & Klessen, R. S. 2012, MNRAS, 422, 347
Staff, J. E., Koning, N., Ouyed, R., Thompson, A., & Pudritz, R. E. 2015, MNRAS, 446, 3975
Tabone, B., Cabrit, S., Pineau des Forêts, G., et al. 2020, A&A, 640, A82

A&A proofs: manuscript no. 44434

## Appendix A: Convergence of the results

A part of the aims of this study is to determine numerical parameter setups that produce consistent results for the disk and outflow dynamics. We present here a selection of the results in search for numerical convergence.

### Appendix A.1: Resolution

From a comparison between the results of Kölligan & Kuiper (2018) and studies that use AMR Cartesian grids, it was clear that resolution of the jet launching region is extremely important for capturing the magneto-centrifugal mechanism and obtaining velocities on the order of $\sim 1000\,\mathrm{km\,s^{-1}}$. In the resolution study we performed, however, we observed several other critical phenomena to be properly resolved by spatial grid.

A proper study of the propagation of the outflow is only possible if the large scales of the cavity are properly resolved. Figure A.1 shows a comparison of the outflow cavity at large scales for all the grids in our investigation. Grid x16 produces an outflow cavity that is well resolved at large scales. The cavity contains the tower flow at large scales, and its thickness changes smoothly with distance. The results for grid x8 show most of the features of grid x16, although the thickness of the cavity does not change as smoothly as in simulation x16 for early times, even though it does for late times when the tower flow broadens. The outer parts of the cavity are resolved by $\sim 6$ grid cells. For the grid x4, geometry of the cavity changes qualitatively. In smaller scales, we observe the flow to be restricted to lobes, while in outer scales the cavity is narrower. A closer look to the outflow cavity for late stages (where the flow is dominated by the tower flow) is offered in Fig. A.2. Beyond $z \sim 6\,000$ au, the cavity is not properly resolved (only 2-3 grid cells) and the toroidal nature of the magnetic field at large scales cannot be seen. The same is true for grids x2 (where the lobes are even smaller) and x1 (where the propagation of the outflow itself is not properly represented any more.

The total outflow momentum (Fig. A.3) is strongly hit by the resolution of the outflow cavity, but also by the minimum density resolved in the simulation. A higher resolution grid is able to produce lower densities as fine structures in the cavity are distinguished instead of being represented by their average density. Lower densities produce a weaker linear momentum. The curves for the total momentum in grids x4, x8 and x16 seem to agree in order of magnitude, which is attributable to a better agreement in the densities and velocities obtained. However, the curves also show a peak at early times only present in simulations x1, x2 and x4, which may be due to the improper resolution of the outflow cavity at large scales.

The narrowing of the cavity wall with the effects of magnetic braking was discussed in Sect. 3.8. We note that, when this width is not properly resolved, the launching point of the magneto-centrifugal mechanism quickly moves outward over time until the jet is completely terminated. This is the reason why in Fig. 11, we only show the results for grids x4 and x8, where the cavity is partially and properly resolved at all times, respectively.

### Appendix A.2: Alfvén limiter

As discussed in Paper I, we use a varying density floor such that the Alfvén speed of a given grid cell does not increase beyond a fixed limit. This Alfvén limiter creates artificial mass as a result. We performed a parameter scan with different values of the maximum allowed Alfvén velocity with the following values: $v^A_{\mathrm{max}} = 200, 500, 1000, 2000$ and $5000\,\mathrm{km\,s^{-1}}$. We monitored the total artificial mass generated in each case, and established a maximum acceptable value of $1\,\mathrm{M_\odot}$, that is, 1% of the mass of the cloud core, for the low-resolution exploratory runs. For grid x2, we observed that this limit was surpassed only for $v^A_{\mathrm{max}} = 200$ and $500\,\mathrm{km\,s^{-1}}$. For this reason, we chose $v^A_{\mathrm{max}} = 2000\,\mathrm{km\,s^{-1}}$ as the fiducial value for grids x1, x2 and x4. In grids x8 and x16, however, another parameter scan revealed that $v^A_{\mathrm{max}} = 1000\,\mathrm{km\,s^{-1}}$ yielded sufficiently low artificial masses (well below $0.005\,\mathrm{M_\odot}$), while saving computational costs, and therefore this value was chosen for the two highest-resolution runs. As a consequence, the artificial mass created by the Alfvén limiter has a negligible impact in the case of the high resolution runs we used for the main parameter scan in this study.

The Alfvén limiter is mostly active in the launching region of the jet (close to the massive protostar) and around the recollimation regions. Therefore, we cannot conclude on the maximum velocities observed in a protostellar jet. This limitation of our setup, which is based on classical physics, leaves theoretical room for the relativistic velocities required for the nonthermal emission observed in recollimation regions in protostellar jets (see, e.g., Moscadelli et al. 2022 and Rodríguez-Kamenetzky et al. 2017).

### Appendix A.3: Sink cell size

Finally, we wanted to check that our choice of a sink cell size does not fundamentally interfere with the physical processes described in this article. To this end, we performed a parameter scan with three values of the radius of the sink cell: 1 au, 3 au (our fiducial case) and 10 au. Due to computational costs, we only display the results for the first 15 kyr of evolution in Fig. A.4. We find that the magneto-centrifugal launching of the jet and the formation of the bow shock occur earlier with a smaller sink cell. However, all the processes described in Sect. 3 are present in all the simulations, and the launching of the jet seems to happen still around $t \sim 5$ kyr for the two smallest sink cell sizes.

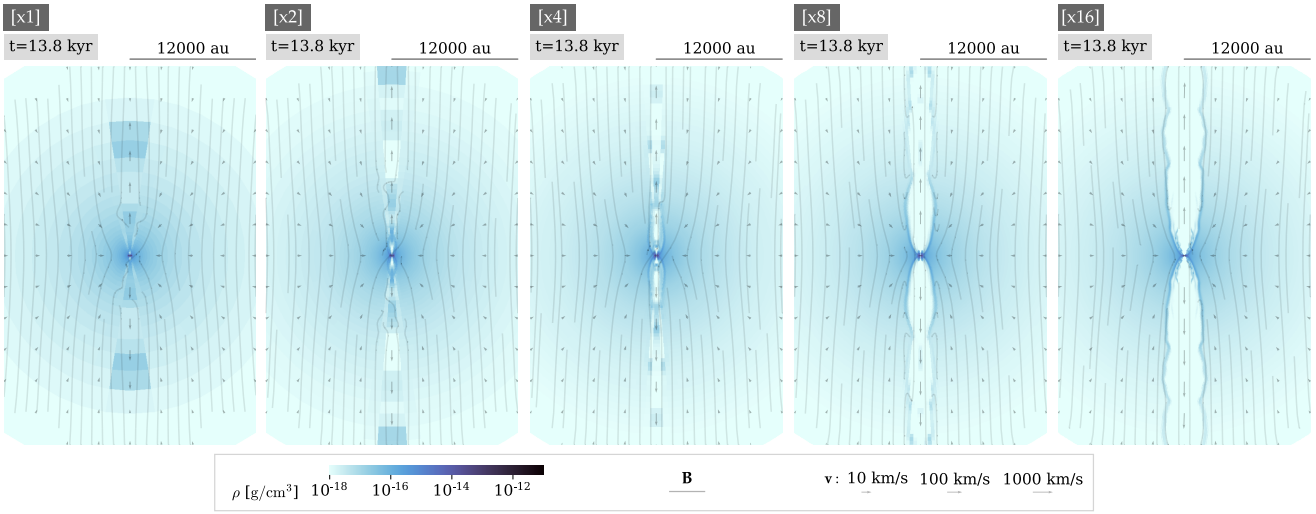



**Fig. A.1.** Convergence of the jet cavity with resolution.

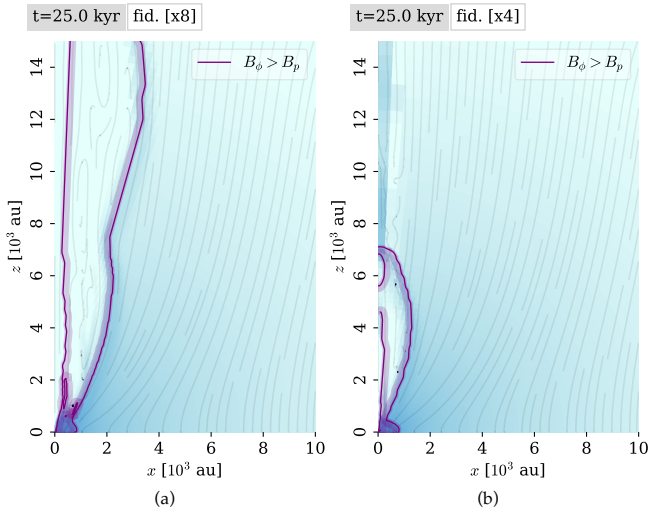



**Fig. A.2.** Convergence of the tower flow with resolution at large scales.

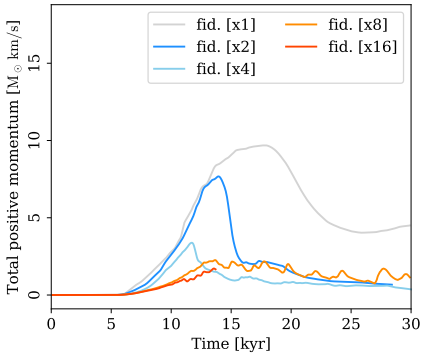



**Fig. A.3.** Convergence of the total jet momentum with resolution.

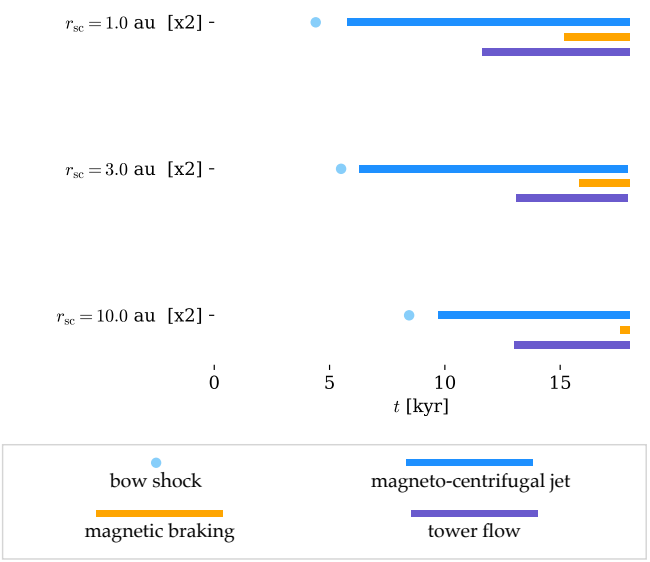



**Fig. A.4.** Convergence of the observed dynamical processes of the magnetic outflows as a function of the size of the sink cell.